

Correlation and fluctuation of particle multiplicity in hadronic and heavy ion collisions.

By

Prithwish Tribedy

Enrollment No. PHYS04201104002

Variable Energy Cyclotron Centre, Kolkata

A thesis submitted to

The Board of Studies in Physical Sciences

In partial fulfillment of requirements for the Degree of

DOCTOR OF PHILOSOPHY

of

HOMI BHABHA NATIONAL INSTITUTE



October, 2014

Homi Bhabha National Institute¹

Recommendations of the Viva Voce Committee

As members of the Viva Voce Committee, we certify that we have read the dissertation prepared by Prithwish Tribedy entitled "Correlation and fluctuation of particle multiplicity in hadronic and heavy ion collisions" and recommend that it may be accepted as fulfilling the thesis requirement for the award of Degree of Doctor of Philosophy.

Chairman - Prof. D.K. Srivastava  **Date:** 13/10/14

Guide / Convener - Prof. Subhasis Chattopadhyay  **Date:** 13/10/14

Co-guide - <Name> (if any) **Date:**

Member 1 - Prof. A. K. Mohanty  **Date:** 13-10-2014

Member 2- Prof. Jane Alam  **Date:** 13/10/2014

Member N - Prof. Raghava Varma 
(External) **Date:** 13/10/2014

Final approval and acceptance of this thesis is contingent upon the candidate's submission of the final copies of the thesis to HBNI.

I/We hereby certify that I/we have read this thesis prepared under my/our direction and recommend that it may be accepted as fulfilling the thesis requirement.

Date: 13/10/2014

Place: VECC-KOLKATA

<Signature>

Co-guide (if applicable)



<Signature>

Guide

¹ This page is to be included only for final submission after successful completion of viva voce.

STATEMENT BY AUTHOR

This dissertation has been submitted in partial fulfillment of requirements for an advanced degree at Homi Bhabha National Institute (HBNI) and is deposited in the Library to be made available to borrowers under rules of the HBNI.

Brief quotations from this dissertation are allowable without special permission, provided that accurate acknowledgement of source is made. Requests for permission for extended quotation from or reproduction of this manuscript in whole or in part may be granted by the Competent Authority of HBNI when in his or her judgment the proposed use of the material is in the interests of scholarship. In all other instances, however, permission must be obtained from the author.



Prithwish Tribedy

DECLARATION

I, hereby declare that the investigation presented in the thesis has been carried out by me. The work is original and has not been submitted earlier as a whole or in part for a degree/diploma at this or any other Institution/University.



Prithwish Tribedy

List of Publications

Journal

For the STAR collaboration

1. “Search for QCD Phase Transitions and the Critical Point utilising Particle Ratio Fluctuations and Transverse Momentum Correlations from the STAR Experiment”
Prithwish Tribedy [for the STAR Collaboration].
[Nucl. Phys. A904-905](#) **2013**, 463c (2013) [arXiv:1211.0171]
2. “Charged-to-neutral correlation at forward rapidity in Au+Au collisions at $\sqrt{s_{NN}}=200$ GeV”
(L. Adamczyk et al.) **Prithwish Tribedy** as PA for the STAR Collaboration
[Phys. Rev. C](#) **91**, 034905 (2015) [arXiv:1408.5017]

Other publications

1. “Saturation models of HERA DIS data and inclusive hadron distributions in p+p collisions at the LHC”
Prithwish Tribedy and Raju Venugopalan.
[Nucl. Phys. A](#) **850**, 136 (2011) [arXiv:1011.1895].
2. “Study of γ -charge correlation in heavy ion collisions, various approaches”
Prithwish Tribedy, Subhasis Chattopadhyay and Aihong Tang.
[Phys. Rev. C](#) **85**, 024902 (2012) [arXiv:1108.2495].
3. “QCD saturation at the LHC: comparisons of models to p+p and A+A data and predictions for p+Pb collisions”
Prithwish Tribedy and Raju Venugopalan.
[Phys. Lett. B](#) **710**, 125 (2012) [arXiv:1112.2445]
4. “Fluctuating Glasma initial conditions and flow in heavy ion collisions”
Björn Schenke, **Prithwish Tribedy** and Raju Venugopalan.
[Phys. Rev. Lett.](#) **108**, 252301 (2012) [arXiv:1202.6646].
5. “Event-by-event gluon multiplicity, energy density, and eccentricities in ultrarelativistic heavy-ion collisions”
Björn Schenke, **Prithwish Tribedy** and Raju Venugopalan.
[Phys. Rev. C](#) **86**, 034908 (2012) [arXiv:1206.6805].

6. “Event-by-event anisotropic flow in heavy-ion collisions from combined Yang-Mills and viscous fluid dynamics”
Charles Gale, Sangyong Jeon, Björn Schenke, **Prithwish Tribedy** and Raju Venugopalan.
[Phys. Rev. Lett. **110**, 012302 \(2013\)](#) [arXiv:1209.6330].
7. “Predictions for p +Pb Collisions at $\sqrt{s_{NN}} = 5$ TeV”
J. L. Albacete *et al.*
[Int. J. Mod. Phys. E **22**, 1330007 \(2013\)](#) [arXiv:1301.3395]
8. “Initial state geometry and the role of hydrodynamics in proton-proton, proton-nucleus and deuteron-nucleus collisions”
Adam Bzdak, Björn Schenke, **Prithwish Tribedy** and Raju Venugopalan.
 [Phys. Rev. C **87**, 064906 \(2013\)](#) [arXiv:1304.3403]
9. “Multiplicity distributions in p+p, p+A and A+A collisions from Yang-Mills dynamics”
Björn Schenke, **Prithwish Tribedy** and Raju Venugopalan.
[Phys. Rev. C **89**, 024901 \(2014\)](#) [arXiv:1311.3636]
10. “Initial state geometry and fluctuations in Au+Au, Cu+Au and U+U collisions at RHIC”
Björn Schenke, **Prithwish Tribedy** and Raju Venugopalan.
[Phys. Rev. C **89**, 064908 \(2014\)](#) [arXiv:1403.2232]

Conferences

1. “Inclusive hadron distributions in p+p collisions from saturation models of HERA-DIS data”
Prithwish Tribedy and Raju Venugopalan.
[Nucl. Phys. A **862-863**, 367-370 \(2011\)](#) - Special Issue [arXiv:1101.5922].
2. “Initial state fluctuations and higher harmonic flow in heavy-ion collisions”
Charles Gale, Sangyong Jeon, Björn Schenke, **Prithwish Tribedy** and Raju Venugopalan.
[Nucl. Phys. A904-905 **2013**, 409c \(2013\)](#) [arXiv:1210.5144].
3. “Glasma fluctuations in heavy-ion collisions”
Björn Schenke, **Prithwish Tribedy** and Raju Venugopalan.
[AIP Conf. Proc. **1560**, 650 \(2013\)](#)
4. “Gluon field fluctuations in nuclear collisions: Multiplicity and eccentricity distributions”
Björn Schenke, **Prithwish Tribedy** and Raju Venugopalan.
[Nucl. Phys. A102-108, 926 \(2014\)](#)[arXiv:1312.5588]
5. “Particle production and final state effects in nuclear collisions”
Charles Gale, Sangyong Jeon, Björn Schenke, **Prithwish Tribedy** and Raju Venugopalan.
[J. Phys. Conf. Ser. **535** \(2014\) 012026.](#)
6. “Initial state geometry and fluctuations in deformed and asymmetric nuclear collisions in the IP-Glasma framework”
Björn Schenke, **Prithwish Tribedy** and Raju Venugopalan.
[Nucl. Phys. A **931**, 288-292 \(2014\)](#)

Dedicated to my grandparents

Acknowledgement

I am extremely thankful to my advisor Prof. Subhasis Chattopadhyay for his constant supervision and training. I admire his patience during the early stages of my training and very much appreciate his encouragement towards independent thinking. I convey my deepest gratitude to my mentor Prof. Raju Venugopalan for his constant teachings and guidance. Words are inadequate for his efforts to enrich my knowledge and to grow my interest towards various open problems through countless number of discussions. Special thank goes to my collaborators Dr. Bjoern Schenke and Dr. Aihong Tang whose caring and invaluable support helped me to commence a major part of my research. I thank the members of my thesis committee and referees for their constructive suggestions. I am grateful to Prof. Jane Alam, Prof. Ashis K Choudhuri, Prof. Sourendu Gupta, Prof. Sangyong Jeon, Prof. Larry McLerran, Prof. Ajit Mohanty, Prof. Tapan K Nayak, Prof. B K Patra, Prof. Bikash Sinha, Prof. Sourav Sarkar, Prof. Dinesh K Srivastava and Prof. Raghava Varma for their teachings, valuable suggestions and encouragements. I would like to convey my heartfelt thanks to my colleagues and collaborators Partha P Bhaduri and Prasad Hedge for sharing their experience and insights with me. I am very much grateful to my senior colleagues Bedanga Mohanty, Anand K Dubey, Sanjib Muhuri, Mriganka M Mondal, Sidharth K Prasad and Jajati K Nayak. Their advice on my research and career have been very useful to me. A special note of thanks goes to Premomoy Ghosh whose constant caring companionship has enriched my personal and professional life. A warm affection and gratitude is extended towards my friends, Debashis Banerjee, Santosh K Dash, Hari Poi, Victor Roy, Nihar R Sahoo, Pratap Roy and Arindam Roy who have helped me in many ways to complete this work. I thank all my fellow collaborators of the STAR experiment at RHIC, particularly Daniel Cebra, Paul Sourensen, Hiroshi Masui and Zhangbu Xu, from whom I have learned a lot over past years. I enjoyed my time of discussion with Raktim Abir, Adam Bzdak, Purnendu Chakraborty, Sandeep Chatterjee, Kevin Dusling, Swagato Mukharjee and Hui Wang. I thank Nuclear theory group of BNL, TPSC of India and department of Physics of IIT Roorkee, IIT Bombay, University of Jammu and Central China Normal University for their hospitality and support. I thank Prof. Sean Gavin, Prof. Xin Nian Wang and Prof. Nu Xu for their kind invitations to present my work. I thank everyone from the PMD collaboration of India. The computing facilities of RCF at BNL, NERSC at LBNL, grid-peer Kolkata, DRONA and PRAFULLA clusters at VECC are acknowledged.

I am very lucky to have a wonderful family that has been the source of endless love and support. I am grateful to my parents, Probir Kumar Tribedy and Anusua Tribedy and also my sister Elora Tribedy for their constant inspiration to pursue a career in research.

Contents

Synopsis	12
List of Figures	15
List of Tables	25
1 Introduction	26
1.1 New form of matter under extreme conditions	26
1.2 Phase transitions in QCD	29
1.3 The Conventional model of Heavy ion collisions and QGP	31
1.4 Observables for HG to QGP transitions in relativistic heavy ion collisions	32
1.4.1 De-confinement transition of the medium	32
1.4.2 Fluid like property of the medium	34
1.4.3 Opacity of the medium	35
1.4.4 Thermal property of the medium	36
1.4.5 Correlation and fluctuations in the medium	39
1.5 Outline of this thesis work	39
1.5.1 Modelling of fluctuations from the initial stages of heavy ion collisions. . .	40
1.5.2 Modelling of fluctuation from the final stages of evolution and detection .	41
1.5.3 Measurement of inclusive charged and neutral multiplicity fluctuation in heavy ion collisions.	42
2 Observables for multiplicity fluctuation and correlation	45
2.1 Introduction: selection of observables	45
2.2 Factorial moments and generating function approach	46
2.3 Observable ν_{dyn} and $r_{m,1}$	49
2.3.1 Effect of efficiency	50
2.3.2 Effect of mis-identification	54
2.3.3 Effect of resonance decay	56
2.3.4 Effect of rapidity gap	58
2.3.5 Effect of centrality selection	58
2.4 Application of the observables in heavy ion collisions : model studies	61
2.4.1 Statistical models for pion production.	62
2.4.2 Transport and Mini-jet model predictions	64

2.5	γ -charge correlation and DCC	65
2.5.1	Effect of mixture of pion sources	68
2.5.2	A Monte-carlo model for DCC formation.	70
2.6	Summary	74
3	Measurement of charge and neutral multiplicity fluctuation in Au+Au collisions	76
3.1	Introduction	76
3.2	Analysis Method	77
3.3	The STAR detector systems	79
3.3.1	Time Projection Chamber	80
3.3.2	Electromagnetic Calorimeter	81
3.3.3	Time of Flight Detector	81
3.3.4	Forward Time Projection Chambers	82
3.3.5	Photon Multiplicity Detector	82
3.3.6	Detector setup for this measurement	83
3.4	Data Cleanup	84
3.4.1	Event selection	84
3.4.2	Data sets and particle identification	85
3.4.3	Quality Assurance studies	86
3.4.4	Run-by-Run QA for removal of bad runs.	89
3.5	Events mixing	89
3.6	Bin-width effect	96
3.7	Error analysis	98
3.7.1	Statistical uncertainty	98
3.7.2	Systematic uncertainty	100
3.8	GEANT simulation for detector response	101
3.9	Results for charge-neutral correlations	105
3.10	Individual charge and neutral fluctuations	105
3.11	charge-neutral correlation and ν_{dyn}	106
3.12	Robust observables	107
3.13	Comparison to net charge correlation	108
3.14	Effect of rapidity gap on $\gamma - \text{ch}$ correlation	109
3.15	N_{part} dependence of $\gamma - \text{ch}$ correlation.	112
3.16	Effect of flow on $\gamma - \text{ch}$ correlation.	113
3.17	An upper limit of DCC like signals from data	116
3.18	Summary	117
4	Modelling fluctuations from the initial stages of collisions	118
4.1	Introduction	118
4.2	The phenomenon of gluon saturation	119
4.3	The small- x problem of QCD	120
4.4	Saturation models of HERA DIS	122
4.4.1	The IP-Sat Model	123

4.4.2	The b-CGC Model	126
4.4.3	The rc-BK Model	128
4.5	Particle production : Perturbative approach	129
4.5.1	Results for p+p collisions	132
4.5.2	Results for p+A/d+A collisions	137
4.5.3	Results for A+A collisions	140
4.5.4	Multiplicity fluctuation in the perturbative framework	143
4.6	Particle production : Non-perturbative approach	150
4.6.1	Results for p+p collisions	156
4.6.2	Results for p+A/d+A collisions	158
4.6.3	Results for A+A	161
4.6.4	Multiplicity fluctuation in the non-perturbative framework	163
4.7	Initial state geometry and fluctuation in heavy ion collisions	168
4.8	Summary	172
	Summary	173
	Bibliography	178
	Index	193

Synopsis

The conventional model of relativistic heavy ion collisions describes two Lorentz contracted sheets of saturated partonic matter colliding to form a high energy density ensemble of gluonic states at the initial stage. This initial phase undergoes a pre-equilibrium evolution and eventually thermalizes to form a strongly correlated Quark Gluon Plasma (sQGP) which subsequently undergoes a transition to hadronic matter. The hadronic matter undergoes further interaction and finally free stream to the detectors. The total number of particles produced (multiplicity) in heavy ion collisions fluctuates from even-to-event.

The goal of this thesis is to study the fluctuations and correlation of inclusive multiplicity in heavy ion collisions. Contributions to multiplicity fluctuation and correlation come from different stages of collisions and can carry information of the evolution of the system. Hadronic collisions serve as reference to set the baseline for various observations in heavy ion collisions. This work addresses the following broad topics :

- 1. Correlation and fluctuation from the initial stages of heavy ion collisions.**

The geometric fluctuation of the overlap zone of two nuclei due to fluctuation of impact parameter is the major source of multiplicity fluctuation in heavy ion collisions. The quantum fluctuation of nucleon positions which are distributed according to Fermi distribution is another dominant source of initial state fluctuation. In addition to that there are sub-nucleonic quantum fluctuations, the dynamics of which is governed by the saturated nuclear wave function at low Bjorken x . The framework of Color Glass Condensate provides an *ab initio* treatment to this problem by including all such sources of fluctuations.

This thesis work includes extraction of hadronic and nuclear wave functions using saturation models of HERA DIS data to predict inclusive multiplicity distributions in p+p, p+A and A+A collisions at RHIC and LHC energies. To study different sources of fluctuation at the initial stages of collisions a new model of initial conditions called the “Impact Parameter dependent Glasma” (IP-Glasma) was developed. This model computes the initial gluon fields and their Yang-Mills evolution on a two dimensional real-time lattice. It naturally describes inclusive multiplicity fluctuations and can be used to study wide range of systems like p+p, p+A/d+A and A+A. When combined with viscous hydrodynamic simulations, at present, “IP-Glasma” is the only model of initial condition that consistently describes all higher orders of anisotropic flow harmonics and their event-by-event fluctuations measured at RHIC and LHC.

2. Correlation and fluctuation from the medium created in heavy ion collisions.

The subsequent stage after the pre-equilibrium evolution is the formation of a medium of Quark-Gluon Plasma. This medium undergoes a phase transition to Hadronic matter. Since experimentally a limited phase space is probed, in the Grand Canonical Ensemble picture, the dynamical fluctuation of conserved charges are sensitive to such a phase transition. The transition from QGP to hadron gas is associated with the QCD chiral phase transition. For such a scenario, there have been predictions about formation of metastable domains of disoriented chiral condensate (DCCs), in which the four component chiral condensate is misaligned w.r.to the vacuum. The decay of such domains produce pions of one particular isospin which would lead to an anti-correlation between observed charged and neutral particles. The later stage of the heavy ion collisions include decays of many massive resonances that affect the correlations between charged and neutral particles. This thesis work includes detailed analysis of data from the STAR experiment to study the dynamical fluctuations of charged and neutral particle (γ) multiplicities and their correlated production in heavy ion collisions. The goal is to search for exotic events like the formation of the domains of Disoriented Chiral Condensates (DCC) during a QCD chiral phase transition.

This thesis work includes the only γ -charge correlation measurement and search for DCCs at RHIC after the WA98 experiment at SPS and the MiniMax experiments at Tevatron. Detailed study includes the measurement of photon and charge particle distributions using a combination of a photon detector and two charge particle detectors separated by a rapidity gap. Observables constructed out of factorial moments of multiplicities have been used as measures of fluctuation and correlation. Energy, centrality and charge dependence of charged-to-neutral particle correlation were compared to the correlation between the multiplicities of positively and negatively charged particles. Mixed event and GEANT simulations were performed to understand the detector effects. Simulations using available hadronic transport and mini-jet models were performed for baseline studies.

3. Correlation and fluctuation from the final stages of detection.

The binomial response of the detector systems naturally induces spurious multiplicity fluctuations in the process of particle detection. Additional effects that might give rise to spurious correlations and fluctuations are decay and mis-identification of particle species. A moment generating function approach has been used to incorporate different sources of such spurious fluctuations. This work includes the design of robust observables and analysis techniques for the STAR experimental setup. Additional studies include : development of methods to quantify the strength of DCC like signals and other signals of dynamical correlation and fluctuation from the measured distributions of photons and charged particles.

List of Figures

1.1	Mass generation at the Electro Weak and the QCD scale, schematic from ref. [36]	28
1.2	Schematic of the QCD phase diagram (conjectured), left panel shows theoretical predictions and right panels shows the trajectories of heavy ion collisions.	30
1.3	Schematic of heavy ion collisions, a figure by S. Bass.	31
1.4	(Left) Lumpy initial parton density in a colliding Au nucleus. Only quantum fluctuations at nucleonic scale are present. (Right) The transverse energy density after collision of two Au nuclei at 200 GeV at zero impact parameter. Quantum fluctuations at both nucleonic and sub-nucleonic scales are present, which will result in fluctuation of global observable such as multiplicity and flow harmonics v_n	40
1.5	Cartoon of the fireball created in heavy ion collisions. Experimentally only a small fraction of the fireball is probed, in which conserved charges can be exchanged, this way a GCE picture is valid.	42
1.6	Spontaneous breaking of chiral symmetry in linear sigma-model. The four component condensate $(\sigma, \vec{\pi})$ is misaligned with its vacuum direction in case of DCC domains. Schematic from Ref. [149].	43

2.1	Effect of efficiency using Monte Carlo simulation. The effect of efficiency is introduced by hand using two random Poisson and Gaussian numbers. It seems that all the observable constructed out of factorial moments are insensitive to the variation of efficiency. A small numerical noise of similar magnitude is observed for all the observables when the scaled difference between the incident and the observed variable is considered. For Poisson distribution the observable $\nu_{\text{dyn}} \sim 0$.	54
2.2	Effect of multiplicity correlation with rapidity gap. The points indicates HIJING simulation. PGV (Pruneau-Gavin-Voloshin) refers to the functional fit of the simulation points using Eq. 2.40 which is taken from Ref. [155].	59
2.3	Multiplicity dependence of observables $r_{1,1}$ and $\Delta\nu_{\text{dyn}}$ as predicted from different models. The curves represent the results for different ensembles of Boltzmann gas of pions from Eq. 2.47 and Eq. 2.49 as described in the text. The markers are from different Monte-Carlo models. The error-bars are statistical.	64
2.4	Sensitivity of the observable $r_{m,1}$ to DCC like signals. Higher orders of $r_{m,1}$ show more sensitivity to small signals of anti-correlation.	67
2.5	Histograms showing distribution of neutral pion fraction for generic and DCC events from HIJING	71
2.6	Multiplicity dependence of observables $r_{1,1}$ and ν_{dyn} as predicted from DCC implemented HIJING model. Here N_{ch} and N_{γ} denote the mean multiplicities of charged particles and photons for various centralities. The gray band shows the statistical uncertainty in model calculation.	72
2.7	Prediction of variables from different models.	72
2.8	Sensitivity of $r_{m,1}$ to DCC like signals.	73
3.1	Layout of the STAR detector system.	80
3.2	Experimental setup for this analysis	83
3.3	Global quality assurance (QA) plots relevant to data analysis.	84
3.4	Quality assurance plot for the FTPCs relevant to this analysis.	87

3.5	Quality assurance plot related to PMD.	88
3.6	Run-by-run QA of common acceptance. The run-by-run $\eta - \phi$ acceptance plot of PMD is shown by orange and FTPC by green points respectively. The common coverage is shown by black points. The range of run numbers for which the common coverage remains unchanged has been used for analysis	90
3.7	Run-by-run variation of various quantities averaged over most central (0-10%) events in a given run. For clarity of the plot, the quantity plotted on x-axis is the index of the run number. The solid line represents the mean value over all the range of runs. The dashed line shown for $\pm\sigma$ variation from the mean values to guide the eye. All the quantities except $\langle N_\gamma \rangle$ and $\langle N_{\text{ch}} \rangle$ have been used to extract bad runs.	91
3.8	Effect of run-by-run QA on final observables. The variation is shown for two different cases of run number cuts along with the case of no cut.	92
3.9	(a-h) Centrality wise N_γ (we also refer as N_γ^{like}) distributions for real and mixed events. (i) Correlation plot between photon clusters and their total ADC.	93
3.10	(a-h) Centrality wise N_{ch} distributions for real and mixed events. (i) Correlation between event-by-event charged particle and photon multiplicity.	94
3.11	Bin width effect for observables ν_{dyn} and $r_{m,1}$	97
3.12	Bin width correction for observables ν_{dyn} and $r_{m,1}$	97
3.13	Statistical uncertainty of ν_{dyn} . The mean and variance of the 100 samples are shown by 3 solid lines (Black line is the mean and blue lines are $\pm\sigma$) which gives the statistical uncertainty from the bootstrap method. Error for individual points are obtained by using the published analytical formula of Ref. [165].	98
3.14	Statistical uncertainty of $r_{1,1}$. The mean and variance of the 100 samples are shown by 3 solid lines (Black line is the mean and blue lines are $\pm\sigma$) which gives the statistical uncertainty from the bootstrap method.	99

3.15	Sources of the systematic uncertainties of ν_{dyn} and $r_{1,1}$. The effect on the observables are shown for variation of different cuts applied.	100
3.16	Centrality wise multiplicity distributions for charged tracks using HIJING and GEANT+HIJING simulations in the FTPCE coverage.	103
3.17	Centrality wise multiplicity distributions for photons for HIJING and GEANT+HIJING simulation in the PMD coverage.	104
3.18	Individual fluctuation of charge and photon multiplicities.	105
3.19	Scaled correlation and ν_{dyn} for charge and photons.	106
3.20	(a) $r_{m,1}$ vs multiplicity for STAR data (Au+Au 200 GeV real events). (b) Robust observable $r_{m,1}$ and its higher moments for Real & Mixed events. Model calculations are shown by bands. Statistical error bars are shown by vertical lines and the systematic error bars are shown by boxes (real events), bars (mixed events) and bands (models).	108
3.21	(left) Charge dependence of the observable ν_{dyn} showing different behaviour for different combinations of $\gamma - \text{ch}$ compared to that of opposite charge combination. Data points plotted are for real events. The statistical error bars are shown by lines. For positive-negative charge correlation the systematic uncertainties are shown by caps. For different combinations of $\gamma - \text{ch}$ correlation, the systematic uncertainties in $\langle N_{\text{ch}} N_{\gamma} \rangle$ are shown by caps whereas the systematic uncertainties in ν_{dyn} are shown by the yellow band. (right) Variation of $r_{m,1}$ with m for $\gamma - \text{ch}$ (real and mixed events) and for opposite charge combination. The results are shown for 0 – 10% centrality only.	109
3.22	Correlation of PMD with east FTPC.	110
3.23	Correlation of PMD with west FTPC.	111

3.24	Robust observable using photons from PMD and charged particles using east and west FTPCs. Yellow bands are simulation results for PMD and West FTPC; the purple bands are simulation results for PMD and East FTPC. In both the cases, the light color solid bands are for GEANT+HIJING calculations and the dark bands are for Raw HIJING.	112
3.25	N_{part} dependence of all terms of ν_{dyn} for PMD-FTPC (East) (same-side)	113
3.26	N_{part} dependence of all terms of ν_{dyn} for PMD-FTPC (West) (opposite-side)	114
3.27	Effect of flow on $\gamma - \text{ch}$ correlation. Data points are also plotted for better comparison. Left: variation of ν_{dyn} with multiplicity. Right: variation of $r_{m,1}$ with m for most central events.	115
3.28	(left) Fit the data points for $r_{m,1}$ as a function of m using the functional form of Eq. 2.67 for two most central events. (right) Parameters of DCC model extracted from data, the shaded region shows the upper limit of DCC formation.	116
4.1	(left)HERA data on structure parton distribution function measured in DIS processes from Ref. [182]. (right) Energy dependence of measured cross sections for pp collision from Ref. [183].	119
4.2	Left: Dipole cross-section in DIS. Right: Overlap of unintegrated gluon distributions in proton-proton collisions.	124
4.3	$dN/d\eta$ obtained from comparing IP-Sat and b-CGC models to data from UA5 [220], ALICE [221] and CMS [222]. The solid green band corresponds to uncertainties from different parameters; the dashed band is due to the variation of the choice of mass term in the Jacobian relating y to η . The two curves at the top in both panels correspond to projections in the two models for $\sqrt{s} = 14$ and 10 TeV respectively.	132

4.4	<p>$dN/d^2p_\perp d\eta$ in the IP-Sat and b-CGC models. The solid (green) band corresponds to uncertainties from different parameters and the dashed (blue) band is due to variation of the mass term in the Jacobian relating η to y. The p_\perp distribution is averaged over the η range of ± 2.4. The experimental data points are from CMS [222], STAR [223] and ATLAS [224]</p>	134
4.5	<p>Average $dN/d\eta _{\eta \approx 0}$ in the IP-Sat and b-CGC models. Left: Data plotted as a function of saturation scales Q_S (at median impact parameter $b_{\text{med}} = 2 \text{ GeV}^{-1}$) for both the models determined from the HERA data. Right: Average $dN/d\eta$ at $\eta = 0$ from the k_\perp-factorized expression in Eq. 4.24 from IP-Sat (solid green) and b-CGC (dashed) models. Experimental data points are from Ref. [222, 223, 226–228]</p>	135
4.6	<p>Average p_\perp obtained from IP-Sat and b-CGC models compared to data. Left: Function of saturation scales fitted for both the models. Right: Average p_\perp from the k_\perp-factorized expression in Eq. 4.24. The thin (colored) bands correspond to uncertainties arising from different parameters in table 4.1 and table 4.2 and mass term = 0.2 GeV. The thick (gray) band shows the sensitivity to variation of mass term in the range 0.2–0.3 GeV (with lower mass corresponding to lower $\langle p_\perp \rangle$). Experimental data points are from Ref. [222, 227, 229, 230].</p>	136
4.7	<p>Pseudo-rapidity and p_\perp distribution in the rc-BK model compared to data. The uppermost two plots in the left panel correspond to predictions for $\sqrt{s} = 14, 10$ TeV with $m = 0.4$ GeV. The p_\perp distribution is averaged over the η range of ± 2.4. The band corresponds to the variation $m = 0.2\text{--}0.4$ GeV in the Jacobian relating η to y.</p>	137
4.8	<p>Transverse momentum distributions at forward rapidities in rcBK and IP-Sat models compared to STAR [231] and BRAHMS [232] data. The gray bands show the uncertainty in the determination of the normalization constant.</p>	138

4.9	Energy dependence of the minimum bias single inclusive multiplicity at $\eta = 0$ in p+A collisions from k_{\perp} -factorized unintegrated distributions determined in the rcBK and IP-Sat models. The distribution is normalized with respect to the PHOBOS d+Au data [233] at 200 GeV. The band represents the uncertainty in the calculation due to the variation of the mass term in the range of 0.2-0.4 GeV.	139
4.10	Pseudo-rapidity distribution for minimum-bias p+A collision at RHIC and LHC energies. Prediction from rcBK shown for mass term $m=0.2$ and 0.4 GeV. Data points are from ref. [233, 234]	140
4.11	Transverse momentum distribution at forward rapidity at the highest RHIC energy and compared to STAR [231] and BRAHMS [232] data. The gray bands show the uncertainty in determination of normalization constant from various sources.	141
4.12	Transverse momentum distribution at mid-rapidity for minimum-bias p+p and p+A collisions.	142
4.13	Nuclear modification factor for charged hadrons at mid-rapidity of the centre of mass frame for p+A collisions at LHC energies.	143
4.14	Left: Energy dependence of the multiplicity per participant pair in the IP-Sat model for p+p and A+A collisions. For the A+A case, the calculation is done for the 0 – 6% centrality. Right: same plot for A+A with fixed (solid) and running (dashed) coupling. Data points for p+p are from ref. [239–242] and for A+A from ref. [243, 244]	144
4.15	Centrality dependence of the inclusive multiplicity in the IP-Sat model compared to RHIC [247] and LHC [248] data. Left: (fixed coupling) 200 GeV values for both data and model are multiplied by a factor 2.08. Right: Same plot comparing running (solid curve) and fixed coupling (dashed curve) results in the IP-Sat model.	145

4.16	Pseudo-rapidity distribution from \mathbf{k}_\perp -factorization formula. Left: fixed coupling results for 200 GeV and 2.76 TeV. Right: Same plot($m=0.4$) at 2.76 TeV with running (solid curve) and fixed coupling(dashed curve) in \mathbf{k}_\perp -factorization formula. Data points are from ref. [249, 250]	146
4.17	Left: Variation of the saturation scale with the collision energy. Right: Variation of $Q_s^2 S_\perp$ for different impact parameters and the c.m. energy of the collision. The solid lines are for the IP-Sat model and crosses for the b-CGC model, in each case for the parameters providing the best fit to the HERA data.	147
4.18	Probability distribution as a function of impact parameter for an inelastic collision computed using Eq. 4.31 for the b-CGC and IP-Sat models.	148
4.19	Probability distribution of the gluon multiplicity computed in the IP-Sat model (parameter set I) and the b-CGC model (parameter set II) compared to the UA5[265] and ALICE[226] data for different η ranges. Left: Multiplicity distribution for the η range ± 0.5 . Right: Multiplicity distribution for the η range ± 1	149
4.20	Left: Multiplicity distribution for Au+Au collisions in the IP-Sat model compared to uncorrected data(histogram [243]) for different values of m . Both data and model plots are normalized for better comparison. Right: Multiplicity distribution for Au+Au collisions at 200 GeV and its sensitivity to the non perturbative constant ζ	150
4.21	Initial state geometry and correlation in the colliding nuclei.	152
4.22	Charged particle multiplicity as a function of pseudo-rapidity compared to experimental data from the UA5 [283] and the CMS collaboration [284]. Thick (colored) lines correspond to the best parameter set for AA collisions. Thin (gray) lines use $m_{\text{eff}} = 200$ GeV which makes the dip around $\eta = 0$ less prominent, and $N_y = 10$, $\tau = 0.5$ fm, and $Q_s/g^2\mu = 0.75$	156

4.23	Charged particle multiplicity obtained using Eq. (4.53) as a function of transverse momentum compared to experimental data from the ATLAS collaboration [287].	158
4.24	Transverse momentum distribution in p+Pb collisions.	159
4.25	Charged particle multiplicity as a function of pseudo-rapidity in d+Au collisions at 200 GeV and p+Pb collisions at 5.02 TeV compared to experimental data from the PHOBOS and BRAHMS collaborations [233, 299] and the ALICE collaboration [300].	160
4.26	Centrality dependence of multiplicity in A+A collisions for different systems. . .	161
4.27	Multiplicity fluctuation in p+p and p+Pb collisions in the IP-Glasma model. . .	163
4.28	(left) Probability distribution of gluon multiplicities dN/dy at $\tau = 0.4$ fm/ c . Shown are also the distributions for some limited ranges of impact parameter b , which are described by negative binomial distributions. (right) Prediction for LHC energy $\sqrt{s} = 2.76$ TeV. Experimental data from STAR [309].	164
4.29	Fluctuation of multiplicity and energy density in IP-Glasma model.	165
4.30	Parameters of NBD in the non-perturbative framework.	167
4.31	Proportionality factor ζ in $k = (\zeta(N_c^2 - 1)/(2\pi))Q_s^2 S_\perp$ as a function of $Q_s^2 S_\perp$ for averaged nucleon positions (squares) and with nucleon fluctuations at fixed impact parameter $b = 0$ fm (circles). At large $Q_s^2 S_\perp$ the result for the smooth distribution approaches a constant as predicted by the Glasma flux tube model for n-gluon correlations. The result for fluctuating nucleon positions at constant $b = 0$ fm is very similar and becomes very weakly dependent on $Q_s^2 S_\perp$	168
4.32	Energy density (arbitrary units) in the transverse plane at $\tau = 0$ fm (upper panel) and $\tau = 0.2$ fm (lower panel). The structures are smoothed by the evolution over the first $\Delta\tau \sim 1/Q_s$	169
4.33	Initial energy density (arbitrary units) in the transverse plane in three different heavy-ion collision events: from left to right, IP-Glasma, MC-KLN and MC-Glauber [318] models.	170

4.34 Even (upper panel) and odd (lower panel) eccentricities from the IP-Glasma model compared to those from MC-KLN.	171
---	-----

List of Tables

2.1	Summary of our estimation of observables $\Delta\nu_{\text{dyn}}^{\gamma\text{-ch}}$ and $r_{m,1}^{\gamma\text{-ch}}$ under different scenarios relevant to heavy-ion collisions. $\Delta\nu_{\text{dyn}}^{\gamma\text{-ch}}$ is either 0 or negative except for DCC case which gives positive value depending on the fraction x and y . $r_{m,1}^{\gamma\text{-ch}}$ shows a particular functional dependence on m for DCC case which is distinct from all other scenarios.	74
3.1	Centrality cuts used in this analysis in terms of reference multiplicity described in the text and corresponding N_{part} obtained from Monte Carlo Glauber model.	85
3.2	Summary of data sets and different kinematic cuts used in this analysis.	86
3.3	List of total systematic uncertainties due to different cuts are listed below.	102
4.1	Parameters of the IP-Sat model obtained from the fit to HERA data [199].	125
4.2	Parameters of the b-CGC model obtained from fits to HERA data [204].The second row of parameters gives the best fit to HERA data.	128
4.3	Comparison between different models of initial conditions.	170

Chapter 1

Introduction

1.1 New form of matter under extreme conditions

Behaviour of matter under extremely high temperature and density became a topic of interest in early 1950's when Fermi proposed the possibility of new states of matter at very large pressure and temperature [1]. Around similar time Pomeranchuk pointed out that hadrons which are the constituent of nuclear matter, and the most dense system known at that time, should have a limiting temperature and density [2]. About a decade after that, Hagedron while studying an ideal gas of resonances proposed an ultimate temperature of strongly interacting matter [3]. With the pioneering discoveries of the asymptotic freedom [4, 5] and the infrared slavery [6, 7] in 1973-74, Quantum Chromodynamics (QCD) was established to be the right theory of strong interaction. QCD being an asymptotically free theory predicts a deconfined system of weakly interacting quarks and gluons at high energy and densities. In 1975 it was realised [8, 9] that matter at very high energy density ($\sim 1 \text{ GeV}/\text{fm}^3$) will no longer consist of separate hadrons but a phase consisting of quarks and gluons. Due to analogy with similar phenomena in atomic physics driven by the laws of Quantum Electrodynamics (QED), in 1980 this new phase of matter was named as the QCD Plasma or Quark-Gluon Plasma(QGP) [10]. The phase transition from Hadronic matter (or a phase of Hadron Gas) to QGP is theoretically

predicted by QCD. Numerical calculations using Lattice QCD also show an approximately first order phase transition [11] for which the temperature and pressure remain nearly constant over a wide range of energy densities from 0.5-1.4 GeV/fm³.

In early 80's it was suggested that by colliding two heavy nuclei it may be possible to excite hadronic matter into the new phase of QGP [10, 12]. Experimental searches of QGP started when the Alternating Gradient Synchrotron (AGS) facility at BNL and the Super Proton Synchrotron (SPS) facility at CERN started colliding heavy ions at relativistic energies, which was explored by several fixed target experiments. SPS collided two Pb nuclei at the centre of mass energy of $\sqrt{s_{NN}} = 17$ GeV which could produce about an initial energy density of 4 GeV/fm³, a favourable scenario to produce the QGP phase. Experimental results from SPS provided first hints of the formation of QGP like medium in heavy ion collisions ¹. The two collider facilities, the Relativistic Heavy Ion Collider at BNL (started in 2000) and the Large Hadron Colliders at CERN (started in 2010) have been providing heavy ion collisions at even higher energy. RHIC can collide various heavy ions up to an energy of 100 GeV/Nucleon. Over the past decade, results from RHIC have provided compelling evidence of the formation of QGP in heavy ion collisions [13–16]. Recent results from LHC which can accelerate heavy ions up to several TeV/nucleon has further strengthened such evidences. Future accelerator facilities like FAIR at GSI will provide relativistic heavy ion collisions at much higher luminosities than RHIC and LHC to search for rare probes that are essential to establish the existence the QGP at high density [17].

There are several motivations to study the properties of QGP. Study of QGP has important connection to cosmology in the context of the evolution of early universe. It is believed that immediately after the Big-Bang explosion, universe has gone through various phases of unified fundamental forces and hot and dense mixture of fundamental particles (see [18]). Time line of evolution of baby universe includes transition through the QGP phase ($\sim 1 \mu s$, $T_c^{QCD} \sim 10^{12}$ K) [19].

¹SPS results indicated a possible onset of de-confinement near the collision energy of $\sqrt{s} = 7$ GeV

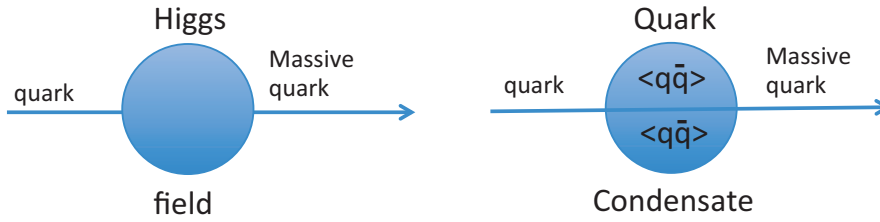


Figure 1.1: Mass generation at the Electro Weak and the QCD scale, schematic from ref. [36]

The transition from hadronic matter to QGP is analogous to phase transitions and critical phenomenon common in condensed matter physics. The theoretical studies of phase transition in condensed matter physics deals with one fermion (electron) and one gauge boson (photon) (as is abelian QED $U(1)$). Whereas physics of QCD phases is a new domain of non-abelian gauge theory which is equivalent to a much more enriched form of condensed matter physics with many “electrons” (N_F flavors $\times 3$ colors) and 8 “photons” (gluons in color $SU(3)$ symmetry) [20, 21]. Although the collective properties of QED that form the basis of condensed matter physics is known at much greater precision, there is a lot more to explore in the sector of QCD. In this context the studies of phase like QGP will help in understanding of collective dynamics in QCD. Another important motivation of studying QGP and hadronic matter at high densities is to understand the origin of mass at the QCD scale. This phenomenon is similar to the phenomenon of mass generation through symmetry breaking at the Electroweak scale (see Fig. 1.1). One consequence of QCD mass generation explains why the current masses of light quarks u , d (s) are much less (5-10 MeV) than their constituent masses (~ 300 MeV) when confined inside hadrons. The QCD mass of a quark disappears in the phase of QGP due to restoration of chiral symmetry. Therefore, the transition from QGP and hadronic matter provides an unique opportunity to study the origin of dynamical masses of quarks (and hadrons).

1.2 Phase transitions in QCD

Asymptotically high energy density can be achieved by modern day accelerators by colliding two heavy ions, at which QCD, the theory of strong interaction predicts the formation of a de-confined systems of quarks and gluons. Due to color confinement, this system of quarks and gluons would eventually cool down and undergo a phase transition to a system of hadronic matter. The phase transition from QGP to hadronic matter (or a hadron gas (HG)) is associated with de-confinement transition and spontaneous breaking of chiral symmetry. This is a consequence of two symmetries of QCD : pure SU(3) gauge symmetry in the limit of infinite quark mass and chiral symmetry in the limit of zero quark mass [22]. The spontaneous breakdown of chiral symmetry is associated with the mass generation at the QCD scale. This is analogous to the phenomenon of mass generation at the Electroweak scale. In such a scenario, the massless elementary particles gain mass by interacting with the Higgs field [23]. In a very similar phenomenon, light quarks interact with the QCD vacuum (or the vacuum quark condensates $\langle 0|q\bar{q}|0\rangle$), and become more massive to form hadrons. In QGP phase where the chiral symmetry is restored, the quark condensate gets melted, and the QCD masses of the light quarks disappear. Lattice QCD calculations predict that at vanishing baryon densities this transition to be a cross-over within a temperature range of $T_c \approx 150-200$ for physical quark masses [24, 25]. On the other hand QCD based models [26–33] including Lattice calculation [34] suggest the transition at larger baryon densities to be a first-order phase transition. The end point of the first order line is the QCD critical point (CP). Ongoing efforts from both theory and experiment show considerable progress in establishing the existence and the location of QCD CP [35].

The QGP may also exist in different phases. The systems formed in heavy ion collisions at RHIC or at LHC that are very close to the temperature and density of QCD chiral phase transition (T_c, μ_c) , manifest liquid like properties. At much higher temperatures (several times $> T_c$) one expects a gaseous plasma that existed in the early universe and at much larger baryon densities (several times $> \mu_c$) it is expected to manifest as a solid or a color superconducting plasma that might exist in the core of neutron star [37, 38]. Several experimental observables

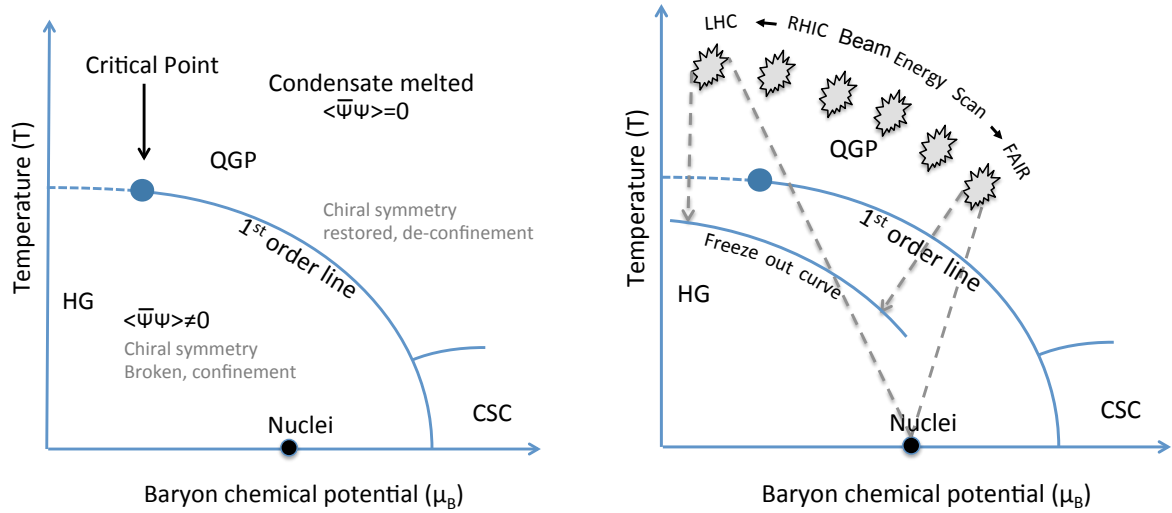


Figure 1.2: Schematic of the QCD phase diagram (conjectured), left panel shows theoretical predictions and right panels shows the trajectories of heavy ion collisions.

suggest that the plasma formed in the heavy ion collisions is a strongly correlated system of QCD matter that flows like a nearly perfect fluid, i.e. primarily a liquid like QGP. These remarkable phenomena together give rise to an enriched phase diagram of QCD matter as shown in Fig. 1.2. The QCD phase diagrams are generally plotted ² in terms of two thermodynamic variables temperature (T) and baryon chemical potential (μ_B). Fig. 1.2 (left) shows the theoretically conjectured phases, the lines of phase transitions. Fig. 1.2 (right) shows the possible trajectories of the matter in heavy ion collision experiments for different colliding energies. Here, the higher collision energies correspond to higher temperature and lower chemical potential. The chiral phase transition line is shown by a (blue) curve which is a first order line at large μ_B that ends with a critical point (CP) for physical quark masses. The order parameter for this phase transition is a condensate of scalar mesons or the chiral condensate $\langle \bar{\psi}\psi \rangle$. This quantity is nonzero in case of Hadronic Matter and zero in the QGP phase. Beyond the CP at very low μ_B that is higher collision energy, the cross over between the QGP phase and the Hadronic Matter is represented by a dotted line.

²Only the location of the point representing the normal nuclear matter (shown by a black circle) is precisely known from the experiments in these figures

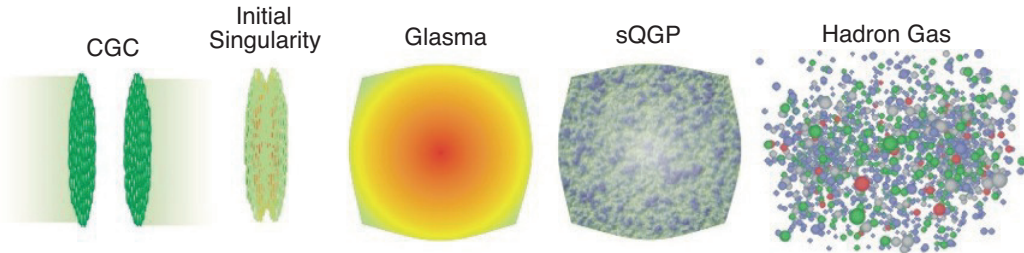


Figure 1.3: Schematic of heavy ion collisions, a figure by S. Bass.

1.3 The Conventional model of Heavy ion collisions and QGP

The conventional model of relativistic heavy ion collisions (see Fig. 1.3) describes two Lorentz contracted sheets of saturated partonic matter colliding to form a high energy density ensemble of gluonic states in the initial stage. This initial phase undergoes a pre-equilibrium evolution and eventually thermalizes to form a strongly correlated Quark Gluon Plasma (sQGP) which subsequently undergoes a transition to hadronic matter. The hadronic matter undergoes further interactions and finally free streams to the detectors.

Nuclei moving at very high energies before collisions are described as Color Glass Condensates (CGC) [39]. They are composed of highly occupied gluonic states, described as highly coherent classical Coulombic fields. CGC is a consequence of the stability of QCD matter at very high energy. With increasing energy, the number of gluons inside a hadron or nucleus increases due to linear perturbative Bremsstrahlung processes. This linear growth is tamed by non-linear QCD process, resulting in a saturated gluon dominated wave-function below a momentum scale Q_S , called the saturation scale.

When two CGCs collide, the color electric and magnetic fields from the two nuclei interact and form an initial state know as the Glasma [40]. Glasma is composed of flux tubes with transverse sizes of inverse nuclear saturation scale $1/Q_S$. Decay of these flux tubes leads to correlated production of gluons. The Glasma gluon fields are nearly boost invariant, which evolve in time and eventually thermalise to form a strongly interacting QGP.

The sQGP medium formed flows hydrodynamically, converting the initial spatial anisotropies to momentum anisotropies at a later time of evolution. The fluid like medium is characterised by quantities like the ratio η/s , the ratio of the shear viscosity to the entropy density, which for a strongly interacting system has been conjectured to have a lower bound of $1/4\pi$ [41, 42].

The most important part of the evolution is the phase transition of the QGP to Hadronic matter. The hadronic matter also flows hydrodynamically until the expansion rate overcomes the scattering rate of its constituents. Finally the matter free stream in 4π directions.

1.4 Observables for HG to QGP transitions in relativistic heavy ion collisions

Following are several experimental observables that have been used to study the properties of matter formed in heavy ion collisions. Equivalent measurements of these observables in case of hadronic collisions or hadron-nuclear collisions have been used as baseline studies since in such cases one does not expect the formation of QGP like medium.

1.4.1 De-confinement transition of the medium

Measures that are sensitive to the color response function ($\Pi_{\mu\nu}^{ab}$) are direct probes of color de-confinement transitions. Suppression of the quarkonia production is an observable that depends on the screening length of the medium λ_D which is directly related to the color response function. The bound states of a heavy quark and its anti-quark which are stable with respect to strong decay into open charm or bottom hadrons are collectively called quarkonia [43]. The medium like QGP, in contrast to hadronic matter, is capable of dissociating quarkonia through Debye screening, so that *quarkonium suppression* may be taken as a signature of de-confined medium or QGP formation in heavy ion collisions [44]. Furthermore, different quarkonia having different binding energies, dissociate at different temperatures. Therefore, the dissociation pattern of quarkonia can serve as a “thermometer” of the fireball. The dissociation points of different

quarkonia states can be used to determine the temperature and the energy density ϵ of the QGP medium [45].

There are two commonly used theoretical approaches to obtain precise predictions for these dissociation points which are either based on potential models or lattice studies. In case of potential model (heavy quarkonia states can be treated non-relativistically) studies one solves the Schrödinger equation with a temperature-dependent potential $V(r, T)$. The form of the potential can either be the Schwinger model [46] which is a modified form of Cornell potential [47] with a temperature dependent “screening mass” $\mu(T)$ that vanishes in the limit $T \rightarrow 0$ or the heavy quark potential from the lattice QCD calculations [48–52]. The alternative approach to predict the dissociation points is to calculate the quarkonia ($c\bar{c}$) spectrum directly on the lattice [53–58]. The former approaches have the problem that the results are dependent on the type of potential chosen, while the latter so far suffers from the fact that the lattice spacing and statistics limit the resolution of peak widths in the spectrum. It is also not easy to identify the continuum region of the spectrum on the lattice [43]. The potential model studies based on the heavy quark internal energy, as well as direct lattice QCD calculations predict the dissociation temperatures to be $T_d \simeq 1.1 T_c$ for ψ' and χ_c and $T_d \geq 1.5 - 2 T_c$ for J/ψ , where T_c is the critical temperature of de-confinement.

Other than the QGP medium effects on the quarkonia production and dissociations, there are substantial amount of nuclear effects that needs to be taken into account. For example the nuclear modification of the initial state parton distribution functions affects the perturbative $q\bar{q}$ production. The $q\bar{q}$ pair during its evolution may get absorbed in the pre-resonance as well as in the resonance stage, due to successive interactions with the target nucleons. Measurements of dilepton, open charm and charmonium production in p-A or d-A collisions can be used to understand these effects.

Another important effect on the final yields of quarkonia like J/ψ is the regeneration due to the statistical recombination process by the charm quarks which are produced initially. One such c quark formed in one NN collision can in principle also bind with a \bar{c} from another NN

collision to create a J/ψ . At sufficiently high energies where charm is abundant this can lead to an enhancement in J/ψ production in AA collisions compared to a scaled pp rates [59–61].

The first signature of J/ψ suppression was observed by NA50 collaboration at SPS in $\sqrt{s_{NN}}=17.3$ GeV Pb+Pb collisions [62–64]. Results at LHC by the CMS collaboration showed that the more massive states of the upsilon are relatively more suppressed in Pb+Pb collisions at 2.76 TeV than in controlled p+p collisions [65]. Another measurement of R_{AA} at LHC indicates that J/ψ s in central Pb+Pb at 2.76 TeV collisions are relatively less suppressed than is the case in central Au+Au collisions at 200 GeV [66, 67]. Recent reviews on quarkonia can be found in ref [68, 69].

1.4.2 Fluid like property of the medium

The collective flow of the medium created in heavy ion collisions are probes to study the fluid like property or the transport property of the medium. The collective flow pattern of the medium is sensitive to the equation of state of the matter [70]. They are classified as radial flow and anisotropic flow.

In non-central collisions the initial spatial anisotropy (pressure gradient) is transformed into the anisotropies in transverse-momentum distributions. The measure of such correlation between spatial positions and momenta of the emitted particles are characterised by the Fourier coefficient v_n of the harmonic decomposition of the azimuthal angle distribution relative to the reaction plane of the collisions [71]. A strong radial flow in central collisions and elliptic flow (v_2) in non-central collisions have been observed in Pb+Pb collisions at SPS [72–74] and in Au+Au collisions at RHIC [75]. Results from RHIC demonstrated, almost 50% larger value of flow coefficient v_2 compared to that at the SPS. A very large value of v_2 was also recently measured at LHC. In all the cases viscous relativistic hydrodynamic calculations did very good job in explaining the data with very low values of shear viscosity to entropy density ratio [76, 77]. This particular feature of the data have lead to a conclusion that the matter created in heavy ion collisions is strongly interacting and behaves like a nearly perfect fluid.

It was found at RHIC that the second Fourier coefficient v_2 , when plotted as a function of transverse kinetic energy E_T for mesons and baryons merge into a universal curve if both v_2 and E_T are scaled by the number of valence quark of the hadron [78, 79]. This indicates the medium formed is composed of de-confined, thermalized and collectively flowing quarks that recombine to form hadrons [80, 81].

The anisotropic flow and its higher order harmonics are sensitive to the details of the initial anisotropy in heavy ion collisions. Due to fluctuation in the initial geometry, a lumpy distribution of the initial energy density distribution leads to non-zero higher harmonic flow v_n in both central and non-central events [82, 83]. The dissipative effects on higher order v_n are supposed to be higher since they are sensitive to the smallest length scale fluctuations in the initial geometry. Thus from the measurement of the v_n coefficients one can learn about the transport coefficient of the medium created as well as the initial state and its fluctuation which are driven by intrinsic properties of QCD. More discussions can be found in recent reviews [84, 85]

1.4.3 Opacity of the medium

In the high momentum part (hard sector) of the spectrum of produced particles, the phenomenon of jet quenching is considered as one of the most important observables that is sensitive to the properties like opacity of the medium created in heavy ion collisions [86–90]. The single inclusive particle spectra measured in heavy ion collisions are compared to the baseline measurement from hadronic collisions where one doesn't expect the formation of a medium like QGP. The observable relevant to jet quenching called R_{AA} is defined as $R_{AA} = (dN^{AA}/d^2p_{\perp}dy) / (\langle T_{AA} \rangle dN^{pp}/d^2p_{\perp}dy)$. The scaling factor $\langle T_{AA} \rangle$ is called the nuclear overlap function which is proportional to the number of binary collisions. In case no medium is present one expects R_{AA} to become unity. Any deviation from unity would either indicate modification of the partonic distribution in the colliding nuclei (initial state effect), or the interaction of a probe with the medium formed after the collisions (medium modification) [90].

The former effect is mostly dominant at the soft part of the hadron spectra which can

be studied in the proton(p)/deuteron(d)-nucleus(A) collisions, and can be constrained by global (deeply inelastic scattering (DIS)) data [91]. Calculation based on color glass condensate (CGC) approach [92, 93], which are constrained by the HERA DIS data, predicted that at very high energy the nuclear modification factor of p+A collisions (R_{pA}) at mid-rapidity is almost unity for $p_T \geq 2$ GeV. Alternative explanations based on inputs from global DGLAP fits of nuclear PDFs (EPS09 and EKS98) predicted similar behaviour of R_{pA} [94]. These predictions were confirmed by the measurements at LHC [95], suggesting the fact that initial state effects (cold nuclear matter effects) on R_{AA} would vanish at high p_T .

The hard part of the hadron spectra is observed to be strongly suppressed in central heavy ion collisions resulting in R_{AA} being much less than unity for $p_T \geq 2$ GeV. This phenomenon known as jet-quenching, was first observed at RHIC in Au+Au collisions at $\sqrt{s_{NN}} = 130$ GeV [96, 97]. Such an effect was found to be absent in d+Au collisions at $\sqrt{s_{NN}}=200$ GeV [98, 99]. First measurements at LHC also showed similar suppression in Pb+Pb collisions at $\sqrt{s_{NN}} = 2.76$ TeV [100, 101] as a further confirmation of a medium formed in Pb+Pb collisions. This phenomena is attributed to the interaction of the energetic partons (that fragment into high p_T hadrons or jets) traversing a hot QCD medium (QGP) formed in heavy ion collisions. The amount of energy loss is related to the hard partonic energy loss parameter \hat{q} which is defined as the typical momentum transfer squared per unit length by the parton in the medium [102–104]. Theoretical models that include different mechanisms of energy loss of a parton (radiative, collisional etc. [105]) can be used to extract \hat{q} from experimental measurements (for a recent development see e.g. [106]). A recent review on hard probes of QGP can be found in ref. [107].

1.4.4 Thermal property of the medium

Electromagnetic probes such as lepton pairs and photons are considered as the cleanest probe to study the strongly interacting matter such as QGP [108–113]. These probes carry information of the earliest phase of the evolution and remain un-affected by the final stage interactions. However these probes suffer considerable background from the electromagnetic decays of hadrons. Yields

of these probes are sensitive to the electromagnetic current response function ($W^{\mu\nu}$) which is sensitive to the thermal state of the medium. A review can be found in ref. [114]

In a medium like QGP the leading logarithmic contribution ($\mathcal{O}(\alpha_s, \alpha_{EM})$) to the rate of thermal photon production is calculated by including two-to-two particle hard collision processes like $qg \rightarrow q\gamma$ [115, 116]. However several inelastic processes also contribute in the same order leading to what is called the Landau-Pomeranchuk-Migdal (LPM) suppression, a full treatment of which should be included to compute the photon emission rate in complete leading order [117]. There have been recent developments to calculate the thermal photon emission rate up to NLO [118] that adds up to 20% correction at RHIC energies.

Along with the contribution from the QGP matter there will be significant amount of the thermal photons production from the hot hadronic matter produced after the hadronization of the QGP [115, 119–123]. The thermal photons from both QGP and hot hadronic matter dominate the lower part of the transverse momentum (p_T) spectrum whereas the large momentum part is dominated by the prompt photons due to direct hard production in primary parton-parton collisions between the nuclei which can be calculated from the NLO pQCD approaches [124]. The intermediate momentum range is dominated by jet-induced photons from the medium due to Compton scattering, annihilation or medium induced Bremsstrahlung [125, 126]. These intermediate momentum photons also carry information about the temperature and other properties of the medium related to jet energy loss. Direct photons from different sources can be separated by choosing different regions of p_T -spectra whereas the decay photons can be excluded from the data sample either by invariant mass or mixed event analysis method [127–129].

Other than thermal photon spectra, the elliptic flow [130] and interferometry [131, 132] of photons can be important probes to determine the collective properties of the system. Since photons are emitted throughout the evolution including very early stage of the collisions, elliptic flow of photons are also sensitive to early pre-equilibrium flow.

Observation of direct photon was first reported by the WA98 experiment in central 158 A GeV Pb+Pb collisions at the CERN SPS. A more recent measurement of direct photon spectra

at RHIC by the PHENIX collaboration have shown an excess yield in central (0-20%) Au+Au collisions compared to p+p collisions at $\sqrt{s_{NN}} = 200\text{GeV}$ at low transverse momentum in the range $1 < p_T < 4 \text{ GeV}/c$ [133]. A similar measurement at LHC in central (0 – 40%) Pb+Pb collisions at $\sqrt{s_{NN}} = 2.76 \text{ TeV}$ also indicates excess yields at low p_T as compared to p+p collisions [134]. Exponential fit to the p_T -spectra at RHIC and LHC correspond to values of slope parameters of 221 MeV and 304 MeV respectively. These measurements are indicative of the formation of a medium with an initial temperature of order 300-600 MeV [133, 134] at which matter is likely to be in the QGP phase.

Di-leptons produced from the virtual photons provide additional kinematic window of invariant mass in addition to p_T to study the different stages of the evolution of the medium created in heavy ion collisions. Massive di-leptons ($M > M_{J/\psi}$) carry information of the early stages of collision which come from Drell-Yan processes or decay of different quarkonia states. These di-leptons can also be used to study suppression of quarkonia states which is discussed in the next section. The intermediate window of di-lepton mass ($M_{J/\psi} > M > M_\phi$) is dominated by emission from the QGP state that carry information about the thermal property of the medium. An enhanced yield of dileptons in this region has been suggested to be a signal of QGP formation [10]. The low mass di-leptons ($M_\phi > M$) are dominated by decays of vector mesons and Dalitz decays. These di-leptons are sensitive to the medium modification of the spectral functions of vector mesons and study of QCD chiral phase transitions [135].

Measurement at the SPS showed enhancement of di-lepton yields at both intermediate and low mass region [136–138], which is consistent with the formation of QGP [135]. The measurements by the NA45 collaboration at SPS [139] and a more recent measurement by the STAR collaboration at RHIC [140] of the di-lepton invariant mass spectrum are found to be consistent with the calculations of strongly broadened ρ spectral function plus a moderate QGP contribution.

1.4.5 Correlation and fluctuations in the medium

Correlation and fluctuation of global observables such as multiplicity, transverse momentum of particle, azimuthal anisotropy of particle distribution (flow harmonics v_n), transverse energy etc. can provide important information about different stages of heavy ion collisions. Further discussions will be mainly focused on multiplicity fluctuation. There are three distinct sources of multiplicity fluctuations. The dominant contribution to inclusive multiplicity fluctuations comes from very early stages of collisions and throughout the pre-equilibrium evolution of the system formed in heavy ion collisions. Such fluctuation and correlation that originate from the early stage of collisions carry important information of the pre-equilibrium dynamics. In the later stage of the evolution, the system is equilibrated and it is expected to be in the phase of QGP. Such a medium eventually undergoes a phase transition to hadronic matter. This phase transition is associated with the de-confinement transition and chiral phase transitions. In the Grand Canonical Ensemble picture, one expects event-by-event fluctuations of conserved charges (which is related to multiplicity of different particle species) from the medium created in heavy ion collisions. Fluctuation of conserved charges are related to corresponding susceptibilities which are thermodynamic response function of the medium created in heavy ion collisions. There are a few other sources of multiplicity fluctuation that come from the late stages of evolution, like decay of massive resonances. One of the other sources of measured multiplicity fluctuations are attributed to artefacts related to the methods of detection. Since the process of detection of a particles is probabilistic and carried out in a limited phase space, spurious fluctuations of multiplicity are unavoidable in the context of experimental measurements.

1.5 Outline of this thesis work

This thesis work includes the study of fluctuations and correlation of inclusive multiplicity in heavy ion collisions. Contributions to multiplicity fluctuation and correlation come from different stages of collisions and can carry information of the evolution of the system as described in next

subsections.

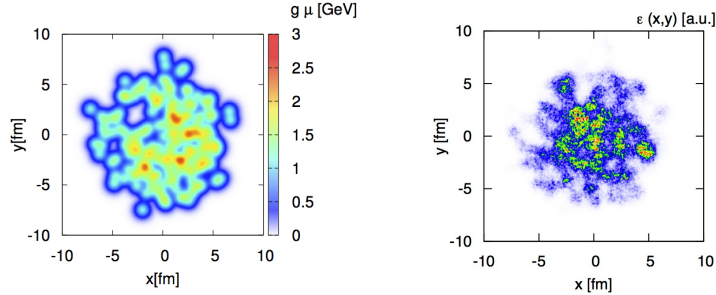


Figure 1.4: (Left) Lumpy initial parton density in a colliding Au nucleus. Only quantum fluctuations at nucleonic scale are present. (Right) The transverse energy density after collision of two Au nuclei at 200 GeV at zero impact parameter. Quantum fluctuations at both nucleonic and sub-nucleonic scales are present, which will result in fluctuation of global observable such as multiplicity and flow harmonics v_n .

1.5.1 Modelling of fluctuations from the initial stages of heavy ion collisions.

There are two distinct sources of correlation and fluctuation from the initial stages of heavy ion collision. The first is the geometric fluctuations due to shapes of nuclei and the impact parameter of collision. The second source is due to the quantum fluctuations generic to the wave function of nuclei and its constituents. The event-by-event geometric fluctuation of the overlap zone of two nuclei due to fluctuation of impact parameter is the major source of multiplicity fluctuation in heavy ion collisions. The quantum fluctuations of nucleon positions which are distributed according to Fermi distribution is another dominant source of initial state fluctuation. In addition to that, there are sub-nucleonic quantum fluctuations, the dynamics of which is governed by the saturated nuclear wave function at low Bjorken x . The combined effect leads to the fluctuation of inclusive multiplicity and transverse energy density. Fluctuation of transverse energy density affects the anisotropic flow coefficients v_n and its fluctuation. Experimental measurements indicate that over a wide-range of energies and systems, the inclusive multiplicity follows a negative binomial distribution. Origin of such distributions from first principle QCD is not well understood.

Experimental measurements have confirmed that the medium created in the subsequent stages of evolution flows like a nearly perfect fluid. The measured anisotropic flow v_n coefficients have been used to determine the transport properties of the fluid like medium created in heavy-ion collisions. A precise determination of such transport coefficients therefore requires a model of initial condition that incorporates different sources of fluctuations and includes an *ab initio* description of multi particle production, as an input to hydrodynamic or transport simulation.

In this thesis work we have developed a framework by including all sources of fluctuations at the initial and the pre-equilibrium stage of heavy ion collisions. The goal is to naturally describe the inclusive multiplicity and transverse energy density fluctuations (negative-binomial fluctuations), develop a new model of initial condition that can serve as an input to the hydrodynamic simulations for the estimation of flow coefficients v_n for the determination of the transport coefficients of the medium created in heavy ion collisions.

1.5.2 Modelling of fluctuation from the final stages of evolution and detection

The final stage of the evolution of the fireball created in heavy ion collisions involves the decay of massive resonances into lighter hadrons. Resonance decay introduces one specific kind of correlation in the multiplicity of inclusive charged and neutral particles, known as decay correlation. The decay correlations can dilute or enhance the signals of dynamical fluctuations or correlations from the medium as discussed in the previous section. Qualitative estimations of the decay correlation observables can be presented using moment generating function approach. Quantitative estimations are done using Monte Carlo models (event generators) that include the processes of resonance decay. Spurious fluctuation and correlation are introduced due the process of detection. Such effects must be eliminated by the construction of observables. Limited efficiency, acceptance and identification capability of the detector systems might also induce multiplicity fluctuations and correlation. An approach based on moment generating function can be used to study such effects. It can be shown that, for observables constructed using proper combination of moments of multiplicity, certain detector related artefacts can be

minimized. Detailed quantitative estimation of measurement related effects can also be studied using a combination of Monte Carlo event generator coupled with detector geometry.

A part of this thesis includes the study of spurious fluctuation and correlation that affect the measurement of dynamical multiplicity fluctuation and correlation using an approach based on moment generating function and Monte Carlo methods.

1.5.3 Measurement of inclusive charged and neutral multiplicity fluctuation in heavy ion collisions.

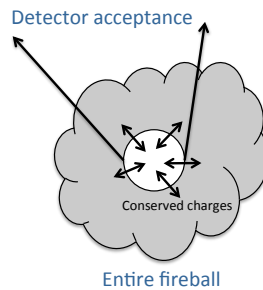


Figure 1.5: Cartoon of the fireball created in heavy ion collisions. Experimentally only a small fraction of the fireball is probed, in which conserved charges can be exchanged, this way a GCE picture is valid.

The subsequent stage after pre-equilibrium evolution is the formation of a equilibrated medium of QCD matter, which undergoes a phase transition to Hadronic matter. Eventually the hadronic matter will expand faster than the scattering rate of its constituents and free stream in 4π direction. Experimental measurements always probe a limited phase space out of the 4π coverage. For a realistic detector acceptance in the Grand Canonical Ensemble picture, the dynamical fluctuation of conserved charges can be a good probe to study the phase transition. For the phase transition from QCD matter to hadronic matter, change in fundamental degrees of freedom associated with de-confinement transition would lead to distinct change in the strength of fluctuations. Therefore measuring quantities like event-by-event h^+/h^- fluctuations can provide a distinct signal of QGP formation [141, 142]. Similarly fluctuations of net baryon number can also be an ideal probe for the de-confinement transition [143]. Event-by-

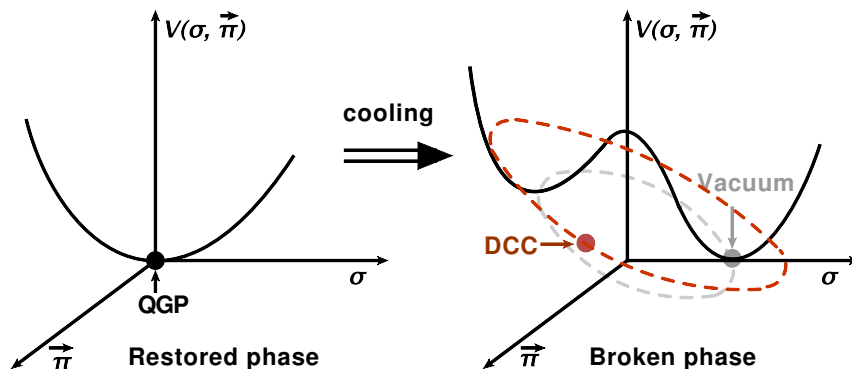


Figure 1.6: Spontaneous breaking of chiral symmetry in linear sigma-model. The four component condensate $(\sigma, \vec{\pi})$ is misaligned with its vacuum direction in case of DCC domains. Schematic from Ref. [149].

event fluctuation of conserved quantities has been argued to be an ideal probe to scan the phase diagram of QCD and to locate the QCD critical point [144].

The transition from QGP to hadron gas is also associated with the QCD chiral phase transition. Although there are several fluctuation measures discussed in the literature [141–143] that are sensitive to de-confinement transitions, very few of them directly probe the chiral phase transition. When the system passes from a chirally symmetric phase to a broken phase, in a scenario of rapid cooling, there could be formation of metastable domains in which the four component chiral condensate $(\sigma, \vec{\pi})$ is misaligned relative to its vacuum orientations. Such domains of disoriented chiral condensates (DCC) leads to coherent emission of soft pions of a particular isospin [145–148]. Such emission eventually leads to a distinct distribution of the neutral pion fraction compared to what is expected from generic production of pions under isospin symmetry [146, 148]. If f denotes the event wise neutral pion fraction (the ratio of the total number of neutral pions over the total number of all pions produced in a single event) a generic production of pions from a thermally equilibrated medium will lead a distribution peaked at $1/3$. It can be shown that, all the pions coming from the decay of a DCC domains exhibit a probability function described by $P(f) = 1/2\sqrt{f}$. These two scenarios lead to a difference in event-by-event correlation of charged and neutral pion multiplicity. In other words, the two scenarios would

lead to difference in the dynamical fluctuation of event-by-event neutral pion fraction. Since pions dominate the inclusive multiplicity in heavy ion collisions, the neutral pion fraction can be shown to be closely related to inclusive charged particle and photon multiplicity ratio $f^{\gamma-\text{ch}}$ (the ratio of the total number of inclusive photons over the total number of inclusive charged particles produced in a single event). Therefore dynamical fluctuation of f is expected to affect the dynamical fluctuation of $f^{\gamma-\text{ch}}$.

The goal of this thesis work is the measurement of inclusive charge and photon multiplicity at the STAR experiment at RHIC and the analysis of data by developing methods to study event-by-event fluctuation (and correlation) of inclusive charged and photon multiplicity. The method involves the construction of observables that are sensitive to DCC formation as a result of the QCD chiral phase transition and at the same time robust against measurement related artefacts. Observables have been constructed from the moments of multiplicities and their robustness and sensitivity to signals have been tested using generating function approach and by Monte-carlo simulations. Further studies include simulations using available hadronic transport and mini-jet models for baseline studies. The fluctuations that originate from the initial stage of collisions as discussed in previous section can also affect the dynamical fluctuations of multiplicity from the medium. Such effects must be taken care of by the construction of suitable observables.

Chapter 2

Observables for multiplicity fluctuation and correlation

2.1 Introduction: selection of observables

In this chapter we discuss how the observed event-by-event multiplicity fluctuation and correlation are affected by various artefacts related to detection of particles. We argue that spurious fluctuations and correlations are unavoidable due to limitations of experimental measurements. As mentioned previously, the binomial responses of particle detectors naturally introduces event-by-event fluctuation of particle multiplicity. Additionally due to limited acceptance of the detector systems, spurious fluctuation can arise from decay of resonances. Mis-identification is also one of the dominant effects that contribute to the spurious correlation. A suitable observable in this case should be robust against detector effects and at the same time sensitive to signal of dynamical fluctuation and correlation in the data sample. It is necessary to quantify the detection related artefacts and design robust observables suitable for studying event-by-event multiplicity fluctuations. These effects can be studied using the moment generating function approach. We discuss here the design and sensitivity of observables for dynamical charge-neutral multiplicity fluctuations and correlations. Formation of the domains of Disoriented Chiral Condensate(DCC)

is one of the proposed sources of dynamical charge-neutral multiplicity correlation. A detailed study of the sensitivity of the observables to DCC formation is studied in the generating function approach. Decay of resonances, also studied in the same approach, has been shown to induce opposing effects (correlation) on the observables in contrast to DCC (anti-correlation).

2.2 Factorial moments and generating function approach

We define efficiency of detection ε as the probability to detect a particle incident on a detector under consideration. Let us assume that out of N particles produced in a given event only n number of particles are detected by the detector of efficiency ε . If $P(N)$ denotes the probability distribution of produced particles then the distribution of detected particles can be given as

$$P(n) = \sum B(n|N, \varepsilon)P(N). \quad (2.1)$$

Here we have assumed the simplest implementation of detector efficiency in terms of a binomial probability distribution function say of the form

$$B(n|N, \varepsilon) = {}^N C_n \varepsilon^n (1 - \varepsilon)^{N-n}, \quad (2.2)$$

which gives

$$\langle n \rangle = \varepsilon \langle N \rangle, \quad (2.3)$$

$$\langle n^2 \rangle = \varepsilon(1 - \varepsilon) \langle N \rangle + \varepsilon^2 \langle N^2 \rangle, \quad (2.4)$$

$$\langle n^3 \rangle = \varepsilon(1 - \varepsilon)(1 - 2\varepsilon) \langle N \rangle + 3\varepsilon^2(1 - \varepsilon) \langle N^2 \rangle + \varepsilon^3 \langle N^3 \rangle. \quad (2.5)$$

i.e. different higher order moments of observed multiplicity n is not proportional to the same order of moments of produced multiplicity N . This way the efficiency term ε does not factorize for variables like variance, skewness and kurtosis. However different order factorial moments of

the detected particles come out to be proportional to the corresponding factorial moments of the parent particles i.e.

$$\langle n(n-1) \rangle = \varepsilon^2 \langle N(N-1) \rangle. \quad (2.6)$$

It is evident that explicit efficiency dependence can be removed by taking ratios of these factorial moments with powers of mean multiplicity.

The above relation can also be obtained in the generating function approach [150]. Along with detection efficiency, various other effects like decay, mis-identification can be incorporated in moments in a moment generating function defined as

$$G(z) = \sum_{N=0}^{\infty} z^N P(N) \quad (2.7)$$

where $P(N)$ denotes the distribution of the parent multiplicity N which subsequently produces two different particles species with multiplicities N_1 and N_2 . Production of these two species may be correlated. Let us consider that $\mathcal{P}(\alpha)$ denotes the event-by-event distribution of $\alpha = N_1/(N_1 + N_2)$ that includes the relevant physics of correlation which is independent of parent distribution so that the modified generating function becomes

$$G(z_1, z_2) = \int_0^1 d\alpha \mathcal{P}(\alpha) \sum_N P(N) [\alpha z_1 + (1-\alpha)z_2]^N, \quad (2.8)$$

where z_1 and z_2 are dummy variables. Different moments of multiplicity are evaluated by first taking the derivatives of $G(z_1, z_2)$ with respect to z_1 and z_2 and then by setting $z_1 = z_2 = 1$. $P(N)$ could correspond to the multiplicity distribution of the initial partons (dominantly gluons) from which all charged and neutral particles are produced. In the simplest picture without considering any kind of decay one can think of N_1 and N_2 as produced charged and neutral particles. In the context of multiplicity correlation for two different particle species (N_1 and

N_2), the generalised factorial moment of order m, n is defined as

$$F_{m,n} = \left\langle \frac{N_1! N_2!}{(N_1 - m)! (N_2 - n)!} \right\rangle = \frac{\partial^{m,n} G(z_1, z_2)}{\partial z_1^m \partial z_2^n} \Big|_{z_1=z_2=1} \quad (2.9)$$

$$= \langle \alpha^m (1 - \alpha)^n \rangle \left\langle \frac{N!}{(N - m - n)!} \right\rangle \quad (2.10)$$

If ε_1 and ε_2 denotes the detection efficiencies for species N_1 and N_2 the generating function of Eq. 2.8 is modified to,

$$G_{\text{obs}}(z_1, z_2) = G(g_1(z_1), g_2(z_2)) , \quad g_{1,2}(z_{1,2}) = (1 - \varepsilon_{1,2}) + \varepsilon_{1,2} z_{1,2} \quad (2.11)$$

The observed factorial moment of multiplicity can be shown to be

$$f_{m,n} = \varepsilon_1^m \varepsilon_2^n F_{m,n}. \quad (2.12)$$

Since efficiency terms factorize, in the simplistic scenario, observables constructed out of ratios of factorial moments would not have explicit efficiency dependence. However factorial moments can be affected by decays and other complicated detector effects like mis-identification of one species in the form of another.

In literature, factorial moments have been used to study fluctuation of particle ratios in case of conserved quantities like net strangeness in terms of kaon-to-pion ratio and for net baryons in terms of proton-to-pion ratios. Observables used in such cases were by design robust against detector inefficiency. In this chapter relevant to the context of isospin, we would like to study photon to charge particle multiplicity ratio. A detailed calculation in the context of charge and neutral particle multiplicity correlation is done in the next section.

2.3 Observable ν_{dyn} and $r_{m,1}$

In hadronic and heavy ion collisions, the produced particles are mostly pions. They contribute to bulk of the charged and neutral particles. The neutral pions are experimentally detected by decay photons. Considering various other aspects of particle ratio-fluctuation in hadronic and heavy ion collisions, two observables were introduced earlier as measures of dynamical fluctuations. An observable ν_{dyn} was introduced in Ref [151] and used by STAR Collaboration [152, 153] to study ratio fluctuation in heavy ion collision and $r_{m,1}$ was introduced by Minimax collaboration[150] for the search of DCC like signal in $p + p$ collision. In this work of correlation and individual fluctuation analysis of charged (mostly charged pions) and neutral (photons) particle both observables are studied extensively and used for analysis of data which is discussed in the next chapter.

The observable ν_{dyn} in the context $\gamma - ch$ can be defined as

$$\nu_{dyn}^{\gamma-ch} = \frac{\langle N_{ch}(N_{ch} - 1) \rangle}{\langle N_{ch} \rangle^2} + \frac{\langle N_{\gamma}(N_{\gamma} - 1) \rangle}{\langle N_{\gamma} \rangle^2} - 2 \frac{\langle N_{ch} N_{\gamma} \rangle}{\langle N_{ch} \rangle \langle N_{\gamma} \rangle} \quad (2.13)$$

$$= \omega_{ch} + \omega_{\gamma} - 2 \times \text{corr}_{\gamma-ch}. \quad (2.14)$$

Here $\langle \dots \rangle$ refers to an average taken over all the events considered. The two terms, ω_{ch} and ω_{γ} , refer to individual charged particle and photon multiplicity fluctuations. The third term, $\text{corr}_{\gamma-ch}$, is the scaled correlation of charged particle and photon multiplicity. The observable $r_{m,1}$ is defined as

$$r_{m,1}^{\gamma-ch} = \frac{\langle N_{ch}(N_{ch} - 1) \dots (N_{ch} - m + 1) N_{\gamma} \rangle \langle N_{ch} \rangle}{\langle N_{ch}(N_{ch} - 1) \dots (N_{ch} - m) \rangle \langle N_{\gamma} \rangle}. \quad (2.15)$$

It is designed such that for Poisson case, $r_{m,1}=0$. Higher order(m) of $r_{m,1}$ are expected to show larger sensitivity to signals.

2.3.1 Effect of efficiency

In this section we would like to discuss the applicability, robustness and sensitivity of these two observables ν_{dyn} and $r_{m,1}$ for studying $\gamma - \text{ch}$ correlation. Since we are interested in fluctuation of the ratio of multiplicities, let us consider $f = N_{\pi^0}/(N_{\pi^0} + N_{\pi^\pm})$ to be the neutral pion fraction. The idea is to choose proper combination of moments such that the efficiency dependence is eliminated and observables are expressed in terms of the fluctuations of the fraction f . The generating function in terms of parent multiplicity distribution $P(N)$ is defined in Eq. 2.7, Here , $N = N_{\pi^0} + N_{\pi^+} + N_{\pi^-}$ denotes sum of multiplicities of neutral and charged pions. Different moments are calculated by taking derivatives of $G(z)$ with respect to the variable z evaluated at $z = 1$. Considering the fact that the neutral pions are distributed according to the probability $\mathcal{P}(f)$ the generating function has to be modified accordingly

$$G(z_{\text{ch}}, z_0) = \int_0^1 df \mathcal{P}(f) \sum_N P(N) [fz_0 + (1-f)z_{\text{ch}}]^N. \quad (2.16)$$

Here $\mathcal{P}(f)$ is the distribution of neutral pion fraction. For propagation of generating function to include the decay of neutral pions to observed photons we apply the ‘‘cluster decay theorem’’ [154]. We can express the overall generating function as

$$G_{\text{obs}}(z_{\text{ch}}, z_\gamma) = G(g_{\text{ch}}(z_{\text{ch}}), g_0(z_\gamma)) \quad (2.17)$$

where $g_0(z_\gamma) = z_\gamma^2$ and $g_{\text{ch}}(z_{\text{ch}}) = z_{\text{ch}}$ considering the fact that every neutral cluster decays into two photons and the charge particles do not decay. To make the scenario more realistic and taking the advantage of same theorem, one can include detection efficiencies in the final form of generating function. We consider the observing and non-observing as different decay modes

with probability equal to the detection efficiency. So for charged and neutral clusters we redefine

$$\begin{aligned} g_{\text{ch}}(z_{\text{ch}}) &= (1 - \varepsilon_{\text{ch}}) + \varepsilon_{\text{ch}} z_{\text{ch}} \\ g_0(z_\gamma) &= ((1 - \varepsilon_\gamma) + \varepsilon_\gamma z_\gamma)^2 \end{aligned} \quad (2.18)$$

Here ε_{ch} is the efficiency of charge particle detection and ε_γ is the efficiency of detecting a photon coming from decay of a neutral pion. In $g_0(z_\gamma)$ one can interpret $(1 - \varepsilon_\gamma)^2$, $2\varepsilon_\gamma(1 - \varepsilon_\gamma)$ and ε_γ^2 as efficiencies of detecting none, single and both of the photons coming from the decay of neutral pion.

Various factorial moments of multiplicity are expressed in terms of derivatives of final generating function. We can define a generalized factorial moment in terms of *observed* particle multiplicity,

$$f_{m,n} = \left. \frac{\partial^{m,n} G_{\text{obs}}(z_{\text{ch}}, z_\gamma)}{\partial z_{\text{ch}}^m \partial z_\gamma^n} \right|_{z_{\text{ch}}=z_\gamma=1} = \left\langle \frac{N_{\text{ch}}! N_\gamma!}{(N_{\text{ch}} - m)! (N_\gamma - n)!} \right\rangle \quad (2.19)$$

It is convenient to express our observables given in Eq. 2.14 and Eq. 2.15 in terms of $f_{m,n}$ as

$$\nu_{dyn}^{\gamma\text{-ch}} = \frac{f_{20}}{f_{10}^2} + \frac{f_{02}}{f_{01}^2} - 2 \frac{f_{11}}{f_{10} f_{01}}, \quad r_{m,1}^{\gamma\text{-ch}} = \frac{f_{m1} f_{10}}{f_{(m+1)0} f_{01}} \quad (2.20)$$

Using Eq. 2.16, Eq. 2.17 and Eq. 2.19 we can express different factorial moments in terms of efficiency and moments of neutral pion fraction as

$$\begin{aligned} f_{10} &= \langle 1 - f \rangle \varepsilon_{\text{ch}} \langle N \rangle \\ f_{01} &= \langle f \rangle 2\varepsilon_\gamma \langle N \rangle \\ f_{11} &= \langle f(1 - f) \rangle 2\varepsilon_\gamma \varepsilon_{\text{ch}} \langle N(N - 1) \rangle \\ f_{20} &= \langle (1 - f)^2 \rangle \varepsilon_{\text{ch}}^2 \langle N(N - 1) \rangle \\ f_{02} &= \langle f^2 \rangle 4\varepsilon_\gamma^2 \langle N(N - 1) \rangle + 2\varepsilon_\gamma^2 \langle f \rangle \langle N \rangle. \end{aligned}$$

The generalised factorial moment for the *incident* particle distribution $F_{m,n}$ would correspond

to $g_0(z_\gamma) = z_\gamma^2$ and $g_{\text{ch}}(z_{\text{ch}}) = z_{\text{ch}}$, given by

$$\begin{aligned}
F_{10} &= \langle 1 - f \rangle \langle N \rangle \\
F_{01} &= \langle f \rangle 2 \langle N \rangle \\
F_{11} &= \langle f(1 - f) \rangle 2 \langle N(N - 1) \rangle \\
F_{20} &= \langle (1 - f)^2 \rangle \langle N(N - 1) \rangle \\
F_{02} &= \langle f^2 \rangle 4 \langle N(N - 1) \rangle + 2 \langle f \rangle \langle N \rangle.
\end{aligned}$$

From which we can clearly see that Eq. 2.12 holds only for $n \leq 1$,

$$f_{m,n}^{\gamma\text{-ch}} = \varepsilon_{\text{ch}}^m \varepsilon_\gamma^n F_{m,n}^{\gamma\text{-ch}}, \quad n \leq 1. \quad (2.21)$$

which can be attributed to the decay of neutral pions carrying relevant physics information into two photons. Since experimental observables are to be constructed of moments of decay photons a robust observable should contain factorial moments with all m but $n \leq 1$.

Substituting these in Eq. 2.14 we can express ν_{dyn} as

$$\nu_{\text{dyn}}^{\gamma\text{-ch}} = \left(\frac{\langle (1 - f)^2 \rangle}{\langle 1 - f \rangle^2} + \frac{\langle f^2 \rangle}{\langle f \rangle^2} - 2 \frac{\langle f(1 - f) \rangle}{\langle f \rangle \langle 1 - f \rangle} \right) \frac{\langle N(N - 1) \rangle}{\langle N \rangle^2} + \frac{1}{2 \langle f \rangle \langle N \rangle}. \quad (2.22)$$

We note here that for the generic case ($\mathcal{P}(f) = \delta(f - 1/3)$) the term inside the bracket is zero and we have

$$\nu_{\text{dyn}}^{\gamma\text{-ch}} \Big|_{\text{generic}} = \frac{1}{2 \langle f \rangle \langle N \rangle}. \quad (2.23)$$

Using proper combination of factorial moments and doing a simple method of event mixing one can extract the generic value of $\nu_{\text{dyn}}^{\gamma\text{-ch}}$. Subtracting the generic value of $\nu_{\text{dyn}}^{\gamma\text{-ch}}$, one can get rid of

the last term in Eq. 2.22. So we propose a modified variable $\Delta\nu_{\text{dyn}}^{\gamma\text{-ch}} = \nu_{\text{dyn}} - \nu_{\text{dyn}}^{\text{generic}}$ given by

$$\Delta\nu_{\text{dyn}}^{\gamma\text{-ch}} = \left(\frac{\langle(1-f)^2\rangle}{\langle 1-f\rangle^2} + \frac{\langle f^2\rangle}{\langle f\rangle^2} - 2 \frac{\langle f(1-f)\rangle}{\langle f\rangle \langle 1-f\rangle} \right) \frac{\langle N(N-1)\rangle}{\langle N\rangle^2}. \quad (2.24)$$

In ideal scenarios when all the particles are detected one can approximate $g_0(z_\gamma) = z_\gamma^2$ and $g_{\text{ch}}(z_{\text{ch}}) = z_{\text{ch}}$. In that case one can show using Eq. 2.17 and Eq. 2.19 that

$$\nu_{\text{dyn}}^{\gamma\text{-ch}} \Big|_{\text{generic}} = \frac{1}{2 \langle N\rangle \langle f\rangle} \approx \frac{1}{\sqrt{\langle N_{\text{ch}}\rangle \langle N_\gamma\rangle}}. \quad (2.25)$$

So in that case the observable $\Delta\nu_{\text{dyn}}$ is expressed as

$$\Delta\nu_{\text{dyn}}^{\gamma\text{-ch}} = \nu_{\text{dyn}}^{\gamma\text{-ch}} - \frac{1}{\sqrt{\langle N_{\text{ch}}\rangle \langle N_\gamma\rangle}}. \quad (2.26)$$

This expression will be used to extract the value $\Delta\nu_{\text{dyn}}$ from models as discussed in section 2.4.1. Following similar approach the variable $r_{m,1}$ is expressed as

$$r_{m,1}^{\gamma\text{-ch}} = \frac{\langle f(1-f)^m\rangle \langle 1-f\rangle}{\langle (1-f)^{m+1}\rangle \langle f\rangle}. \quad (2.27)$$

In Fig. 2.1 we show the results of a Monte Carlo simulation to test the efficiency dependence of factorial moments. We generate random numbers from two Poisson (and Gaussain) distributions which represents the charged particles and photons in a given event. In the next step, we implement the detector efficiency for the number of charged particles and photons according to a Binomial distribution as follows. A random number is generated between zero and unity from a uniform distribution corresponding to each charge particles and photons. The cases for which the generated number is above a given fraction ϵ are counted as new multiplicities of photons and charged particles. This naturally implements a detector efficiency of ϵ on the number of charge particles and photons according to a Binomial distribution with probability ϵ . Observables are calculated using the number of charge particles and photons before and after the implementation

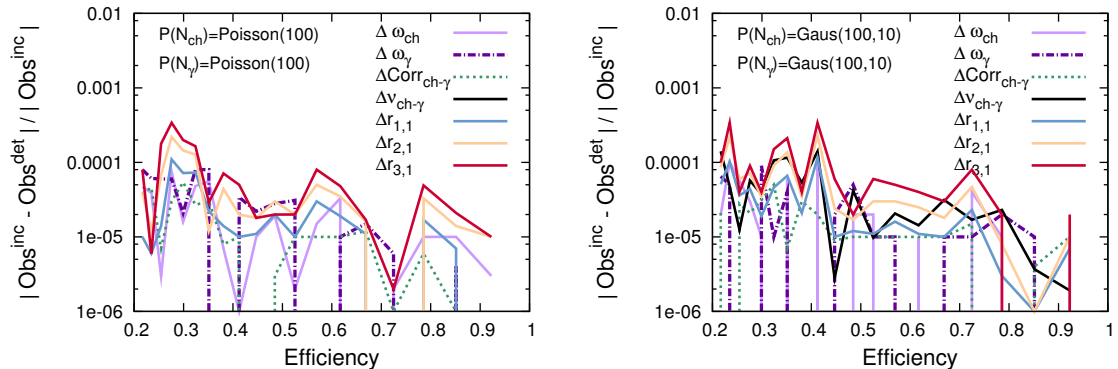


Figure 2.1: Effect of efficiency using Monte Carlo simulation. The effect of efficiency is introduced by hand using two random Poisson and Gaussian numbers. It seems that all the observable constructed out of factorial moments are insensitive to the variation of efficiency. A small numerical noise of similar magnitude is observed for all the observables when the scaled difference between the incident and the observed variable is considered. For Poisson distribution the observable $\nu_{\text{dyn}} \sim 0$.

of efficiency. Fig. 2.1 shows the scaled difference of the observables before (Obs^{inc}) and after (Obs^{det}) efficiency implementation as a function of efficiency. We find that the scaled difference is only a numerical noise ($10^{-4} - 10^{-5}$), independent of the observables that depends only on the statistics. Which indicates that the factorial moments cancel the effects of efficiency.

2.3.2 Effect of mis-identification

There are additional complications in realistic scenarios that have not been taken care of in the above prescriptions. The study of $\gamma - \text{ch}$ correlation is often complicated by mis-identification of charge particles as photons and vice versa. High value of energy loss of charged hadrons can lead to the formation of clusters in the photon detector. Similarly, photon conversion can show up as single or doubly detected tracks or clusters in charge particle detectors. In both the cases, the measurements get affected. Following the approach of the application of cluster decay

theorem discussed in previous section, we obtain the modified forms of the generating functions

$$\begin{aligned}
g_{\text{ch}}(z_{\text{ch}}, z_{\gamma}) &= (1 - \varepsilon_{\text{ch}} - \varepsilon_{\text{ch},\gamma}) + \varepsilon_{\text{ch}} z_{\text{ch}} + \varepsilon_{\text{ch},\gamma} z_{\gamma} \\
g_0(z_{\text{ch}}, z_{\gamma}) &= ((1 - \varepsilon_{\gamma} - \varepsilon_{\gamma,\text{ch}} - \varepsilon_{\gamma,2\text{ch}}) + \varepsilon_{\gamma} z_{\gamma} \\
&\quad + \varepsilon_{\gamma,\text{ch}} z_{\text{ch}} + \varepsilon_{\gamma,2\text{ch}} z_{\text{ch}}^2)^2,
\end{aligned} \tag{2.28}$$

where we view neutral pions decay with 100% “efficiency” into two photons which themselves “decay” with a few modes. ε_{ch} and ε_{γ} are the efficiencies of detecting a charged particle and a photon, respectively. $\varepsilon_{\text{ch},\gamma}$ is the probability of a charged particle being identified as a photon. $\varepsilon_{\gamma,\text{ch}}$, $\varepsilon_{\gamma,2\text{ch}}$ are the probabilities of a photon being identified as one or two charged particles, respectively. Substituting these in Eq. 2.17 one can calculate different factorial moments as,

$$\begin{aligned}
f_{10} &= \langle (1 - f)\varepsilon_{\text{ch}} + 2f(\varepsilon_{\gamma,\text{ch}} + 2\varepsilon_{\gamma,2\text{ch}}) \rangle \langle N \rangle \\
f_{01} &= \langle (1 - f)\varepsilon_{\text{ch},\gamma} + 2f\varepsilon_{\gamma} \rangle \langle N \rangle \\
f_{11} &= \langle N(N - 1) ((1 - f)\varepsilon_{\text{ch}} + 2f(\varepsilon_{\gamma,\text{ch}} + 2\varepsilon_{\gamma,2\text{ch}})) \\
&\quad \times ((1 - f)\varepsilon_{\text{ch},\gamma} + 2f\varepsilon_{\gamma}) + 2Nf\varepsilon_{\gamma}(\varepsilon_{\gamma,\text{ch}} + 2\varepsilon_{\gamma,2\text{ch}}) \rangle \\
f_{20} &= \langle N(N - 1) ((1 - f)\varepsilon_{\text{ch}} + 2f(\varepsilon_{\gamma,\text{ch}} + 2\varepsilon_{\gamma,2\text{ch}}))^2 \\
&\quad + 2Nf(2\varepsilon_{\gamma,2\text{ch}} + (\varepsilon_{\gamma,\text{ch}} + 2\varepsilon_{\gamma,2\text{ch}})^2) \rangle \\
f_{02} &= \langle N(N - 1)((1 - f)\varepsilon_{\text{ch},\gamma} + 2f\varepsilon_{\gamma})^2 + 2Nf\varepsilon_{\gamma}^2 \rangle.
\end{aligned} \tag{2.29}$$

This would lead to very complicated dependencies of $\Delta\nu_{\text{dyn}}$ and $r_{m,1}$ on various efficiency factors. However simplified expressions can be achieved in the limit $\varepsilon_{\gamma,2\text{ch}} \rightarrow 0$ and $\varepsilon_{\gamma,\text{ch}}$ as follows

$$\Delta\nu_{\text{dyn}}^{\gamma\text{-ch}} = \left(\frac{\langle (1-f)^2 \rangle}{\langle 1-f \rangle^2} + \frac{\langle \left((1-f)^{\frac{\varepsilon_{\text{ch},\gamma}}{\varepsilon_\gamma} + 2f} \right)^2 \rangle}{\langle (1-f)^{\frac{\varepsilon_{\text{ch},\gamma}}{\varepsilon_\gamma} + 2f} \rangle^2} \right. \\ \left. - 2 \frac{\langle (1-f) \left((1-f)^{\frac{\varepsilon_{\text{ch},\gamma}}{\varepsilon_\gamma} + 2f} \right) \rangle}{\langle 1-f \rangle \langle (1-f)^{\frac{\varepsilon_{\text{ch},\gamma}}{\varepsilon_\gamma} + 2f} \rangle} \right) \frac{\langle N(N-1) \rangle}{\langle N \rangle^2} \quad (2.30)$$

where the generic value of ν_{dyn} will be given by

$$\nu_{\text{dyn}}^{\gamma\text{-ch}} \Big|_{\text{generic}} = \frac{1}{2 \langle f \rangle \langle N \rangle \left(\frac{\varepsilon_{\text{ch},\gamma}}{\varepsilon_\gamma} + 1 \right)}. \quad (2.31)$$

The robust variable $r_{m,1}$ can be expressed as

$$r_{m,1}^{\gamma\text{-ch}} = \frac{\langle (1-f)^m \left((1-f)^{\frac{\varepsilon_{\text{ch},\gamma}}{\varepsilon_\gamma} + 2f} \right) \rangle \langle 1-f \rangle}{\langle (1-f)^{m+1} \rangle \langle (1-f)^{\frac{\varepsilon_{\text{ch},\gamma}}{\varepsilon_\gamma} + 2f} \rangle}. \quad (2.32)$$

Unlike previous case it is not possible to eliminate the efficiency factors in Eq. 2.30 and Eq. 2.32.

2.3.3 Effect of resonance decay

Resonance decays like $\omega \rightarrow \pi^0 + \pi^\pm$ or $\rho \rightarrow \pi^\pm \gamma$ would give rise to correlation in the pions. The effect of resonance decays can be implemented using generating function approach in the following way. We consider event by event measurement of two particle species with efficiencies ε_1 and ε_2 respectively. We assume f_R as the fraction of neutral resonances out of total N number of produced particles which fully decay into two species considered.

Similar to Eq. 2.8 we can write a generating function of the form,

$$G(z_1, z_2, z_R) = \int_0^1 df_R \mathcal{P}(f_R) \sum_N P(N) \left[(1-f_R) \int [\alpha z_1 + (1-\alpha)z_2] \mathcal{P}(\alpha) d\alpha + f_R z_R \right]^N. \quad (2.33)$$

Here $\mathcal{P}(f_R)$ and $\mathcal{P}(\alpha)$ are probability distributions related to event-by-event fluctuations of resonance fraction and particle ratio fluctuation. For simplicity we can assume $\mathcal{P}(f_R) = \delta(f_R - \bar{f}_R)$ and $\mathcal{P}(\alpha) = \delta(\alpha - \bar{\alpha})$. We can now replace $z_{1,2,R}$ by

$$g_1(z_1) = (1 - \varepsilon_1) + \varepsilon_1 z_1 \quad (2.34)$$

$$g_2(z_2) = (1 - \varepsilon_2) + \varepsilon_2 z_2 \quad (2.35)$$

$$g_R(z_R) = (1 - \varepsilon_{R1} - \varepsilon_{R2} - \varepsilon_{R3}) + \varepsilon_{R1} z_1 + \varepsilon_{R2} z_2 + \varepsilon_{R3} z_1 z_2. \quad (2.36)$$

Here the efficiencies $\varepsilon_{R1,R2,R3}$ take care of the probability of observing single or double products coming from resonance decay, a similar implementation was used for decay of neutral pions in the previous sections (Eq. 2.18).

First few factorial moments are given as

$$\begin{aligned} f_{m0} &= \left[[1 - \bar{f}_R] \bar{\alpha} \varepsilon_1 + \bar{f}_R (\varepsilon_{R1} + \varepsilon_{R3}) \right]^m \langle N(N-1) \cdots (N-m+1) \rangle, \\ f_{0n} &= \left[[1 - \bar{f}_R] (1 - \bar{\alpha}) \varepsilon_2 + \bar{f}_R (\varepsilon_{R2} + \varepsilon_{R3}) \right]^n \langle N(N-1) \cdots (N-n+1) \rangle, \\ f_{11} &= \bar{f}_R \varepsilon_{R3} \langle N \rangle + \left[[1 - \bar{f}_R] \bar{\alpha} \varepsilon_1 + \bar{f}_R (\varepsilon_{R1} + \varepsilon_{R3}) \right] \times \left[[1 - \bar{f}_R] (1 - \bar{\alpha}) \varepsilon_2 + \bar{f}_R (\varepsilon_{R2} + \varepsilon_{R3}) \right]. \end{aligned} \quad (2.37)$$

For example the observable $\nu_{\text{dyn}}^{1,2}$ in this case would be

$$\nu_{\text{dyn}}^{1,2} = \frac{-\bar{f}_R \varepsilon_{R3}}{\langle N \rangle \left[[1 - \bar{f}_R] \bar{\alpha} \varepsilon_1 + \bar{f}_R (\varepsilon_{R1} + \varepsilon_{R3}) \right] \left[[1 - \bar{f}_R] (1 - \bar{\alpha}) \varepsilon_2 + \bar{f}_R (\varepsilon_{R2} + \varepsilon_{R3}) \right]}. \quad (2.38)$$

Here since all the terms in the denominator are positive we can see that for generic production ($\mathcal{P}(\alpha) = \delta(\alpha - \bar{\alpha})$) with resonance decays $\nu_{\text{dyn}} < 0$. This expression agrees with similar expression derived in Ref. [155] in a different approach. Similarly for the observable $r_{1,1}$ one gets

$$r_{1,1} = 1 + \frac{\bar{f}_R \varepsilon_{R3} \langle N \rangle}{f_{10} f_{01} \langle N(N-1) \rangle / \langle N \rangle^2} \quad (2.39)$$

which indicates that for correlated production due to resonance decay $r_{1,1} > 1$. So it turns out that the decay of resonances gives rise to an effect that is opposite to the effect due to the DCC-like signal. Although qualitatively we can study the affect of resonance decay on observables it is difficult to get quantitative estimation from the above expressions without putting realistic numbers for the efficiencies. To study the effect of resonances in a more detailed way (sec.2.4.1, 2.5.2) we have used Monte-Carlo models in which resonance productions are included.

2.3.4 Effect of rapidity gap

In this section we would like to discuss the effect of rapidity gap ($\Delta\eta$) in the study of multiplicity correlation. According to reference [155], the rapidity dependence of correlation is given by

$$\text{Corr}_{1,2}^{\text{PGV}} = \frac{\langle N_1 N_2 \rangle}{\langle N_1 \rangle \langle N_2 \rangle} \approx 1 + \frac{\mathcal{C}}{x^2} [\sqrt{\pi} x \text{erf}(x) - (1 - e^{-x^2})] \quad (2.40)$$

where $x = \sqrt{2}\Delta\eta/\sigma$, in which $\Delta\eta$ is the rapidity gap over which the correlation is studied. \mathcal{C} and σ are constants related to systems size, energy, centrality of collisions and species of particles considered for the study of correlation. The above dependence can also be studied in HIJING simulation taking photons in a window of unit rapidity and charged particles with same window at rapidity separated by a gap of $\Delta\eta$. Fig. 2.2 shows the variation of the $\gamma - \text{ch}$ correlation using HIJING model; the simulation points are fitted with Eq. 2.40 (shown by grey curve).

2.3.5 Effect of centrality selection

In heavy ion collision experiment, observables are commonly studied with respect to the centrality that is related to the number of participating nucleons. It is therefore necessary that we study the nominal effect of the superposition of nucleons on the observables. In this section we would like to study the centrality dependence of the $\gamma - \text{ch}$ correlation using an approach based on the ‘‘Central Limit Theorem’’ (CLT). Importance and applicability of CLT in the context of correlation analysis in heavy ion collision has previously been discussed in detail in ref.[156]. In

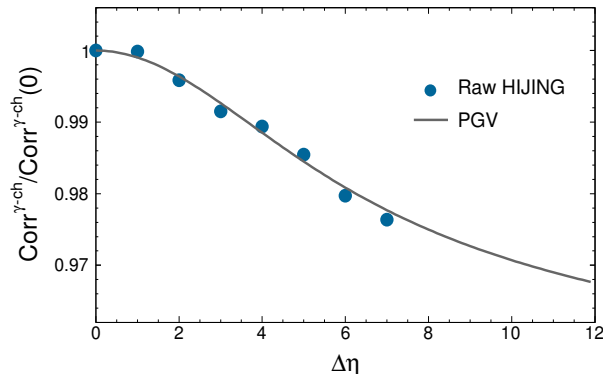


Figure 2.2: Effect of multiplicity correlation with rapidity gap. The points indicates HIJING simulation. PGV (Pruneau-Gavin-Voloshin) refers to the functional fit of the simulation points using Eq. 2.40 which is taken from Ref. [155].

a heavy ion collision, let us consider, that N_S number of identical sources are responsible for particle production. If N_i is the number of particles produced from i -th source, any variable $V(N_i)$ will have a distribution identical for all the sources. If we assume heavy-ion collision to be a linear superposition of many identical nucleon-nucleon collisions, under identical source approximation we can calculate the centrality dependence of the variable using CLT [157]. From CLT it follows that mean and variance of multiplicity would be given by

$$\begin{aligned}
 M(N) &= M\left(\sum_i^{N_S} N_i\right) = \sum_i^{N_S} M(N_i) = N_S M(N_i) \\
 \sigma^2(N) &= \sigma^2\left(\sum_i^{N_S} N_i\right) = \sum_i^{N_S} \sigma^2(N_i) = N_S \sigma^2(N_i).
 \end{aligned}
 \tag{2.41}$$

Since we have already assumed a collection of identical sources we can take $M(N_i) = \alpha$ and $\sigma^2(N_i) = \beta$ to be constant numbers same for all emission sources. So from CLT we have the dependence $M(N) = \alpha N_S$ and $\sigma(N) = \beta\sqrt{N_S}$. In our case N could refer to total number of produced pions, photons or charged particles. In that case similar argument also holds for $M(N_\pi, N_{\text{ch}} \text{ or } N_\gamma) \sim \alpha_{\pi, \text{ch}, \gamma} N_S$ and $\sigma(N_\pi, N_{\text{ch}} \text{ or } N_\gamma) \sim \beta_{\pi, \text{ch}, \gamma} \sqrt{N_S}$ where (α_π, β_π) , $(\alpha_{\text{ch}}, \beta_{\text{ch}})$ and $(\alpha_\gamma, \beta_\gamma)$ are sets of constants corresponding to pion, charged particle or photon multiplicities for identical sources respectively.

Let us assume N to be equal to the total number of produced pions where we have $N_\pi = aN_{\text{ch}} + bN_\gamma$. Where a and b are the fraction of charged pions and decay photons respectively¹. Using Eq. 2.41 one gets the mean and variance of pions as

$$\begin{aligned}\langle N_\pi \rangle &= \alpha_\pi N_S \\ \sigma^2(N_\pi) &= \left(\langle N_\pi^2 \rangle - \langle N_\pi \rangle^2 \right) \sim \beta_\pi^2 N_S \\ \langle N_\pi^2 \rangle &= \langle (aN_{\text{ch}} + bN_\gamma)^2 \rangle \sim \beta_\pi^2 N_S + \alpha_\pi^2 N_S^2\end{aligned}\quad (2.42)$$

and if we express pion multiplicity in terms of charged and photons we get,

$$\begin{aligned}\langle N_{\text{ch}}^2 \rangle &\sim \beta_{\text{ch}}^2 N_S + \alpha_{\text{ch}}^2 N_S^2 \\ \langle N_\gamma^2 \rangle &\sim \beta_\gamma^2 N_S + \alpha_\gamma^2 N_S^2 \\ \langle N_{\text{ch}} N_\gamma \rangle &\sim \beta_{\gamma\text{-ch}}^2 N_S + \alpha_{\gamma\text{-ch}}^2 N_S^2\end{aligned}\quad (2.43)$$

where $\alpha_{\gamma\text{-ch}}$ and $\beta_{\gamma\text{-ch}}$ are constants expressible² in terms of $a, b, \alpha_{\pi,\text{ch},\gamma}$ and $\beta_{\pi,\text{ch},\gamma}$. Using above relations, Eq. 2.14 and Eq. 2.15 we can calculate the centrality dependence of the observables.

For ν_{dyn} we have

$$\nu_{\text{dyn}}^{\gamma\text{-ch}} \sim A + \frac{B}{N_S} \equiv A' + \frac{B'}{\sqrt{\langle N_\gamma \rangle \langle N_{\text{ch}} \rangle}}. \quad (2.44)$$

All three terms in Eq. 2.14 have similar centrality dependence. Here we note that the constants A' and B' (or A and B) could be either positive or negative depending on which term in Eq. 2.14 is dominant. The variable $\Delta\nu_{\text{dyn}}$ would have the similar centrality dependence which is evident from the form of Eq. 2.26. In heavy ion collisions, the number of sources participating in particle production can also be assumed to be proportional to number of participants ($N_S \sim N_{\text{part}}$) of the collision. In that case $\nu_{\text{dyn}}^{\gamma\text{-ch}}$ is expected to show a scaling behavior of the form $A + B/X$ with X being either observed multiplicity or a Glauber variable N_{part} . However in case of

¹Note that $N_\pi = N_{\pi^+} + N_{\pi^-} + N_{\pi^0} \approx N_{\text{ch}} + 0.5N_\gamma; a \sim 1, b \sim 0.5$.

²it can be shown that $\alpha_{\gamma\text{-ch}}^2 = (\alpha_\pi^2 - a^2\alpha_{\text{ch}}^2 - b^2\alpha_\gamma^2)/2ab$, $\beta_{\gamma\text{-ch}}^2 = (\beta_\pi^2 - a^2\beta_{\text{ch}}^2 - b^2\beta_\gamma^2)/2ab$

experimental measurements it is more convenient to express fluctuation variables in terms of measured multiplicities.

Based on similar approach one can extract the centrality dependence of $r_{m,1}$. In the most general case one has

$$r_{m,1} = \frac{\sum_{p=1}^m \alpha_p (N_S)^p}{\sum_{p=1}^m \beta_p (N_S)^p} \quad (2.45)$$

which shows that both numerator and denominator have identical dependence on N_S . So according to CLT, behavior of $r_{m,1}$ with multiplicity depends on the coefficients α_p and β_p .

It must be noted that breakdown of scaling from CLT would have several implications. The picture of identical source emission may not be valid in the case for formation of domains of DCC where one might observe deviation from proposed scaling.

2.4 Application of the observables in heavy ion collisions : model studies

In this section we study correlation and fluctuations of charged and neutral particle multiplicity using various models widely discussed in the literature. A simple statistical model of particle production from a system of Boltzmann gas of pions in the Grand Canonical Ensemble is discussed in the first section. In the subsequent sections we discuss the predictions from monte-carlo mini-jets and transport models which includes various realistic effects such as decays, resonance, flow etc. Finally we study the sensitivity of the observables in the context of DCC formation. A simple approximation has been used to introduce DCC like (anti-correlation) in the generating function approach and the effects on the observables are studied in analytical approach. None of these conventional Monte Carlo event generator models include the physics of DCC. In this section we implement a Mont-carlo DCC model using inputs from HIJING event generators.

2.4.1 Statistical models for pion production.

Theoretical predictions of isospin fluctuation for a statistical system of pions can be found in references [158, 159]. However the discussion is limited to only charged and neutral pion fluctuations. In this section we use the result mentioned in above references and quantify in terms of experimental observables of $\gamma - \text{ch}$ correlation under some approximations.

It can be shown that a system of Boltzmann gas of pions in the grand canonical ensemble (GCE), gives $\langle N_{\pi^0} \rangle = \langle N_{\pi^\pm} \rangle = \zeta$, where ζ is the single particle partition function[158, 159]

$$\zeta = \frac{V}{2\pi} \int_0^\infty p^2 dp \exp\left(-\frac{\sqrt{p^2 + m^2}}{T}\right), \quad (2.46)$$

Here V, m and T are volume, pion mass and temperature of the system. In that case the mean-square of pion multiplicity and charge-to-neutral pion correlation are related to mean multiplicities as

$$\begin{aligned} \langle N_{\pi^0}^2 \rangle &= \langle N_{\pi^0} \rangle + \langle N_{\pi^0} \rangle^2 \\ \langle N_{\pi^\pm}^2 \rangle &= \langle N_{\pi^\pm} \rangle + \langle N_{\pi^\pm} \rangle^2 \\ \langle N_{\pi^0} N_{\pi^\pm} \rangle &= \langle N_{\pi^0} \rangle \langle N_{\pi^\pm} \rangle \end{aligned} \quad (2.47)$$

In ref[159] it was shown that for an ideal scenario where one assumes the total isospin of the system to be zero, above mentioned relationships would become complicated. An ensemble of the total isospin $I=0$ as shown in [159] would give

$$\langle N_{\pi^0} \rangle = \langle N_{\pi^\pm} \rangle = \frac{\zeta^2}{3} + \frac{\zeta^3}{6} \quad (2.48)$$

and in that case the mean-square pions multiplicities are modified as

$$\begin{aligned}\langle N_{\pi^0}^2 \rangle &\approx \langle N_{\pi^0} \rangle + \frac{\zeta^2}{3} + \frac{\zeta^4}{15} \\ \langle N_{\pi^\pm}^2 \rangle &\approx \langle N_{\pi^\pm} \rangle + \frac{\zeta^4}{10}.\end{aligned}\tag{2.49}$$

We can generalize these results and apply in case of our observables of $\gamma - \text{ch}$ correlation. The dependence on ζ can be eliminated and final observables can be expressed in terms of experimentally observed quantities like measured multiplicity (say $\sqrt{\langle N_{\text{ch}} \rangle \langle N_\gamma \rangle}$). In this case one has $\langle N_\gamma \rangle = 2 \langle N_{\pi^0} \rangle$ and $\langle N_{\text{ch}} \rangle = \langle N_{\pi^+} + N_{\pi^-} \rangle = 2 \langle N_{\pi^\pm} \rangle$. Also for decay of neutral pions we have used the relation $\sigma_\gamma^2 \approx \mathcal{C} \sigma_{\pi^0}^2$, and we have used $\mathcal{C}=2$ for our calculation³. Choice of \mathcal{C} mostly affects the observables at low multiplicity. With these assumptions we can express the mean-square multiplicities to be

$$\langle N_\gamma^2 \rangle = 4 \langle N_{\pi^0}^2 \rangle, \quad \langle N_{\text{ch}}^2 \rangle = 2 \langle N_{\pi^\pm}^2 \rangle + 2 \langle N_{\pi^+} N_{\pi^-} \rangle\tag{2.50}$$

and the correlation term will be given by $\langle N_\gamma N_{\text{ch}} \rangle = 4 \langle N_{\pi^0} N_{\pi^\pm} \rangle$. Now we have

$$\begin{aligned}\frac{f_{20}}{f_{10}^2} &= \frac{1}{2} \left(\frac{\langle N_{\pi^\pm} (N_{\pi^\pm} - 1) \rangle}{\langle N_{\pi^\pm} \rangle^2} + \frac{\langle N_{\pi^+} N_{\pi^-} \rangle}{\langle N_{\pi^\pm} \rangle^2} \right) \\ \frac{f_{02}}{f_{01}^2} &= \frac{1}{2} \left(\frac{\langle N_{\pi^0} (N_{\pi^0} - 1) \rangle}{\langle N_{\pi^0} \rangle^2} + 1 \right) \\ \frac{f_{11}}{f_{10} f_{01}} &= \frac{\langle N_{\pi^0} N_{\pi^\pm} \rangle}{\langle N_{\pi^0} \rangle \langle N_{\pi^\pm} \rangle}\end{aligned}\tag{2.51}$$

So using Eq. 2.47, Eq. 2.49 and Eq. 2.51 we can estimate $\nu_{\text{dyn}}^{\gamma-\text{ch}}$ and $r_{1,1}$ for GCE and I=0 systems. For GCE we get from Eq. 2.47 and Eq. 2.51, $\nu_{\text{dyn}} = 1/\sqrt{\langle N_{\text{ch}} \rangle \langle N_\gamma \rangle}$, which gives correct multiplicity dependence as predicted from CLT. So from Eq. 2.26 we have $\Delta \nu_{\text{dyn}}^{\gamma-\text{ch}} = 0$ for GCE. The system of I=0 gives $\Delta \nu_{\text{dyn}}^{\gamma-\text{ch}} \sim -0.98/\sqrt{\langle N_{\text{ch}} \rangle \langle N_\gamma \rangle}$ which also agrees with the CLT

³For Poissonian case $\sigma_\gamma = \sqrt{\langle N_\gamma \rangle} = \sqrt{2 \langle N_{\pi^0} \rangle} = \sqrt{2} \sigma_{\pi^0}$ gives $\mathcal{C}=2$; incase one detects all photons from π^0 one has a maximum value of $\mathcal{C}=4$ which is not in accordance with CGE picture where limited phase space of a system is probed.

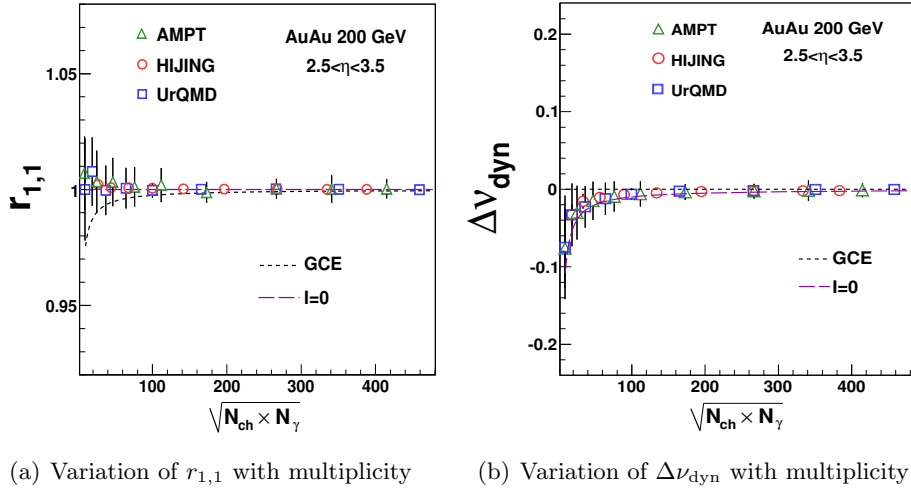


Figure 2.3: Multiplicity dependence of observables $r_{1,1}$ and $\Delta\nu_{\text{dyn}}$ as predicted from different models. The curves represent the results for different ensembles of Boltzmann gas of pions from Eq. 2.47 and Eq. 2.49 as described in the text. The markers are from different Monte-Carlo models. The error-bars are statistical.

predictions as shown in Fig. 2.3(b). In case of GCE $r_{1,1}$ is predicted to be $2/(1+1/\sqrt{\langle N_{\text{ch}} \rangle \langle N_{\gamma} \rangle})$ which becomes 1 for large values of multiplicity. For a system of $I=0$, $r_{1,1} \sim 1$ for all values of $\sqrt{\langle N_{\text{ch}} \rangle \langle N_{\gamma} \rangle}$ as shown in Fig. 2.3(a).

2.4.2 Transport and Mini-jet model predictions

We have also estimated various observables and their centrality dependences using different monte-carlo event generators like HIJING[160], AMPT [161] and UrQMD[162] for top RHIC energy. For our calculation we choose one unit of rapidity in forward direction ⁴ but no cut off has been applied on transverse momentum. We do the centrality selection based on putting cuts on impact parameter following Glauber model calculation. Fig. 2.3 shows the centrality dependence of the observables. The variable $r_{1,1}$ shows flat centrality dependence within error bars. The results from different monte-carlo models are consistent with each other and the values from the statistical model of Boltzman gas are consistent with other models towards

⁴both STAR and ALICE experiments has the setup of simultaneous measurements of charged and photon in one unit of rapidity.

higher multiplicity as shown in Fig. 2.3(a) and Fig. 2.3(b). At lower multiplicities they have qualitatively different nature, probably due to presence of various other effects in the monte-carlo models.

Fig. 2.7(a) shows the variation of $r_{m,1}$ with its order m . Results from all the models are consistent with the generic case of pion production. Fig. 2.7(b) shows the centrality dependence of ν_{dyn} and $\Delta\nu_{\text{dyn}}$ predicted for HIJING. For comparison of centrality dependence predicted from CLT, we have fitted the points with functional form of $A + B/\sqrt{\langle N_{\text{ch}} \rangle \langle N_{\gamma} \rangle}$. This yields a value of $A \approx 5 \times 10^{-5}$ and $B = -0.6$ for $\Delta\nu_{\text{dyn}}$. We also note here that the sign of $\Delta\nu_{\text{dyn}}$ is negative for low multiplicity. This shows that HIJING includes some intrinsic $\gamma - \text{ch}$ correlation making the last term of Eq. 2.24 to dominate over individual fluctuation. This can be attributed to the resonance decays present in HIJING model. For DCC like signal sign of $\Delta\nu_{\text{dyn}}$ should become positive for all centralities.

2.5 γ -charge correlation and DCC

Formation of domains of DCC is one of the possible sources of dynamical $\gamma - \text{ch}$ correlation. Isospin symmetry for a system pions corresponds to a generic case of pion productions for which $\mathcal{P}(f) = \delta(f - 1/3)$. In case of DCC like events[146, 148] this distribution is modified to $\mathcal{P}(f) = 1/2\sqrt{f}$. One can study the sensitivity of $\Delta\nu_{\text{dyn}}$ and $r_{m,1}$ to a given fraction of DCC like signal. If x -fraction of events have DCC domain formation, in simplistic case one can assume the distribution of neutral pion fraction to be a combination of generic and DCC probability distributions given by

$$\mathcal{P}(f) = x \frac{1}{2\sqrt{f}} + (1 - x) \delta\left(f - \frac{1}{3}\right). \quad (2.52)$$

So for $\Delta\nu_{\text{dyn}}$ we get

$$\begin{aligned}\Delta\nu_{\text{dyn}}^{\gamma\text{-ch}} &= \left(\frac{\langle(1-f)^2\rangle}{\langle1-f\rangle^2} + \frac{\langle f^2\rangle}{\langle f\rangle^2} - 2 \frac{\langle f(1-f)\rangle}{\langle f\rangle\langle1-f\rangle} \right) \Big|_{\text{signal}} \frac{\langle N(N-1)\rangle}{\langle N\rangle^2} \\ &= \frac{x}{5/9} \frac{\langle N(N-1)\rangle}{\langle N\rangle^2},\end{aligned}\tag{2.53}$$

which is proportional to the fraction of DCC events. $\Delta\nu_{\text{dyn}}$ shows very high sensitivity to DCC like signal but it is dependent on the parent multiplicity and consequently to the collisions centrality. In a later section we would discuss this issue in detail. In case the parent distribution is Poisson, the fluctuation term $\langle N(N-1)\rangle/\langle N\rangle^2$ would be equal to 1 giving $\Delta\nu_{\text{dyn}}^{\gamma\text{-ch}} \sim x/(5/9)$.

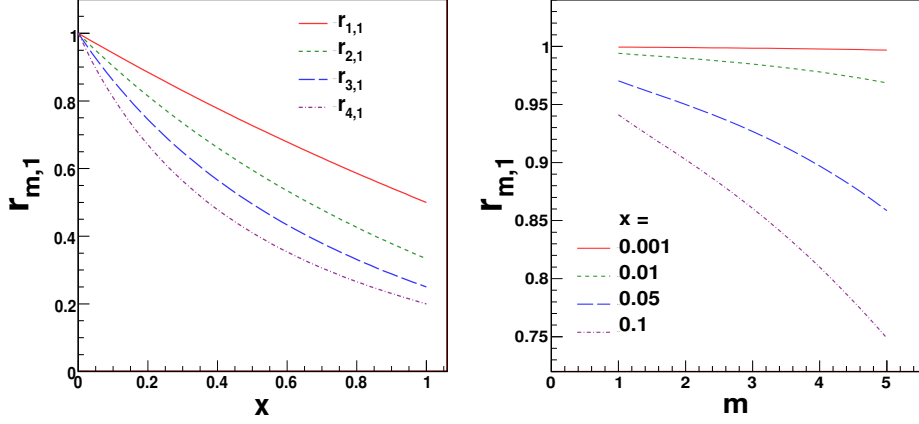
The observable $r_{m,1}$ expressed in Eq. 2.27 would have a very particular x dependence given by

$$r_{m,1}^{\gamma\text{-ch}} = 1 - \frac{mx}{(m+1)} F(m, x)\tag{2.54}$$

where the function $F(m, x)$ is given by

$$F(m, x) = \frac{1}{x + (1-x) \frac{2}{\sqrt{\pi}} \left(\frac{2}{3}\right)^{m+1} \frac{\Gamma(m+5/2)}{\Gamma(m+2)}}.\tag{2.55}$$

For ideal DCC case ($x=1$), the function $F(m, x)=1$ for all values of m giving $r_{m,1} = 1/(m+1)$. For generic case ($x=0$), $r_{m,1}=1$ for all m . Fig.1 shows the sensitivity of $r_{m,1}$ for small signals of DCC. The functional form given in Eq. 2.54 can be used to extract x from a fit of $r_{m,1}$ with m . In the derivation of Eq. 2.53 and Eq. 2.54 we have assumed that the parent multiplicity distribution are similar for both the generic and DCC cases. The efficiency factors are assumed to be constant and independent of multiplicity and other kinematic parameters.



(a) Variation of $r_{m,1}$ with fraction of DCC signal (b) Variation of $r_{m,1}$ with higher order moments

Figure 2.4: Sensitivity of the observable $r_{m,1}$ to DCC like signals. Higher orders of $r_{m,1}$ show more sensitivity to small signals of anti-correlation.

For x -fraction of DCC signals Eq. 2.53 and Eq. 2.54 will be modified to

$$\Delta\nu_{\text{dyn}}^{\gamma\text{-ch}} = \frac{x}{5/9} \frac{1}{\left(\frac{\varepsilon_{\text{ch},\gamma}}{\varepsilon_{\gamma}} + 1\right)^2} \frac{\langle N(N-1) \rangle}{\langle N \rangle^2}$$

$$r_{m,1} = 1 - \frac{mx}{m+1} \frac{1}{\left(\frac{\varepsilon_{\text{ch},\gamma}}{\varepsilon_{\gamma}} + 1\right)} F(m, x) \quad (2.56)$$

where $F(m, x)$ is given by Eq. 2.55. We can see that mis identification of charged particles as photons reduces the effective fraction of DCC events. The contamination factor in Eq. 2.56 appears as a ratio of $\varepsilon_{\text{ch},\gamma}/\varepsilon_{\gamma}$ keeping the functional form of the observables (Eq. 2.53, Eq. 2.54) unchanged. We also note here that $\Delta\nu_{\text{dyn}}^{\gamma\text{-ch}}$ has a quadratic dependence on contamination factor whereas $r_{1,1}$ is affected only by a linear factor. This is because $\Delta\nu_{\text{dyn}}^{\gamma\text{-ch}}$ contains an extra photon fluctuation term which is absent in $r_{m,1}$.

2.5.1 Effect of mixture of pion sources

In this section we would like to discuss the effect on the observables when event-wise pion sources are independent of each other. So far we have considered that in a DCC event, all the pions detected in a given coverage are coming from the decay of the domains of DCC. This assumption might be valid when the detector coverage is same as the combined size of DCC domains. The realistic scenario is when the size of the domain of DCC is smaller than the detector coverage. Also DCC pions are dominantly from lower part of the momentum distribution. In both the cases of considering bulk multiplicity for correlation analysis, the candidates carrying actual signal would be a fraction total pions considered. Let us consider a case when x -fraction of events analyzed has DCC like fluctuation carried by y -fraction of total pions. So for DCC pions we have $\langle N \rangle_D = y \langle N \rangle$ and for generic pions we have $\langle N \rangle_G = (1 - y) \langle N \rangle$, N being the total number of pions. The probability to find N_D pions carrying DCC signal will be given by $P(N_D, N, y) = {}^N C_{N_D} y^{N_D} (1 - y)^{N - N_D}$, which would give $\langle N(N - 1) \rangle_D = y^2 \langle N(N - 1) \rangle$. Now in this case the generating function of Eq. 2.16 will be replaced by

$$G_{obs} = x' G_{DCC} + x G_{DCC} G_{generic} + (1 - x - x') G_{generic} \quad (2.57)$$

in which we view cases with 100% DCC production (x' fraction of events), 100% generic production and a mixture of two as three “decay modes” of a super cluster. Here G_{DCC} includes probability distribution $\mathcal{P}(f) = 1/2\sqrt{f}$ and $G_{generic}$ includes $\mathcal{P}(f) = \delta(f - 1/3)$. Since we consider the case of 100% DCC production is the least realistic, in the following we simplify our expression by taking $x' = 0$. Now different factorial moments will become functions of x and y

as

$$\begin{aligned}
f_{10} &= \langle 1 - f \rangle \varepsilon_{\text{ch}} \langle N \rangle \\
f_{01} &= \langle f \rangle 2\varepsilon_{\gamma} \langle N \rangle \\
f_{11} &= \left(2xy(1-y) \langle f \rangle \langle 1-f \rangle \langle N \rangle^2 + ((1-xy(2-y)) \langle f(1-f) \rangle_G \right. \\
&\quad \left. + xy^2 \langle f(1-f) \rangle_D) \langle N(N-1) \rangle \right) 2\varepsilon_{\gamma} \varepsilon_{\text{ch}}
\end{aligned} \tag{2.58}$$

$$\begin{aligned}
f_{20} &= \left(2xy(1-y) \langle 1-f \rangle^2 \langle N \rangle^2 + ((1-xy(2-y)) \langle (1-f)^2 \rangle_G \right. \\
&\quad \left. + xy^2 \langle (1-f)^2 \rangle_D) \langle N(N-1) \rangle \right) \varepsilon_{\text{ch}}^2
\end{aligned} \tag{2.59}$$

$$\begin{aligned}
f_{02} &= \left(2xy(1-y) \langle f \rangle^2 \langle N \rangle^2 + ((1-xy(2-y)) \langle f^2 \rangle_G \right. \\
&\quad \left. + xy^2 \langle f^2 \rangle_D) \langle N(N-1) \rangle \right) 4\varepsilon_{\gamma}^2 + 2\varepsilon_{\gamma}^2 \langle f \rangle \langle N \rangle
\end{aligned} \tag{2.60}$$

$$\tag{2.61}$$

In this case the observables are modified accordingly , for $\Delta\nu_{\text{dyn}}$ Eq. 2.26 gives,

$$\Delta\nu_{\text{dyn}} = \frac{x}{5/9} y^2 \frac{\langle N(N-1) \rangle}{\langle N \rangle^2} \tag{2.62}$$

which consistent with the expression Eq. 2.53 for $y = 1$ case. For Poisson like parent distribution $\Delta\nu_{\text{dyn}}$ can be expressed as

$$\Delta\nu_{\text{dyn}} = \frac{x}{5/9} y^2. \tag{2.63}$$

We note here that $\Delta\nu_{\text{dyn}}$ still shows the proportionality with the fraction of DCC events x . And the interesting fact is that quadratic dependence on y means $\Delta\nu_{\text{dyn}}$ is more sensitive to the change of fraction of pions carrying DCC-like signals.

In similar approach we can express $r_{1,1}$ to be

$$r_{1,1} = \frac{5 - 2xy^2}{5 + xy^2}. \tag{2.64}$$

This expression is consistent with the approximate expression of $r_{1,1}$ given in Ref.[163] for small

values of x . The higher order moments will have corrections from higher powers of y which will have smaller contributions like

$$\begin{aligned} r_{1,1} &= \frac{5 - 2xy^2}{5 + xy^2} \\ r_{2,1} &= \frac{35 - xy^2(21 - 4y)}{35 + xy^2(21 - 2y)} \end{aligned} \quad (2.65)$$

and so on. The general formula for $r_{m,1}$ is given by

$$r_{m,1} = 1 - \frac{mxy^2}{(m+1)} F(m, xy^2) + \mathcal{O}(xy^3) \dots \quad (2.66)$$

in which $r_{m,1}$ will have contribution up to xy^{m+1} . Since $y \leq 1$ higher order contribution of y are smaller and the approximate form of the above expression would be given by

$$r_{m,1} \approx 1 - \frac{mxy^2}{(m+1)} F(m, xy^2) \quad (2.67)$$

where $F(m, xy^2)$ is given by Eq. 2.55.

So to the lowest order approximation, the expression given by Eq. 2.54 is still valid with fraction x replaced by xy^2 . A functional fit of $r_{m,1}$ with m to experimental data by the above expression can restrict the contours of x and y .

2.5.2 A Monte-carlo model for DCC formation.

We have tried to implement DCC like anti-correlation signals in HIJING events. In a given event we change the neutral pion fraction to follow $1/2\sqrt{f}$ distribution by flipping π^0 to π^\pm . And finally we decay the neutral pions to photons. In the process of flipping we make sure that the charge and isospin conservations are maintained. Fig. 2.5 shows the f -distribution after the implementation of DCC in HIJING. For generic event the neutral pion fraction is peaked at $1/3$ and for DCC events it has a long tail. Since the variation of DCC like domain formation with rapidity and azimuthal angle is not known, we perform this flipping for all the

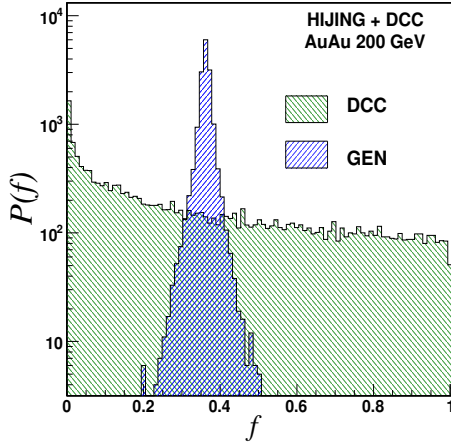


Figure 2.5: Histograms showing distribution of neutral pion fraction for generic and DCC events from HIJING

particles. This produces uniform $1/2\sqrt{f}$ like distribution over all phase space. To make the scenario more realistic we do the calculation of the final variables using total number of detected photons and charged particles rather than considering only pions. Other dominant sources of photons and charged particles include η , charged kaons and protons respectively. It is difficult to extract the fraction of primordial pions on which the DCC-like probability distribution could be implemented. HIJING has minijet like environment in which the production mechanism is “string fragmentation” and the abundance of particles are weighted by the spin giving large fraction of pions coming from decay of resonances. The primordial pions coming directly from string fragmentation are much smaller. Alternative environment like hydro models where the massive resonances are exponentially suppressed would give large fraction of soft pions. The difference between the two models of string fragmentation is discussed in Ref.[164]. We therefore randomly choose pions produced in HIJING events, treat them to be thermal and implement $1/2\sqrt{f}$ distribution. Fig. 2.6 shows the centrality dependence of the two observables and their sensitivity to different fraction of DCC events. $r_{1,1}$ shows almost flat dependence on multiplicity and we also find similar dependence for all higher moments of $r_{m,1}$. Absolute values of $r_{1,1}$ are consistent with the prediction ($r_{1,1} = (5 - 2x)/(5 + x)$) from Eq. 2.54. For higher fraction of DCC events the centrality dependence has slight non-monotonic behavior. This is also seen in

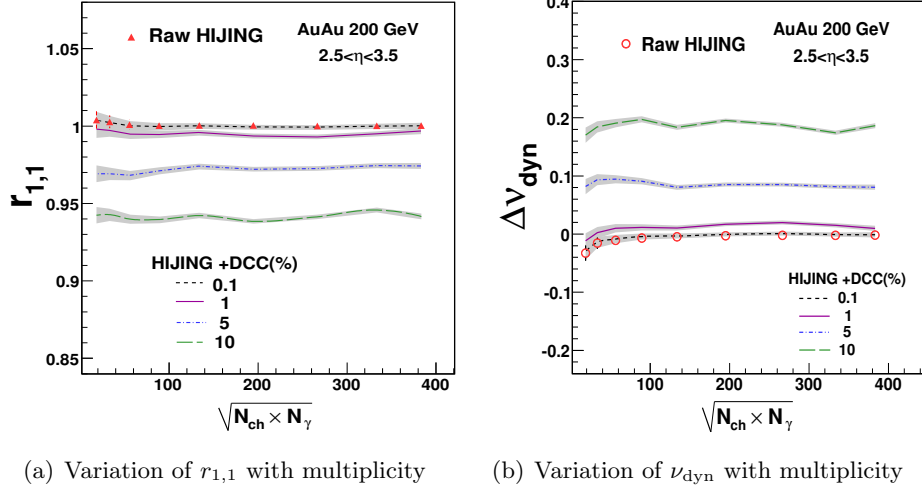
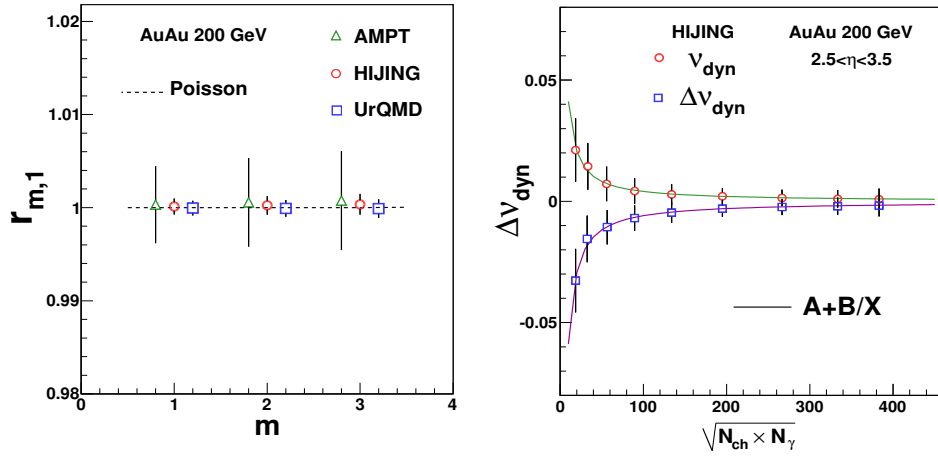
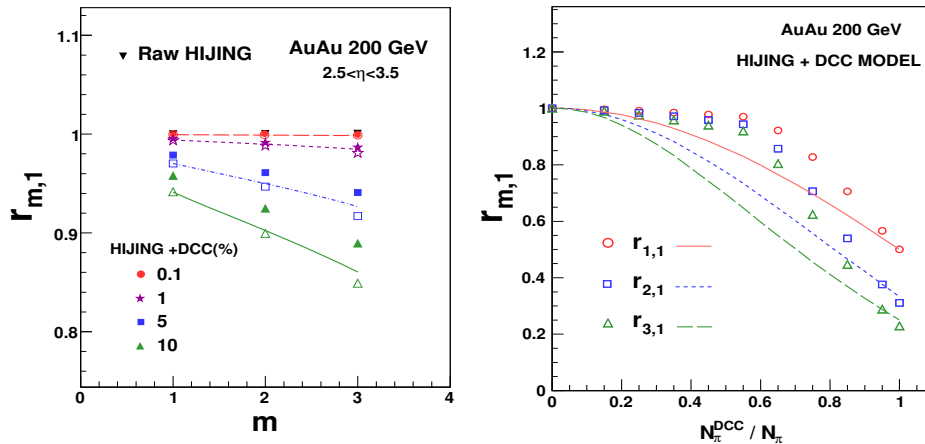


Figure 2.6: Multiplicity dependence of observables $r_{1,1}$ and ν_{dyn} as predicted from DCC implemented HIJING model. Here N_{ch} and N_{γ} denote the mean multiplicities of charged particles and photons for various centralities. The gray band shows the statistical uncertainty in model calculation.



(a) Variation of $r_{m,1}$ with m from different models. The m values of the points for AMPT and UrQMD have been shifted horizontally for better clarity. (b) Centrality dependence of variable ν_{dyn} and $\Delta \nu_{\text{dyn}}$ and fits predicted from CLT. Here N_{ch} and N_{γ} refer to the mean multiplicities of charged particles and photons.

Figure 2.7: Prediction of variables from different models.



(a) Value of $r_{m,1}$ with m for various fractions of DCC events. The solid markers are when N_{ch} and N_{γ} includes all the charged particles and photons and the hollow markers are when only pions are source of charged particles and photons. The curves are estimations from Eq. 2.54 and points are from DCC implemented HIJING.

(b) Variation of $r_{m,1}$ in DCC events with fraction of pions coming from decay of DCC domains. Curves are estimations from Eq. 2.67.

Figure 2.8: Sensitivity of $r_{m,1}$ to DCC like signals.

$\Delta\nu_{\text{dyn}}$. As expected from Eq. 2.53, the values of $\Delta\nu_{\text{dyn}}$ show proportionality with the fraction of DCC events. The absolute values of $\Delta\nu_{\text{dyn}}$ are also very close to $\approx x/(5/9)$ as predicted in Eq. 2.53. The centrality dependence causes $\approx 15\%$ variation of the values of most central to peripheral events for $\Delta\nu_{\text{dyn}}$. Fig. 2.8(a) shows the variation of $r_{m,1}$ with m . The results from DCC model match the theoretical curve (Eq. 2.54) when one considers only pions as source of charged particles and photons, however when all other sources are considered the results are slightly off towards Poissonian expectations. A more detailed study of the sensitivity to fraction of DCC pions is shown in Fig. 2.8(b) where we have shown the sensitivity of $r_{m,1}$ with the fraction of detected pions carrying DCC-signals. In Fig. 2.8(b) we also plot the curves obtained from Eq. 2.67. The effect of resonances present in HIJING seems to be resulting in reduced sensitivity of $r_{m,1}$ for lower fraction of DCC pions.

2.6 Summary

In this chapter we have discussed the methods for studying inclusive charge-neutral multiplicity fluctuations and correlations. The primary motivations is to study γ -charge correlation in heavy-ion collisions and the search for DCC-like anti-correlation signals relevant to the ongoing heavy ion program at RHIC and LHC. Two widely used measures in this context discussed in the literatures are ν_{dyn} and $r_{m,1}$. Using the method of moment generating functions we have studied the robustness of two observables. The sensitivity of the variables has been studied with the fraction of DCC type events(x). We propose a modification to the observable ν_{dyn} and extract the functional form in terms of x and y . Higher orders of $r_{m,1}$ show higher sensitivity to x and can have contribution up to y^{m+1} . A simplified form of the functional dependence of $r_{m,1}$ with m has been calculated in generating function approach for lowest order of y^2 . This would be useful to restrict the signal strength xy^2 by fitting the experimental data.

The centrality(multiplicity) dependence of the observables are extracted using Central Limit Theorem assuming identical source approximation for particle production. For generic case of particle production from CLT, it is predicted to be inversely proportional to multiplicity. The variation of the observable $r_{m,1}$ seem to be flat with centrality.

Scenarios	$\Delta\nu_{\text{dyn}}^{\gamma\text{-ch}}$	$r_{m,1}^{\gamma\text{-ch}}$
Generic pion production	0.	1
GCE for Boltzman pion gas	0.	~ 1 ($m=1$, higher multiplicity)
System of total $I = 0$	$\frac{-0.98}{\sqrt{\langle N_{\text{ch}} \rangle \langle N_{\gamma} \rangle}}$	1 ($m=1$)
HIJING, AMPT UrQMD (resonances)	negative	1
DCC (anti-correlation)	$\approx \frac{x}{5/9}y^2$	$\approx 1 - \frac{mxy^2}{(m+1)}F(m, xy^2)$

Table 2.1: Summary of our estimation of observables $\Delta\nu_{\text{dyn}}^{\gamma\text{-ch}}$ and $r_{m,1}^{\gamma\text{-ch}}$ under different scenarios relevant to heavy-ion collisions. $\Delta\nu_{\text{dyn}}^{\gamma\text{-ch}}$ is either 0 or negative except for DCC case which gives positive value depending on the fraction x and y . $r_{m,1}^{\gamma\text{-ch}}$ shows a particular functional dependence on m for DCC case which is distinct from all other scenarios.

Observables have been estimated from different models relevant to heavy-ion collisions that

do not include the physics of DCC. DCC-like anti-correlation signals are expected to be carried by pions in limited kinematic range in both co-ordinate and momentum space. We summarize our estimations for different scenarios in table 4.1. We have also developed a Monte-Carlo model where DCC domains have been implemented using inputs from HIJING event generator to study the sensitivity of those variables with DCC signals. Our results show that the model predictions of the variables are consistent with the theoretical predictions using generating function approach. Various detector effects like efficiency of detection, mis-identification have been implemented in this approach. We have shown that the mis-identification reduces the effective signal strength for which an approximate expression has been derived in generating function approach. The observable $r_{m,1}$ has been found to be more robust towards mis-identification of photons as compared to $\Delta\nu_{\text{dyn}}$. The resonance decay can induce correlation which can suppress the anti-correlating DCC signal. A quantitative idea of resonance can be obtained from DCC implemented Monte Carlo model. We have studied the sensitivity of $r_{m,1}$ for varying fraction of DCC candidates.

Chapter 3

Measurement of charge and neutral multiplicity fluctuation in Au+Au collisions

3.1 Introduction

In this chapter we discuss the details of the measurement and analysis of event-by-event fluctuation of the ratio of multiplicities of charged and neutral particles (photons) at the forward rapidity in Au+Au collision at $\sqrt{s_{NN}}=200$ GeV using STAR detector systems at RHIC. The e-by-e measurement of the multiplicities of charged particles and photons is done using the Forward Time Projection Chamber (FTPC) and the Photon Multiplicity Detector (PMD) respectively. Observables, $\nu_{\text{dyn}}^{\gamma\text{-ch}}$ and $r_{m,1}^{\gamma\text{-ch}}$ (m=1 - 3), have been used as measures of fluctuation and the method discussed in previous chapter is employed for this analysis. Based on these observables, the measured ratio fluctuations have been interpreted in terms of DCC-like phenomenon. Details of the procedure of data analysis like, bin-width correction, event mixing have been discussed in the following sections. GEANT simulations have been performed to study the responses of the detector systems. The statistical bootstrap method has been implemented to

perform error analysis of the moments.

3.2 Analysis Method

The event-by-event measurement of the charged particle and photon multiplicities within the pseudo-rapidity interval of $-3.7 < \eta < -2.8$, has been presented here. In order to eliminate the effect of the event-by-event variation of the common acceptance, the collision vertex position along the beam axis from the center of TPC (V_z) is restricted over a narrow range of $-5 < V_z < 5$ cm. For similar reason, the mixed event analysis is also performed in a given centrality and with collision vertex lying between ± 5 cm around the collision point. All the simulations using different event generators like AMPT [161], UrQMD [162] and HIJING [160], and for GEANT implemented HIJING are done using similar kinematic cuts as used for data.

Since we are interested in fluctuations of ratio of multiplicities, we consider the fraction, $f = N_{\pi^0}/(N_{\pi^0} + N_{\pi^\pm})$, which can be approximated as $f^{\gamma\text{-ch}} \approx N_\gamma/(N_\gamma + 2N_{\text{ch}})$. HIJING simulation shows that these two ratios differ by only 6% at forward rapidity region considered here. The idea is to choose proper combination of moments such that the efficiency dependence is eliminated and observables are expressed in terms of the fluctuations of the fraction f . The observables for charge-to-neutral fluctuation have to be robust against detector efficiencies and at the same time sensitive to small signals of γ -ch correlation. As shown in Sec.2.3.1, using proper combination of factorial moments of multiplicities of charged particles and photons, one can express the observable in term of the moments of f .

The observable $\nu_{\text{dyn}}^{\gamma\text{-ch}}$, introduced in Eq. 2.14 of Sec.2.3 is defined in this context as

$$\begin{aligned} \nu_{\text{dyn}}^{\gamma\text{-ch}} &= \frac{\langle N_{\text{ch}}(N_{\text{ch}} - 1) \rangle}{\langle N_{\text{ch}} \rangle^2} + \frac{\langle N_\gamma(N_\gamma - 1) \rangle}{\langle N_\gamma \rangle^2} - 2 \frac{\langle N_{\text{ch}} N_\gamma \rangle}{\langle N_{\text{ch}} \rangle \langle N_\gamma \rangle} \\ &= \omega_{\text{ch}} + \omega_\gamma - 2 \times \text{corr}_{\gamma\text{-ch}} \end{aligned} \quad (3.1)$$

$$= \left(\frac{\langle (1-f)^2 \rangle}{\langle 1-f \rangle^2} + \frac{\langle f^2 \rangle}{\langle f \rangle^2} - 2 \frac{\langle f(1-f) \rangle}{\langle f \rangle \langle 1-f \rangle} \right) \frac{\langle N(N-1) \rangle}{\langle N \rangle^2} + \frac{1}{2 \langle f \rangle \langle N \rangle}. \quad (3.2)$$

The first two terms ω_{ch} and ω_γ are measures of individual charge and photon number fluctu-

ations and the third term $\text{corr}_{\gamma\text{-ch}}$ corresponds to scaled $\gamma\text{-ch}$ correlation. For Poissonian fluctuations each of these terms individually becomes unity. So ν_{dyn} would become zero for purely statistical (Poisson) fluctuation and non-zero only in the presence of dynamical fluctuation of any form of origin [151–153]. The advantage of this variable is that it is robust against detector efficiency and involves only lowest orders of factorial moments which reduces statistical uncertainties [165]. $\nu_{\text{dyn}}^{\gamma\text{-ch}}$ has dependence on the parent (initial gluons) multiplicity N [166], which will lead to a strong centrality dependence of the observable. In Sec.2.3.5, it was shown that an application of the ‘‘Central Limit Theorem (CLT)’’ [156, 157] for generic case of pion production, $\nu_{\text{dyn}}^{\gamma\text{-ch}}$ leads to $A + B/\sqrt{\langle N_{\text{ch}} \rangle \langle N_{\gamma} \rangle}$ dependence on multiplicity [166]. This behavior is also consistent with system of Boltzmann gas of pions in the grand canonical ensemble (GCE) [158, 159]. Throughout this analysis we have studied the centrality dependence of the observables in terms of the experimental quantity $\sqrt{\langle N_{\text{ch}} N_{\gamma} \rangle}$ which is the average multiplicity in the acceptance of interest.

Another variable called $r_{m,1}$, introduced in Eq. 2.15 is defined as

$$r_{m,1}^{\gamma\text{-ch}} = \frac{\langle N_{\text{ch}}(N_{\text{ch}} - 1) \cdots (N_{\text{ch}} - m + 1) N_{\gamma} \rangle \langle N_{\text{ch}} \rangle}{\langle N_{\text{ch}}(N_{\text{ch}} - 1) \cdots (N_{\text{ch}} - m) \rangle \langle N_{\gamma} \rangle} = \frac{\langle f(1-f)^m \rangle \langle 1-f \rangle}{\langle (1-f)^{m+1} \rangle \langle f \rangle}. \quad (3.3)$$

It is designed such that for all the moments it gives a value equal to unity for the Poisson case and the higher order moments show higher sensitivity to (anti-)correlated signals. The advantage of this variable is that it is robust against detector efficiency and also independent of the parent multiplicity distribution [150, 166, 167]. It follows from Eq.(2.14) and Eq.(2.15), that the lowest order of this observable can be expressed as $r_{1,1} = \text{corr}_{\gamma\text{-ch}}/\omega_{\text{ch}}$. The functional dependence of $r_{m,1}$ with its order m is given by Eq. 2.54

$$r_{m,1}^{\gamma\text{-ch}} = 1 - \frac{m\xi}{(m+1)} F(m, \xi) \quad (3.4)$$

where the function $F(m, \xi)$ is given by

$$F(m, \xi) = \frac{1}{\xi + (1 - \xi) \frac{2}{\sqrt{\pi}} \left(\frac{2}{3}\right)^{m+1} \frac{\Gamma(m+5/2)}{\Gamma(m+2)}}. \quad (3.5)$$

where ξ is a parameter related to the strength of $\gamma - \text{ch}$ (anti-)correlation. Approximately, positive values of ξ would correspond to anti-correlation and negative ξ would correspond to correlation. For $m > 0$, the value $\xi = 0$ corresponds to Poisson like fluctuation. The generic production of pions under isospin symmetry would also correspond to $\xi = 0$ making ($r_{m,1}^{\text{GEN}} = 1$) [150, 166, 167]. In case all the charged and neutral particles coming from the decay of DCC domains, ξ becomes unity so that the observable $r_{m,n}^{\text{DCC}} = 1/(m + 1)$ [150, 166, 167]. It should be noted both $\nu_{\text{dyn}}^{\gamma-\text{ch}}$ and $r_{m,n}^{\gamma-\text{ch}}$ are not immune to any form of contamination effect that introduces spurious correlation between charge and photons. Using an approach based on generating function [150, 166, 167] it can be shown that $r_{m,1}$ is relatively more robust to contamination effects compared to ν_{dyn} . In this analysis to reduce contamination effects we have put strict criteria on photon-hadron discrimination and also compared our results with GEANT simulation which includes such detector effects.

In this analysis we have studied the centrality and charge dependence of the observables ν_{dyn} and $r_{m,1}$ and compared with the expectation from the ‘‘Central Limit Theorem’’. We have compared these observables with GEANT simulation, mixed events, different models like HIJING, AMPT, UrQMD and their respective Poissonian limits.

3.3 The STAR detector systems

One of the major goal of the STAR experiment at RHIC is to investigate the behaviour of strongly interacting systems and to search for the QGP in ultra-relativistic heavy ion collisions. STAR focuses on the measurement of hadron production over a large solid angle, featuring detector systems for high precision tracking, momentum analysis, and particle identification. In this section we briefly discuss about some of the major component of the STAR experiment, a

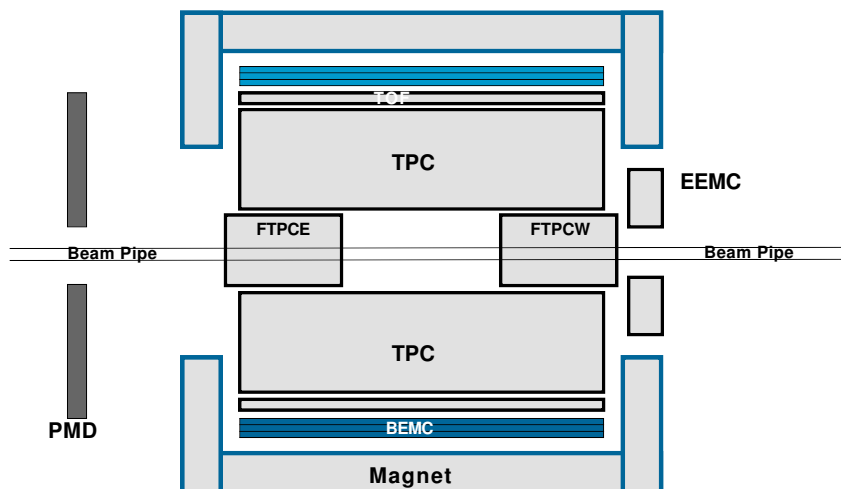


Figure 3.1: Layout of the STAR detector system.

schematic of which is shown in Fig. 3.1.

3.3.1 Time Projection Chamber

Time projection chamber (TPC) is the main tracking detector of STAR. It surrounds the beam-beam interaction region of RHIC in such a way that the collisions take place near the centre of TPC. The gas volume (10% CH₄, 90% Ar at 2 mbar [169]) of TPC is of cylindrical in shape with inner and out diameter of 1m and 4 m respectively. It has a length of 4.2 m and sits inside the large solenoidal STAR magnet which produces 0.5 T magnetic field [170]. The electric field of ≈ 135 V/cm is applied in the active medium of TPC by a high voltage vertical membrane that sits at the centre along the length of TPC. The read out pads of TPC are made of Multi-Wire Proportional Chambers (MWPC) and placed at end cap of the chamber on both sides. The primary ionizing particles passing through the gas volume of TPC are reconstructed from the secondary electrons drifting to these readouts. TPC has been used to identify charged particles by measuring the ionization energy loss dE/dx and to measure their momenta in its acceptance. It covers the pseudo-rapidity range of ± 1.8 and has full azimuthal angle coverage. TPC can measure the momentum of inclusive charged particles over a range of 100 MeV/c to 30 GeV/c, however the particle identification is done over a range of 100 MeV/c to 1 GeV/c. A

full description of TPC can be found in Ref.[168].

3.3.2 Electromagnetic Calorimeter

Barrel Electromagnetic Calorimeter

The goal of the STAR Barrel Electromagnetic Calorimeter (BEMC) is to trigger on and study rare, high transverse momentum processes like jets, direct photons and heavy quarks. It also provides a wide acceptance for the measurement of photons, electrons, neutral pions and η mesons. BEMC has an acceptance equal to that of the TPC. Details of BEMC can be found in Ref. [171].

Endcap Electromagnetic Calorimeter

The goal of STAR Endcap Electromagnetic Calorimeter (EEMC) is to trigger higher energy electromagnetic probes at forward rapidity. It has the capability to detect photons and electromagnetically decaying mesons like π^0 and η and to identify electrons and positrons in the pseudo-rapidity range of $1 < \eta < 2$. It includes a scintillator shower-max detector of 5 radiation length and has two pre-shower and post-shower layers. The details of EEMC can be found in Ref. [172].

3.3.3 Time of Flight Detector

The Time of flight (TOF) detector system at STAR is made of two subsystems, one called the pseudo-vertex position detector (pVPD) and Time of Flight Patch (TOFp). pVPD provides the start time and TOFp provides the stop time for the particle time of flight measurements. There are two pVPDs which are positioned very close to the beam pipe on both side of the collision point outside the STAR magnet. Along with the start time of TOF, the two VPDs also provide the z-component of the vertex position of a collision. The TOFp is placed inside the STAR magnet and surrounds the STAR TPC. It therefore covers approximately one unit of pseudo-rapidity ($|\eta| < 1$) and azimuthal angle of 2π . TOFp consists of 120 trays of Multigap

Resistive Plate Chamber (MRPC). The time resolution of TOF is about 87ps. The combination of STAR TPC and TOF provides an improved particle identification by allowing pion, kaon and proton discrimination up to a momentum range of 1.8GeV. A detailed description of TOF can be found in Ref. [173].

3.3.4 Forward Time Projection Chambers

The two cylindrical forward TPCs (FTPC) extend the phase space coverage of the STAR experiment for charged particle detection. They are located on both sides of the collision point in the pseudorapidity range of $2.5 < |\eta| < 4.0$ and measure charge state and momentum of tracks. Each FTPC has a diameter of 75 cm and is 120 cm in length. FTPC has 10 rows of readout pads, called pad-rows, which are further subdivided into six sectors. Each sector has 160 pads. The first pad-row is located at about 163 cm away from the collision point. Ar and CO₂ in the ratio of 50:50 by weight form the sensitive medium of the FTPC. In order to optimize the available space and to cope with high particle density the drift field in the FTPC is radial and hence perpendicular to the solenoidal magnetic field of the STAR magnet. This leads to the achievement of two track resolution up to 2 mm. It was shown in Ref. [174] using model studies that about 6-7% of the total charged particles produced fall within the acceptance of each of the FTPCs. The detailed descriptions of FTPC can be found in Ref. [175].

3.3.5 Photon Multiplicity Detector

Photon Multiplicity Detector (PMD) is a pre-shower detector designed to measure event-by-event photon multiplicity in the pseudorapidity region of $-3.7 \leq \eta \leq -2.3$. It is located 5.4 meter away from the collision point along the beam axis outside the STAR magnet. PMD consists of a highly granular (41,472 cells in each plane) pre-shower plane placed behind a lead converter of 3 radiation length thickness. A second detector plane called the charged particle veto (CPV) identical in granularity and dimension with the pre-shower is placed before the lead plate. They work on the principle of gas proportional counters with a sensitive medium of Ar and CO₂ in a

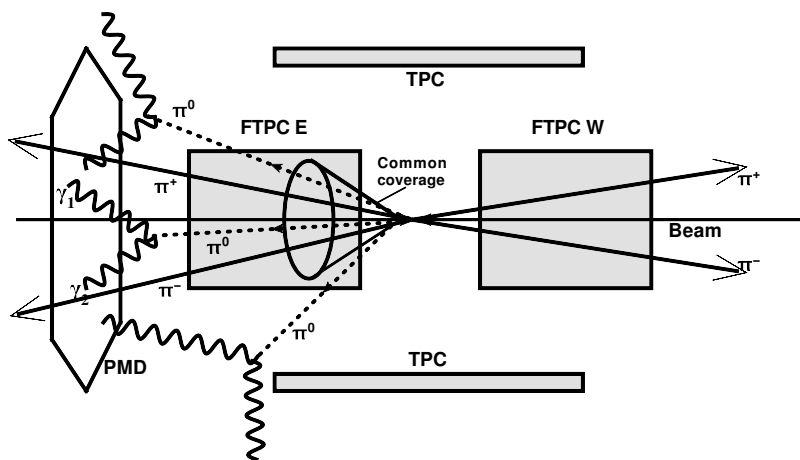


Figure 3.2: Experimental setup for this analysis

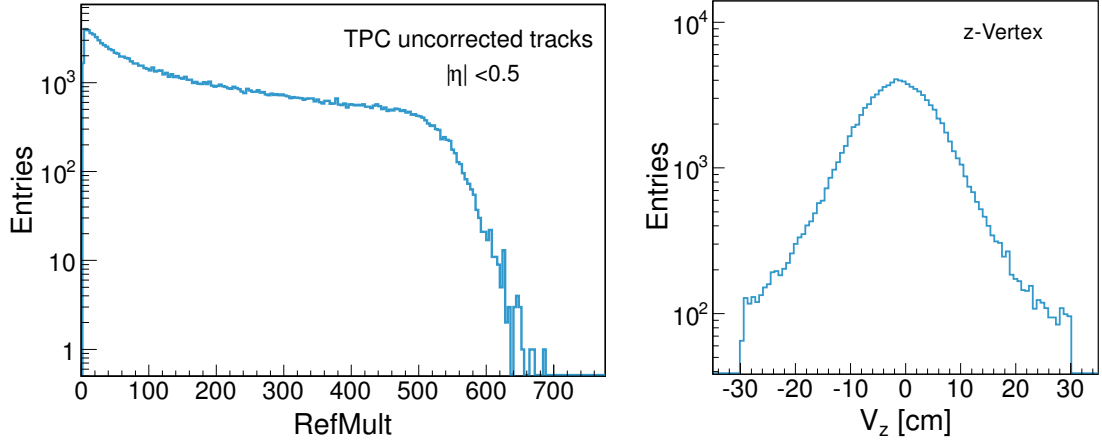
weight ratio of 70:30. The photons falling on the lead converter produce electromagnetic shower which spread over several cells on the pre-shower plane leading to a larger cluster compared to a charged particle. Both the CPV and pre-shower planes share common electronics and data acquisition system. Since photon clusters are identified from the hits in the pre-shower plane, relevant to the present analysis, only the data from the pre-shower plane has been used. The charged particle veto plane has been used for data cleanup.

Based on studies shown in Ref. [174, 176] it is known that $\sim 10\%$ of the total photons produce fall within the acceptance of PMD. Photon production in the kinematic region considered is dominantly (93-96%) from the decay of neutral pions. Detailed description of the PMD can be found in Ref. [176].

3.3.6 Detector setup for this measurement

Fig. 3.2 shows a schematic of the experimental setup used for this measurement. Two detectors PMD and FTPC covering a common acceptance in the forward rapidity region have been used for simultaneous measurement of photons and charged particles. A combination of detectors such as the Zero Degree Calorimeter (ZDC) and the Vertex Position Detector (VPD) have been used for minimum bias trigger selection. The Time Projection Chamber (TPC) [168] has been

used to determine the collision centrality.



(a) Distribution of reference multiplicity from TPC.

(b) z-vertex distribution, a cut of ± 5 cm has been used for this analysis.

Figure 3.3: Global quality assurance (QA) plots relevant to data analysis.

3.4 Data Cleanup

3.4.1 Event selection

This analysis is performed within a pseudo rapidity range of $-3.7 < \eta < -2.8$, and the centrality selection is done using the distribution of uncorrected charged multiplicity (called as Reference multiplicity in the STAR collaboration) within the pseudo-rapidity range of $-0.5 < \eta < 0.5$ (see Fig. 3.3). This method of centrality selection ensures that no biasing is introduced due to the same coverage of charged particles for centrality and correlation measurement. Table-3.1 shows different centrality cuts used in this analysis. For this analysis we have used z-vertex cut of $-5 < V_z < 5$ (cm) for final results. We have studied the effect of the variation of this cut over the range of $-15 < V_z < 15$ (cm). The distribution of V_z is shown in Fig. 3.3. In the transverse plane a vertex cut of $V_r < 1$ cm has been used. Same cut has been used also for GEANT simulation and mixed event analysis.

Table 3.1: Centrality cuts used in this analysis in terms of reference multiplicity described in the text and corresponding N_{part} obtained from Monte Carlo Glauber model.

Centrality	N_{part}	Reference Multiplicity
0-5 %	352.4 +3.4 -4.0	520
5-10 %	299.3 +6.6 -6.7	441
10-20 %	234.6 +8.3 -9.3	319
20-30 %	166.7 +9.0 -10.6	222
30-40 %	115.5 +8.7 -11.2	150
40-50 %	76.6 +8.5 -10.4	96
50-60 %	47.8 +7.6 -9.5	57
60-70 %	27.4 +5.5 -7.5	31
70-80 %	14.1 +3.6 -5.0	14

3.4.2 Data sets and particle identification

For this analysis we have used data from Au+Au collisions at $\sqrt{s} = 200$ GeV (STAR Run 7 data set with production id **P08ic**). This data set includes approximately 1M minimum bias events. After choosing the best common working zone of the two detectors (FTPC and PMD) and applying data cleanup cuts, the statistics reduces to 0.5 M. For mixed event analysis 10 times higher statistics has been used to reduce the statistical error bars. GEANT simulation using standard STAR Monte Carlo package (STAR MC production dataset **P08if**) that uses the same detector geometry as data has been performed.

Different cuts used for Charged particle and photon identification using FTPC and PMD are shown in table-3.2. The standard kinematic cuts were used for charged track selection in FTPC. For selection of photon clusters using PMD, a method in which contiguous hit cells are joined to form a cluster has been used. The photon-hadron discrimination cuts are mentioned in table-3.2. For clean-up of pile-up events a cut on cluster ADC per number of cluster of Charge-Particle-Veto (CPV) plane have been used. These steps are explained in detail in the next section.

Table 3.2: Summary of data sets and different kinematic cuts used in this analysis.

Data set used: Run 7 (Au+Au) (total 1 M events, 0.5M after correction) P08ic	
FTPC:	Primary track : number of fit points > 5 $-3.7 < \eta < -2.8$ (Common $\eta - \phi$ with PMD) $0.15 < p_T < 1.5$ GeV/c $dca < 3$ cm
PMD:	Cluster ADC cut $> n \times \text{MIP}$ (with $n = 6 - 8$) $-3.7 < \eta < -2.8$ (Common $\eta - \phi$ with FTPC) number of cells in a cluster > 1 ADC per cluster on CPV plane $\geq 1.8 \times 10^2$

3.4.3 Quality Assurance studies

Fig. 3.4 shows some of the QA plots specific to FTPC relevant to this analysis. One of the main motivation for this analysis is to search for DCC-like signal which are carried by soft pions. Therefore, only charged tracks which are below 1.5 GeV have been used for the analysis. FTPC doesn't provide particle identification, so we have included all charged tracks in this analysis, although our primary interests are pions with lower momentum.

Fig. 3.5 shows some of the QA plots for PMD relevant to this analysis. For PMD, cell wise gain normalization has been performed by the gain factors obtained by fitting the MIP (minimum ionizing particle) ADC distribution. Cell-wise MIP ADC follows a Landau distribution. Mean values of individual cells give rise to a Gaussian distribution and the overall mean of that Gaussian distribution has been used for gain normalization. The value of this mean (referred as MIP cut) in terms of cluster ADC of PMD is 100, for photon hadron discrimination the minimum value of cluster ADC used is $3 \times \text{MIP mean}$ [174].

For the measurement of inclusive multiplicity and pseudo-rapidity distribution one uses a cut of $3 \times \text{MIP}$. However, to obtain considerably higher purity of the photon data sample for fluctuation and correlation analysis, one can put stricter cuts on PMD cluster ADC. For this analysis we have used 8 times MIP cut on cluster ADC to obtain more than 70% purity. Fig. 3.5(a) shows the variation of PMD purity and efficiency with the MIP cuts. Beyond a cut of $6 \times \text{MIP}$ the purity becomes almost flat and doesn't change final results. Application of higher MIP cuts

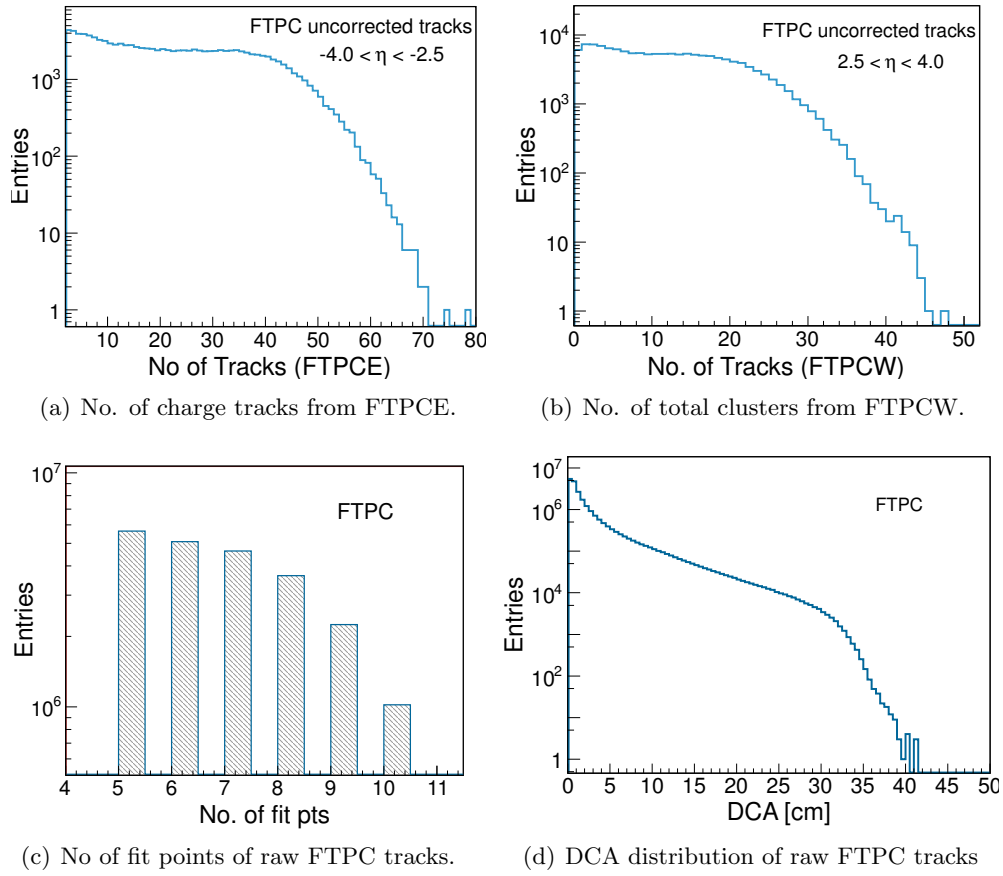
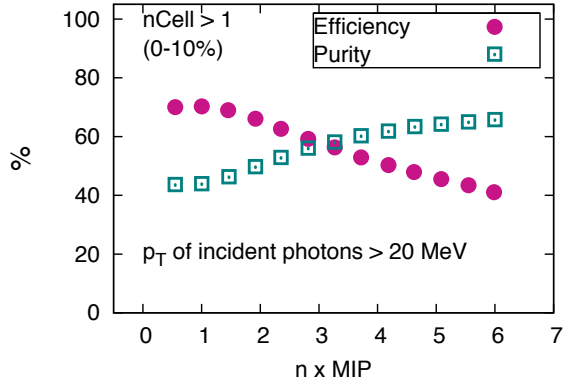


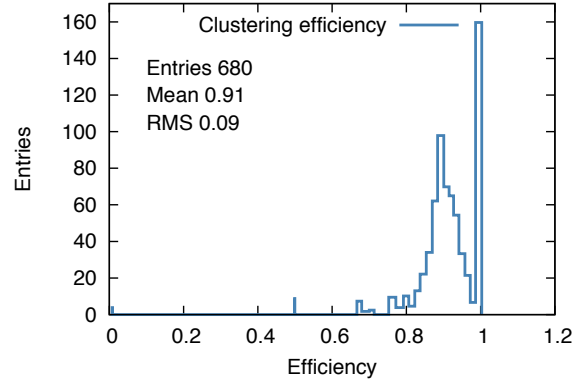
Figure 3.4: Quality assurance plot for the FTPCs relevant to this analysis.

reduces efficiency further. Photon counting efficiency may further decrease when clusters due to two incident photons merge to produce a single cluster. Figure.3.5(b) shows that the cluster merging effect has 9% effect on photon counting efficiency, which does not change with incident multiplicity or centrality.

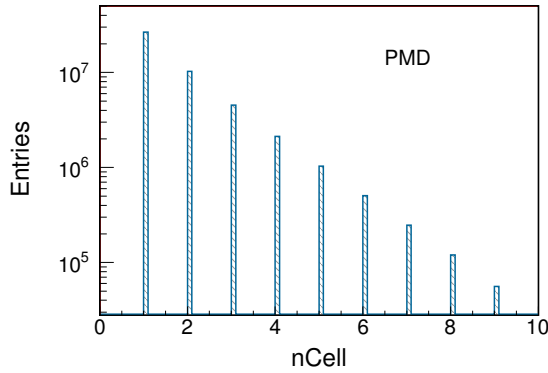
The average number of cells (n_{Cell}) in a cluster from charged hadron is ~ 1 , so we have used criterion of $n_{Cell} > 1$ for reducing the contamination(Fig. 3.5(c)). The pile-up affects both the planes of PMD (the pre-shower plane and the CPV plane) equally. We use a cut on the ratio of total ADC of the CPV cluster and total number of CPV cluster (see Fig. 3.5(e)) to clean up the pile-up events since the use of other detector plane CPV for cleanup doesn't bias the



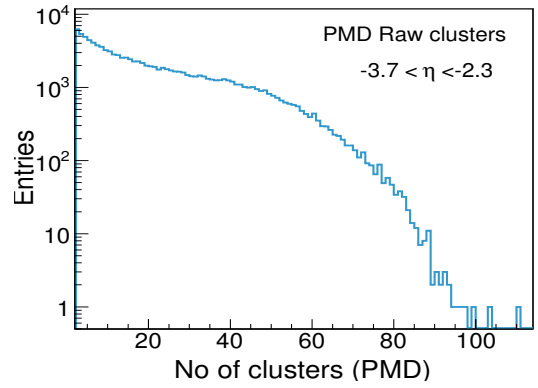
(a) Variation of efficiency and purity of PMD for different MIP cuts



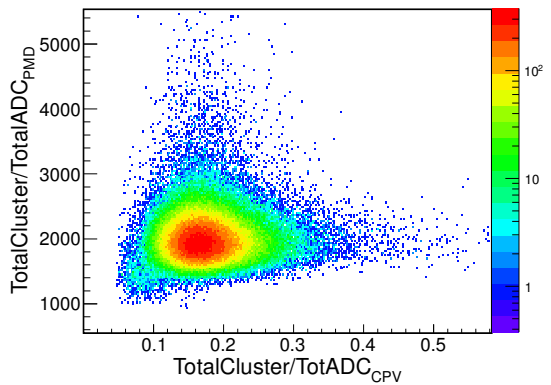
(b) Clustering efficiency of PMD.



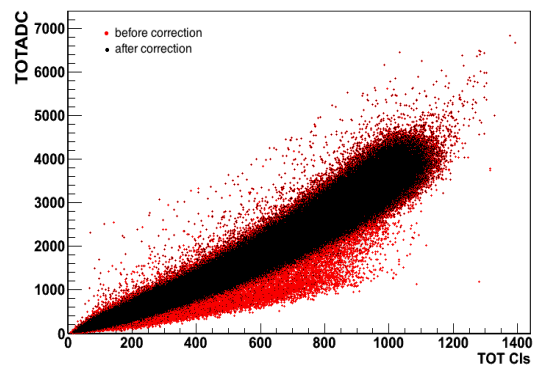
(c) Distribution of number of cells of PMD clusters.



(d) Minimum bias distribution of total PMD clusters.



(e) Correlation plot of total ADC per cluster from PMD and CPV plane, used to clear pile-up events.



(f) Correlation between total clusters and total ADC before and after pile-up correction.

Figure 3.5: Quality assurance plot related to PMD.

data sample. Fig. 3.5(f) shows the correlation of total ADC and total clusters from PMD plane, the two bands (shown in red and black) demonstrate how the clean-up cut removes the pile-up events from the data sample without biasing it.

3.4.4 Run-by-Run QA for removal of bad runs.

The run-by-run QA is carried out by studying the run-wise variation of the common $\eta - \phi$ acceptance. The run-by-run $\eta - \phi$ acceptance plot of PMD and FTTPC is shown in Fig. 3.6 by orange and green points respectively. The common coverage is shown by black points. This analysis is performed over the range of run numbers 8096500-8100500 where the common acceptance of the two detectors are stable. The second step of run-by-run QA is performed as follows. Various quantities related to photon and charge multiplicities are plotted with respect to the run numbers as shown in Fig 3.7 and a 2σ -cut is applied to extract bad runs. The variation of different quantities like $\langle n_{\gamma, \text{ch}} \rangle$, $\langle \phi_{\gamma, \text{ch}} \rangle$, $\langle p_{T, \text{ch}} \rangle$, $\langle DCA_{\text{ch}} \rangle$, $\langle nCell_{\gamma} \rangle$ are evaluated for each run number by averaging over all the events in that particular run. Bad runs are identified by their values exceeding 2σ away from the overall mean values of the range of run numbers considered. Fig. 3.7 also shows the variation of $\langle N_{\gamma} \rangle$ and $\langle N_{\text{ch}} \rangle$ but those quantities are not used for determination of bad runs to avoid biasing the data sample. Fig. 3.8 shows the effect of the application of bad run cuts on final observables. We see the difference is negligible from the reference value without any cut.

3.5 Events mixing

Mixed event analysis provides a good baseline for this correlation analysis. By mixing tracks from different events one can get rid of any form of (anti-)correlation, although many other detector effects like overall gain, efficiency, acceptance etc. will still be present in the mixed event. Since the physics signal we are looking for in this analysis are correlation(or anti-correlation), we need to make sure that by construction event mixing should get rid of any form of such correlations. We also note that any form of mis-identification (in this case the FTTPC tracks giving clusters

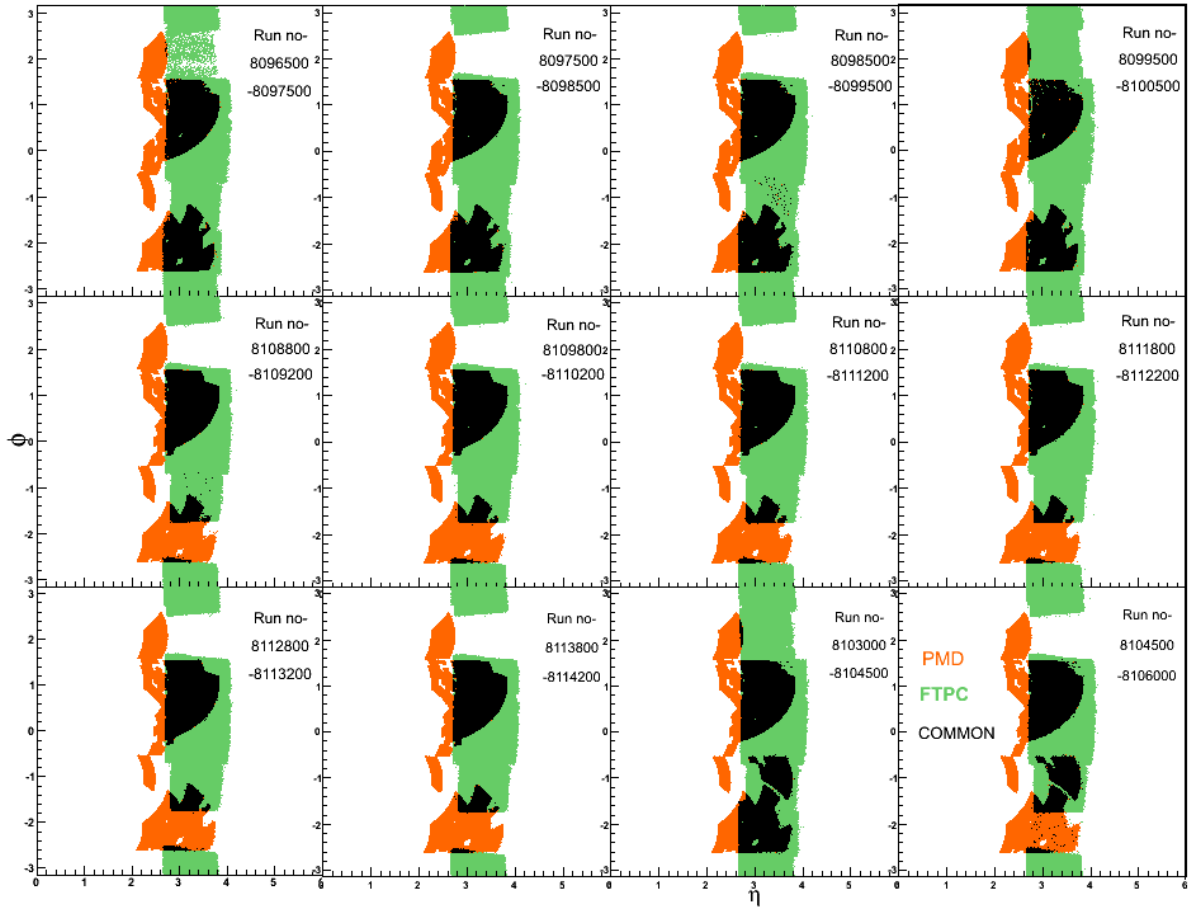


Figure 3.6: Run-by-run QA of common acceptance. The run-by-run $\eta - \phi$ acceptance plot of PMD is shown by orange and FTFC by green points respectively. The common coverage is shown by black points. The range of run numbers for which the common coverage remains unchanged has been used for analysis

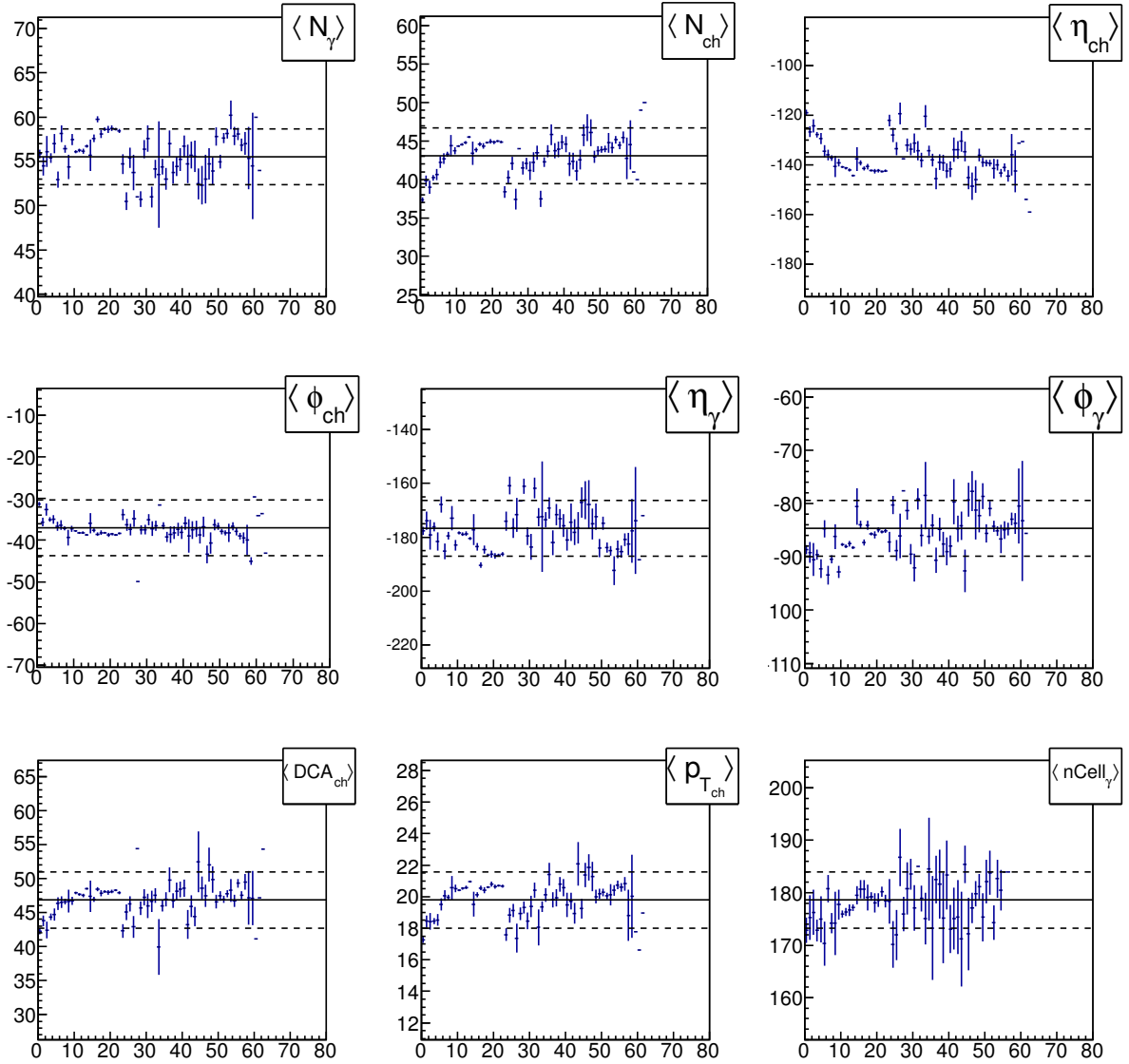


Figure 3.7: Run-by-run variation of various quantities averaged over most central (0-10%) events in a given run. For clarity of the plot, the quantity plotted on x-axis is the index of the run number. The solid line represents the mean value over all the range of runs. The dashed line shown for $\pm\sigma$ variation from the mean values to guide the eye. All the quantities except $\langle N_\gamma \rangle$ and $\langle N_{ch} \rangle$ have been used to extract bad runs.

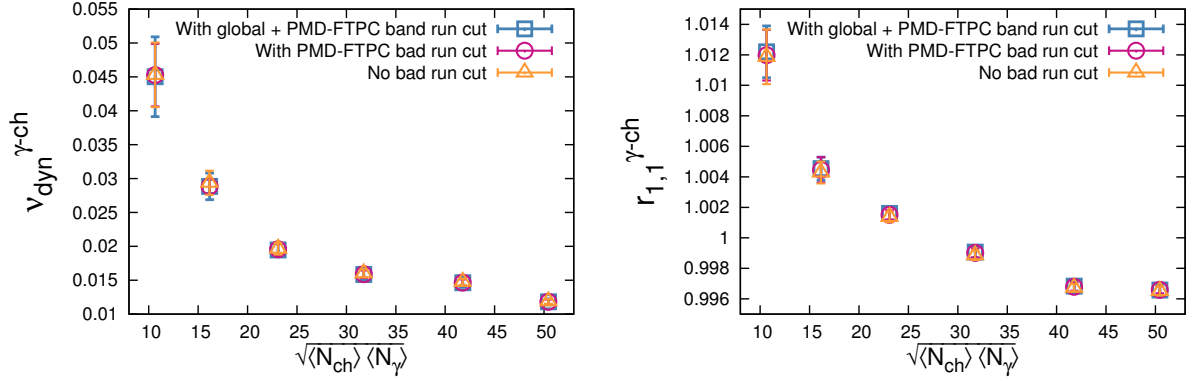


Figure 3.8: Effect of run-by-run QA on final observables. The variation is shown for two different cases of run number cuts along with the case of no cut.

in the PMD) that leads to spurious correlation will also be absent in the mixed events. By picking up random raw tracks or a clusters from random events one can get rid of any form of correlation. The main criteria for construction of a mixed event that is followed in this analysis is to construct an event which has same multiplicity of raw tracks and of clusters as the real event. The steps used for event mixing were as follows.

- Raw tracks and clusters are mixed between events of same centrality and of narrow range of z-vertex.
- Total number of raw tracks and clusters are kept same as of a particular real event.
- Finally kinematic and other cuts are applied for calculation of N_{ch} and N_{γ} .

This mixed event analysis is done with z-vertex bins of ± 5 cm. There are two ways of dealing with z-vertex. In case of asymmetric mixing the whole range of V_z is divided into bins of 5 cm and the mixed event procedure is done for every bins separately. Finally all events are merged together with equal weight for analysis.

The other way is to do mixing without making any subgroups. If a particular real event has z-vertex value of V_z , tracks and cluster are picked up from any events within the range $V_z = \pm 5$ cm. We've found that both the methods give identical results. Fig. 3.9 shows the multiplicity

distribution of γ -like clusters for different centralities for real and mixed events. These plots show that the real and mixed event multiplicity distributions on an average looks alike.

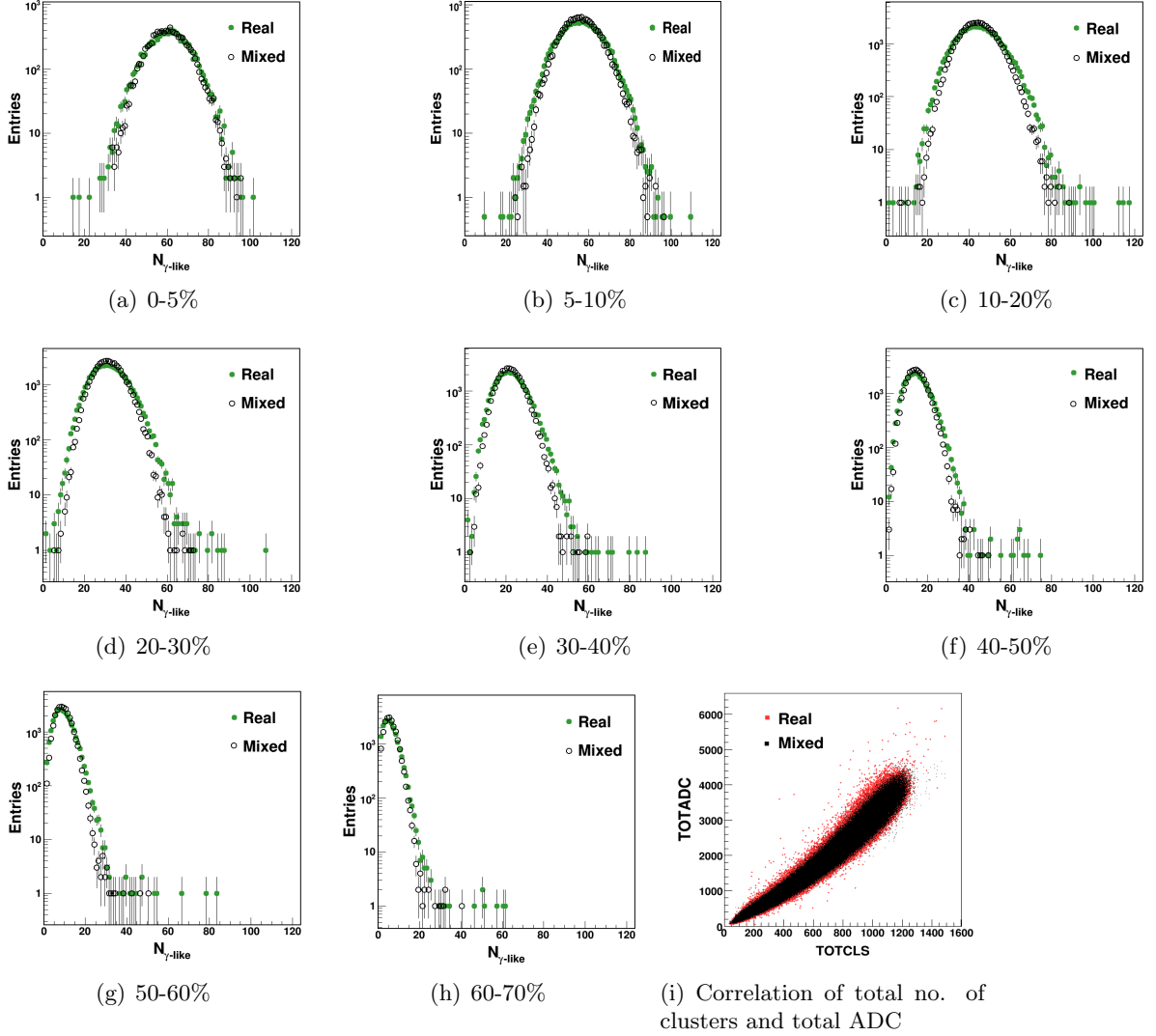


Figure 3.9: (a-h) Centrality wise N_{γ} (we also refer as N_{γ}^{like}) distributions for real and mixed events. (i) Correlation plot between photon clusters and their total ADC.

Fig. 3.9 (i) shows the correlation plot of the total number of raw clusters vs. the total ADC of all raw clusters from PMD for real and mixed events. For quality assurance of the mixed events, one needs to ensure that they overlap with each other. Individual centrality wise multiplicity distributions also look alike for data and mixed events. In every case we observe that although

the means of the multiplicity distributions(peak) are very close (agree within 2%) for real and mixed events, the widths are slightly higher for real events. This can be attributed to the presence of non-Poissonian signals present in actual data compared to the Poisson(statistical) expectations from mixed events.

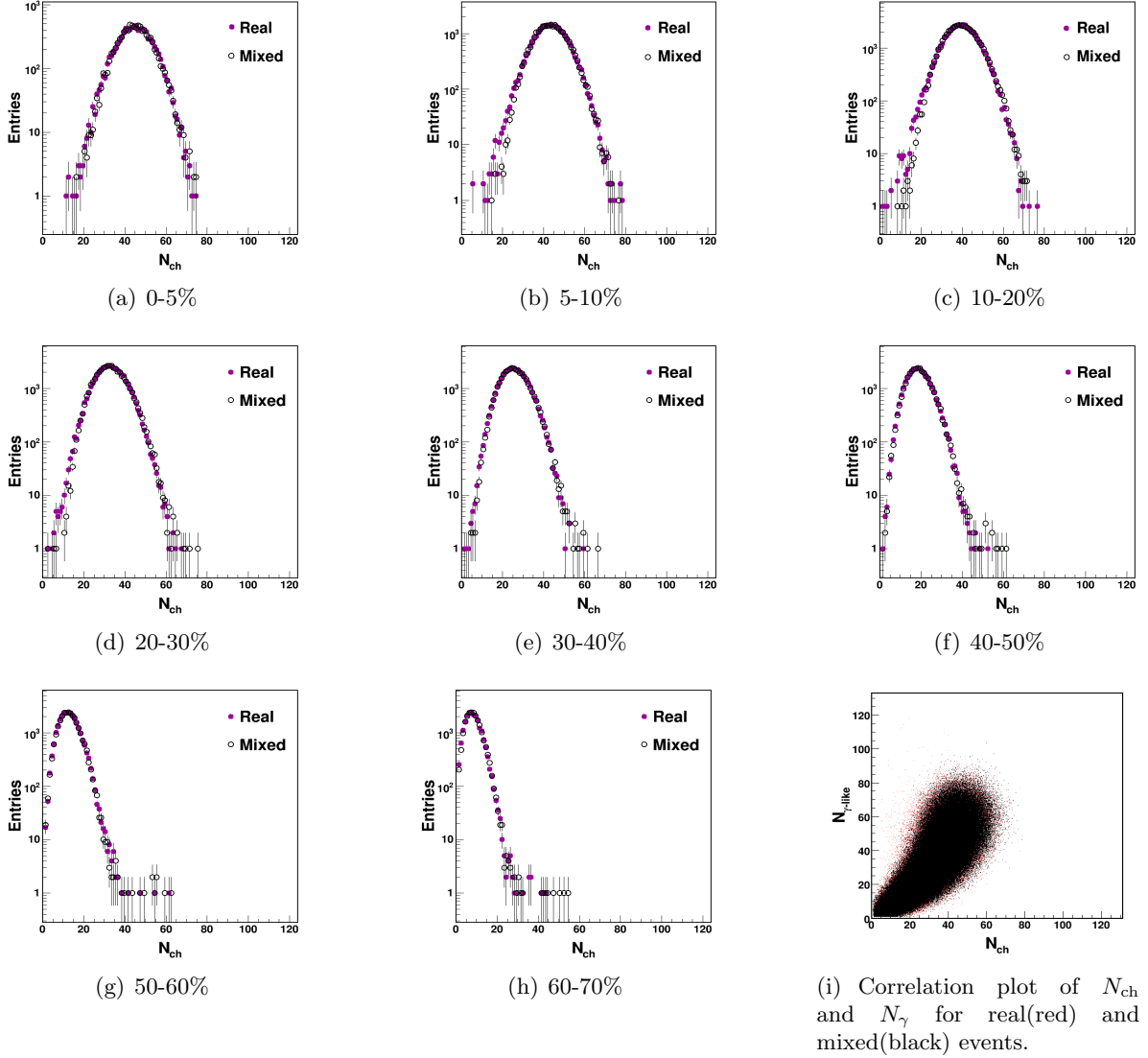


Figure 3.10: (a-h) Centrality wise N_{ch} distributions for real and mixed events. (i) Correlation between event-by-event charged particle and photon multiplicity.

Fig. 3.10 shows the multiplicity distributions of charged tracks for different centralities. The real and mixed event distributions overlap reasonably well with each other. The last plot, Fig. 3.10(i) shows the correlation plot of photon and charged multiplicity for real and mixed events. We see they almost fall on each other. Once the multiplicity distributions are reproduced we can proceed with calculation of different moments for mixed events and compare with data.

3.6 Bin-width effect

Bin-width effect is one of the most important corrections that needs to be considered for any centrality-dependent event-by-event multiplicity fluctuation analysis [177–179]. This effect is a consequence of the fact that the centrality selection uses a distribution which is not flat.

So while doing event-by-event average of any quantity such as photon or charge multiplicity one should take a weighted average with the reference multiplicity distribution. Let us consider that $P(N^{ref})$ is the reference multiplicity distribution from which we are doing the centrality selection. Let $P(N_i^{ref}) = \omega_i$ corresponds to the weight for the i 'th bin of the distribution. A given centrality bin is generally defined by the cut of reference multiplicity between N_{min}^{ref} and N_{max}^{ref} . For this centrality bin we calculate any observables X_i for each bin separately. The bin width corrected observable is then given by

$$X = \frac{\sum_{i=min}^{i=max} \omega_i X_i}{\sum_{i=min}^{i=max} \omega_i} \quad (3.6)$$

If the reference multiplicity distribution is not normalized the weight factors would simply be the number of events in each bin. Here note that if the reference multiplicity distribution was flat then all the weight factors would be same and there would be no need of bin width correction. Due to rapid falling shape of any min-bias multiplicity distribution the central events would require larger bin-width correction compared to the mid-central events. The correction factor would be larger for a wider centrality bin that includes a wide variation of the shape of the reference multiplicity distribution. This correction is however independent of the nature of the distribution for which the observable under consideration (in this analysis for example the photon or the charge particle multiplicity distribution) and solely depends on the nature of the distribution from which the centrality selection is being done.

This effect was demonstrated using URQMD model calculation in Ref.[177]. The Fig. 3.11 shows the centrality dependence of the observable ν_{dyn} and $r_{1,1}$ for different bin size of centrality

classes before bin-width correction. The centrality classes are divided in 5%, 10% and 20% bins. For a given value of multiplicity (on the x-axis), calculated observables for different centrality bins vary significantly. The plots in Fig. 3.12 show that with the application of binwidth correction, observables are independent of the chosen centrality bin width and lie on top of each other. This correction has been included throughout our analysis and all the discussion made in the previously can be demonstrated for the observables used in this analysis.

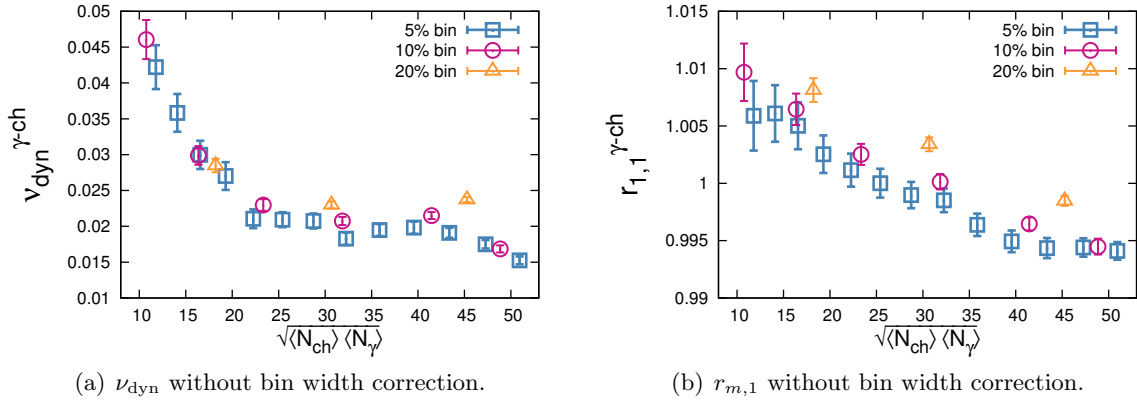


Figure 3.11: Bin width effect for observables ν_{dyn} and $r_{m,1}$.

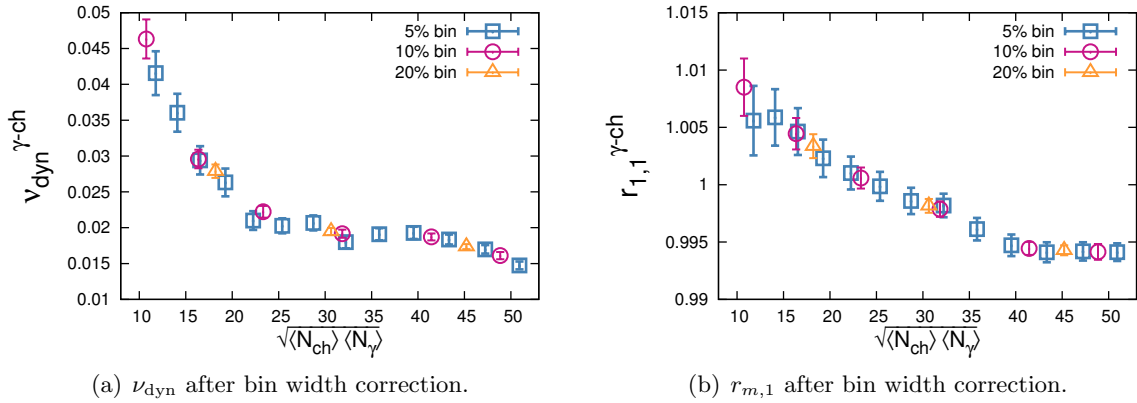


Figure 3.12: Bin width correction for observables ν_{dyn} and $r_{m,1}$.

3.7 Error analysis

3.7.1 Statistical uncertainty

Calculations of statistical uncertainty have been done using both the analytical and the bootstrap method. The bootstrap method is a Monte Carlo method which can be summarized as follows.

- Identical n samples of minimum bias dataset are created by shuffling the event number.
- Bin width corrected observables ν_{dyn} and $r_{m,1}$ have been calculated for each centrality separately for every sample.
- Estimated observables for these n different samples would give an approximate Gaussian distribution. The variance of this distribution is the statistical uncertainty from bootstrap method.

We note here that these identical samples are not independent, n is varied till the estimated uncertainty converges. For this analysis we found that 100 samples provide good convergence.

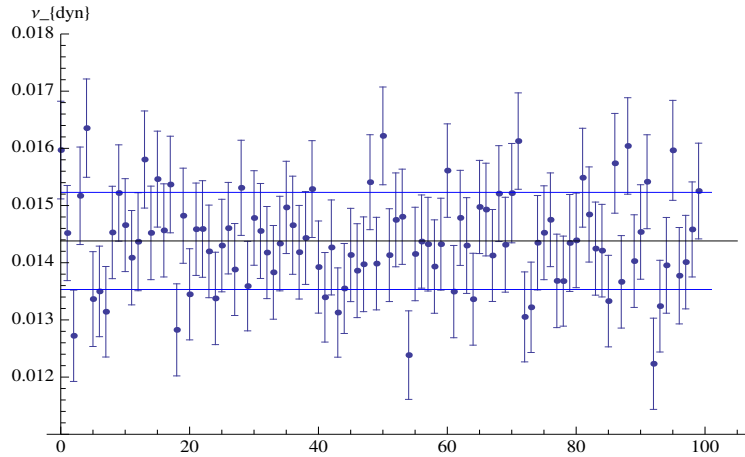


Figure 3.13: Statistical uncertainty of ν_{dyn} . The mean and variance of the 100 samples are shown by 3 solid lines (Black line is the mean and blue lines are $\pm\sigma$) which gives the statistical uncertainty from the bootstrap method. Error for individual points are obtained by using the published analytical formula of Ref. [165].

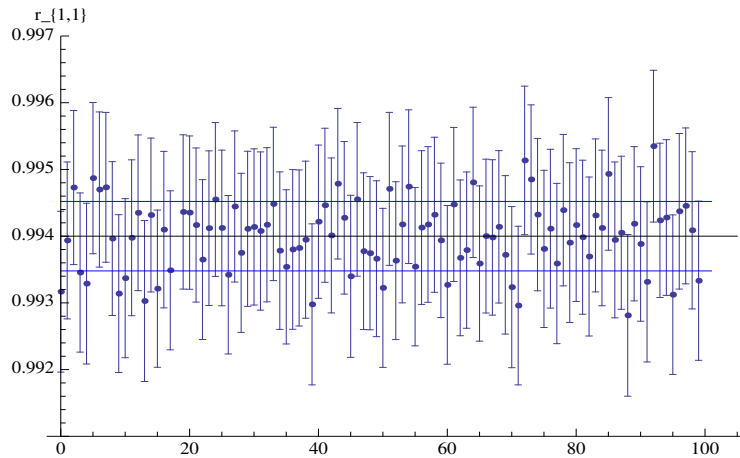


Figure 3.14: Statistical uncertainty of $r_{1,1}$. The mean and variance of the 100 samples are shown by 3 solid lines (Black line is the mean and blue lines are $\pm\sigma$) which gives the statistical uncertainty from the bootstrap method.

Application of delta-theorem is probably the most efficient method to incorporate all covariance terms that appear in the analytical error formula. It is a straightforward method when the quantity of interest includes only one variable. For observable involving multiple variables, for e.g. this analysis, which involves two variables N_{ch} and N_{γ} , one needs to work out the bi-variate expression of the delta-theorem. An analytical expression for the statistical uncertainty of the observable ν_{dyn} can be found in Ref. [165]. We have used this published expression for statistical uncertainty estimation of the variable ν_{dyn} . We have found that the estimated uncertainties from bootstrap method is consistent with that from the published expression of Ref.[165]. For the other observable $r_{m,1}$, we have used the bootstrap method for uncertainty estimation as no analytic expression exists for statistical uncertainty estimation, in the literature and it requires bi-variate form of delta-theorem. Possible reason could be the analytical complexity of the bi-variate delta-theorem approach. We therefore have not used any analytical approach for the estimation of statistical uncertainty of $r_{m,1}$. We argue that since the observables involved in this analysis do not include higher order moments of multiplicity the uncertainty estimated in bootstrap method is expected to be consistent with the delta-theorem method. Fig. 3.13 and Fig. 3.14 shows that the individual samples (points) are having uncertainties which are

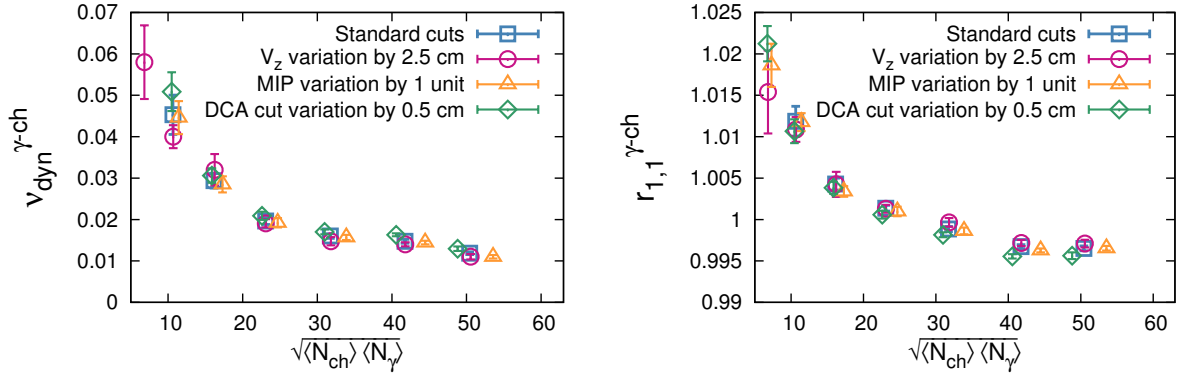


Figure 3.15: Sources of the systematic uncertainties of ν_{dyn} and $r_{1,1}$. The effect on the observables are shown for variation of different cuts applied.

estimated from published error formula are very close to the uncertainty estimated from the bootstrap method shown by two parallel blue lines ($\pm\sigma$) on both side of the black line (mean). Also the blue lines contain more than 68% of all the points.

3.7.2 Systematic uncertainty

Systematic uncertainties are obtained by varying different quality cuts on charged tracks and photon clusters.

About $\sim 8\%$ variation in the value of the observables have been found when the maximal distance of closest approach of a track to the primary vertex is varied by 0.5 cm. The effect of possible charge contamination effect present in the photon sample has been included in the systematic uncertainties. The systematic uncertainty from contamination is obtained by varying the cut for photon-hadron discrimination. Variation of this cut by one unit of the average response of all isolated cells (also called MIP cut, standard cut is 8 MIP) causes $\sim 6\%$ variation of the value of ν_{dyn} . A significant fraction of systematic the systematic uncertainty can arise due to the variation of the position of primary vertex in the z -direction (V_z). For example, 5 cm variation of V_z introduces approximately 8% variation of the observable ν_{dyn} . The overall systematic uncertainty is estimated to be $\sim 15\%$ within the centrality range of 0 – 60%. Similar cuts applied to evaluate the systematic uncertainties of the quantity $\sqrt{\langle N_{\text{ch}} \rangle} \langle N_{\gamma} \rangle$ is estimated to be

$\sim 7\%$. The total systematic uncertainty is obtained by adding different sources of uncertainties in quadrature. If $\nu_{\text{dyn}}^{\text{STD}}$ denotes the value of ν_{dyn} with standard cuts the systematic uncertainty is evaluated as

$$\text{sysErr}(\nu_{\text{dyn}})^{\text{total}} = \sqrt{\left(\nu_{\text{dyn}}^{\text{STD}} - (\nu_{\text{dyn}})\Delta V_z\right)^2 + \left(\nu_{\text{dyn}}^{\text{STD}} - (\nu_{\text{dyn}})\Delta_{\text{MIP}}\right)^2 + \left(\nu_{\text{dyn}}^{\text{STD}} - (\nu_{\text{dyn}})\Delta_{\text{DCA}}\right)^2} \quad (3.7)$$

and similarly for $r_{m,1}$

$$\text{sysErr}(r_{m,1})^{\text{total}} = \sqrt{\left(r_{m,1}^{\text{STD}} - (r_{m,1})\Delta V_z\right)^2 + \left(r_{m,1}^{\text{STD}} - (r_{m,1})\Delta_{\text{MIP}}\right)^2 + \left(r_{m,1}^{\text{STD}} - (r_{m,1})\Delta_{\text{DCA}}\right)^2} \quad (3.8)$$

Variation of cuts changes the total multiplicity of charged tracks and photons. The variation of quality cuts are chosen in a way that multiplicity variation in a given centrality ($\sqrt{\langle N_{\text{ch}} \rangle \times \langle N_{\gamma} \rangle}$) does not exceed $> 10\%$ of actual value. Lists of systematic uncertainties for different quantities are listed in Table. 3.3. The variation of quality cuts on the observable ν_{dyn} and $r_{1,1}$ is shown in Fig. 3.15.

3.8 GEANT simulation for detector response

Events from HIJING monte-carlo event generator is passed through GEANT to simulate the detector response. GEANT events are simulated with exactly similar detector geometry of data taking (which is set by the software libraries under STAR production run **P08if**). During analysis for both Raw and GEANT implemented HIJING, similar common acceptance as shown in Fig. 3.6 has been used. For GEANT simulation, detector cuts equivalent to that of data analysis has been used and the centrality selection is done using the uncorrected number of tracks in a way similar to that of data analysis. GEANT simulation shows effective decrease of multiplicity for both charged particles and photons due to detector efficiencies as shown by the multiplicity distributions in different centralities in Fig. 3.8 and Fig. 3.17. These results would serve important baseline for studying the observables as discussed in the next section.

Table 3.3: List of total systematic uncertainties due to different cuts are listed below.

$\sqrt{\langle N_{\text{ch}} \rangle \langle N_{\gamma} \rangle}$	$\text{Err}(\sqrt{\langle N_{\text{ch}} \rangle \langle N_{\gamma} \rangle})$	$\nu_{\text{dyn}}^{\text{real}}$	$\text{Err}(\nu_{\text{dyn}}^{\text{real}})$
50.43	3.52	0.0119	0.0016
41.76	2.95	0.0148	0.0017
31.75	2.27	0.0160	0.0016
23.08	1.68	0.0196	0.0014
16.15	1.18	0.0294	0.0030
10.65	0.79	0.0453	0.0077
$\sqrt{\langle N_{\text{ch}} \rangle \langle N_{\gamma} \rangle}$	$\text{Err}(\sqrt{\langle N_{\text{ch}} \rangle \langle N_{\gamma} \rangle})$	$\nu_{\text{dyn}}^{\text{mixed}}$	$\text{Err}(\nu_{\text{dyn}}^{\text{mixed}})$
49.73	3.49	0.00028	0.00018
41.23	2.92	0.00038	0.00026
31.29	2.24	0.00043	0.00028
22.7	1.65	0.00058	0.00028
15.85	1.17	-8.4e-05	0.00062
10.45	0.783	-0.00094	0.00120
$\sqrt{\langle N_{\text{ch}} \rangle \langle N_{\gamma} \rangle}$	$\text{Err}(\sqrt{\langle N_{\text{ch}} \rangle \langle N_{\gamma} \rangle})$	$r_{1,1}^{\text{real}}$	$\text{Err}(r_{1,1}^{\text{real}})$
50.43	3.52	0.9965	0.001053
41.76	2.95	0.9967	0.001342
31.75	2.27	0.9989	0.001084
23.08	1.68	1.001	0.0008891
16.15	1.18	1.004	0.0009978
10.65	0.789	1.012	0.001574
$\sqrt{\langle N_{\text{ch}} \rangle \langle N_{\gamma} \rangle}$	$\text{Err}(\sqrt{\langle N_{\text{ch}} \rangle \langle N_{\gamma} \rangle})$	$r_{1,1}^{\text{mixed}}$	$\text{Err}(r_{1,1}^{\text{mixed}})$
49.73	3.49	0.999968	0.00011
41.23	2.92	0.999906	0.00021
31.29	2.24	0.999889	0.0003
22.7	1.65	0.999673	0.00037
15.85	1.17	1.00005	0.00029
10.45	0.783	1.00253	0.00046

$\sqrt{\langle N_{\text{ch}} \rangle \langle N_{\gamma} \rangle}$	$\text{Err}(\sqrt{\langle N_{\text{ch}} \rangle \langle N_{\gamma} \rangle})$	$\nu_{\text{dyn}}^{\text{ch}\pm}$	$\text{Err}(\nu_{\text{dyn}}^{\text{ch}\pm})$	m	$\text{Err}(m)$	$r_{m,1}^{\text{real}}$	$\text{Err}(r_{m,1}^{\text{real}})$
50.43	3.52	-0.003667	0.0005637	1	0	0.9965	0.001053
41.76	2.95	-0.00483	0.001404	2	0	0.9942	0.001958
31.75	2.27	-0.005901	0.002031	3	0	0.9927	0.002825
23.08	1.68	-0.008079	0.0009888				
16.15	1.18	-0.009648	0.0008874				
10.65	0.789	-0.02846	0.002168				

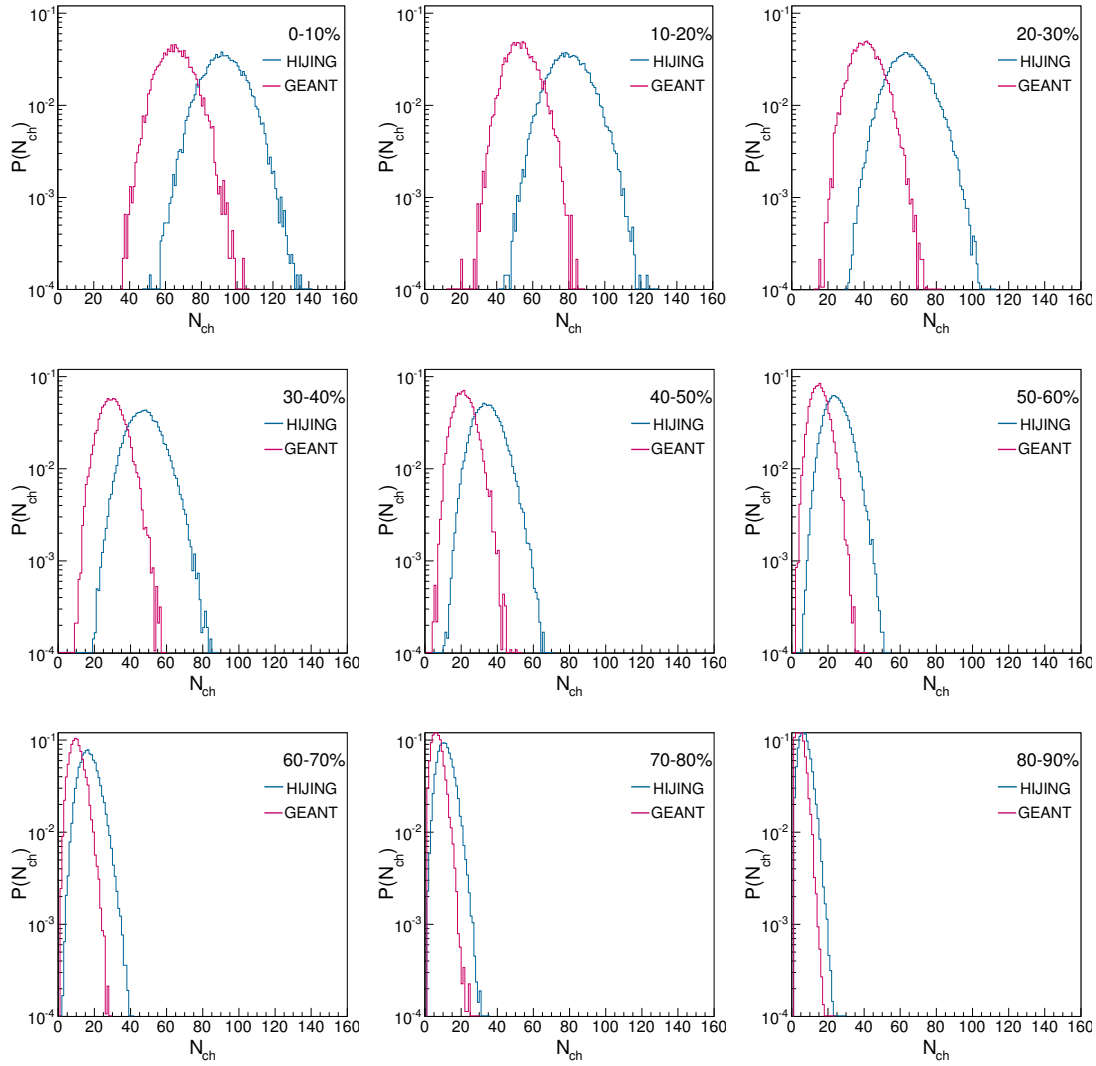


Figure 3.16: Centrality wise multiplicity distributions for charged tracks using HIJING and GEANT+HIJING simulations in the FTPCE coverage.

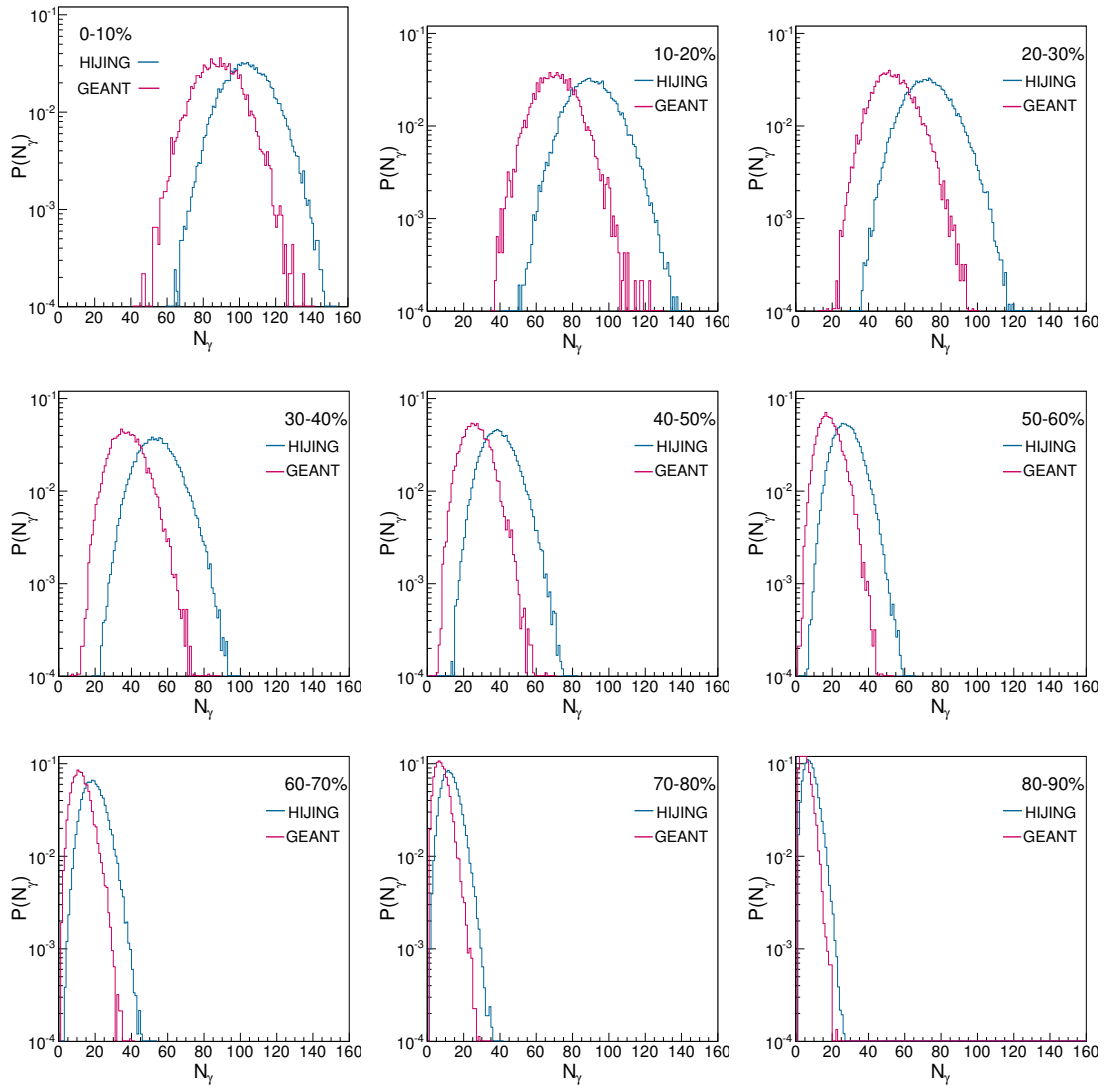


Figure 3.17: Centrality wise multiplicity distributions for photons for HIJING and GEANT+HIJING simulation in the PMD coverage.

3.9 Results for charge-neutral correlations

In this section we discuss the results of the measurement of charge-neutral correlations using the observables and method described in previous sections. The measured values of the observables are compared with various models, mixed events and respective Poissonian limits. ν_{dyn} results indicate the presence of non-zero dynamical signal when compared to mixed events, raw and GEANT implemented HIJING. ν_{dyn} also shows approximate multiplicity scaling as predicted from the ‘‘Central Limit Theorem’’. Variation of $r_{m,1}$ with its order ‘‘m’’ shows a trend opposite when compared to that from different models and HIJING simulated through GEANT.

3.10 Individual charge and neutral fluctuations

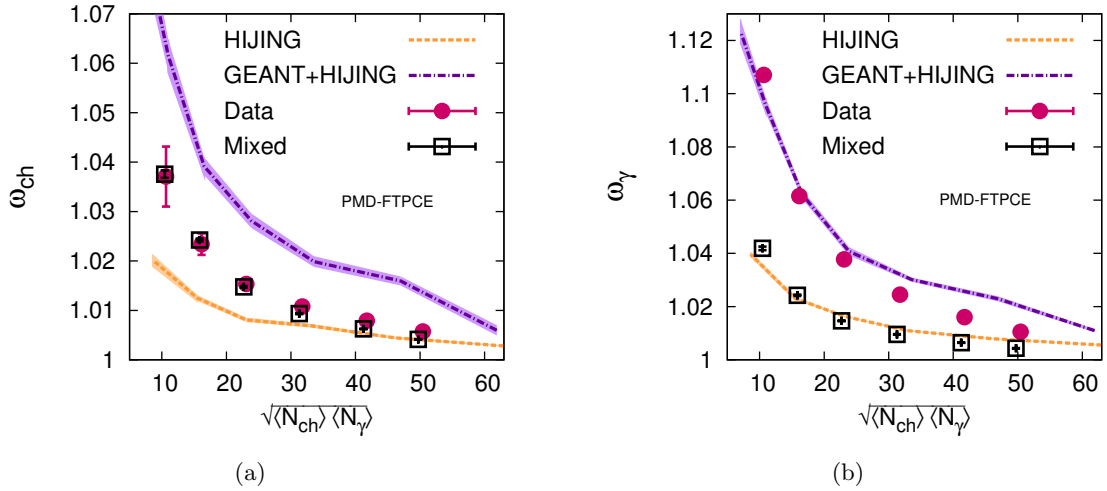


Figure 3.18: Individual fluctuation of charge and photon multiplicities.

Figure 3.18 and Fig. 3.19 show multiplicity (centrality) dependence of different terms of the variable ν_{dyn} for real and mixed events. We see that all three terms approach their respective Poisson limits ($=1$) for higher values of multiplicity. The individual scaled fluctuation terms ω_{ch} and ω_{γ} shown in Fig. 3.18 are higher for real events compared to mixed events showing presence of additional non-statistical fluctuation in the data. This is also visible from Fig. 3.9

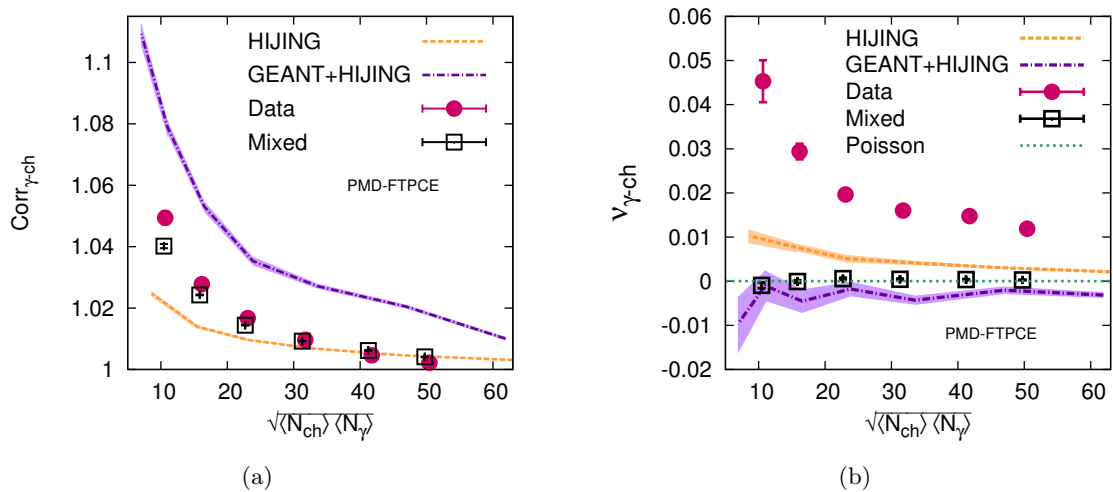


Figure 3.19: Scaled correlation and ν_{dyn} for charge and photons.

and Fig. 3.10. The fluctuation term for photon is higher compared to the charge fluctuation term when compared to the mixed event. This can be attributed to the fact that the dominant contribution to charged fluctuation comes only from the charged pion fluctuation whereas the photon fluctuation is dominantly from neutral pions combined with the decay effects which is responsible for broadening the width of photon multiplicity distribution.

3.11 charge-neutral correlation and ν_{dyn}

The scaled correlation term is shown in Fig. 3.19(a), the term $\text{corr}_{\gamma\text{-ch}}$ for real events is higher compared to mixed events at peripheral bins, becomes comparable for the mid-central events and finally becomes lower compared to that of the mixed event, this might indicate the presence of anti-correlation in the data towards higher centralities. We see similar trends with multiplicity ($\sqrt{\langle N_{\text{ch}} \rangle \langle N_{\gamma} \rangle}$) for all the three terms. Fig. 3.19(b) shows the variation of $\nu_{\text{dyn}}^{\gamma\text{-ch}}$ with $\sqrt{\langle N_{\text{ch}} \rangle \langle N_{\gamma} \rangle}$ for real and mixed events. It can be seen that the mixed event result is consistent with the Poissonian expectation at all centralities. We have fitted the data points for real events with a function of the form $A + B/\sqrt{\langle N_{\text{ch}} \rangle \langle N_{\gamma} \rangle}$ as predicted from CLT, the fit yields $\chi^2/\text{dof} \sim 2$. In the same plot we show the raw HIJING and HIJING + GEANT results for compar-

ison. The value of ν_{dyn} is very close to the Poisson limit for HIJING in more central events, with a positive value that shows a similar trend as the data. Results from HIJING events simulated through GEANT are also close to the Poisson expectation within statistical uncertainties. We argue that this small difference between the HIJING and the HIJING+GEANT curves is due to the spurious correlation coming from mis-identification of photons that can not be eliminated even by the construction of the observable ν_{dyn} . The difference between the HIJING curve and the HIJING+GEANT curve serves as a reference to how much this detector effect is still present in the data sample that can not be excluded from the presented analysis. It must be noted that this detector effect does not change the conclusion that the observed value of $\nu_{\text{dyn}}^{\gamma-\text{ch}}$ is positive, since the contamination has the opposite effect to the deviation seen in data. For the present measurement it is evident that the model curve shows very small deviations from the Poisson curve compared to data. Data show non-zero positive values for all centrality bins, indicating the presence of dynamical fluctuation for all centralities.

3.12 Robust observables

The nature and strength of the $\gamma - \text{ch}$ correlation are further explored using the observable $r_{m,1}$. This observable was designed to study its deviation from generic pion production scenario which would correspond to a value of unity. Fig. 3.20(a) shows the variation of the variable $r_{1,1}$ with $\langle N_{\text{ch}}N_{\gamma} \rangle$ for real and mixed events. The Raw and GEANT implemented HIJING curves are also shown in the same plot. $r_{1,1}$ is nearly constant with $\langle N_{\text{ch}}N_{\gamma} \rangle$ for both HIJING and mixed-event. Multiplicity dependence (with $\langle N_{\text{ch}}N_{\gamma} \rangle$) of $r_{1,1}$ shows that data points are lower than mixed-event, Raw HIJING and GEANT+HIJING towards higher centrality. We see that the mixed event results are consistent with the generic limit of the observable. The Raw HIJING values are also very close to the generic limit. This could indicate that the correlated production of pions in HIJING is very similar to that of generic production phenomenon, which is also consistent for the observable ν_{dyn} . However for data we see a deviation from such a trend. A similar trend is also observed in GEANT implemented HIJING but the values of $r_{1,1}$ is always above unity.

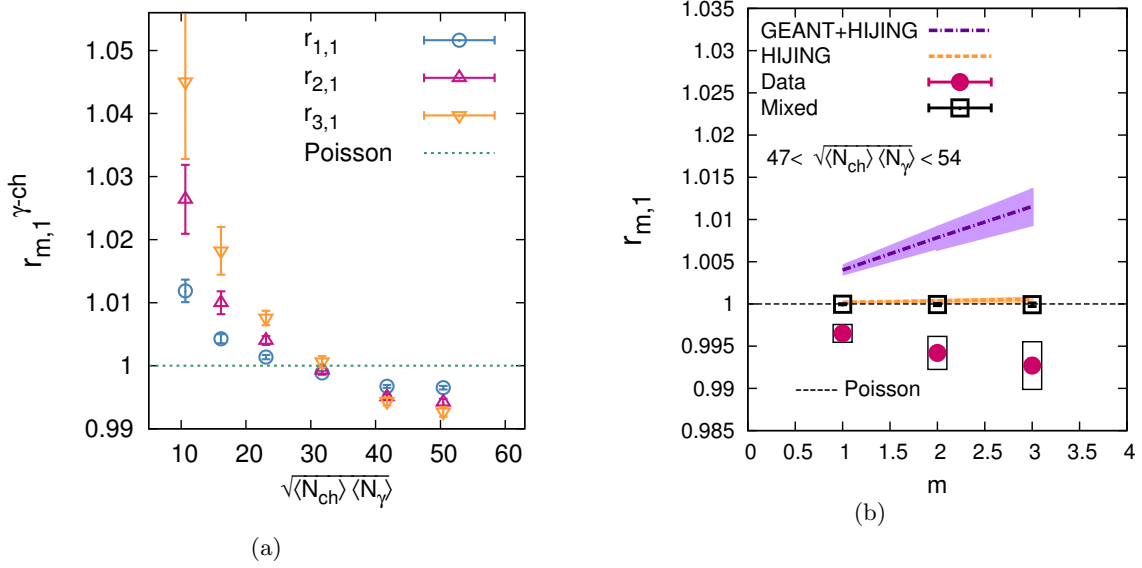


Figure 3.20: (a) $r_{m,1}$ vs multiplicity for STAR data (Au+Au 200 GeV real events). (b) Robust observable $r_{m,1}$ and its higher moments for Real & Mixed events. Model calculations are shown by bands. Statistical error bars are shown by vertical lines and the systematic error bars are shown by boxes (real events), bars (mixed events) and bands (models).

Inclusion of GEANT with HIJING changes $r_{1,1}$ in a direction opposite to that seen in the data. For data $r_{1,1}$ goes slightly below unity for higher multiplicities showing small deviation from generic case. This would correspond to $\xi \leq 0.01$ in Eq. 3.4 above a value of $\langle N_{\text{ch}} N_{\gamma} \rangle \sim 40$. Since we expect higher orders of $r_{m,1}$ to be more sensitive to any form of deviation from generic limit, we plot in Fig. 3.20(b), the variation of $r_{m,1}$ with its higher order moments for 0–10% centrality. Higher moments of $r_{m,1}$ with m show opposite trend (slope) compared to different models, GEANT simulation and mixed event. However for each order the deviation from generic case is very small and lie within a range of $0.99 - 1$.

3.13 Comparison to net charge correlation

Fig. 3.21 shows the charge dependence of ν_{dyn} . Results for combinations of photon with individual positive and negative charges are very close to that of photon and total charge. The positive-

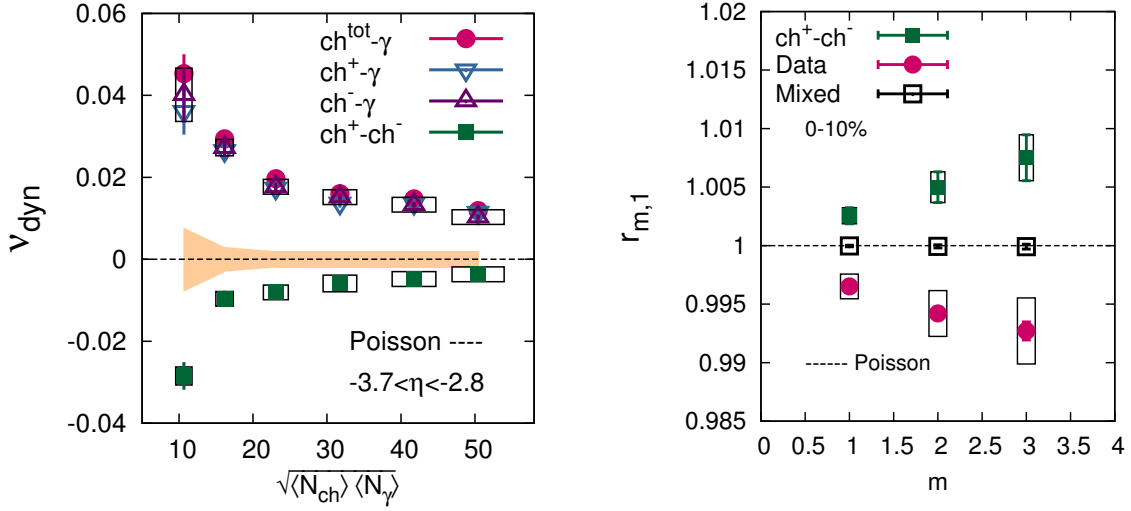


Figure 3.21: (left) Charge dependence of the observable ν_{dyn} showing different behaviour for different combinations of $\gamma - \text{ch}$ compared to that of opposite charge combination. Data points plotted are for real events. The statistical error bars are shown by lines. For positive-negative charge correlation the systematic uncertainties are shown by caps. For different combinations of $\gamma - \text{ch}$ correlation, the systematic uncertainties in $\langle N_{\text{ch}} \rangle \langle N_{\gamma} \rangle$ are shown by caps whereas the systematic uncertainties in ν_{dyn} are shown by the yellow band. (right) Variation of $r_{m,1}$ with m for $\gamma - \text{ch}$ (real and mixed events) and for opposite charge combination. The results are shown for 0 – 10% centrality only.

negative charge correlation is very different from the $\gamma - \text{ch}$ correlation. ν_{dyn} for positive-negative charge which is negative is dominated by the large correlation term since the charged particles are produced in pairs. This result is consistent with the previous measurement by STAR at mid-rapidity [180] in Au+Au collision at $\sqrt{s_{NN}} = 200$ GeV. However, data indicated a completely different behaviour of $\gamma - \text{ch}$ correlation from the correlation of oppositely charged particles. This indicates that a different mechanism of particle production is responsible for correlated production of neutral and charged particles.

3.14 Effect of rapidity gap on $\gamma - \text{ch}$ correlation

The observables estimated using charge tracks from east (same side) and west (away side) FTPC with photons from PMD (located in the east side) is shown in Fig. 3.22 and Fig. 3.23. Because

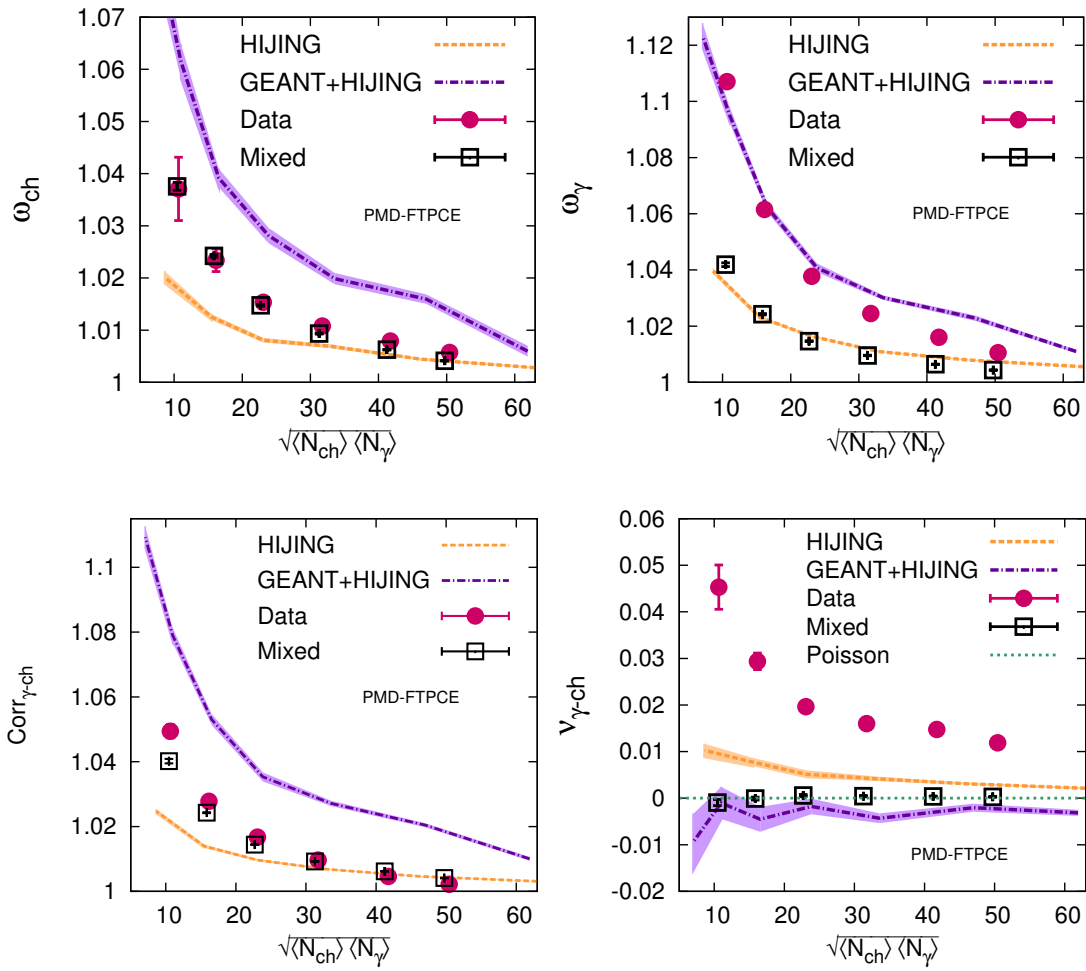


Figure 3.22: Correlation of PMD with east FTPC.

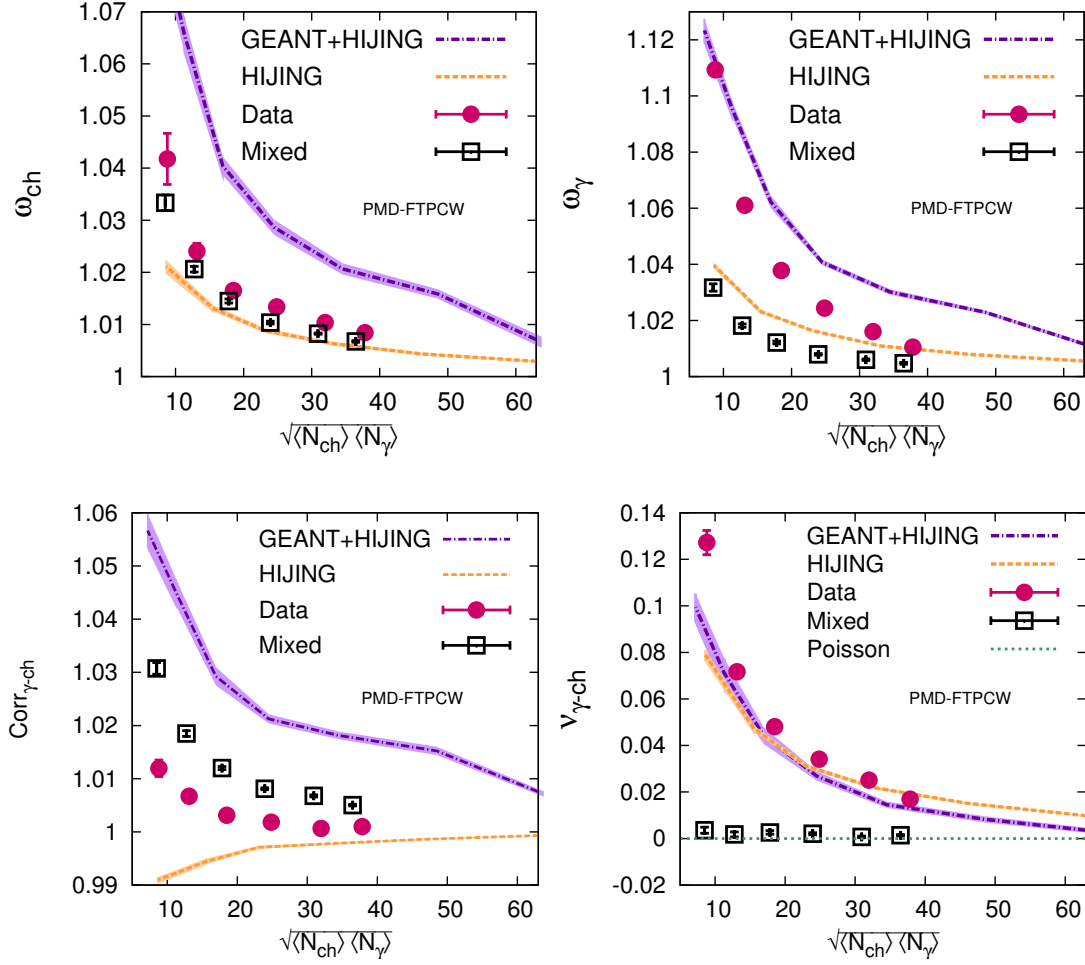


Figure 3.23: Correlation of PMD with west FTFC.

of gain difference between east and west FTFC, the average multiplicity $\sqrt{\langle N_{\gamma} \rangle \langle N_{ch} \rangle}$ is smaller for PMD-west FTFC combination. The same $\eta - \phi$ acceptance as shown in Fig. 3.6 (coverage contour) has been used for all the three detectors and the models. The Raw HIJING and GEANT implemented HIJING are shown by bands.

HIJING does not include any physics of dynamical $\gamma - ch$ correlation. We see that for same side (PMD-FTPCE) correlation, data is above the models with a clear separation but for the away side (PMD-FTPCW) correlation data falls on top of models. A similar study was done for the observable $r_{m,1}$ as shown in Fig. 3.24. For the same side correlation the data deviates from

both the model calculations using Raw HIJING and GEANT+HIJING. For the away side data lie between Raw HIJING and GEANT+HIJING results. This might indicate a presence of non-zero dynamical localised signal when overlapping acceptance is considered for γ -charge correlation.

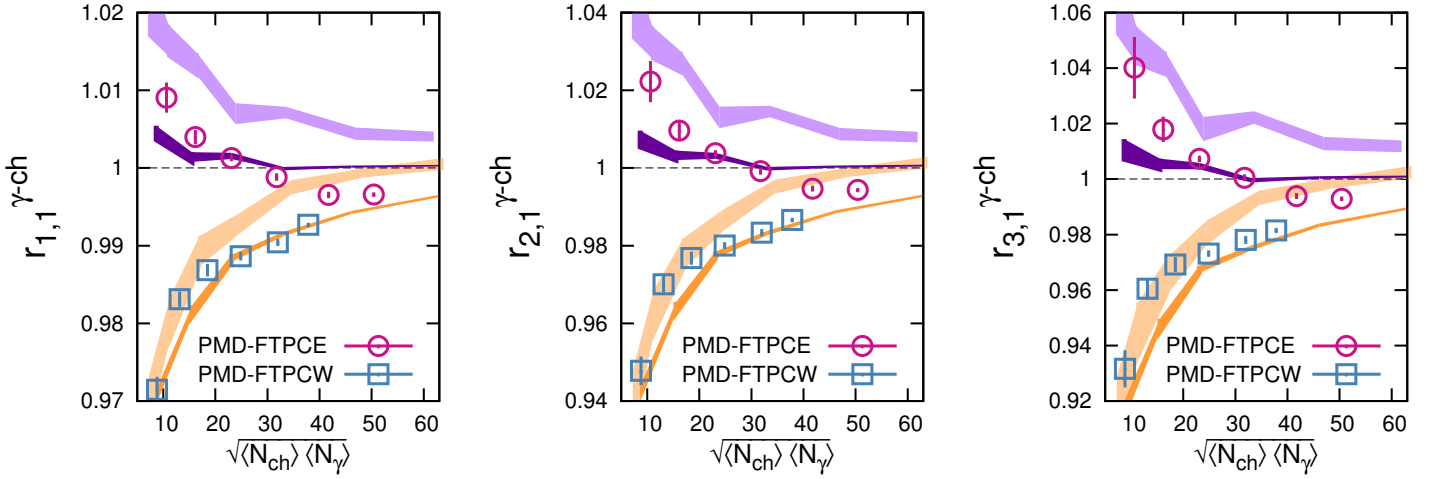


Figure 3.24: Robust observable using photons from PMD and charged particles using east and west FTPCs. Yellow bands are simulation results for PMD and West FTPC; the purple bands are simulation results for PMD and East FTPC. In both the cases, the light color solid bands are for GEANT+HIJING calculations and the dark bands are for Raw HIJING.

3.15 N_{part} dependence of $\gamma - \text{ch}$ correlation.

In Fig. 3.25, the N_{part} dependence of all terms of ν_{dyn} for PMD-FTPC (East) i.e. for same-side correlation. The similar plot for PMD-FTPC(West) or away-side, which are separated by a rapidity gap of about unit size is shown in Fig. 3.26. Fig.3.25 shows individual terms of ν_{dyn} for which one can see slightly different trend compared to the earlier plots shown in Fig. 3.18 and Fig.3.19. However the question comes which quantity controls the physics of fluctuation, is it the geometry (Glauber observables are measure of that) or the multiplicity that goes in the calculation of fluctuation observables. Choice of this would affect the physics message one is trying to highlight.

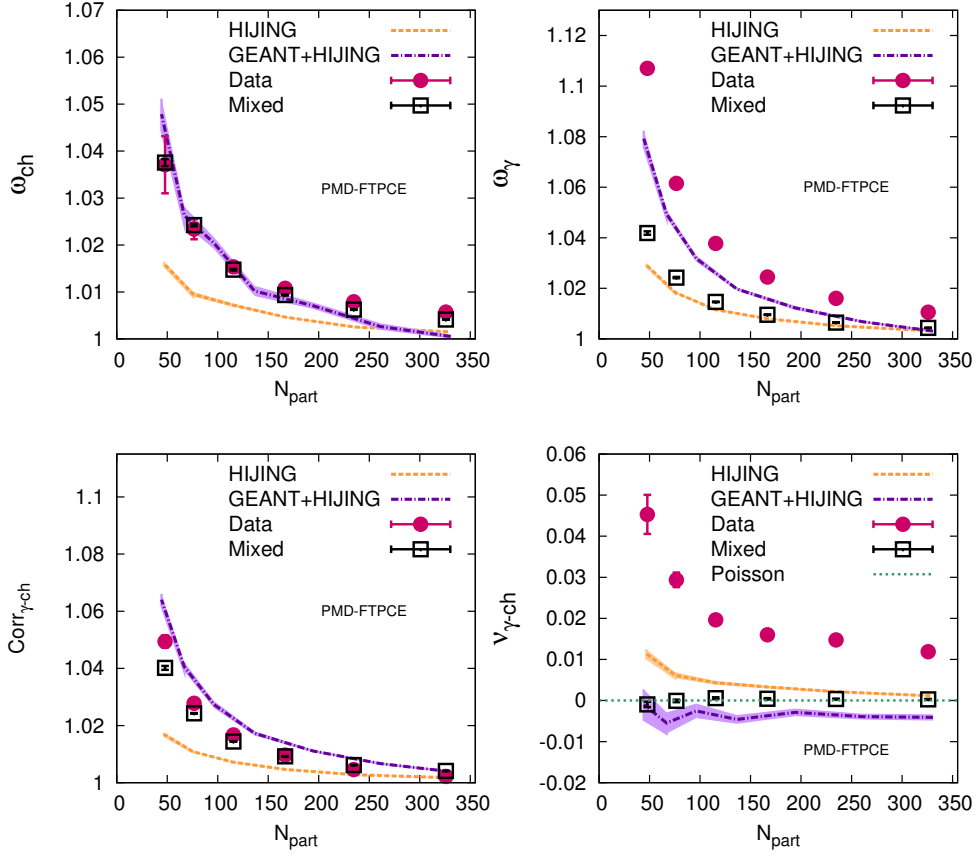


Figure 3.25: N_{part} dependence of all terms of ν_{dym} for PMD-FTPCE (East) (same-side)

3.16 Effect of flow on $\gamma - \text{ch}$ correlation.

In order to investigate the effect of flow in this analysis with non-uniform acceptance we have used a toy model to introduce flow in HIJING. As mentioned in Ref.[181], event-by-event flow can be introduced by changing the azimuthal angle of each particle

$$\phi \rightarrow \phi' = \phi + \Delta\phi \quad (3.9)$$

where

$$\Delta\phi = \sum_n \frac{-2}{n} \tilde{v}_n \sin[n(\phi - \psi_0)], \quad (3.10)$$

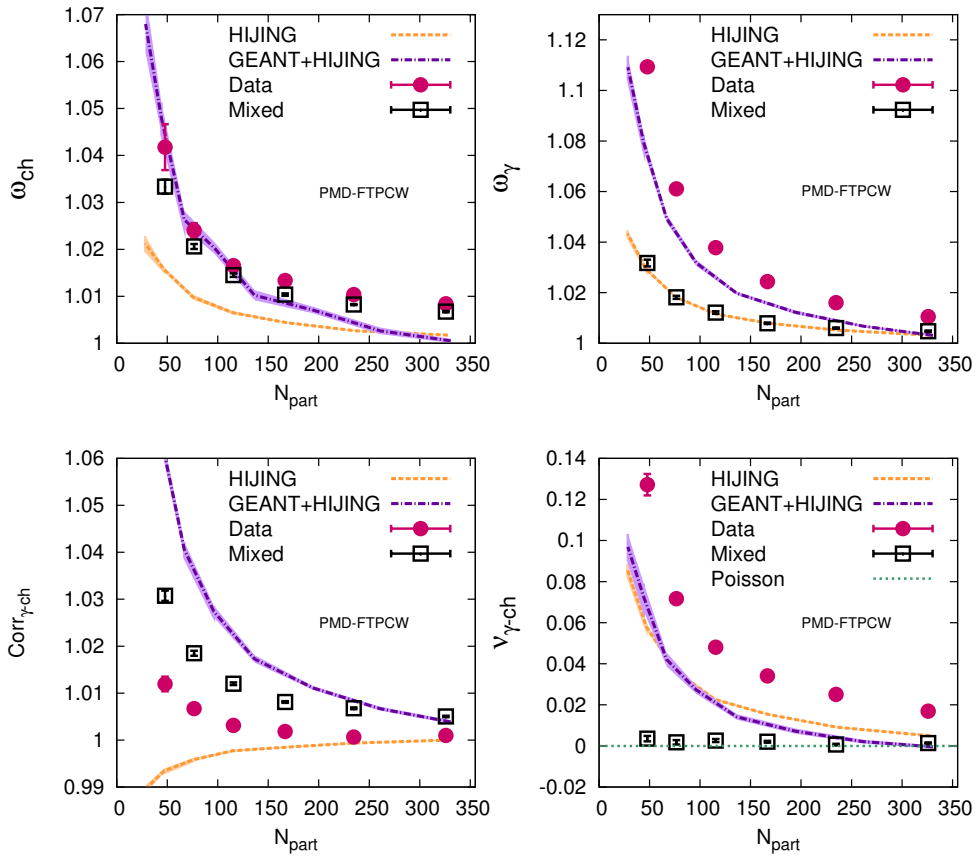


Figure 3.26: N_{part} dependence of all terms of ν_{dyn} for PMD-FTPCW (West) (opposite-side)

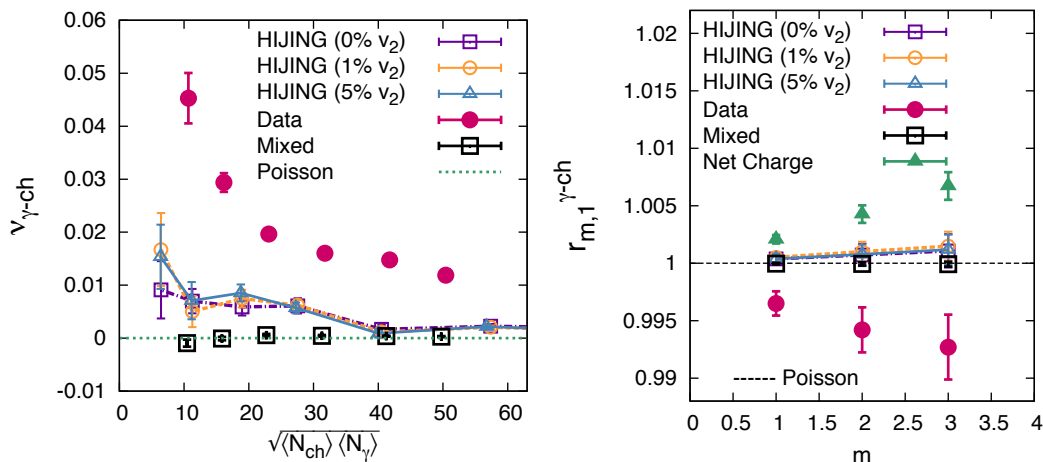


Figure 3.27: Effect of flow on $\gamma - \text{ch}$ correlation. Data points are also plotted for better comparison. Left: variation of ν_{dyn} with multiplicity. Right: variation of $r_{m,1}$ with m for most central events.

\tilde{v}_n are the n different coefficients of flow and ψ_0 is the direction of the added flow. For HIJING simulations we choose $\psi_0 = 0$ and consider $n = 2$ to study this effect. We have introduced v_2 for all pions and charged hadrons in the range of 0 – 5% and calculated the final observables ν_{dyn} and $r_{m,1}$ for different centralities. For neutral pions we first introduce v_2 on every π^0 in a given event and then decay them to photons, uniformly in their rest frame. In this simple toy model v_2 is assumed to be a constant parameter independent of rapidity, transverse momentum and centrality. We have used the same $\eta - \phi$ acceptance contour we have used for data. Results for observables ν_{dyn} and $r_{m,1}$ for different values of v_2 are shown in Fig. 3.27. We see that our observable are insensitive to v_2 in the range 0 – 5% introduced using the toy model described above. This result is consistent with previous results obtained using AMPT event generator shown in previous section using same acceptance as has been used here. AMPT includes flow effect in realistic proportion and is known to describe RHIC data even at forward rapidity (the region of interest for this analysis and flow is less compared to mid-rapidity). One of the possible explanation of the fact that $\gamma - \text{ch}$ correlation is insensitive to flow could be due to the fact the both charged and neutral pions are expected to have same flow. Flow although modifies the azimuthal density of pions it doesn't modify the relative abundance of pions of different isospin.

3.17 An upper limit of DCC like signals from data

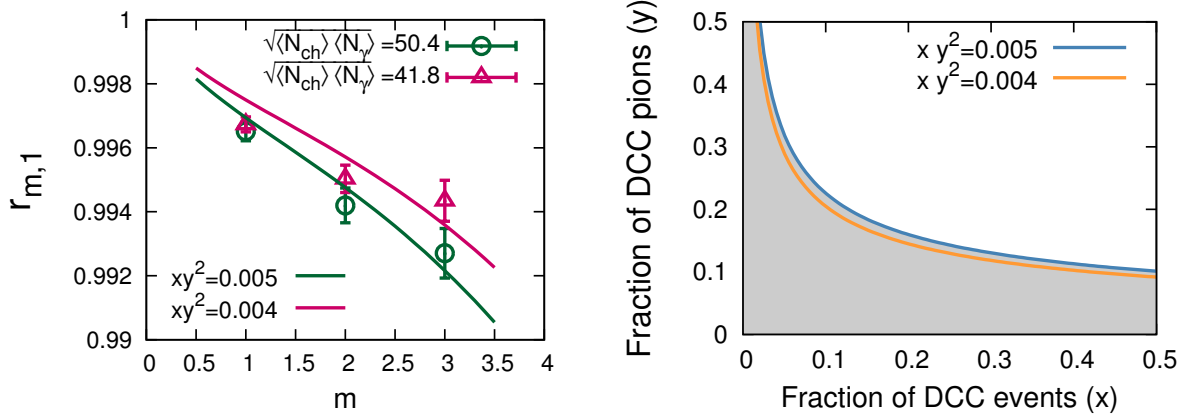


Figure 3.28: (left) Fit the data points for $r_{m,1}$ as a function of m using the functional form of Eq. 2.67 for two most central events. (right) Parameters of DCC model extracted from data, the shaded region shows the upper limit of DCC formation.

As shown in Fig. 3.20, $r_{m,1} < 1$ for two centralities corresponding to $\sqrt{\langle N_{\text{ch}} N_{\gamma} \rangle} = 50.4$ and $\sqrt{\langle N_{\text{ch}} N_{\gamma} \rangle} = 41.8$. As discussed in Sec.2.3.3 and Eq. 2.39, for these two centralities, one can unambiguously conclude that the correlation between charged particles and photons are not dominated by decay correlations, which mostly comes from the decays of resonances. As a next step we have tried to interpret the results in terms of predictions based on DCC model. In order to estimate an upper limit of DCC like signal we fit the data for $r_{m,1}$ vs m with the Eq. 2.67

$$r_{m,1} \approx 1 - \frac{mxy^2}{(m+1)} F(m, xy^2) \quad (3.11)$$

where $F(m, xy^2)$ is given by Eq. 2.55. The two free parameters in DCC model are x and y which correspond to the fraction of DCC events in the data sample and fraction of DCC pions in such events respectively in the coverage considered. Results of fitting is shown in Fig. 3.17 (left). Due to the functional form of Eq. 3.11, the parameters x and y can not be determined independently. The fitting yields values of $xy^2 = 0.005$ and $xy^2 = 0.004$ for the centralities corresponding to $\sqrt{\langle N_{\text{ch}} N_{\gamma} \rangle} = 50.4$ and $\sqrt{\langle N_{\text{ch}} N_{\gamma} \rangle} = 41.8$ respectively. In Fig. 3.17 we show the possible region allowed for DCC like signals in terms of the parameters x and y .

3.18 Summary

Correlation between photon & charged particle multiplicities have been measured at $-3.7 < \eta < -2.8$ in a limited but overlapping azimuthal coverage of PMD and FTPC at $\sqrt{s_{NN}}=200$ GeV. ν_{dyn} and $r_{m,1}$ have been used as measures of correlation. ν_{dyn} shows an approximate $\sim 1/\sqrt{\langle N_{\text{ch}}N_{\gamma} \rangle}$ dependence as expected from the Central Limit Theorem (CLT). ν_{dyn} shows dynamical fluctuation in excess to HIJING, mixed event and GEANT+HIJING. A detailed analysis of systematic uncertainties have been quantified. Model studies show that other collective effects such as flow doesn't seem to affect the $\gamma - \text{ch}$ correlation. The charge dependence of the ν_{dyn} shows that different combination of $\gamma - \text{ch}$ correlation are alike but show a very different behaviour from positive-negative charge correlation measured in the same acceptance. The result is indicative of the fact that a different mechanism of particle production is responsible for correlated production of neutral and charged particles which is not present in conventional models.

A second measure $r_{m,1}$ has been used to extract deviation of $\gamma - \text{ch}$ correlation from expectation of generic pion production. The centrality dependence of the lowest order moment of the observable $r_{m,1}$ shows different trend compared to mixed event and HIJING. $r_{1,1}$ goes below the generic limit at higher multiplicity. For central events, $r_{m,1}$ shows a trend opposite to that from the models, thereby suggesting deviation from generic expectation of the observable in the data. The deviation quantified by fits to the functional form of Eq. 2.67 and upper limit of DCC formation has been estimated in terms of contours of the fraction of DCC events and fraction of DCC candidates (pions).

Chapter 4

Modelling fluctuations from the initial stages of collisions

4.1 Introduction

In this chapter, we discuss how different sources of initial state fluctuations contribute to the fluctuations of global observables such as charged and neutral particle multiplicities in hadronic and heavy ion collisions. At very high energies the early stages of hadronic or heavy ion collisions are dominated by fluctuation of coherent gluon fields which evolves over a pre-equilibrium phase that can be described by Yang-Mills evolution. The sources of initial state fluctuations of gluon numbers are due to geometric and quantum fluctuations. A first principle approach to solve this problem in conventional perturbation theory is extremely difficult since the dominant fraction of initial gluons that produces the bulk multiplicity comes from soft modes ($Q \sim \Lambda_{QCD}$) for which the effective coupling ($\alpha_S(Q)$) is quite large. The Color Glass Condensate (CGC) is a framework, that includes various possible sources of initial state fluctuations, and hence can provide an *ab initio* approach to such problems [39]. The details of the framework and the approach to calculate inclusive multiplicity and its fluctuation in CGC approach will be discussed in this chapter.

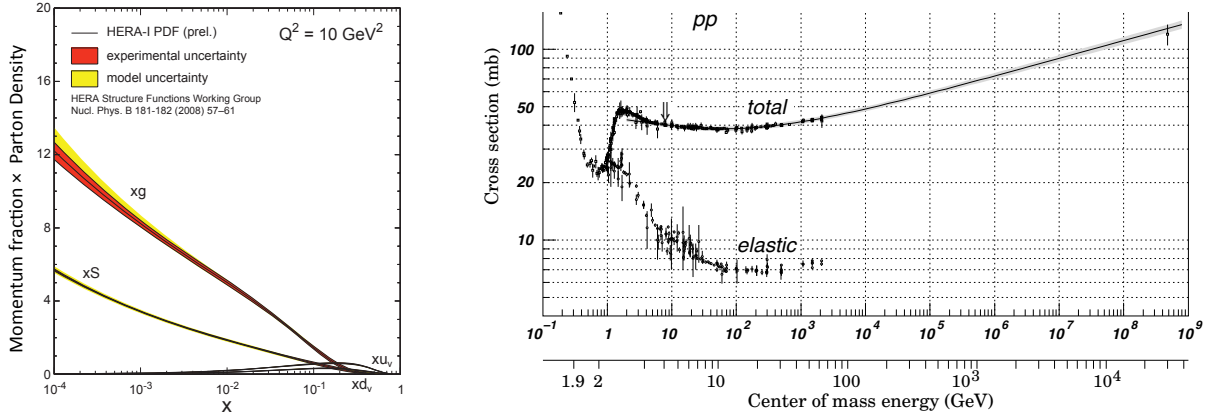


Figure 4.1: (left) HERA data on structure parton distribution function measured in DIS processes from Ref. [182]. (right) Energy dependence of measured cross sections for pp collision from Ref. [183].

4.2 The phenomenon of gluon saturation

Deeply inelastic scattering (DIS) results from HERA on structure functions demonstrate a rapid bremsstrahlung growth of the gluon density at small x [184] (Fig. 4.1(left)). Here x denotes the momentum fraction of hadron carried by a parton. Such a linear growth in gluon density would correspond to a rapid increase in the total cross section for pp or $p\bar{p}$ collisions with energy ¹. However experimental measurement shows only a logarithmic growth of the total cross section with collisions energy (Fig.4.1(right)). This indicates that the gluon density inside a hadron must saturate by the underlying dynamics of QCD in the limit of high energy or small x . When interpreted in the framework of the parton model, the bremsstrahlung growth of gluon is predicted to saturate because the gluon occupation number in hadron wave functions saturate at a value maximally of order $1/\alpha_S$; dynamically, nonlinear effects such as gluon recombination and screening by other gluons deplete the growth of the gluon distribution [185]. As a result the gluon modes with $k_T < Q_S(\gg \Lambda_{QCD})$ are maximally occupied, where $Q_S^2(x)$ is a dynamically generated semi-hard scale called the saturation scale.

¹It can be shown that $x \sim 1/E_{\text{cms}}$, E_{cms} is the centre of mass energy of collision.

4.3 The small- x problem of QCD

The small- x limit of QCD (also called the Regge-Gribov limit, $x \rightarrow 0$) is important for the description of multi particle production in hadronic and heavy ion collisions at high energies. We define the momentum fraction of hadron carried by a parton as $x = k^+/P^+$. At high energy x is closely related to the kinematic variable introduced [186] by Bjorken $x_{\text{BJ}} \sim Q^2/s$ (Q^2 , the resolution scale at which the parton is probed and s is the Mandelstam variable). Here k^+ and P^+ are the light front (LF) momenta of the parton and the hadron respectively. This definition is a direct consequence of the parton model [186] which is formulated in the “infinite momentum frame” (IMF) in which hadrons are collection of “quasi-free” partons. It turns out that introduction of light front (LF) co-ordinates [187] is equivalent to considering IMF (also called limiting reference frame [189] or light cone frame)². The idea is to approach the small- x problem in QCD by developing a many body effective field theory on the light front [190]. This would require an assumption that there is a Born-Oppenheimer (BO) separation between the large- x and the small- x modes of the quantum fields on the LF. Born-Oppenheimer separation is useful approximation in the study of molecular dynamics. It enables one to treat the motion of the slow moving heavy nuclei and the fast moving light electrons separately. Over the time scales of the motion of slow nuclei, the light electrons can almost instantaneously adjust to its most stable configurations. The electronic degrees of freedom can be integrated out of the problem to contribute to the effective potential for the motion of the nuclei. Similarly inside a hadron or nuclei at high energies, one can separate the large- x and the small- x degrees of freedom since, on the time scales of the small- x wee partons (slow), the distribution of large- x partons (fast) can be viewed as static distribution of charges due to time dilation. Thus one can develop an effective theory with the static sources of color charges ρ (large- x modes) with momenta $k^+ > \Lambda^+$ which couples to the dynamical wee gluon fields A^μ with momenta $k^+ < \Lambda^+$.

²Introduction of LF co-ordinate has many other advantages such as some of the complicated problems of Quantum Field Theory like vacuum effects disappear on LF [188]. It can be shown that a Poincare group on the LF is isomorphic to a Galilean sub-group of 2D quantum mechanics [189]. Thus a relativistic system of particles boosted in z-direction to infinite momentum, the dynamics on the transverse plane (x-y) would simplify to a two dimensional system of non-relativistic particles.

Where Λ^+ is the separation scale between fast and slow modes. The statistical distribution of the static color sources ρ are given by universal density matrices $\mathcal{W}_{\Lambda^+}[\rho]$ defined at the scale Λ^+ . Finally in this framework expectation value of any operator $\mathcal{O}[\rho]$ that is related to a physical observable is obtained by averaging over all possible configuration of color sources as

$$\langle \mathcal{O} \rangle_{\Lambda^+} \equiv \int [D\rho] \mathcal{W}_{\Lambda^+}[\rho] \mathcal{O}[\rho]. \quad (4.1)$$

However any physical observable has to be independent of the separation scale Λ^+ between the slow and the fast modes, which give rise to renormalisation group (RG) equations. The RG equations evolves the distribution $\mathcal{W}_{\Lambda^+}[\rho]$ to the distribution $\mathcal{W}_{\Lambda'^+}[\rho']$ of charge density $\rho' = \rho + \delta\rho$ defined at a new scale Λ'^+ by integrating out the modes between $\Lambda'^+ < k^+ < \Lambda^+$. The change of the weight functional $\mathcal{W}[\rho]$ with $x(=k^+/P^+)$ is described by the well known Jalilian Marian-Iancu-McLerran-Weigert-Leonidov-Kovner (JIMWLK) nonlinear RG equation [191] expressed as

$$\frac{\partial \langle \mathcal{O} \rangle_Y}{\partial Y} = \langle \mathcal{H} \mathcal{O} \rangle_Y, \quad (4.2)$$

where $Y = \ln(x/x_0)$, x_0 being the initial scale for x evolution. A simpler form (mean-field approximation) of the JIMWLK equation in the limit of large number of colors $N_c \rightarrow \infty$ is the Balitsky-Kovchegov (BK) equation which will be discussed in the later sections. It should be noted that in this framework the initial distribution of $\mathcal{W}[\rho]$ at the starting scale (at x_0) is unknown which is generally set by a model. A physically motivated model in case of the ρ distribution in a large nucleus is the McLerran-Venugopalan (MV) model [192]. In this model the $\mathcal{W}[\rho]$ is a Gaussian distribution, the variance of which provides a semihard scale (μ^2) in the theory, which at small x or for large nucleus is large enough to make weak coupling ($\alpha_S(\mu) \ll \alpha_S(\Lambda_{QCD})$) computations feasible. This weak coupling effective field theory to treat the dynamics of small- x degrees of freedom in QCD is universal in nature and known as the framework of Color Glass Condensate (CGC). The word ‘‘Color’’ indicates that the degrees of freedom in this theory are colored. The word ‘‘Glass’’ is derived from the analogy of glass which

is a disordered system and liquid like on long time scales but behaves like a solid on a short time scale. In a similar way the stochastic distribution of static sources appears to be frozen due to time dilation compared to the natural time scale of strong interaction. It is called a “Condensate” due to high occupancy of states ($\mathcal{O}(1/\alpha_s(\mu))$) of gluons with momenta peaked around the saturation momenta Q_s^2 which is proportional to scale μ^2 in this theory.

4.4 Saturation models of HERA DIS

One of the motivation to study saturation models that parametrize the Deeply Inelastic Scattering (DIS) is to set the initial distribution of color charge density $\mathcal{W}[\rho]$ which is an input to the framework of CGC. These models are implemented with realistic assumptions by incorporating the essence of saturation physics. The $e + p$ DIS in the CGC framework is treated by assuming that the virtual photon coming from the electron form a color dipole which then scatters off the dense saturated gluon field inside the proton. At leading order in α_s [192] in the dipole picture, the inclusive virtual photon hadron cross section is expressed as [193]

$$\sigma_{L,T}^{\gamma^*p} = \int d^2\mathbf{r}_\perp \int_0^1 dz \left| \Psi_{L,T}^{\gamma^*} \right|^2 \int d^2\mathbf{b}_\perp \frac{d\sigma_{\text{dip}}^p}{d^2\mathbf{b}_\perp}. \quad (4.3)$$

Here $\left| \Psi_{L,T}^{\gamma^*}(\mathbf{r}_\perp, z, Q) \right|^2$ represents the probability for a virtual photon to produce a quark–anti-quark pair of size $r = |\mathbf{r}_\perp|$ and $\frac{d\sigma_{\text{dip}}^p}{d^2\mathbf{b}_\perp}(\mathbf{r}_\perp, x, \mathbf{b}_\perp)$ denotes the *dipole cross section* for this pair to scatter off the target at an impact parameter \mathbf{b}_\perp . The former is well known from QED, while the latter represents the dynamics of QCD scattering at small x . One of the simplest example of a saturation model is the Golec-Biernat–Wusthoff (GBW) model [194]. It implements saturation in the dipole cross-section through the parametrization $\frac{d\sigma_{\text{dip}}^p}{d^2\mathbf{b}_\perp} = 2(1 - e^{-r^2 Q_{s,p}^2(x)/4})$, where $Q_{s,p}^2(x) = (x_0/x)^\lambda \text{ GeV}^2$, gives a good qualitative fit to the HERA inclusive and diffractive cross section data for $x_0 = 3 \cdot 10^{-4}$ and $\lambda = 0.288$. GBW model explained very simply the key features of the HERA data and was suggestive of the possible role of a semi-hard saturation scale in the hadron. This model was refined in more sophisticated models that treat the impact

parameter dependence of the dipole cross-section more accurately. As we shall discuss further in the next section, these models give excellent fits to small x inclusive, diffractive and exclusive HERA data. The common ingredient in these combined fits is the dipole cross-section.

The dipole cross-section, to leading logarithmic accuracy, is a universal quantity which can be applied to compute inclusive quantities in hadron-hadron collisions. It is defined in terms of the real part of the forward scattering amplitude $\mathcal{N}(\mathbf{r}_\perp, x, \mathbf{b}_\perp)$ as

$$\frac{d\sigma_{\text{dip}}^{\text{p}}}{d^2\mathbf{b}_\perp}(\mathbf{r}_\perp, x, \mathbf{b}_\perp) = 2 \mathcal{N}(\mathbf{r}_\perp, x, \mathbf{b}_\perp) \equiv 2 \left(1 - \frac{1}{N_c} \left\langle \text{tr} \left(\tilde{U}(\mathbf{b}_\perp + \frac{\mathbf{r}_\perp}{2}) \tilde{U}^\dagger(\mathbf{b}_\perp - \frac{\mathbf{r}_\perp}{2}) \right) \right\rangle_x \right), \quad (4.4)$$

where $\tilde{U}(\mathbf{b}_\perp \pm \frac{\mathbf{r}_\perp}{2})$ is a Wilson line in the fundamental representation representing the interaction between a quark and the color fields of the target. The expression inside the $\langle \dots \rangle_x$ is an average over these color fields; the energy dependence of the correlator as a function of x (or the rapidity $Y = \ln(1/x)$) is given by the JIMWLK equation [195]. In the large N_c limit, the equation for the energy evolution of this correlator is the Balitsky-Kovchegov (BK) equation [196]. We note however that neither JIMWLK nor BK is equipped to deal well with the impact parameter dependence of the dipole cross-section; the dipole cross-section in this formalism expressed in Eq. (4.4) is independent of the impact parameter. To address the impact parameter dependence of this equation, one resorts to models which parametrize both saturation effects and the impact parameter dependence.

4.4.1 The IP-Sat Model

The impact parameter dependent dipole saturation model (IP-Sat) [197] is a refinement of the Golec-Biernat–Wusthoff dipole model [194] to give the right perturbative limit when $\mathbf{r}_\perp \rightarrow 0$ [198]. It is equivalent to the expression derived in the classical effective theory of the CGC, to leading logarithmic accuracy [192]. The proton dipole cross-section in this model is expressed

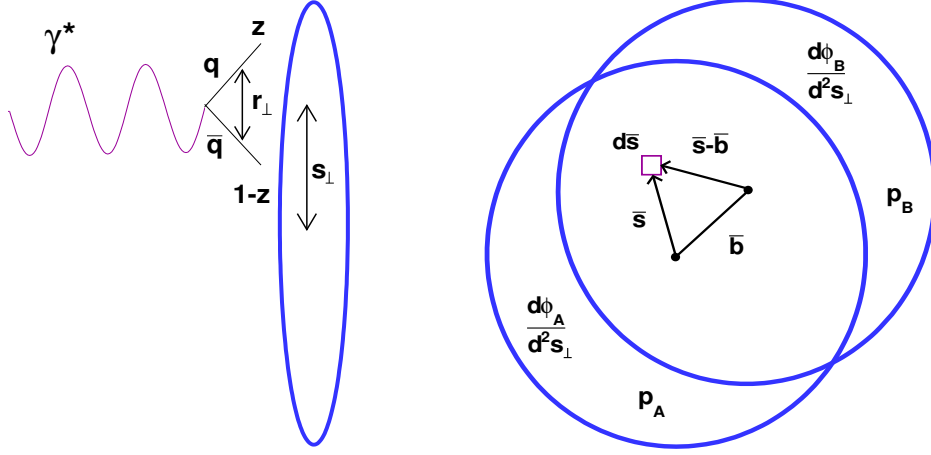


Figure 4.2: Left: Dipole cross-section in DIS. Right: Overlap of unintegrated gluon distributions in proton-proton collisions.

as

$$\frac{d\sigma_{\text{dip}}^p}{d^2\mathbf{b}_\perp}(\mathbf{r}_\perp, x, \mathbf{b}_\perp) = 2 \left[1 - \exp \left(-\frac{\pi^2}{2N_c} \mathbf{r}_\perp^2 \alpha_S(\mu^2) x g(x, \mu^2) T_p(\mathbf{b}_\perp) \right) \right]. \quad (4.5)$$

Here the scale μ^2 is related to dipole radius \mathbf{r}_\perp (see Fig. 4.2) as

$$\mu^2 = \frac{4}{\mathbf{r}_\perp^2} + \mu_0^2, \quad (4.6)$$

where the leading order expression for the running coupling is

$$\alpha_S(\mu^2) = \frac{12\pi}{(33 - 2n_f) \log(\mu^2/\Lambda_{QCD}^2)} \quad (4.7)$$

with $n_f=3$, $\Lambda_{QCD}=0.2$ GeV. The model includes saturation as eikonized power corrections to the DGLAP leading twist expression and may be valid in the regime where logs in Q^2 dominate logs in x . The saturation scale for a fixed impact parameter is determined self-consistently by requiring that the dipole amplitude (within brackets in Eq. 4.5) have the magnitude $\mathcal{N}(x, r_S, \mathbf{b}_\perp) = 1 - e^{-1/2}$, with $Q_{s,p}^2 = 2/r_S^2$. We note that there is an overall logarithmic uncertainty in the determination of $Q_{s,p}^2(x, \mathbf{b}_\perp)$.

For each value of the dipole radius, the gluon density $xg(x, \mu^2)$ is evolved from μ_0^2 to μ^2 using LO DGLAP evolution equation without quarks,

$$\frac{\partial xg(x, \mu^2)}{\partial \log \mu^2} = \frac{\alpha_S(\mu^2)}{2\pi} \int_x^1 dz P_{gg}(z) \frac{x}{z} g\left(\frac{x}{z}, \mu^2\right) \quad (4.8)$$

Here the gluon splitting function with n_f flavor and $C_A=3$ & $T_R=1$ is

$$P_{gg}(z) = 6 \left[\frac{z}{(1-z)_+} + \frac{1-z}{z} + z(1-z) \right] + \left(\frac{11}{2} - \frac{n_f}{3} \right) \delta(1-z) \quad (4.9)$$

The initial gluon density at the scale μ_0^2 is taken to be of the form

$$xg(x, \mu_0^2) = A_g x^{-\lambda_g} (1-x)^{5.6} \quad (4.10)$$

An important feature of the IP-Sat model is the b -dependence of the dipole cross-section, which is introduced through a gluon density profile function $T(b)$. This profile function is normalized to unity and is chosen to have the Gaussian form

$$T_p(\mathbf{b}_\perp) = \frac{1}{2\pi B_G} \exp\left(\frac{-\mathbf{b}_\perp^2}{2B_G}\right), \quad (4.11)$$

where B_G is a parameter fit to the HERA diffractive data. This corresponds to $\langle b^2 \rangle = 2B_G$, the average squared *gluonic* radius of the proton.

Sets of parameters obtained from optimal fits of the IP-Sat model to HERA data [199] are listed in table 4.1. All data sets except the last use $m_{u,d,s} = 0.14$ GeV; the last set corresponds to

m_c	$B_G(\text{GeV}^{-2})$	$\mu_0(\text{GeV}^2)$	A_g	λ_g
1.4	4.0	1.17	2.55	0.020
1.35	4.0	1.20	2.51	0.024
1.5	4.0	0.77	2.64	0.011
1.4	4.0	1.50	3.61	-0.118

Table 4.1: Parameters of the IP-Sat model obtained from the fit to HERA data [199].

$m_{u,d,s} = 0.05$ GeV. The parameters of the initial gluon distribution are determined from fits to the HERA F_2 data [200, 201] with a $\chi^2 \sim 1$. For charm quarks, $x = x_{\text{bj}}(1 + 4m_c^2/Q^2)$. The value of B_G is determined primarily from the t -distributions of J/ψ mesons measured by ZEUS [202] and H1 [203]. With these parameters, excellent agreement is obtained with the HERA exclusive vector meson and DVCS data. For a detailed comparison of this model to the HERA data, we refer the reader to Ref. [199].

4.4.2 The b-CGC Model

At very small x , quantum evolution in the CGC describing both the bremsstrahlung limit of linear small x evolution as well as nonlinear RG evolution at high parton densities, combined with a realistic b -dependence, is very well captured in the bCGC model [199, 204, 205]. The proton dipole cross-section in this case is expressed as

$$\frac{d\sigma_{\text{dip}}^{\text{p}}(\mathbf{r}_{\perp}, x, \mathbf{b}_{\perp})}{d^2\mathbf{b}_{\perp}} = 2 \times \begin{cases} \mathcal{N}_0 \left(\frac{\mathbf{r}_{\perp} \bar{Q}_s}{2} \right)^{2\left(\gamma_s + \frac{1}{\kappa\lambda Y} \ln\left(\frac{2}{\mathbf{r}_{\perp} \bar{Q}_s}\right)\right)} & : \mathbf{r}_{\perp} \bar{Q}_s \leq 2; \\ 1 - \exp\left(-A \ln^2(B \mathbf{r}_{\perp} \bar{Q}_s)\right) & : \mathbf{r}_{\perp} \bar{Q}_s > 2; \end{cases} \quad (4.12)$$

In this model, in contrast to the IP-sat model, the impact parameter dependence is introduced through the quantity $\bar{Q}_s(x, \mathbf{b}_{\perp})$, defined as

$$\bar{Q}_s(x, \mathbf{b}_{\perp}) = \left(\frac{x_0}{x}\right)^{\lambda/2} \left[\exp\left(-\frac{\mathbf{b}_{\perp}^2}{2B_{\text{CGC}}}\right) \right]^{\frac{1}{2\gamma_s}} \quad (4.13)$$

As previously, for comparison of scales among different saturation models, the relevant saturation scale for a fixed impact parameter is determined self-consistently by requiring that the dipole amplitude (the expression to the right of the curly bracket in Eq. 4.12) have the magnitude $\mathcal{N}(x, r_S, \mathbf{b}_{\perp}) = 1 - e^{-1/2}$, with the saturation scale defined as $Q_{s,p}^2 = 2/r_S^2$. The coefficients A and B are obtained by requiring the two asymptotic forms of the dipole cross-section and their

first derivatives are continuous at $\mathbf{r}_\perp \bar{Q}_s = 2$:

$$A = \frac{\mathcal{N}_0^2 \gamma_S^2}{(1 - \mathcal{N}_0)^2 \ln(1 - \mathcal{N}_0)} \quad \& \quad B = \frac{1}{2} (1 - \mathcal{N}_0)^{-\frac{(1 - \mathcal{N}_0)}{\mathcal{N}_0 \gamma_S}} \quad (4.14)$$

The parameter $\kappa = 9.9$ is fixed from the leading order BFKL value for this quantity.

Table 4.2 presents the parameters of the model that are fitted to the HERA data [204]. The parameter B_{CGC} is determined from the t -dependence of exclusive J/ψ photo-production. For the b-CGC model, this parameter however cannot be easily interpreted as giving the square mean gluonic radius of the proton. The parameters presented in the table in the first and fourth lines do not give good fits to the data. The fit corresponding to the second line of the table gives the best fit to the data with $\chi^2 \sim 1$. The third line of the table corresponds to a fit where no saturation form is employed (namely, the perturbative expression, without the diffusion term proportional to $Y = \ln(x_0/x)$, is extended to $\mathbf{r}_\perp \bar{Q}_s \geq 2$); it gives equally good fits to the data. However, it should be noted that this choice of parameters will violate perturbative unitarity for large dipole sizes $\mathbf{r}_\perp > 1/\bar{Q}_s$.

In section 4.5.4 we discuss the dependence of the saturation scale $Q_{s,p}^2(x, \mathbf{b}_\perp)$ as a function of x for different \mathbf{b}_\perp (and vice versa) in the IP-Sat and b-CGC (see Fig. 4.17). In both cases, the fits to the HERA data result in a semi-hard scale ($Q_S^2 \gg \Lambda_{\text{QCD}}^2$) with decreasing x and b values probed in the collisions. The existence of such scales and their increase with energy is what validates the whole approach of treating high parton densities in weak coupling. It would of course be naive to interpret the extracted numerical value of Q_S as being precisely the scale that controls the running of the coupling. As is well known, the scale that controls the running of the coupling can differ considerably from this “bare” scale in a given scheme for any given process.

γ_s	$B_{CGC}(\text{GeV}^{-2})$	\mathcal{N}_0	x_0	λ
0.63	5.5	0.417	$5.95 \cdot 10^{-4}$	0.159
0.46	7.5	0.558	$1.84 \cdot 10^{-6}$	0.119
0.43	7.5	0.565	$1.34 \cdot 10^{-6}$	0.109
0.54	6.5	0.484	$3.42 \cdot 10^{-5}$	0.149

Table 4.2: Parameters of the b-CGC model obtained from fits to HERA data [204]. The second row of parameters gives the best fit to HERA data.

4.4.3 The rc-BK Model

The forward scattering amplitude $\mathcal{N} = \frac{1}{2} \frac{d\sigma_{\text{dip}}^p}{d^2\mathbf{b}_\perp}$, in the rc-BK model [206] satisfies the equation,

$$\frac{\partial \mathcal{N}(\mathbf{r}_\perp, Y)}{\partial Y} = \int d\mathbf{r}_1 \mathcal{K}_{\text{rc}}(\mathbf{r}_\perp, \mathbf{r}_1, \mathbf{r}_2) \times [\mathcal{N}(\mathbf{r}_1, Y) + \mathcal{N}(\mathbf{r}_2, Y) - \mathcal{N}(\mathbf{r}_\perp, Y) - \mathcal{N}(\mathbf{r}_1, Y) \mathcal{N}(\mathbf{r}_2, Y)], \quad (4.15)$$

where $\mathbf{r}_2 \equiv \mathbf{r}_\perp - \mathbf{r}_1$ and the rc-kernel (where running coupling corrections are taken into account) is given by

$$\mathcal{K}_{\text{rc}}(\mathbf{r}_\perp, \mathbf{r}_1, \mathbf{r}_2) = \frac{\alpha_S(\mathbf{r}_\perp) N_c}{\pi} \left[\frac{\mathbf{r}_\perp^2}{\mathbf{r}_1^2 \mathbf{r}_2^2} + \frac{1}{\mathbf{r}_1^2} \left(\frac{\alpha_S(\mathbf{r}_1^2)}{\alpha_S(\mathbf{r}_2^2)} - 1 \right) + \frac{1}{\mathbf{r}_2^2} \left(\frac{\alpha_S(\mathbf{r}_2^2)}{\alpha_S(\mathbf{r}_1^2)} - 1 \right) \right]. \quad (4.16)$$

This expression is based on considerable recent work to include running coupling corrections to the BK equation [207, 208]. It should be noted that the expression does not include other next-to-leading log contributions to the kernel that have been computed recently [209]. Also of relevance to us is the assumption in the evolution equation in Eq. 4.15 that the dependence on the impact parameter and the dipole size factorize in the dipole amplitude as

$$\mathcal{N}(\mathbf{r}_\perp, x, \mathbf{b}_\perp) = 2 \mathcal{T}(\mathbf{b}_\perp) \mathcal{N}(\mathbf{r}_\perp, x). \quad (4.17)$$

The factorization here of impact parameter dependence and dipole size is very problematic conceptually and is an important limitation in applying these approaches to comparisons with data, except perhaps for final states that have limited sensitivity to the impact parameter

dependence. How to include the impact parameter dependence in the BK/JIMWLK equations is an open question of great interest [210].

The rc-BK model was applied in refs. [211] to a phenomenological study of the HERA data on the proton structure function F_2 . In this model, the impact parameter dependence of the dipole amplitude is taken to be a step function. The initial condition for the dipole amplitude is given by the MV model [190] as

$$N(r, Y = 0) = 1 - \exp \left[- \left(\frac{Q_{s_0}^2 r^2}{4} \right)^\gamma \ln \left(\frac{1}{r\Lambda_{QCD}} + e \right) \right] \quad (4.18)$$

This parametrization for protons was determined from a global fit of F_2 data in the work of [211]. In this work, we use $Q_{s_0,p}^2 = 0.15 \text{ GeV}^2$ and $\gamma = 1.13$, as mentioned in [211].

4.5 Particle production : Perturbative approach

In the collision of two dilute systems or a dilute and a dense system, one can derive at leading order the expression [215]

$$\frac{dN_g(\mathbf{b}_\perp)}{dy d^2\mathbf{p}_\perp} = \frac{4\alpha_S}{\pi C_F} \frac{1}{p_\perp^2} \int \frac{d^2\mathbf{k}_\perp}{(2\pi)^5} \int d^2\mathbf{s}_\perp \frac{d\phi_A(x_1, \mathbf{k}_\perp | \mathbf{s}_\perp)}{d^2\mathbf{s}_\perp} \frac{d\phi_B(x_2, \mathbf{p}_\perp - \mathbf{k}_\perp | \mathbf{s}_\perp - \mathbf{b}_\perp)}{d^2\mathbf{s}_\perp} \quad (4.19)$$

This equation is a generalization of the well known k_\perp factorization expression for inclusive gluon production [216] to include the impact parameter dependence of the unintegrated gluon distributions. Here $C_F = (N_c^2 - 1)/2N_c$ is the Casimir for the fundamental representation. Using a relation between quark and gluon dipole amplitudes strictly valid in the large N_c limit, the unintegrated gluon distribution in the target/projectile can be expressed in terms of the corresponding dipole cross-section measured in DIS as [217]

$$\frac{d\phi(x, \mathbf{k}_\perp | \mathbf{s}_\perp)}{d^2\mathbf{s}_\perp} = \frac{\mathbf{k}_\perp^2 N_c}{4\alpha_S} \int_0^{+\infty} d^2\mathbf{r}_\perp e^{i\mathbf{k}_\perp \cdot \mathbf{r}_\perp} \left[1 - \frac{1}{2} \frac{d\sigma_{\text{dip}}^p(\mathbf{r}_\perp, x, \mathbf{s}_\perp)}{d^2\mathbf{s}_\perp} \right]^2 \quad (4.20)$$

Thus the impact parameter dependent dipole cross-section determined from HERA $e-p$ data can be used to compute the single inclusive gluon distribution in proton-proton collisions with no additional parameters. This assumption is strictly valid to leading log accuracy for momenta $k_{\perp}^2 > Q_{s,p}^2$. Since this is a leading order computation, the overall normalization is not constrained and is determined from data as described later. For the integrated multiplicities, there is a logarithmic infrared divergence that can be regulated by introducing a mass term. The solutions of Yang-Mills equations that treat the infrared behavior properly give infrared finite distributions which will be discussed in the next section.

It must be noted that, the dipole cross-sections are fit to HERA data for $x \leq 0.01$. One therefore needs to make an assumption for $\phi(x, k_{\perp}, b_{\perp})$ for larger $x > x_0 = 0.01$ values that kinematic regions of the proton-proton data are sensitive to. We use the parametrization [217]

$$\phi(x, k_{\perp}, b_{\perp}) = \left(\frac{1-x}{1-x_0} \right)^{\beta} \left(\frac{x_0}{x} \right)^{\lambda_0} \phi(x_0, k_{\perp}, b_{\perp}), \quad x > x_0. \quad (4.21)$$

This parametrization of the large x unintegrated gluon distribution is motivated by quark counting rules with fixed $\beta = 4$ and the parameter λ_0 which ranges from 0–0.2 in fits to the data.

The single inclusive gluon distribution in Eq. 4.19 has a logarithmic infrared divergence which can be regulated either by putting a cutoff on lower limit of p_{\perp} or replacing p_{\perp} by $m_{\perp} = \sqrt{p_{\perp}^2 + m^2}$ where the mass is a free parameter. The single inclusive p_{\perp} distribution is sensitive to the choice of m , which is fixed to be the same for data at all energy ranges.

Eq. 4.19 corresponds to the rapidity distribution of inclusive gluons at a fixed impact parameter. However, what is measured is the pseudo-rapidity distribution; the rapidity can be expressed in terms of the pseudo-rapidity most generally as

$$y(\eta, p_{\perp}, m) = \frac{1}{2} \left[\frac{\sqrt{m^2 + p_{\perp}^2} \cosh^2 \eta + p_{\perp} \sinh \eta}{\sqrt{m^2 + p_{\perp}^2} \cosh^2 \eta - p_{\perp} \sinh \eta} \right]. \quad (4.22)$$

The single inclusive distribution with respect to the pseudo-rapidity therefore contains a Jaco-

bian from the conversion of the expression with respect to the rapidity. We choose for economy of parameters the mass term in Eq. 4.22 to be the same as the one that regulates the infrared divergence.

The minimum-bias single inclusive gluon distribution is obtained from the expression

$$\frac{d\bar{N}_g}{d^2p_\perp dy} = \frac{\int d^2\mathbf{b}_\perp \frac{dN_g}{d^2p_\perp dy}(\mathbf{b}_\perp)}{\int d^2\mathbf{b}_\perp} \quad (4.23)$$

In the IP-Sat model, the proton profile does not change with energy. The transverse diffusion of the proton, often termed Gribov diffusion [218], is not fully accounted for by the diffusion of the unintegrated single inclusive gluon distribution because this growth does not automatically ensure the proper growth of the inelastic cross-section. To implement such effect, we parametrize the maximum limit of b-integration to take the form $b_{\max.} = b_0 + C \ln(s)$. Fitting the available data on average $dN/d\eta$ as a function of energy we can extract b_0 and C .

For first set of parameters in table 4.1, the IP-Sat model gives $b_0=5.17 \text{ GeV}^{-1}$ and $C=0.19$ with a choice of the mass term=0.4 GeV used in the Jacobian. This value of b_0 is close to $2 b_{\text{rms.}}$ in the IP-Sat model, where $b_{\text{rms.}}$ is the root mean square gluonic radius of the proton. The quantity $\pi b_{\text{max.}}^2$, which is the denominator of Eq. 4.23 can be interpreted as being closely related to the inelastic cross section contributing to particle production. A similar form of b_{max} when used to fit average $dN/d\eta$ for b-CGC model gives $C \sim 0$. This suggests that because the impact parameter dependence of the dipole cross-section in the b-CGC model is tied in with its x dependence (see Eq. 4.12), the non-trivial relation of the two in this model may well approximate the physics of Gribov diffusion.

The single inclusive hadron distribution is obtained by convolving Eq. 4.23 with the fragmentation function for gluons into charged hadrons,

$$\frac{d\bar{N}_h}{d^2p_\perp dy} = \int_{z_{\min.}}^1 \frac{dz}{z^2} \frac{d\bar{N}_g}{d^2q_\perp dy} D_{g \rightarrow h} \left(z = \frac{p_\perp}{q_\perp}, \mu^2 \right), \quad (4.24)$$

where $D_{g \rightarrow h}(z, \mu^2)$ is chosen to be $6.05 z^{-0.714} (1-z)^{2.92}$, corresponding to the LO parameter

set of [219]. The lower limit of the integral is determined from the kinematic requirement that $x_{1,2} \leq 1$.

4.5.1 Results for p+p collisions

In this section we present the results on rapidity and transverse momentum distributions for a wide range of collider energies up to the presently available highest at the LHC energy of $\sqrt{s} = 7$ TeV. We compare our results from different models to available data and make predictions for $\sqrt{s} = 10, 14$ TeV.

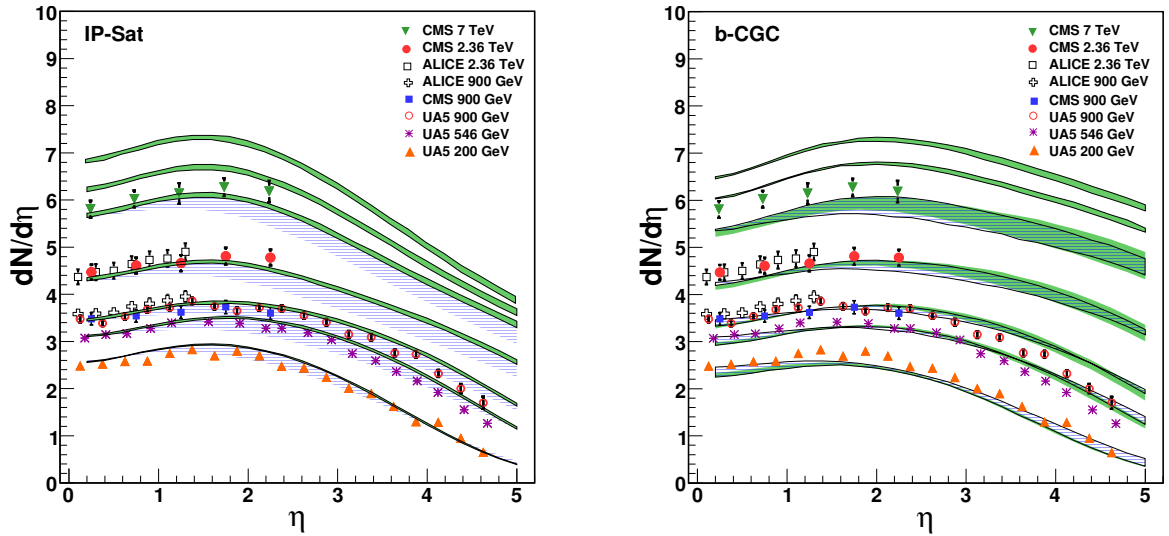


Figure 4.3: $dN/d\eta$ obtained from comparing IP-Sat and b-CGC models to data from UA5 [220], ALICE [221] and CMS [222]. The solid green band corresponds to uncertainties from different parameters; the dashed band is due to the variation of the choice of mass term in the Jacobian relating y to η . The two curves at the top in both panels correspond to projections in the two models for $\sqrt{s} = 14$ and 10 TeV respectively.

Fig. 4.3 shows the pseudo-rapidity distribution obtained by integrating Eq. 4.19 over p_{\perp} for different mass terms in the Jacobian and parameters given in the tables 4.1 and 4.2 for the IP-Sat and b-CGC dipole models respectively. The uncertainties corresponding to the choices of parametrizations and the infrared mass scale are shown in bands. In the IP-Sat model, the normalization is performed to the \sqrt{s} dependence of $dN/d\eta$ at $\eta = 0$ as shown in Fig. 4.5—this

fixes the two parameters in b_{max} . we discussed previously. In the b-CGC model, because there is one less parameter (the coefficient of $\ln s$ in b_{max} is zero), the normalization can be performed to the rapidity distribution at one fixed energy. In Fig. 4.3(left), the normalization is performed for $\sqrt{s} = 900$ GeV; choosing a lower energy corresponds to a $< 10\%$ uncertainty in the overall normalization.

We do not use a fragmentation function in computing the pseudo-rapidity distributions because the rapidity distribution is vastly dominated by contributions below $p_{\perp} = 1$ GeV, where fragmentation functions are likely not reliable. We have varied the mass term in the Jacobian corresponding to Eq. 4.22 in the range 0.2–0.4 GeV, corresponding to an infrared scale of order Λ_{QCD} . (In each case we chose this mass term to be equal to the one we use to regulate the infrared divergence of the unintegrated gluon distribution in Eq. 4.20). The effect of the extrapolation parameter λ_0 in Eq. 4.21 is significant only at lower energies and at higher values of η . The agreement with data of both models is quite good with the IP-Sat model providing a somewhat better agreement at the highest energies.

In Fig. 4.4 we present the corresponding p_{\perp} distributions with the previously specified fragmentation prescription. The IP-Sat model shows a poor agreement with data for the lower energies at high p_{\perp} , as does the b-CGC model with some of the HERA parameter sets. At higher p_{\perp} , the results are sensitive to physics at $x \geq 0.01$, which is an approximation in this approach. Also, one should anticipate a better agreement in the same p_{\perp} window at higher energies. Indeed, a systematically better agreement is seen in both models with the data at the higher energies for all parameter sets.

Fig. 4.5 shows the average value of $dN/d\eta$ calculated at $\eta=0$. The left plot of Fig. 4.5 shows a fit of $dN/d\eta$ using different functional forms for the saturation scales. We considered both Q_S^2 and $Q_S^2/\alpha_S(Q_S)$. In the CGC framework, one would expect the latter to be more appropriate. However, if the running is not significant in the energy range of interest, the former form can also be applied. A good fit to the CMS data was obtained in Ref. [225] with a simple form of the saturation scale using the Golec-Biernat model [194]. In our case, the comparison is made

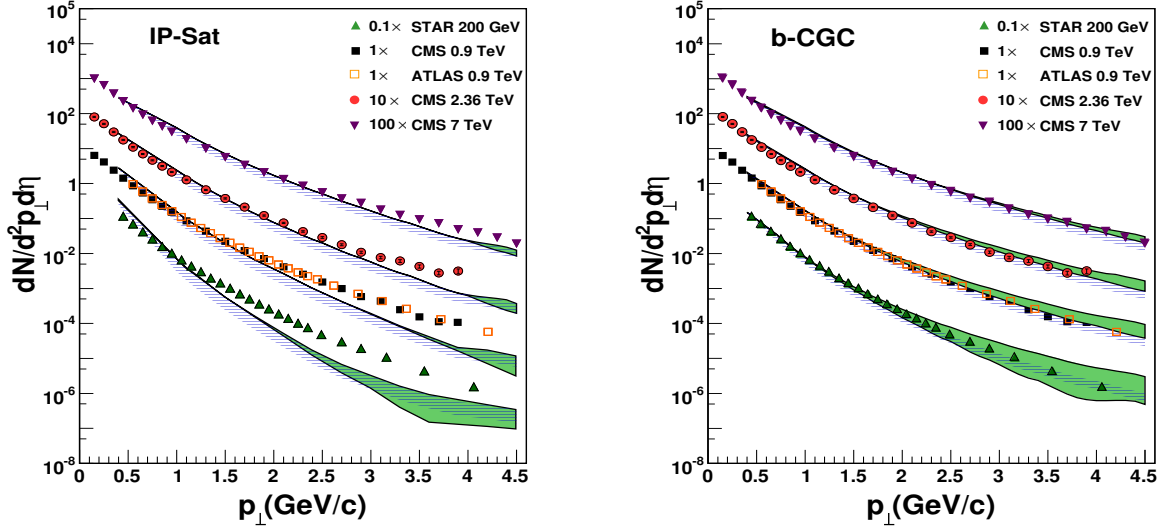


Figure 4.4: $dN/d^2p_{\perp}d\eta$ in the IP-Sat and b-CGC models. The solid (green) band corresponds to uncertainties from different parameters and the dashed (blue) band is due variation of the mass term in the Jacobian relating η to y . The p_{\perp} distribution is averaged over the η range of ± 2.4 . The experimental data points are from CMS [222], STAR [223] and ATLAS [224]

within the framework of the IP-Sat and b-CGC models both of which give better fits to the HERA data and are sensitive to the impact parameter profile of the gluon distribution in the proton. For the comparison with the LHC data in the left panel of Fig. 4.5, we use the value of Q_S at the median value of $s_{\perp}=2 \text{ GeV}^{-1}$. The dependence of $dN/d\eta$ on the purely Q_S^2 functional form is not very good, while the $Q_S^2/\alpha_S(Q_S)$ form does much better for the IP-Sat model. For the running of α_S , we chose $Q_S^2(s_{\perp})$ at $s_{\perp}=0$ to restrict its running to α_S below 0.5. Fig. 4.5 (right panel) shows by way of comparison, a comparison of $dN/d\eta$ at $\eta = 0$ as a function of \sqrt{s} to IP-Sat and b-CGC models. In the IP-Sat model, a good fit is ensured because a fit to this energy dependence is what determines the parameters of b_{max} , as discussed previously. In the b-CGC model, the curve is a prediction and is seen to be a very good fit to the data.

The energy dependence of $\langle p_{\perp} \rangle$ is shown in Fig. 4.6. In the left panel, it is shown that in this case one obtains a good linear dependence of $\langle p_{\perp} \rangle$ on Q_S in both the IP-Sat and b-CGC models as the c.m energy is varied. This is as seen previously [225]. The right plot shows $\langle p_{\perp} \rangle$ versus \sqrt{s} computed in the IP-Sat and b-CGC models. Here one sees that the results are quite

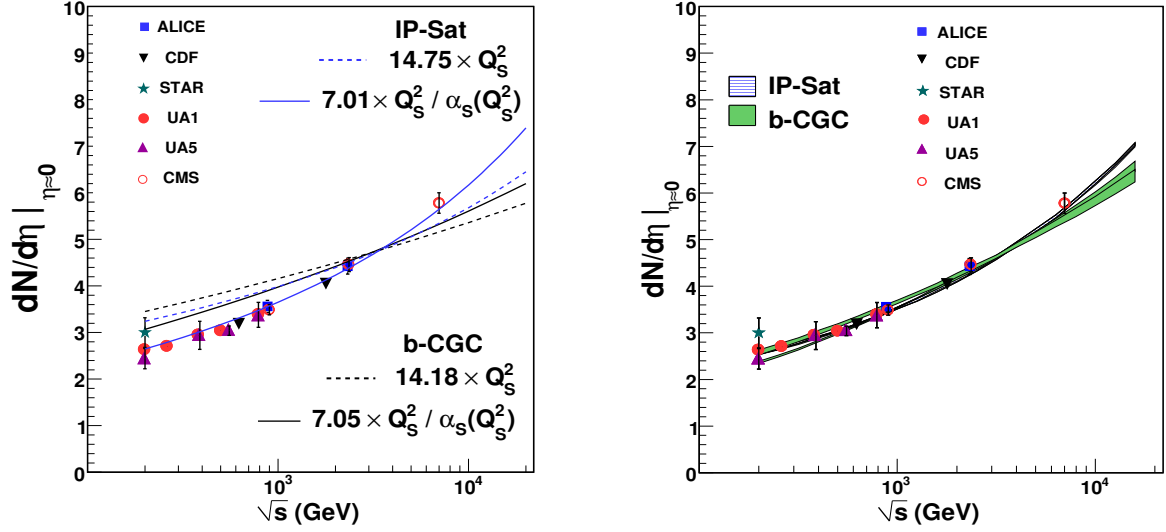


Figure 4.5: Average $dN/d\eta|_{\eta=0}$ in the IP-Sat and b-CGC models. Left: Data plotted as a function of saturation scales Q_S (at median impact parameter $b_{\text{med}} = 2 \text{ GeV}^{-1}$) for both the models determined from the HERA data. Right: Average $dN/d\eta$ at $\eta = 0$ from the k_{\perp} -factorized expression in Eq. 4.24 from IP-Sat (solid green) and b-CGC (dashed) models. Experimental data points are from Ref. [222, 223, 226–228]

sensitive to choice of the infrared cut-off.

Fig. 4.7 shows the η and p_{\perp} distributions computed in the rc-BK model. Only MV initial conditions are considered. In this model, the impact parameter dependence of the inclusive gluon multiplicity is given by

$$\mathcal{T}(b) = \frac{1}{\pi b_{\text{max}}^2} \Theta(b_{\text{max.}} - b) .$$

Therefore $d\bar{N}_g(b)/d\eta = d\bar{N}_g/d\eta \mathcal{T}(b)$, where $b_{\text{max.}}$ is a parameter that can be absorbed in the normalization. If no dependence of $b_{\text{max.}}$ on \sqrt{s} is assumed, the model considerably overestimates the single inclusive data at LHC energies. This is likely a consequence of the fact that the rc-BK doesn't take into account the impact parameter dependence of the saturation scale. In this case, the values for the inclusive gluon multiplicity correspond to the values for the zero impact parameter, which is considerably higher than the minimum bias values. The agreement with data is improved considerably by allowing $b_{\text{max.}}$ to depend on \sqrt{s} . The denominator $\pi b_{\text{max.}}^2$

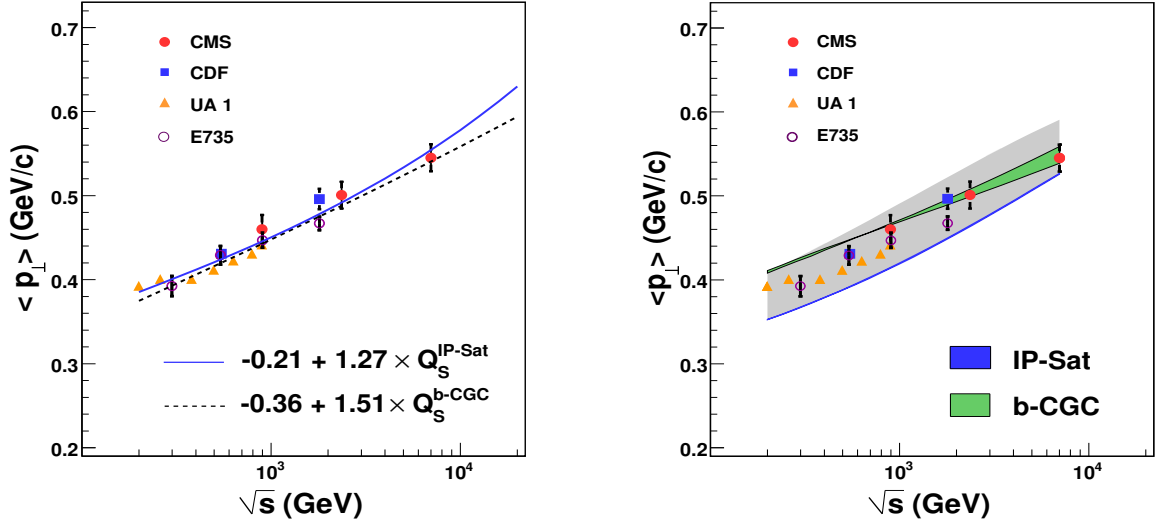


Figure 4.6: Average p_{\perp} obtained from IP-Sat and b-CGC models compared to data. Left: Function of saturation scales fitted for both the models. Right: Average p_{\perp} from the k_{\perp} -factorized expression in Eq. 4.24. The thin (colored) bands correspond to uncertainties arising from different parameters in table 4.1 and table 4.2 and mass term=0.2 GeV. The thick (gray) band shows the sensitivity to variation of mass term in the range 0.2–0.3 GeV (with lower mass corresponding to lower $\langle p_{\perp} \rangle$). Experimental data points are from Ref. [222, 227, 229, 230].

therefore provides an energy dependent normalization. The same approach discussed previously for the IP-Sat model is employed to extract the \sqrt{s} dependence of b_{\max} , chosen to be of the form $b_{\max} = b_0 + C \ln(s)$. From a fit to the average $dN/d\eta$ as a function of energy, one obtains $b_0 \sim 5.6 - 7.55 \text{ GeV}^{-1}$ and $C \sim 0.23 - 0.46$ depending on the choice of infrared cut-off.

In Fig. (4.8), we show the results of the rc BK and IP-Sat models for forward rapidities for RHIC p+p collision at 200 GeV. For both IP-Sat and rcBK we have used an overall normalization extracted from energy dependence of the single inclusive multiplicity of the form: $A/(\pi b_{\max}^2)$ with $b_{\max} = b_0 + C \ln(\sqrt{s})$. This form absorbs the uncertainties in the inelastic cross-section and higher order effects (K -factors). For the IP-Sat (rcBK) model, one finds $A = 0.23(6.15)$, $b_0 = 5.77(5.14)$ and $C = 0.32(0.76)$ using mass term $m = 0.4 \text{ GeV}$ by fitting data points at $\eta = 0$ over the range of energy shown in Fig. 4.14. For rc-BK model the constant term A absorbs the prefactors of Eq. 4.19 which includes unknown overlap area and other terms that cannot be separated from the “K factor”. The results are rather insensitive to the infrared

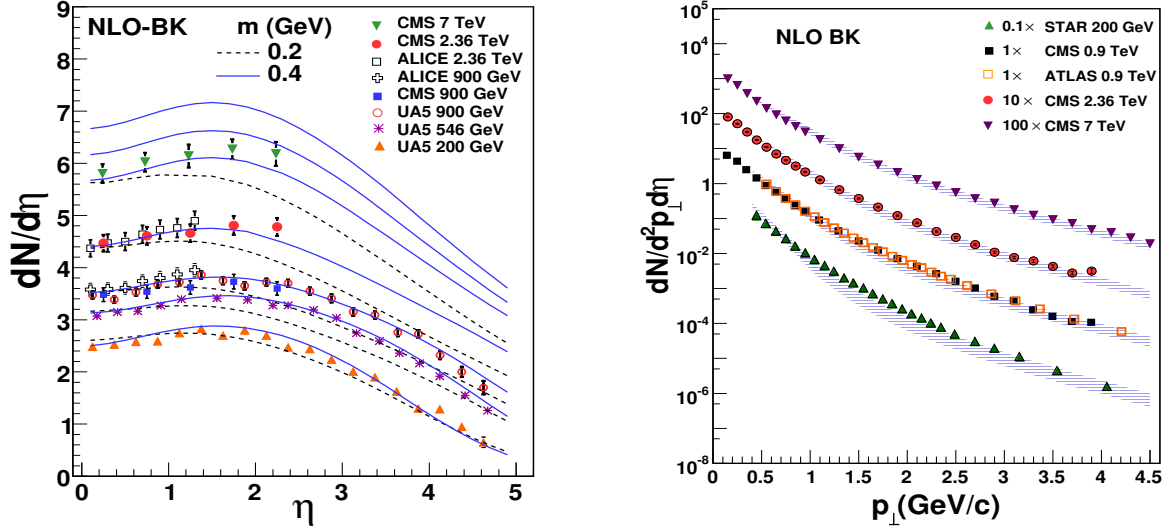


Figure 4.7: Pseudo-rapidity and p_{\perp} distribution in the rc-BK model compared to data. The uppermost two plots in the left panel correspond to predictions for $\sqrt{s} = 14, 10$ TeV with $m = 0.4$ GeV. The p_{\perp} distribution is averaged over the η range of ± 2.4 . The band corresponds to the variation $m = 0.2\text{--}0.4$ GeV in the Jacobian relating η to y .

cut-off m . However, one finds a $\sim 10\%$ variation of the normalization when the constants are extracted by a) fitting the full pseudo rapidity at RHIC energy, b) considering data points from different experiments. This variation, along with the numerical uncertainties, contributes to the gray bands shown in Fig. 4.8. We see that the agreement at forward rapidities is significantly better than our previous comparison to the mid-rapidity distribution; this result provides a good benchmark for computing R_{pA} at RHIC and in predictions of the same for p+Pb collisions at the LHC.

4.5.2 Results for p+A/d+A collisions

In this section we present the results for the min-bias average multiplicity at mid-rapidity using the IP-Sat and rc-BK models for p+A collisions. The result is normalized to the PHOBOS 200 GeV d+Au data [233]. The energy dependence of the average multiplicity is shown in Fig. (4.9), the band corresponds to the variation of m in the range of 0.2-0.4 GeV. Both the models give a comparable energy dependence, with the IP-Sat model giving a slightly higher multiplicity at

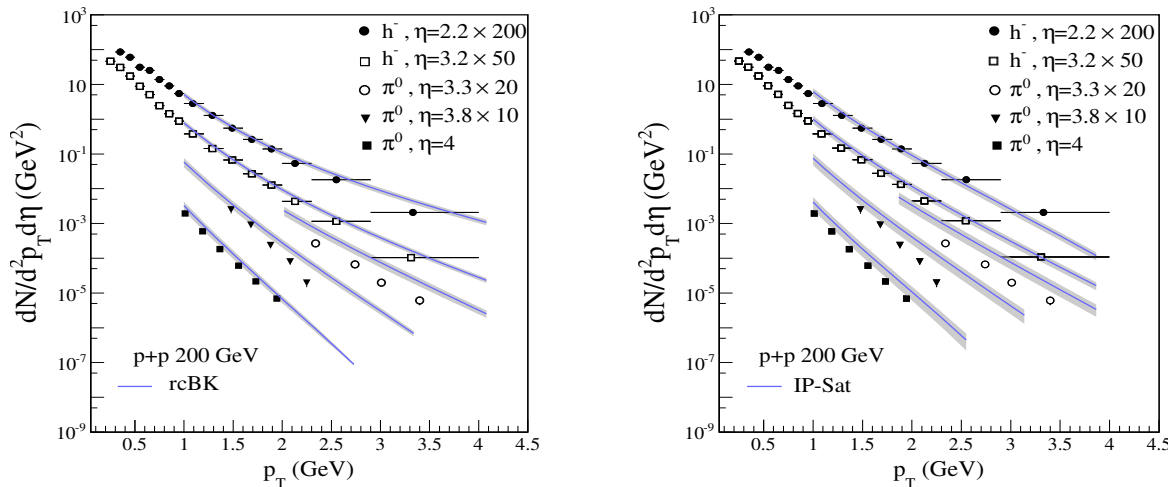


Figure 4.8: Transverse momentum distributions at forward rapidities in rcBK and IP-Sat models compared to STAR [231] and BRAHMS [232] data. The gray bands show the uncertainty in the determination of the normalization constant.

the highest energies. The rapidity distributions at the RHIC energies in the two models and predictions for LHC energies are shown in Fig. 4.10. The models agree with the RHIC data with an accuracy of $\approx 10\%$, which is within the theoretical systematic uncertainty.

Fig. 4.11 shows the transverse momentum distribution using two models as compared to BRAHMS [232] and STAR [231] data at 200 GeV for h^- and π^0 at forward rapidities. For the h^- case, we have included 15% isospin correction in the normalization constant. Predictions for the $p + A$ transverse momentum distributions for charged hadrons at $\eta = 0$ for LHC energies with this fixed normalization are shown in Fig. 4.12.

We show the nuclear modification factor anticipated in $p + A$ collisions at the LHC in the IP-Sat and rcBK models in Fig. 4.13. R_{pA} in both the models, at $\sqrt{s} = 4.4$ TeV/nucleon, approaches unity at $p_{\perp} \sim 5$ GeV. For $\sqrt{s} = 8.8$ TeV/nucleon, the suppression persists to higher p_{\perp} . The slope of R_{pA} however appears quite different in the two models.

For the IP-Sat model in case of $p+A$ collisions, the form of the normalization used is $A/(\pi b_{\max}^2)$ where, $A = 0.25$ with mass term $m = 0.4$ GeV. Unlike $p + p$, here $b_{\max} = 9.5$ fm is a fixed number which is the maximum value of the impact parameter to obtain the minimum

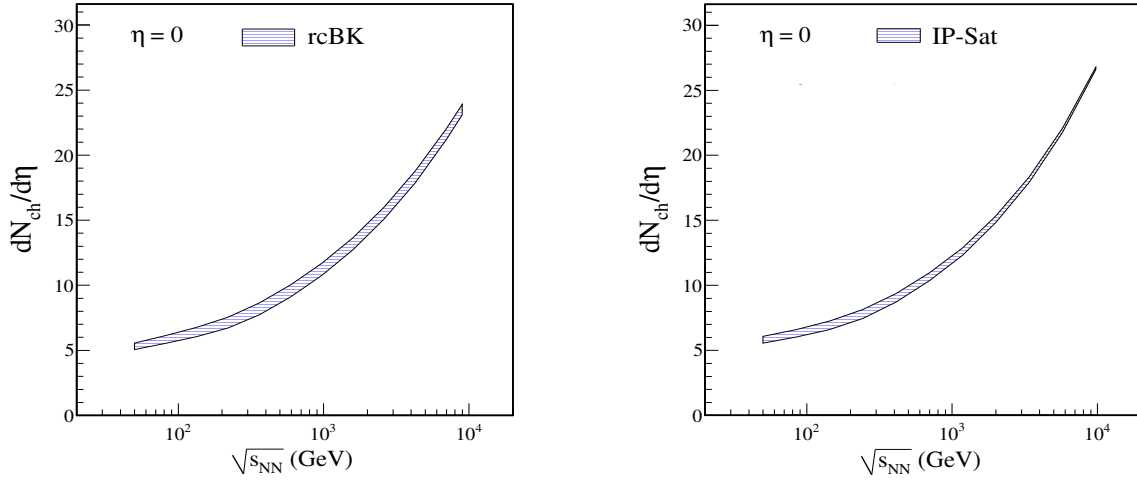


Figure 4.9: Energy dependence of the minimum bias single inclusive multiplicity at $\eta = 0$ in p+A collisions from k_{\perp} -factorized unintegrated distributions determined in the rcBK and IP-Sat models. The distribution is normalized with respect to the PHOBOS d+Au data [233] at 200 GeV. The band represents the uncertainty in the calculation due to the variation of the mass term in the range of 0.2-0.4 GeV.

bias distribution and does not change with energy. For the rc-BK model, a single normalization constant $A = 0.032$ (with $m = 0.4$ GeV) absorbs³ all the constant pre factors of Eq. 4.19. These normalization constants are obtained from a fit to the PHOBOS pseudo rapidity distribution; one obtains an $\sim 8\%$ higher value of A when the fit is performed only to the data points at $\eta = 0$. The BRAHMS data for normalization also gives higher values for A which, along with other numerical uncertainties, contributes to the bands shown in Fig. 4.11. The significant difference in A for IP-Sat and rcBK for d+Au collisions is because the area of overlap and other terms in the pre-factor of kt-factorization are absorbed in A for the rc-BK model and cannot be separated from the “ K factor”. For the IP-Sat model, Eq. (4.20) includes those factors and A is of the order of 1. This apparent difference in the two models does not affect any of our final results since same normalization is consistently used everywhere. In conversion from d+Au to p+A numbers we have used an additional factor of 1.6/2 in the normalization, which is standard in such conversions in

³Eq. 4.19 for min-bias p+A collision the rc-BK model normalization constant includes the pre factor $(\frac{4\alpha_S}{\pi C_F (2\pi)^5} \frac{S_{p,A}}{(\pi R_p^2)(\pi R_A^2)})$; here R_p, R_A corresponds to the radii of the proton and nucleus and $S_{p,A}$ is the overlap area.

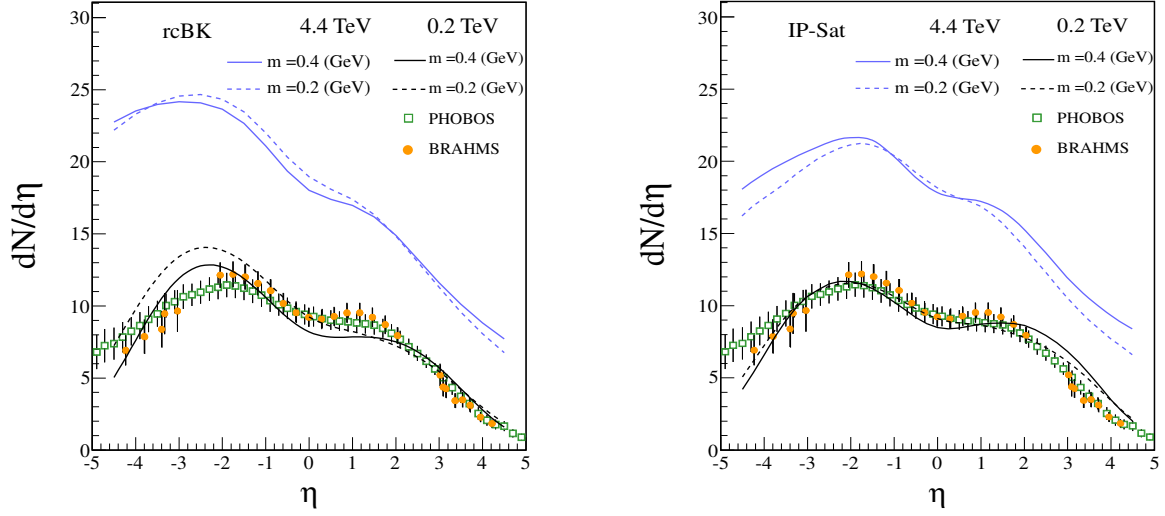


Figure 4.10: Pseudo-rapidity distribution for minimum-bias p+A collision at RHIC and LHC energies. Prediction from rcBK shown for mass term $m=0.2$ and 0.4 GeV. Data points are from ref. [233, 234]

the literature. In computing R_{pA} , the result depends on N_{coll} , which is sensitive to the proton inelastic cross-section. Since $b_{\text{max,proton}}$ grows with energy, one finds for the energies $\sqrt{s} = 4.4, 8.8$ TeV that ratio $b_{\text{max,proton}}^2(8.8\text{TeV})/b_{\text{max,proton}}^2(4.4\text{TeV}) \sim N_{\text{coll}}(8.8\text{TeV})/N_{\text{coll}}(4.4\text{TeV})$, a result consistent with expectations of N_{coll} from Glauber approaches [235]; numbers quoted are in agreement with our ratio to 5%.

4.5.3 Results for A+A collisions

For a large nucleus, in the IP-Sat model, we can approximate the dipole-nucleus cross section to be

$$\frac{d\sigma_{\text{dip}}^A}{d^2\mathbf{s}_{\perp}} \approx 2 \left[1 - \exp \left\{ -\frac{AT_A(\mathbf{s}_{\perp})}{2} \sigma_{\text{dip}}^p(\mathbf{r}_{\perp}, x) \right\} \right] \quad (4.25)$$

where $\sigma_{\text{dip}}^p(\mathbf{r}_{\perp}, x)^p$ is obtained from integrating the dipole-proton cross section in Eq. (4.4) over the impact parameter distribution in the proton. This form of the dipole-nucleus cross-section was shown previously [236] to give reasonable fits to the limited available fixed target e+A inclusive data. The initial conditions for rcBK evolution for a nucleus were similarly fixed by

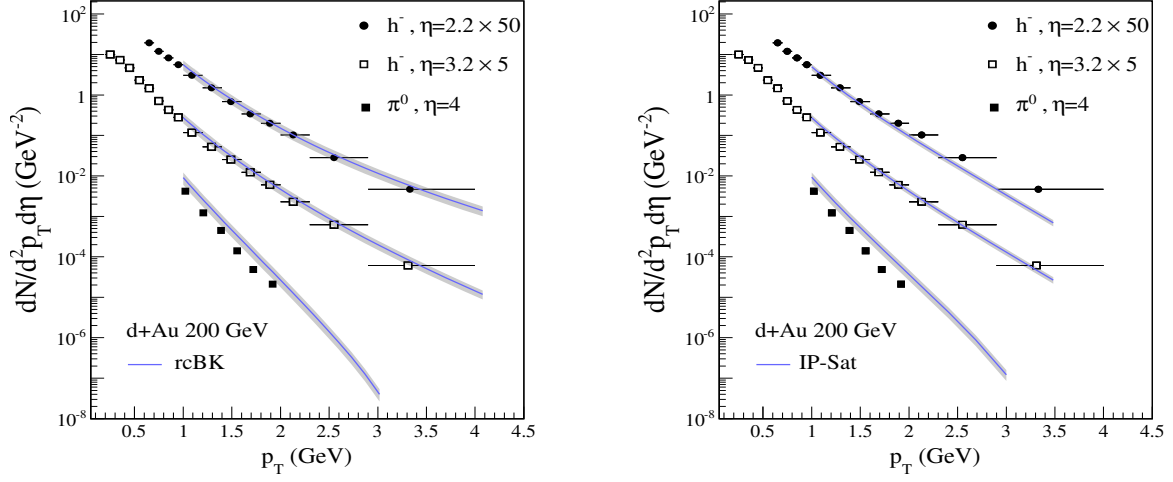


Figure 4.11: Transverse momentum distribution at forward rapidity at the highest RHIC energy and compared to STAR [231] and BRAHMS [232] data. The gray bands show the uncertainty in determination of normalization constant from various sources.

comparisons to the e+A data [237].

Substituting the expression for the dipole-nucleus cross-section in eqs. (4.19), and likewise the latter in (4.20), one can compute the nuclear multiplicity distributions. The infrared divergence in the multiplicity distribution is regulated in exactly the same way as was the case for the p+p multiplicity distribution, by replacing p_{\perp} by $m_{\perp} = \sqrt{p_{\perp}^2 + m^2}$, with m varied between 0.2-0.4 GeV. Wherever we have considered fixed coupling, we have used $\alpha_S=0.2$; for the running coupling case, we run α_S with the scale $Q_S = \max. \{Q_S(x_1, s_{\perp}), Q_S(x_2, s_{\perp} - \mathbf{b}_{\perp})\}$.

Fig. (4.14) shows the energy dependence of average multiplicity for most central Au+Au collision for fixed and running coupling in the IP-Sat model. The number of participants⁴ at a given impact parameter is determined from the Glauber relation [238]

$$N_{part}(\mathbf{b}_{\perp}) = A \int T_A(\mathbf{s}_{\perp}) \{1 - [1 - T_B(\mathbf{s}_{\perp} - \mathbf{b}_{\perp})\sigma_{NN}]^B\} d^2\mathbf{s}_{\perp} + B \int T_B(\mathbf{s}_{\perp}) \{1 - [1 - T_A(\mathbf{s}_{\perp} - \mathbf{b}_{\perp})\sigma_{NN}]^A\} d^2\mathbf{s}_{\perp} \quad (4.26)$$

The results shown in Fig. (4.14) are for 0-6% centrality, which corresponds to a median $\mathbf{b}_{\perp} \approx 12.2$

⁴In this expression, $\sigma_{NN} \sim 62$ mb for 2.76 TeV and $\sigma_{NN} \sim 41$ mb at 200 GeV.

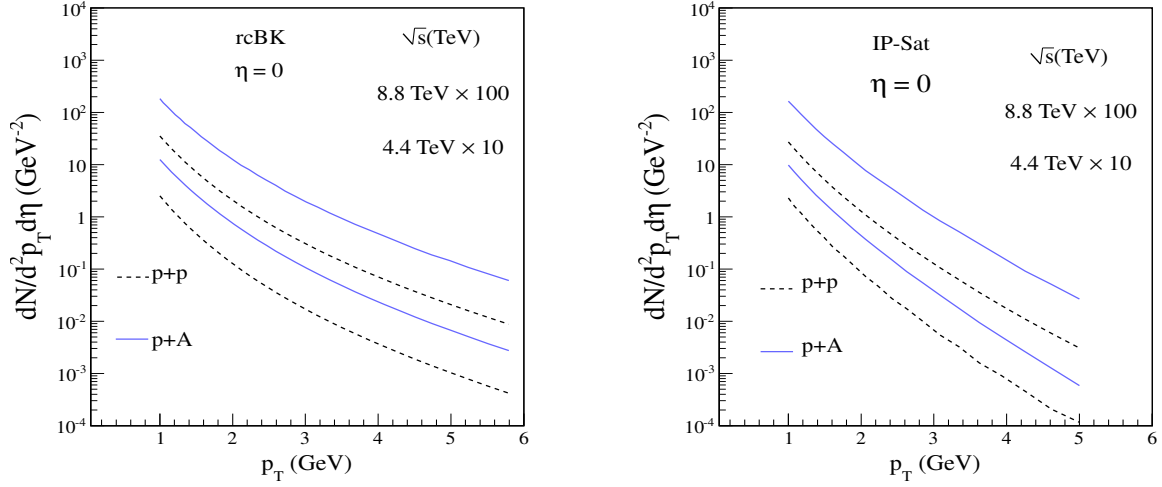


Figure 4.12: Transverse momentum distribution at mid-rapidity for minimum-bias p+p and p+A collisions..

GeV^{-1} ; we compute $\frac{dN_{\text{ch.}}(\mathbf{b}_{\perp})}{d\eta}$ and $N_{\text{part}}(\mathbf{b}_{\perp})$ for this median value. We observe that a fairly good agreement with data is obtained for the infrared cut-off given by $m = 0.4 \text{ GeV}$. The prescription for the running coupling gives a variation that corresponds to a 20% uncertainty at lower energies, which decreases significantly at higher energies.

We calculate the centrality dependence of the multiplicity at RHIC ($\sqrt{s} = 200 \text{ GeV}$) and LHC ($\sqrt{s} = 2.76 \text{ TeV}$) in the IP-Sat model. While the agreement of the model with data shown in Fig. (4.15) is reasonably good for the most central collisions, a systematic deviation is seen for lower centralities, and the model underpredicts the data. While within the range of the theoretical uncertainties outlined thus far, this systematic discrepancy leaves significant room for final state entropy production, which is expected to be more significant for more peripheral collisions. See for instance Refs. [245, 246] that estimate the amount of entropy production. As the right plot of Fig. (4.15) shows, running coupling effects are less important for the most central collisions but introduce significant uncertainties relative to the fixed coupling results for more peripheral collisions.

Fig. (4.16) shows the pseudo-rapidity distributions in the IP-Sat model compared to data for Au+Au collisions at 200 GeV (PHOBOS) and Pb+Pb collisions at 2.76 TeV (ALICE and CMS).

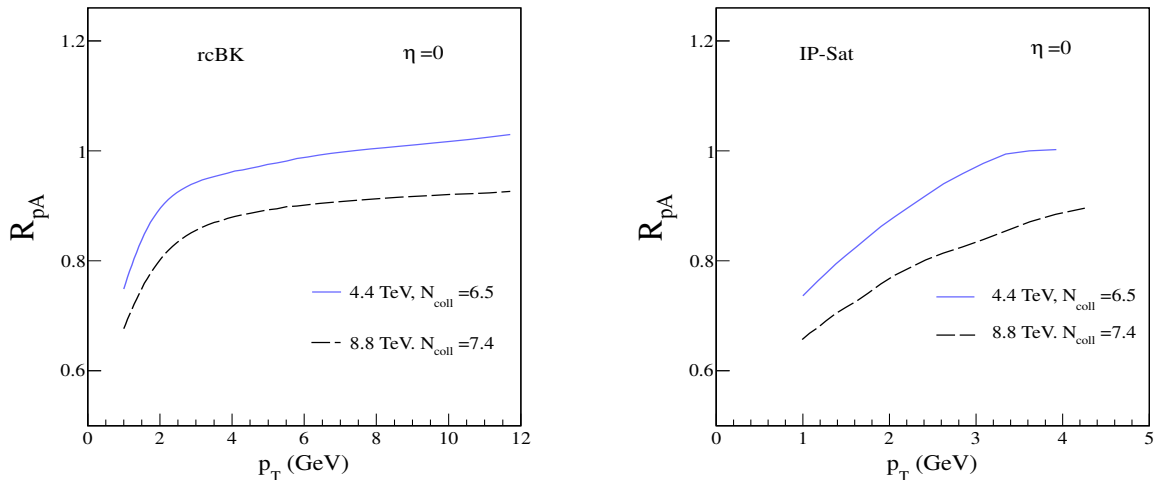


Figure 4.13: Nuclear modification factor for charged hadrons at mid-rapidity of the centre of mass frame for p+A collisions at LHC energies.

Firstly, one sees that the results are sensitive to the infrared cut-off, with improved agreement seen for $m = 0.4$ GeV. Further, the rapidity distributions are sensitive to the extrapolation of the model to larger $x \geq 0.01$ values. We also note that a significantly better fit to the data at higher energies is obtained by including running coupling effects.

4.5.4 Multiplicity fluctuation in the perturbative framework

There are several sources of multiplicity fluctuations in high energy hadronic collisions. These can arise from fluctuations in the number of wee partons, in their distribution with impact parameter and their distribution in rapidity [251]. For further discussion we will consider particle production in a relatively small rapidity window (parametrically of order $\Delta\eta \leq 1/\alpha_S$), so fluctuations in rapidity will not be an important source of fluctuations. Let us first consider fluctuations in multiplicity for a fixed impact parameter. In this case, the CGC framework allows for a systematic treatment of inclusive multi-particle production [252] in the Glasma [253]. The largest contribution to multi-particle production comes from diagrams that appear superficially disconnected, but are connected by averaging over color correlations in an event and over all events. This is the formal basis of the Glasma flux tube picture [254], and was previously used

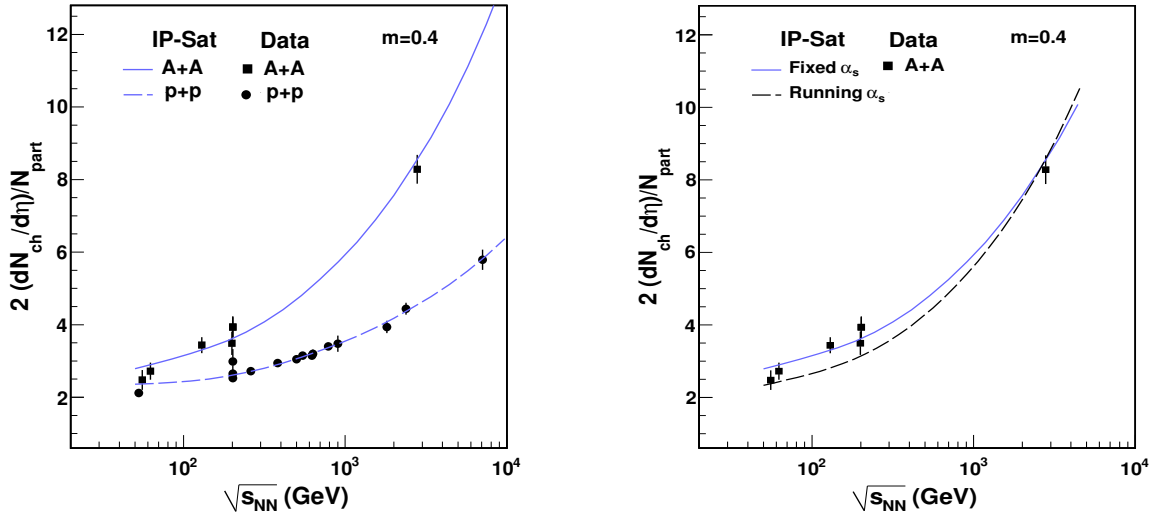


Figure 4.14: Left: Energy dependence of the multiplicity per participant pair in the IP-Sat model for p+p and A+A collisions. For the A+A case, the calculation is done for the 0 – 6% centrality. Right: same plot for A+A with fixed (solid) and running (dashed) coupling. Data points for p+p are from ref. [239–242] and for A+A from ref. [243, 244]

to compute backward-forward correlations [255, 256], two particle correlations [212, 254], three particle correlations [257], and n-particle correlations [40]. The n-particle correlations is relevant for the description of multiplicity fluctuations. It can be shown that, in LO the n-particle correlations obtained by averaging over color sources in the CGC picture are those that would be generated by a negative binomial distribution [40].

The negative binomial distribution (NBD) is given by

$$P_n^{\text{NB}}(\bar{n}, k) = \frac{\Gamma(k+n)}{\Gamma(k)\Gamma(n+1)} \frac{\bar{n}^n k^k}{(\bar{n}+k)^{n+k}}. \quad (4.27)$$

NBD is characterized by two parameters, the mean multiplicity \bar{n} and the parameter k . As is well known, in the limit $k \rightarrow \infty$, this distribution reduces to the Poisson distribution. In the limit $k \rightarrow 1$, one obtains the Bose-Einstein distribution. The variance of the distribution is given by $\sigma^2 = \bar{n}^2 - \bar{n}^2 = \bar{n} + \bar{n}^2/k$. In the Glasma flux tube approach, k is not an arbitrary parameter;

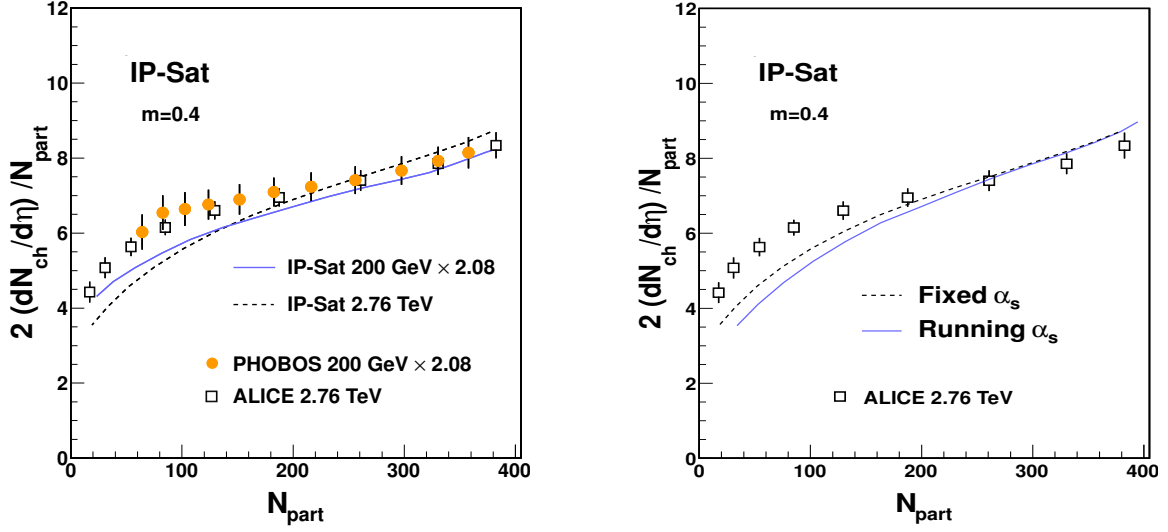


Figure 4.15: Centrality dependence of the inclusive multiplicity in the IP-Sat model compared to RHIC [247] and LHC [248] data. Left: (fixed coupling) 200 GeV values for both data and model are multiplied by a factor 2.08. Right: Same plot comparing running (solid curve) and fixed coupling (dashed curve) results in the IP-Sat model.

instead, it is computed to be

$$k = \zeta \frac{(N_c^2 - 1) Q_S^2 S_\perp}{2\pi}, \quad (4.28)$$

where ζ is a dimensionless non-perturbative parameter which will be discussed in detail in the next sections. S_\perp is the overlap area of the two hadrons.

As we mentioned previously, the negative binomial distribution is obtained at a fixed impact parameter, so $\bar{n} \equiv \bar{n}(b)$ and $k \equiv k(b)$. In particular, the latter parameter must be interpreted as being proportional to the number of flux tubes (or interacting “hot spots”) $S_\perp/1/Q_S^2$ at a given impact parameter. Because Q_S^2 grows with energy, k has a very particular energy dependence. Here, the parameter k in Eq. 4.28 is determined as follows. For a given impact parameter, we define

$$Q_S^2 S_\perp = \int d^2 x_\perp Q_S^2(x_\perp),$$

where the integral on the r.h.s is performed over the overlap area of the two protons at a given parameter. At each given transverse position x_\perp in the overlap area, we choose $Q_S(x_\perp) =$

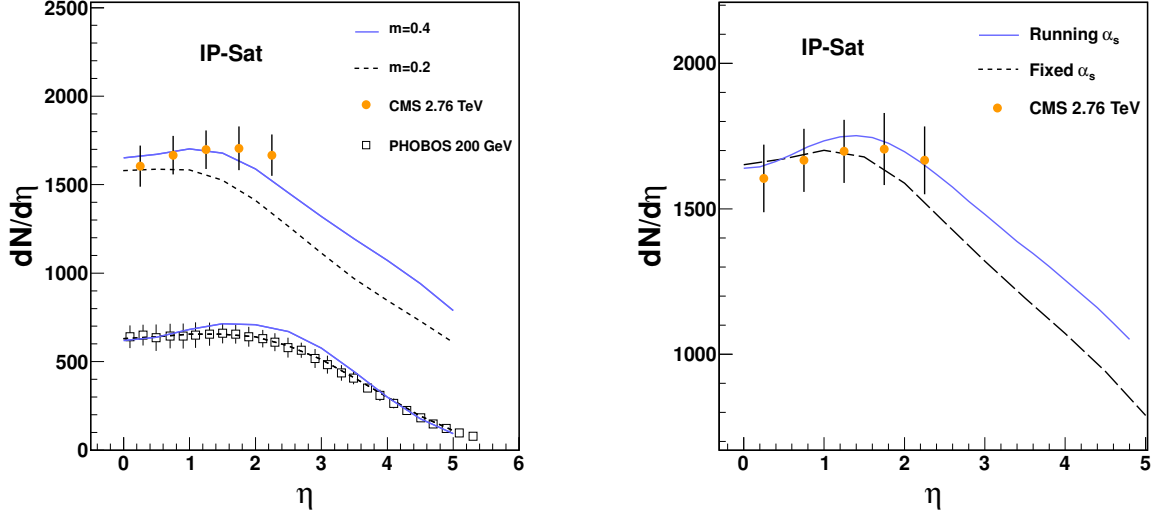


Figure 4.16: Pseudo-rapidity distribution from \mathbf{k}_\perp -factorization formula. Left: fixed coupling results for 200 GeV and 2.76 TeV. Right: Same plot ($m=0.4$) at 2.76 TeV with running (solid curve) and fixed coupling (dashed curve) in \mathbf{k}_\perp -factorization formula. Data points are from ref. [249, 250]

$\min. \{Q_S^A, Q_S^B\}$, where Q_S^A and Q_S^B are respectively the saturation scales of the two colliding protons at that x_\perp . This choice is motivated by the fact that the inclusive multiplicity of produced gluons is much more sensitive to the smaller of the two saturation scales [260]. In Fig. 4.17 (left) we plot the saturation scale as a function of \sqrt{s} for different impact parameters. The right plot has on the y -axis the quantity that appears in Eq. 4.28 determined by the procedure we described. We observe that a stronger dependence of this quantity is seen for the b-CGC model. With the exception of the parameter ζ , we have everything necessary to compute Eq. 4.27 at a given impact parameter.

Fluctuations in impact parameter are treated as follows. The overlap function for two protons at a given impact parameter (see Fig. 4.2 (right)) can be expressed as

$$T_{pp}(\mathbf{b}_\perp) = \int d^2\mathbf{s}_\perp T_p(\mathbf{s}_\perp) T_p(\mathbf{s}_\perp - \mathbf{b}_\perp) \quad (4.29)$$

where T_p is given for instance in the IP-Sat model by Eq. 4.11. Our knowledge of the HERA

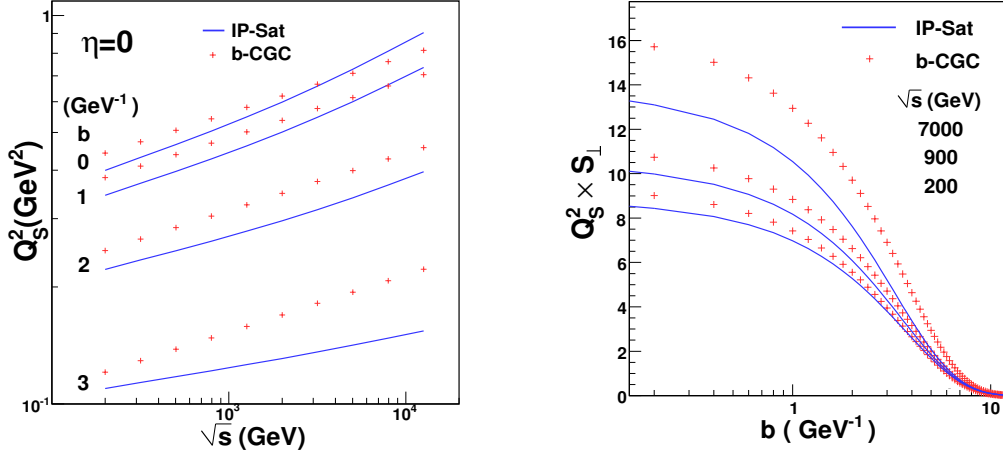


Figure 4.17: Left: Variation of the saturation scale with the collision energy. Right: Variation of $Q_s^2 S_\perp$ for different impact parameters and the c.m. energy of the collision. The solid lines are for the IP-Sat model and crosses for the b-CGC model, in each case for the parameters providing the best fit to the HERA data.

diffractive data therefore allows one to compute T_{pp} in the saturation models. The probability distribution for an inelastic collision at a given impact parameter is given in impact parameter eikonal models as [261–263]

$$\frac{dP_{\text{inel.}}^{\text{eik.}}}{d^2\mathbf{b}_\perp} = \frac{1 - \exp(-\sigma_{gg} T_{pp})}{\int d^2\mathbf{b}_\perp (1 - \exp(-\sigma_{gg} T_{pp}))}. \quad (4.30)$$

In general, σ_{gg} is an energy dependent quantity estimated to be the elementary cross-section for gluon-gluon scattering. Alternately, in the \mathbf{k}_\perp -factorization framework, an estimate for this quantity without involving any additional parameters is

$$\frac{dP_{\text{inel.}}^{\text{dip.}}}{d^2\mathbf{b}_\perp} = \frac{\frac{dN_g}{dy}(\mathbf{b}_\perp)}{\int d^2\mathbf{b}_\perp \frac{dN_g}{dy}(\mathbf{b}_\perp)}. \quad (4.31)$$

This expression becomes unity when both sides are integrated over impact parameter. The result for $2\pi b \frac{dP_{\text{inel.}}^{\text{dip.}}}{d^2\mathbf{b}_\perp}$ at a fixed $\sqrt{s} = 900$ GeV is shown in Fig. 4.18 and is a sharply peaked distribution at ~ 3 GeV $^{-1}$. The distribution plotted is insensitive to \sqrt{s} and to the infrared scale m .

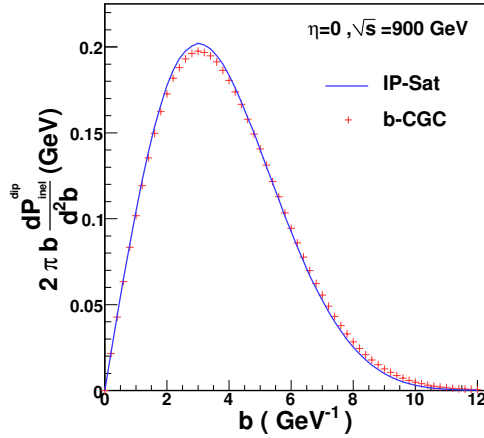


Figure 4.18: Probability distribution as a function of impact parameter for an inelastic collision computed using Eq. 4.31 for the b-CGC and IP-Sat models.

With the stated assumptions we compute the probability distribution as a function of multiplicity. By convolving the probability distribution for producing n particles at a given impact parameter (Eq. 4.27) with the probability for an inelastic collision at that impact parameter (from Eq. 4.31), one obtains the expression

$$P(n) = \int d^2\mathbf{b}_\perp \frac{dP_{\text{inel.}}}{d^2\mathbf{b}_\perp} P_n^{\text{NB}}(\bar{n}(\mathbf{b}_\perp), k(\mathbf{b}_\perp)) \quad (4.32)$$

The results for this quantity are shown in Fig. 4.29(a). Note that since the input here is the average inclusive multiplicity at a given impact parameter (as opposed to the minimum bias inclusive multiplicity that was compared to data), this quantity needs to be normalized as well. We do so by fitting the multiplicity distribution corresponding to the lowest energy UA5 data set at $\sqrt{s} = 200$ GeV for the normalization of \bar{n} . In the b-CGC model, a fit of the overall normalization to the single inclusive minimum bias distribution at a given energy gives the same value (to an accuracy of $< 5\%$) as that obtained for the same quantity if fit to the multiplicity distribution instead. In the IP-Sat model, one obtains the same normalization constant if $b_{\text{max.}} = 2b_{\text{rms.}}$. If one chooses the form $b_{\text{max.}} = b_0 + C \ln(s)$ we described previously, there is a 60% discrepancy between the two choices of fixing the normalization. The agreement

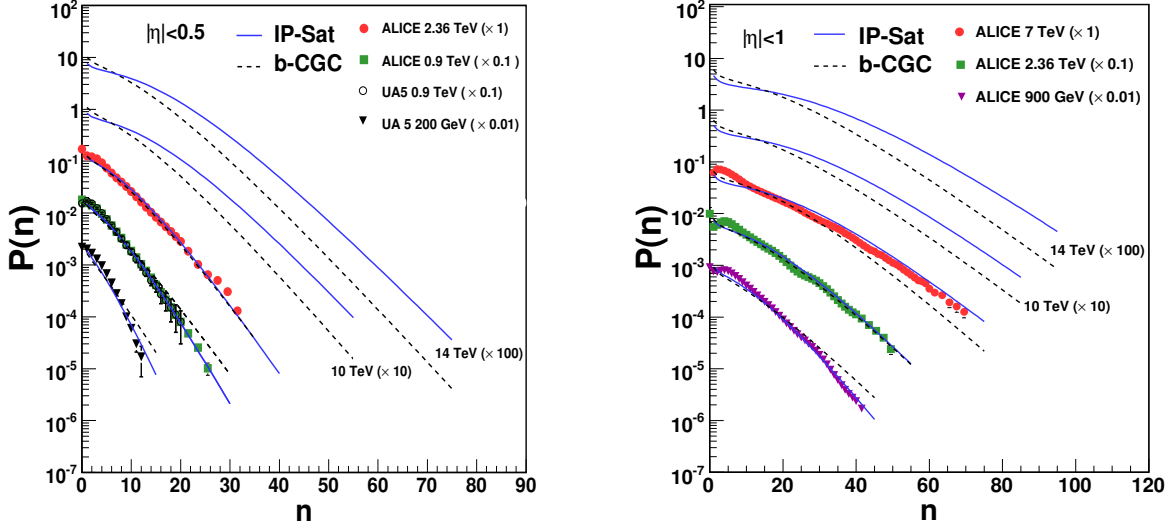


Figure 4.19: Probability distribution of the gluon multiplicity computed in the IP-Sat model (parameter set I) and the b-CGC model (parameter set II) compared to the UA5[265] and ALICE[226] data for different η ranges. Left: Multiplicity distribution for the η range ± 0.5 . Right: Multiplicity distribution for the η range ± 1 .

between data and model is remarkably good for IP-Sat distribution for all energies and rapidity cuts. For the b-CGC model, the agreement with data for $|\eta| < 0.5$ is quite good for the 2.36 TeV ALICE data [226] but shows deviations at other energies at the highest multiplicities.

An important point regarding the comparison of the models to data in Fig. 4.29(a) concerns the magnitude of the parameter ζ in Eq. 4.28 which is fit to the data. In the b-CGC model, it is extracted to be 0.25 and it is 0.35 in the IP-Sat model. Estimation of this quantity in non-perturbative framework will be discussed in the next section.

We employ Eq. (4.32) to compute the multiplicity distribution in A+A collisions. While Eq. (4.27) is computed identically to the p+p case, we need to determine the impact parameter distribution differently from the prescription used for the p+p case in Eq. (4.31). The expression

$$\frac{dP_{\text{inel.}}}{d^2\mathbf{b}_{\perp}} = \frac{1 - (1 - \sigma_{\text{NN}}T_{\text{AB}})^{AB}}{\int d^2\mathbf{b}_{\perp} (1 - (1 - \sigma_{\text{NN}}T_{\text{AB}})^{AB})}, \quad (4.33)$$

gives a better description of the impact parameter distribution in A+A collisions. As in the

computation of N_{part} , $\sigma_{\text{NN}} \sim 62$ (41) mb for 2.76 (0.2) TeV, is standard and not varied. The saturation scale in this computation is determined at the median value of the impact parameter $\mathbf{b}_{\perp}^{\text{med.}} = 15 \text{ GeV}^{-1}$. With these assumptions, the only parameters in computing $P(n)$ are m and ζ , the parameter controlling the width of the multiplicity distributions. In Fig. (4.20) (left) we see that the multiplicity distributions are insensitive to variations in m . Fig. (4.20) (right) shows the result of varying $\zeta = 0.01$ -1. Interestingly, we find that the best fit is found for the value of $\zeta = 0.155$ that also gives the best fit to the $p + p$ data.

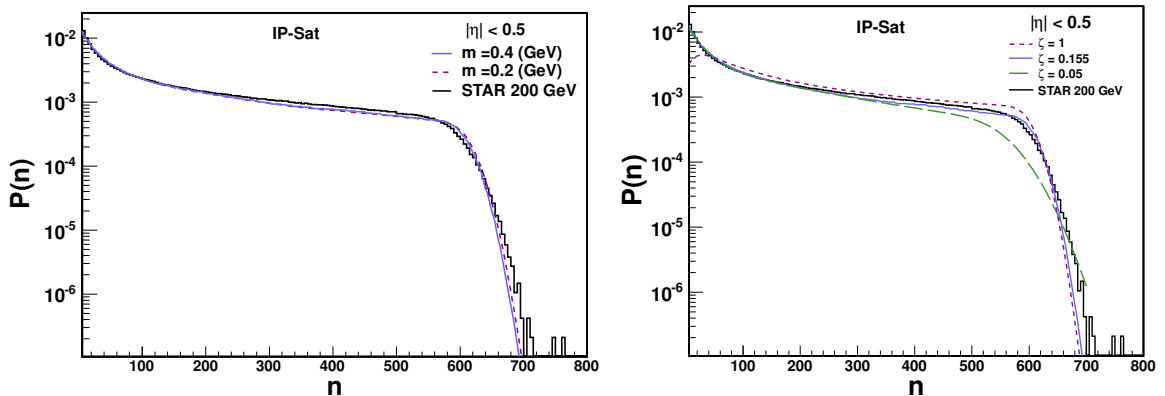


Figure 4.20: Left: Multiplicity distribution for Au+Au collisions in the IP-Sat model compared to uncorrected data (histogram [243]) for different values of m . Both data and model plots are normalized for better comparison. Right: Multiplicity distribution for Au+Au collisions at 200 GeV and its sensitivity to the non-perturbative constant ζ .

4.6 Particle production : Non-perturbative approach

In this section we discuss the computation of multiplicity in a non-perturbative approach by combining the IP-Sat (Impact Parameter Saturation Model) model [266, 267] of high energy nucleon (and nuclear) wavefunctions with the classical Yang-Mills (CYM) dynamics of the Glasma fields produced after the heavy-ion collision [268–270, 272, 274, 275]. We call this newly developed framework as the IP-Glasma (Impact Parameter Dependent Glasma) model. A detailed description of the IP-Glasma model can be found in [276–278]. Parameters of IP-Glasma model are constrained by global fits to the HERA data.

In the IP-Glasma model we use the impact parameter dependent dipole saturation model (IP-Sat) to extract the nuclear saturation scale in the colliding nuclei. The proton-dipole scattering matrix of Eq. 4.5 is

$$S_{\text{dip}}^p(\mathbf{r}_\perp, x, \mathbf{b}_\perp) = \exp\left(-\frac{\pi^2}{2N_c} \mathbf{r}_\perp^2 \alpha_S(\tilde{\mu}^2) x g(x, \tilde{\mu}^2) T_p(\mathbf{b}_\perp)\right) \quad (4.34)$$

Here the gluon density at the transverse distance \mathbf{b}_\perp from the centre of the proton is parametrized using the Gaussian thickness profile $T_p(\mathbf{b}_\perp)$. The momentum scale $\tilde{\mu}$ is related to dipole size \mathbf{r}_\perp as $\tilde{\mu}^2 = 4/\mathbf{r}_\perp^2 + \mu_0^2$. The parameters μ_0 and the width of the Gaussian profile $T_p(\mathbf{b}_\perp)$ and the gluon distribution $xg(x, \tilde{\mu}^2)$ at scale μ_0 are obtained from the fits to HERA data. $xg(x, \tilde{\mu}^2)$ is evolved from μ_0 to $\tilde{\mu}$ using LO DGLAP evolution. The dipole-nucleus scattering matrix can be expressed in terms of the product of individual dipole-nucleon scattering matrices as

$$S_{\text{dip}}^A(\mathbf{r}_\perp, x, \mathbf{b}_\perp) = \prod_{i=0}^A S_{\text{dip}}^p(\mathbf{r}_\perp, x, \mathbf{b}_\perp - \mathbf{b}_i) \quad (4.35)$$

Here \mathbf{b}_i denotes the positions of individual nucleons which are distributed according to the Fermi distribution (Woods-Saxon) inside a nucleus [279] given by

$$\rho(r, \theta) = \frac{\rho_0}{1 + \exp([r - R'(\theta)]/a)}, \text{ with } R'(\theta) = R [1 + \beta_2 Y_2^0(\theta) + \beta_4 Y_4^0(\theta)],$$

where ρ_0 denotes the nucleon density at the center of the nucleus. The spherical harmonic functions $Y_l^m(\theta)$ and the parameters β_2 and β_4 account for the deformation from the spherical shape. For a perfectly spherical nucleus $\beta_2 = \beta_4 = 0$. The nuclear saturation scale at a given transverse position \mathbf{b}_\perp inside the nucleus $Q_S(\mathbf{b}_\perp, x)$ is determined using the condition $S_{\text{dip}}^A(\mathbf{r}_\perp = r_S, x, \mathbf{b}_\perp) = \exp(-1/2)$ with $Q_S^2 = 2/r_S^2$. The saturation scale at a given \sqrt{s} and at transverse position \mathbf{b}_\perp is obtained by self-consistently solving $x = Q_S(\mathbf{b}_\perp, x)/\sqrt{s}$. The transverse distribution of $Q_S(\mathbf{b}_\perp, \sqrt{s})$ generates the lumpy distribution of color charge density $g^2\mu(\mathbf{b}_\perp, \sqrt{s})$ in the colliding nuclei as shown in Fig. 4.21(a). The factor relating Q_S and $g^2\mu$ has

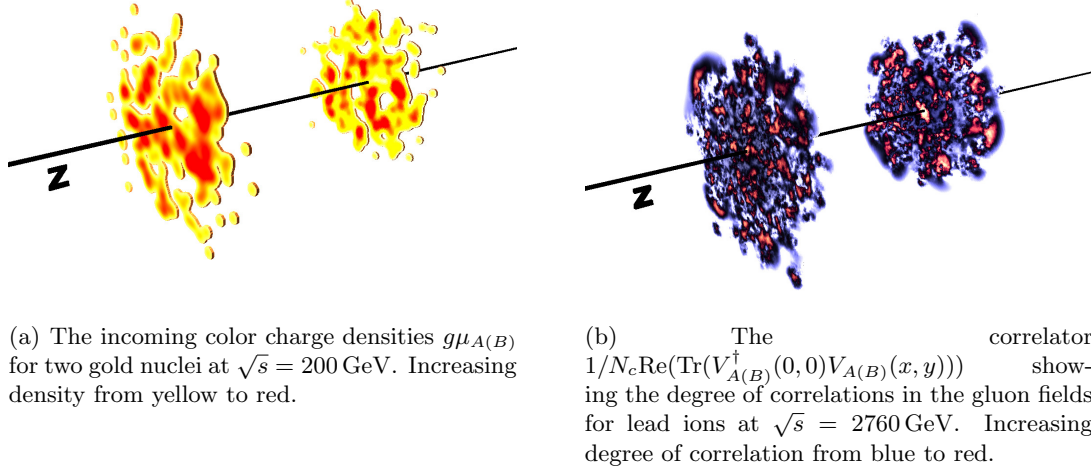


Figure 4.21: Initial state geometry and correlation in the colliding nuclei.

been computed numerically [280], in our model it is tuned to adjust the normalization between data and the calculated multiplicity at $\tau = 0.4$. An average ratio $Q_S/g^2\mu = 0.65$ provides good fit to the centrality dependence of average multiplicity in $Au + Au$ collisions at 200 GeV [278]. For smaller sized systems, additional fluctuation leading to event-by-event variation of this ratio has to be included [278]. To avoid numerical noise the value of $g^2\mu(\mathbf{b}_\perp, \sqrt{s})$ is set to zero at a distance $r_{max} \approx 1.2$ fm from the center of a nucleon. The sensitivity due to the variation of r_{max} on the final state observables are discussed in [278].

Random distribution of color charge $\rho^a(\mathbf{x}_\perp)$ on the transverse plane of the colliding nuclei is sampled from the Gaussian distribution

$$\langle \rho_{A(B)}^a(\mathbf{x}_\perp) \rho_{A(B)}^b(\mathbf{y}_\perp) \rangle = g^2 \mu_{A(B)}^2(\sqrt{s}, \mathbf{x}_\perp) \delta^{ab} \delta^{(2)}(\mathbf{x}_\perp - \mathbf{y}_\perp). \quad (4.36)$$

The sampled color charge distribution generates the color current $J^\nu = \delta^{\nu\pm} \rho_{A(B)}(x^\mp, \mathbf{x}_\perp)$ which⁵ according to the MV model [192] acts as the source for classical Glasma gluon fields. The

⁵here we assume a gauge $A^\mp = 0$

classical gluon fields in each nucleus are obtained by solving the Yang-Mills equations

$$[D_\mu, F^{\mu\nu}] = J^\nu. \quad (4.37)$$

Solution of Eq. (4.37) in Lorentz gauge $\partial_\mu A^\mu = 0$ can be written as

$$A_{A(B)}^\pm = -\frac{\rho_{A(B)}(x^\mp, \mathbf{x}_\perp)}{\nabla_\perp^2 + m^2}, \quad (4.38)$$

where the infra-red regulator $m \sim \Lambda_{QCD}$ is introduced to incorporate color confinement at the nucleon level. $m = 0.1$ GeV provides the best fit to RHIC Au+Au data. Variation of m affects the centrality dependence of multiplicity, a detailed study can be found in ref.[278]. The solution of Eq. 4.38 can be transformed to light-cone gauge $A^+(A^-) = 0$ as, [191, 192, 281]

$$A_{A(B)}^i(\mathbf{x}_\perp) = \theta(x^-(x^+)) \frac{i}{g} V_{A(B)}(\mathbf{x}_\perp) \partial_i V_{A(B)}^\dagger(\mathbf{x}_\perp), \quad (4.39)$$

$$A^-(A^+) = 0. \quad (4.40)$$

where $V_{A(B)}$ are path-ordered Wilson lines in the fundamental representation. Fig. 4.21(b) shows the quantity $1/N_c \text{Re}(\text{Tr}(V_{A(B)}^\dagger(0,0)V_{A(B)}(x,y)))$ (for a given configuration of two colliding nuclei) which is the measure of the correlation in the gluon fields between two points $((0,0)$ and (x,y)), which is again related to the dipole-nucleus amplitude defined in Eq. 4.4. The Glasma fields at time $\tau = 0$ is given by the solution of classical Yang-Mills equations in Fock-Schwinger gauge $A^\tau = (x^+ A^- + x^- A^+)/\tau = 0$. In this gauge, the fields after collision are expressed in

terms of the fields of the colliding nuclei as

$$A^i = A_{(A)}^i + A_{(B)}^i, \quad (4.41)$$

$$A^\eta = \frac{ig}{2} [A_{(A)}^i, A_{(B)}^i], \quad (4.42)$$

$$\partial_\tau A^i = 0, \quad (4.43)$$

$$\partial_\tau A^\eta = 0 \quad (4.44)$$

The Glasma fields are evolved in time τ according to Eq. 4.37.

We follow the numerical implementation of [272, 274, 275] for solving Eq. 4.37 on a 2+1 dimensional lattice. The details of this implementation in our model can be found in Ref. [277]. The path ordered integral of Eq. 4.39 is estimated by discretizing the longitudinal direction (x^\mp) in $N_y = 100$ steps as

$$V_{A(B)}(\mathbf{x}_\perp) = \prod_{k=1}^{N_y} \exp \left(-ig \frac{\rho_k^{A(B)}(\mathbf{x}_\perp)}{\nabla_\perp^2 + m^2} \right) \quad (4.45)$$

Choosing a value of $N_y \leq 50$ would affect the absolute normalization of multiplicity [278].

Since in Fock–Schwinger gauge ($A^\tau = 0$) the gauge links in temporal direction become unit matrices, the evolution of the Glasma fields in τ are performed by solving discretized Hamilton’s equations. Once the field tensor is known the stress energy tensor $T^{\mu\nu}$ at each transverse position is calculated at a given τ from the relation

$$T^{\mu\nu} = -g^{\mu\alpha} g^{\nu\beta} g^{\gamma\delta} F_{\alpha\gamma} F_{\beta\delta} + \frac{1}{4} g^{\mu\nu} g^{\alpha\gamma} g^{\beta\delta} F_{\alpha\beta} F_{\gamma\delta} \quad (4.46)$$

The transverse distribution of energy density $\epsilon(\mathbf{x}_\perp, \tau)$ in the fluid’s rest frame and the flow velocity are obtained by solving $u_\mu T^{\mu\nu} = \epsilon u^\nu$.

Gluon multiplicity per unit rapidity is calculated at a time τ by fixing transverse Coulomb

gauge ($\partial_i A^i = 0$, with i summed over 1,2). The lattice expression of dN_g/dy is given by [275, 282]

$$\frac{dN_g}{dy} = \frac{2}{N^2} \int \frac{d^2 k_T}{\tilde{k}_T} \left[\frac{g^2}{\tau} \text{tr} (E_i(\mathbf{k}_\perp) E_i(-\mathbf{k}_\perp)) + \tau \text{tr} (\pi(\mathbf{k}_\perp) \pi(-\mathbf{k}_\perp)) \right], \quad (4.47)$$

where

$$k_T^2 = 4 \left[\sin^2 \frac{k_x}{2} + \sin^2 \frac{k_y}{2} \right], \quad (4.48)$$

denotes the effective lattice momentum squared and N is the number of lattice sites in each direction of the 2D lattice. We use a multiplicative factor $2/3$ to convert the gluon multiplicity dN_g/dy to charge particle multiplicity dN_{ch}/dy . The coupling constant appears as a multiplicative factor in the final multiplicity. There are several schemes to introduce running coupling effects in the calculation of multiplicity. In Ref. [278] it was shown that running the coupling with a scale $k_T/2$ provides good description of rapidity and centrality dependence of multiplicity for a wide range of systems. The running coupling is introduced by multiplying the terms inside the parenthesis of Eq. 4.47 with a factor $g^2/(4\pi\alpha_s(\mu))$ where

$$\alpha_s(\mu = k_T/2) = \frac{4\pi}{\beta \ln [(\mu_0/\Lambda_{\text{QCD}})^{2/c} + (\mu/\Lambda_{\text{QCD}})^{2/c}]^c}. \quad (4.49)$$

The parameters used here are $\mu_0 = 0.5\text{GeV}$, $c = 0.2$, $N_c = 3$, $\beta = 11 - 2N_F/3$ with number of flavours $N_F = 3$ and $\Lambda_{\text{QCD}} = 0.2\text{GeV}$.

For conversion between rapidity and pseudo-rapidity density of multiplicity we use a Jacobian factor,

$$\frac{dN_{\text{ch}}}{d\eta} = \frac{\cosh \eta}{\sqrt{\cosh^2 \eta + m_{\text{eff}}^2/P^2}} \frac{dN_{\text{ch}}}{dy}, \quad (4.50)$$

where the effective mass term $m_{\text{eff}} = 0.35 \text{ GeV}$ and momentum $P = 0.13 \text{ GeV} + 0.32 \text{ GeV}(\sqrt{s}/(1 \text{ TeV}))^{0.115}$ are obtained from the parameterization given in ref [93].

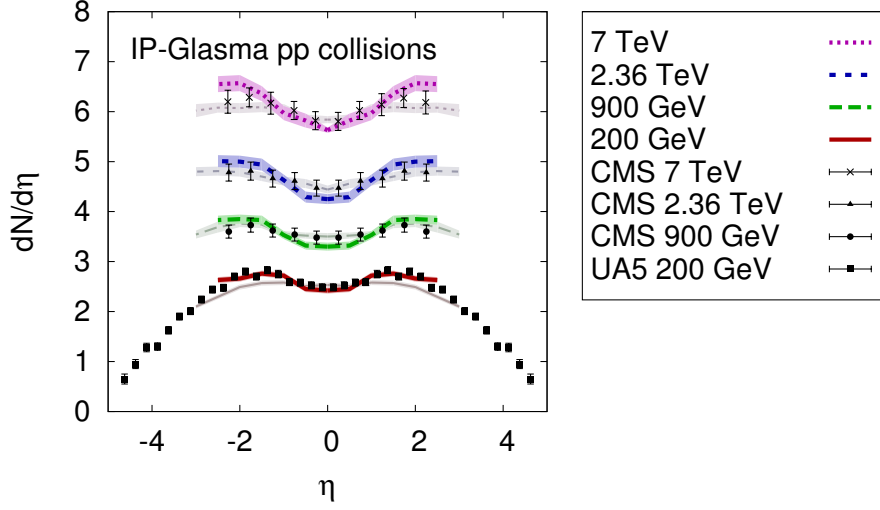


Figure 4.22: Charged particle multiplicity as a function of pseudo-rapidity compared to experimental data from the UA5 [283] and the CMS collaboration [284]. Thick (colored) lines correspond to the best parameter set for AA collisions. Thin (gray) lines use $m_{\text{eff}} = 200$ GeV which makes the dip around $\eta = 0$ less prominent, and $N_y = 10$, $\tau = 0.5$ fm, and $Q_s/g^2\mu = 0.75$.

4.6.1 Results for p+p collisions

The overlap function of a proton+proton collision at impact parameter b is a convolution of the corresponding thickness functions

$$T_{pp}(b) = \int dx dy T_p^A(x + b/2, y) T_p^B(x - b/2, y). \quad (4.51)$$

With this quantity in hand, we can define the probability density for an inelastic parton-parton interaction as a function of the impact parameter. This is parametrized as

$$\frac{d^2 P}{d^2 b}(b) = \frac{1 - e^{-\sigma_{gg} N_g^2 T_{pp}(b)}}{\int d^2 b \left(1 - e^{-\sigma_{gg} N_g^2 T_{pp}(b)}\right)}, \quad (4.52)$$

with an effective parton number N_g and effective parton-parton cross section σ_{gg} [235]. The denominator of Eq.(4.52) is the inelastic proton+proton cross section $\sigma_{pp}^{\text{inel}}$, and we fix the value of $\sigma_{gg} N_g^2$ to reproduce its experimentally determined value $\sigma_{pp}^{\text{inel}} = 68$ mb for $\sqrt{s} = 7$ TeV

($\sigma_{pp}^{\text{inel}} = 42 \text{ mb}$ for $\sqrt{s} = 0.2 \text{ TeV}$) [285]. In practice, we sample b from a uniform distribution between $b_{\text{min}} = 0 \text{ fm}$ and $b_{\text{max}} = 4 \text{ fm}$ and weight each event with the factor $b \left(1 - e^{-\sigma_{gg} N_g^2 T_{pp}(b)}\right)$.

The expression in Eq. (4.52) describes the likelihood of an inelastic proton-proton collision. Given such a collision, we next follow the procedure described earlier to compute the configuration of gauge fields created in the collision, and from these gauge fields, the gluon multiplicity using Eq. (4.47).

Results for $dN_{\text{ch}}/d\eta$ are shown in Fig. 4.22, with statistical errors indicated by bands. We see that the IP-Glasma model gives a good description of the energy and rapidity distribution. Thick (colored) lines are for the parameters that gave the best description in A+A collisions. Thin (gray) lines are for a different set, using $m_{\text{eff}} = 200 \text{ GeV}$, $N_y = 10$, $\tau = 0.5 \text{ fm}$, and $Q_s/g^2\mu = 0.75$. The main difference is caused by the smaller m_{eff} in the Jacobian, which makes the dip around $\eta = 0$ weaker. We are able to determine the multiplicity as a function of rapidity only on average because the result in a single event is strictly boost-invariant. However, varying the rapidity y in $x = (Q_s(\mathbf{x}_{\perp}, x)/\sqrt{s}) \exp(\pm y)$ will vary the magnitude of Q_s in both protons in opposite ways—this feature of the model leads to the observed rapidity dependence of the multiplicity.

To check whether we can also reproduce the experimentally determined charged particle multiplicities as a function of transverse momentum, we compute the charged hadron distribution from the gluon distribution using the next-to-leading order (NLO) KKP [286] fragmentation functions:

$$\frac{dN^h}{dyd^2p_T} = \int_{0.05}^1 \frac{dz}{z^2} D_g^h \left(z = \frac{p_T}{k_T}, Q = k_T \right) \frac{dN^g}{dyd^2k_T}, \quad (4.53)$$

where $D_g^h(z, Q)$ is the probability to produce a charged hadron with momentum $p_T = zk_T$ from a gluon with momentum k_T at the scale Q . We have restricted the integral to $z \geq 0.05$ so that the fragmentation function parametrizations are not used too far outside the x range selected for the fits [286].

The result is presented in Fig. 4.23. Here we employ a lattice spacing of $a = 0.015 \text{ fm}$ to increase the momentum range on the lattice to higher momenta. We show both the gluon

distribution and the charged hadron distribution after fragmentation. The agreement with experimental data from the ATLAS collaboration [287] is very good at low momenta. At higher transverse momentum ($\gtrsim 3$ GeV), we see a similar overestimation of the experimental data as found in calculations using the McLerran-Venugopalan (MV) model [288]. Since we have not attempted to introduce an anomalous dimension, or similar modification [289, 290], or higher order ρ^a -correlators [291], we anticipated the somewhat harder spectra at large momentum.

Furthermore, the quark contribution is ignored completely. It is well known that quark-gluon scattering can provide a significant contribution to the multiplicity as $x \rightarrow 0.01$ and above [292]. Note that the normalization factor is now somewhat different from the previous result for $dN/d\eta$, because the conversion from gluons to hadrons is taken care of by the fragmentation function. Given these limitations, the overall agreement with the data is in fact surprisingly good. The shape of the spectrum in the range $0.5 \text{ GeV} < p_T < 2 \text{ GeV}$ is well reproduced.

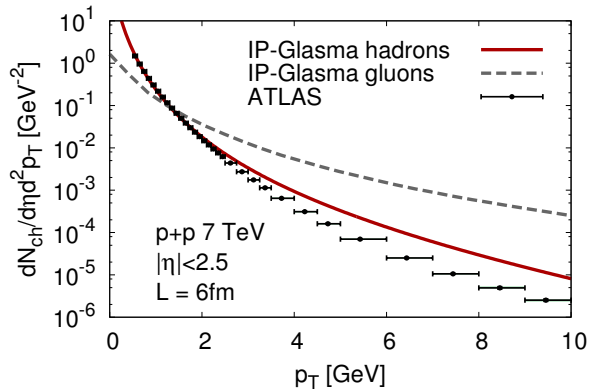


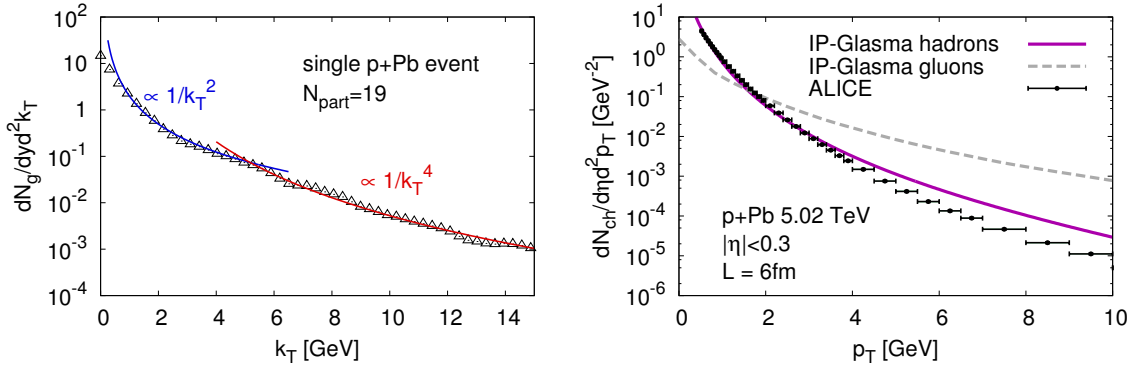
Figure 4.23: Charged particle multiplicity obtained using Eq. (4.53) as a function of transverse momentum compared to experimental data from the ATLAS collaboration [287].

4.6.2 Results for p+A/d+A collisions

In this section, we present results for Proton-lead collisions at center of mass energies of $\sqrt{s} = 5020 \text{ GeV}$ at the LHC and d+A collisions at $\sqrt{s} = 200 \text{ GeV}$ at RHIC using IP-Glasma model. We follow the same procedure for computing the multiplicity in p+A as in p+p collisions, using

the weight in Eq. (4.52). We then compute the configuration of gauge fields created in the collision and from those the gluon multiplicity according to Eq. (4.47).

First, we show the unintegrated distribution $dN_g/dy d^2k_T$ in transverse Coulomb gauge for a single event in Fig. 4.24(a).



(a) Gluon transverse momentum distribution in a single p+Pb event at $\sqrt{s} = 5020$ GeV with $N_{\text{part}} = 19$. The solid line indicates the functional behavior Eq. (4.53) compared to experimental data from the $\sim 1/k_T^2$, the dashed line $\sim 1/k_T^4$. (b) Charged particle multiplicity in pPb collisions as a function of transverse momentum obtained using the ALICE collaboration [95].

Figure 4.24: Transverse momentum distribution in p+Pb collisions.

We see that at large $k_T \gtrsim 5$ GeV we recover the standard perturbative behavior $\sim 1/k_T^4$ up to possible logarithmic corrections. Within the MV model, this limiting behavior was shown analytically in [293, 294]. In the saturation regime at small $k_T \lesssim Q_s^{\text{Pb}}$, we find the expected $\sim 1/k_T^2$ behavior for a system with two differing saturation scales, with a flatter distribution at very low $k_T \lesssim Q_s^{\text{proton}}$. This behavior was discussed in detail in [295, 296] and was previously observed numerically in [272].

In Fig. 4.24(b) we show the p_T distribution of charged hadrons after fragmentation with the KKP fragmentation function, as in the p+p case. The result is similar to the one in p+p collisions, with a good description for $p_T \lesssim 3$ GeV but an overestimate in the high p_T region.

The p_T integrated distribution has the functional form $(Q_s^{\text{min}})^2 \ln(Q_s^{\text{max}}/Q_s^{\text{min}})/\alpha_S$, where $\{Q_s^{\text{min}}, Q_s^{\text{max}}\}$ denote respectively the smaller and larger saturation scales at a given rapidity. It was shown previously to give good agreement with RHIC deuteron-gold data [297]. A

compilation of predictions in various saturation models—all computed with the k_T factorization approximation—agree with the LHC p+Pb rapidity distribution to within 20% [298].

In Fig. 4.25 we present results in the IP-Glasma framework for rapidity distributions in d+Au and p+Pb collisions. We have approximated the shift of the rapidity to the laboratory frame, in which the data is presented, by a shift of the same amount in pseudo-rapidity. In d+Au the shift is 0.11 units of rapidity in the proton going direction, in p+Pb it is 0.465 units.

It is important to note that all but one parameter are the same as in p+p collisions (thick lines in Fig. 4.22). The only exception is the energy dependent normalization used in the plot. We find $\mathcal{N} \approx 0.14 \ln(\sqrt{s}/1 \text{ GeV})$, so that at a given energy the normalization constant \mathcal{N} is approximately 15% smaller than that for p+p collisions. However, this is well within the systematic uncertainties of our framework. The rapidity dependence is somewhat flatter than the data in d+Au collisions and slightly steeper in the higher energy p+Pb collisions. At large absolute values of η either target or projectile are probed in the large- x region that we have little theoretical control over. We thus do not expect a very good description in the very forward and backward directions.

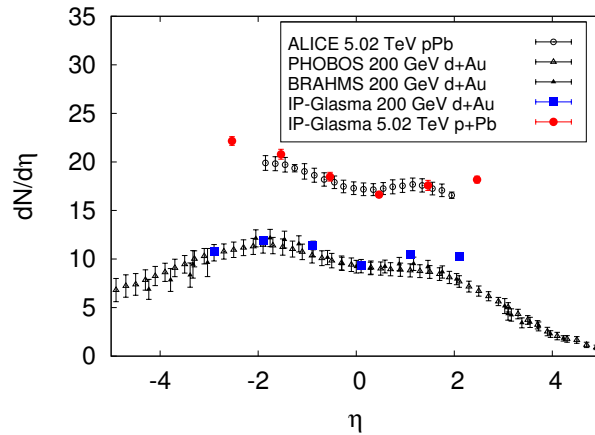
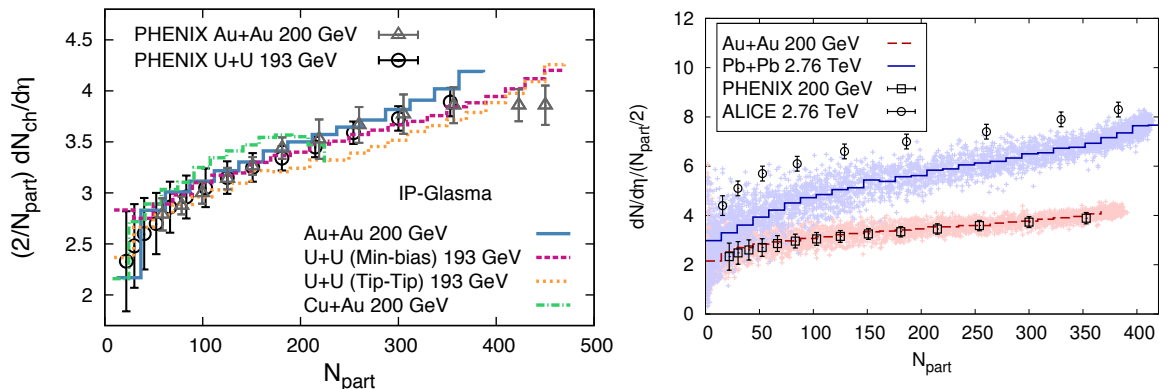


Figure 4.25: Charged particle multiplicity as a function of pseudo-rapidity in d+Au collisions at 200 GeV and p+Pb collisions at 5.02 TeV compared to experimental data from the PHOBOS and BRAHMS collaborations [233, 299] and the ALICE collaboration [300].



(a) Centrality dependence of mean multiplicity per participant pair for different systems. Plotted data points are from Ref. [301, 302]. (b) Charged particle multiplicity divided by $N_{\text{part}}/2$ as a function of N_{part} compared to experimental data from the PHENIX [302] and the ALICE [303] collaborations. The bands are a collection of the multiplicities for individual events, with the solid lines representing the average multiplicity.

Figure 4.26: Centrality dependence of multiplicity in A+A collisions for different systems.

4.6.3 Results for A+A

To study A+A collisions in the the IP-Glasma model, Yang-Mills equations are solved up to time $\tau = 0.4 \text{ fm}/c$, and the transverse Coulomb gauge is fixed, to compute the gluon multiplicity per unit rapidity. A multiplicative factor of $2/3$ then converts the gluon multiplicity to the charged particle multiplicity. The systems studied here are Au+Au, Cu+Au and U+U at RHIC and Pb+Pb collisions at LHC.

Experimental results for multiplicities are typically presented as a function of N_{part} , the number of participant nucleons. In the IP-Glasma framework, N_{part} does not enter in any of the computations. However, to make comparisons to the experimental data plotted as a function of N_{part} , the value of N_{part} is determined geometrically as follows. Two nucleons have an inelastic collision whenever their geometric distance is less than $\sigma_{NN} = 42 \text{ mb}$, the nucleon-nucleon inelastic cross section at the top energy of the Relativistic Heavy Ion Collider (RHIC). We define the total number of nucleons that undergo at least one such inelastic collision to be N_{part} .

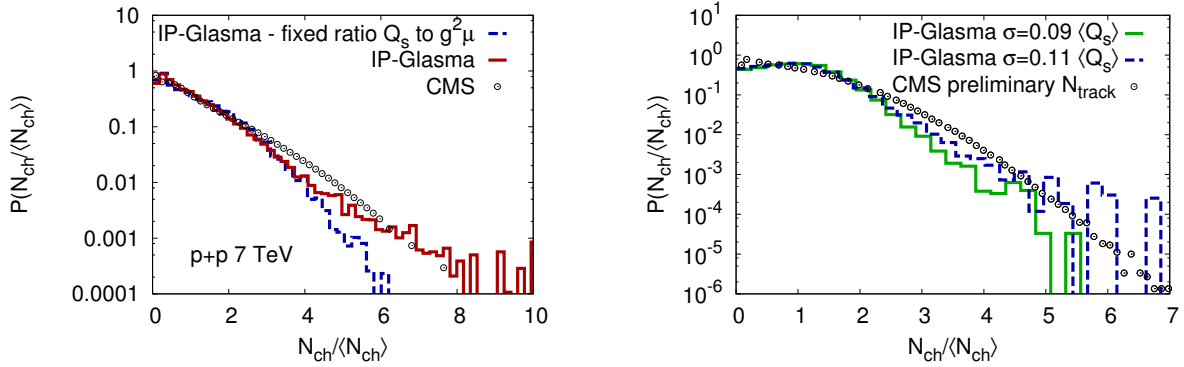
The centrality dependence of the mean produced multiplicity density per participant pair

$(2/N_{\text{part}}) dN_{\text{ch}}/d\eta$ at $\eta = 0$ for various systems is shown in Fig. 4.26(a). Computations of multiplicities in the IP-Glasma model are compared to the available Au+Au data at 200 GeV/nucleon and preliminary results for U+U 193 GeV/nucleon collisions from the PHENIX collaboration [301]. Fig. 4.26(a) also presents the result for Cu+Au collisions, for which no data are as yet available. For Cu+Au there will be a shift of the rapidity distribution in the laboratory frame by about 0.07 units in the Cu going direction which is negligible and ignored in our calculation. The results are very similar for different systems. A weak system size dependence is observed showing that the smaller sized systems Cu+Au and Au+Au produce slightly higher multiplicities per participant compared to U+U collisions. Tip-tip U+U collisions produce fewer particles per participant than random collisions for most values of N_{part} . Only for the most central events, does the tip-tip configuration produce as many particles per participant as in the random case.

For Cu+Au collisions we see an interesting centrality dependence of multiplicity which is not seen in case of other systems. As shown in Fig. 4.26(a), the centrality dependence of $(2/N_{\text{part}}) dN_{\text{ch}}/d\eta$ for Cu+Au flattens out above $N_{\text{part}} > 180$. One possible interpretation could be that the Cu nucleus is completely surrounded by the Au nucleus for most central Cu+Au collisions. In this case, the minimum saturation scale among the two nuclei that controls the multiplicity does not grow fast enough with further increase of N_{part} .

Fig. 4.26(b) shows the new results for the charged particle multiplicity as a function of N_{part} in Au+Au collisions at RHIC and Pb+Pb collisions at the LHC. We underestimate the Pb+Pb data at the higher \sqrt{s} after fixing the normalization for Au+Au at $\sqrt{s} = 200$ GeV. At low N_{part} the result is about 30% too low, at large N_{part} only 15%. Note however that additional entropy can be generated at the end of the Glasma stage. In particular, increased entropy production at higher energy (larger effective η/s) and in more peripheral events could provide a natural explanation for this difference. In [304], the IP-Glasma Yang-Mills dynamics was matched event-by-event to the MUSIC relativistic hydrodynamical model [85, 305, 306].

4.6.4 Multiplicity fluctuation in the non-perturbative framework



(a) Minimum-bias charged particle multiplicity distribution scaled by the mean multiplicity compared to experimental data from the CMS collaboration [307]. We show the distribution with (solid) and without (dashed) smearing of the relation between Q_s and the color charge density $g^2\mu$.

(b) Scaled distribution of the number of tracks N_{track} in the range $p_T > 0.4 \text{ GeV}$ and $|y| < 2.4$ for p+Pb collisions at $\sqrt{s} = 5020 \text{ GeV}$. The solid line is the IP-Glasma result including fluctuations of the number of gluons in the incoming nucleons, characterized by fluctuations of $g^2\mu^2$ at a given Q_s^2 the same as in $p+p$ collisions. The dashed line is the result for Gaussian fluctuations with a larger variance.

Figure 4.27: Multiplicity fluctuation in p+p and p+Pb collisions in the IP-Glasma model.

One of the most striking result from this approach is that the IP-Glasma naturally produces Negative-Binomial fluctuation of multiplicity and energy density.

In Fig. 4.27(a) we show the multiplicity distribution of p+p collisions at 7 TeV scaled by the mean multiplicity. We find that when fixing the ratio of Q_s to the color charge density $g^2\mu$, the distribution is too narrow, missing fluctuations in the tail of the distribution. One possible reason for this could be that there are additional sources of fluctuations in QCD that go beyond those included in our framework (see [308]). If we allow $g^2\mu$ to fluctuate around its mean value with a Gaussian distribution whose width is 9% of that mean value, the result is closer to the experimental data. The choice of a Gaussian distribution is merely an ansatz chosen for simplicity. As detailed discussion on this context can be found in Ref. [278]. The discrepancy between our result and the experimental data suggests that the exact form of these fluctuations is non-Gaussian. In Fig. 4.27(b) we present the same distribution for $p+Pb$ collisions

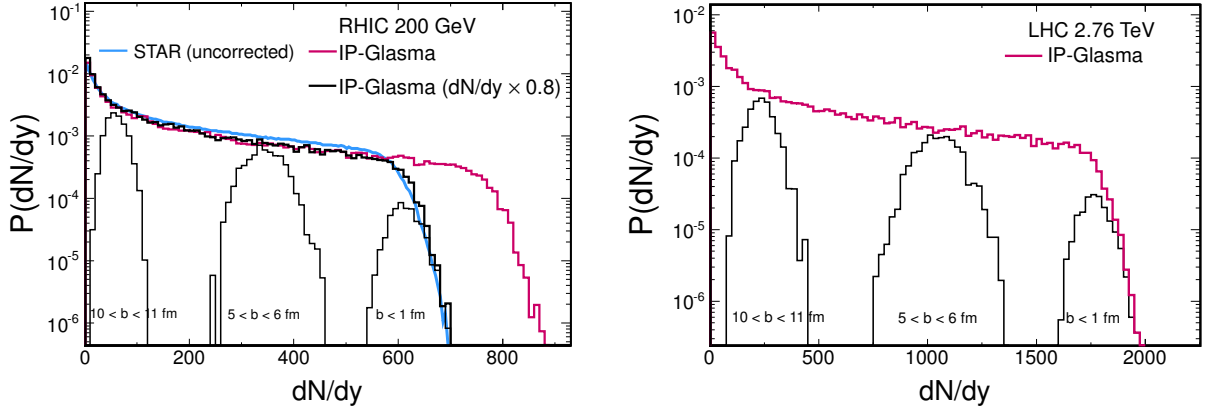


Figure 4.28: (left) Probability distribution of gluon multiplicities dN/dy at $\tau = 0.4$ fm/c. Shown are also the distributions for some limited ranges of impact parameter b , which are described by negative binomial distributions. (right) Prediction for LHC energy $\sqrt{s} = 2.76$ TeV. Experimental data from STAR [309].

at $\sqrt{s} = 5020$ GeV.

In Fig. 4.28 we present the probability distribution of dN_g/dy at RHIC energies. An essential ingredient is the probability distribution of impact parameters, which is determined by the Glauber model to be

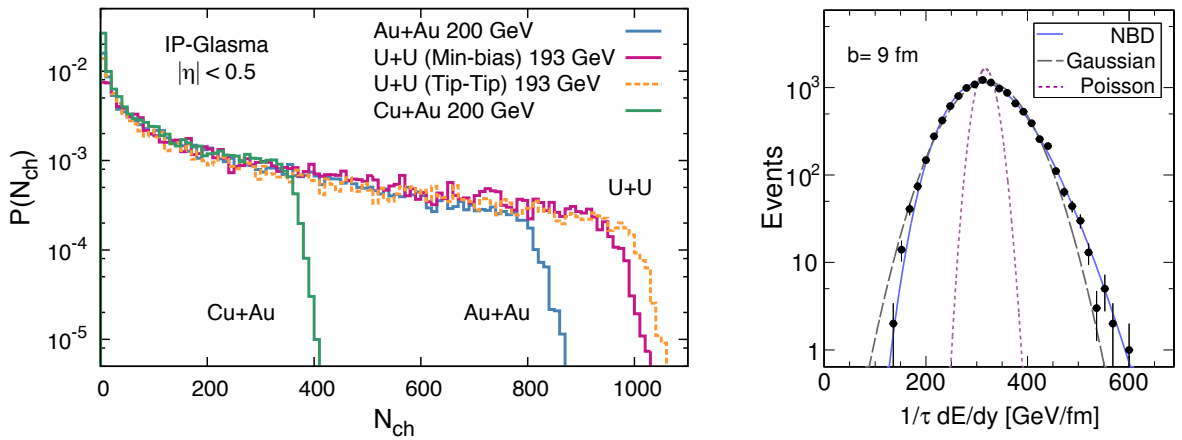
$$\frac{dP_{\text{inel}}}{d^2\mathbf{b}_\perp} = \frac{1 - (1 - \sigma_{NN}T_{AB})^{AB}}{\int d^2\mathbf{b}_\perp (1 - (1 - \sigma_{NN}T_{AB})^{AB})}, \quad (4.54)$$

with the overlap function T_{AB} . One could in principle compute this distribution in the Glasma framework, but a first principles computation is extremely difficult. The probability for no inelastic interaction (an essential ingredient in the above equation) at a given impact parameter requires an understanding of diffractive/elastic interactions which is incomplete at present in all QCD based frameworks. The Glauber model, with parameters tuned to data, is therefore a good effective model for this aspect of our computation.

We compute the n-particle multiplicity distribution by first sampling the impact parameter b from a uniform distribution, computing the resulting dN_g/dy from the IP-Glasma model, and when binning these values into the histogram shown in Fig. 4.28, weight the result with a factor $2\pi b dP_{\text{inel}}/d^2\mathbf{b}_\perp$ depending on the b value used in a given event. The STAR data shown is uncorrected, which makes a direct comparison difficult. We therefore scale dN/dy by a factor

of 0.8 and achieve good agreement with the data. This factor is very close to the ratio of the un-corrected to corrected mean multiplicity for 0-5% most central STAR data as quoted in ref [309]. Note, however, that this comparison is approximate since the correction depends on dN/dy [309] which would modify the shape of overall multiplicity distribution.

The multiplicity distributions of charged particles N_{ch} at mid-rapidity ($|\eta| < 0.5$) for different systems are shown in Fig. 4.29(a).



(a) Probability distributions of charge particle multiplicity for different systems.

(b) The IP-Glasma event-by-event distribution in energy for $b = 9$ fm on the lattice compared to different functional forms. The negative binomial distribution (NBD) gives the best fit.

Figure 4.29: Fluctuation of multiplicity and energy density in IP-Glasma model.

We also show three distributions obtained by constraining the impact parameter range to demonstrate that their shape resembles a negative binomial distribution (NBD). The negative binomial fluctuations of the transverse energy as emerging from the IP-Glasma model is shown in Fig. 4.29(b). Here we show that they also appear in the multiplicity distribution. In the Glasma flux tube framework [310, 311], negative binomial distributions given in Eq.4.27 with

$$k = \zeta \frac{N_c^2 - 1}{2\pi} Q_s^2 S_{\perp} \quad (4.55)$$

arise [312], with k inversely proportional to the width of the NBD. k here is proportional to the

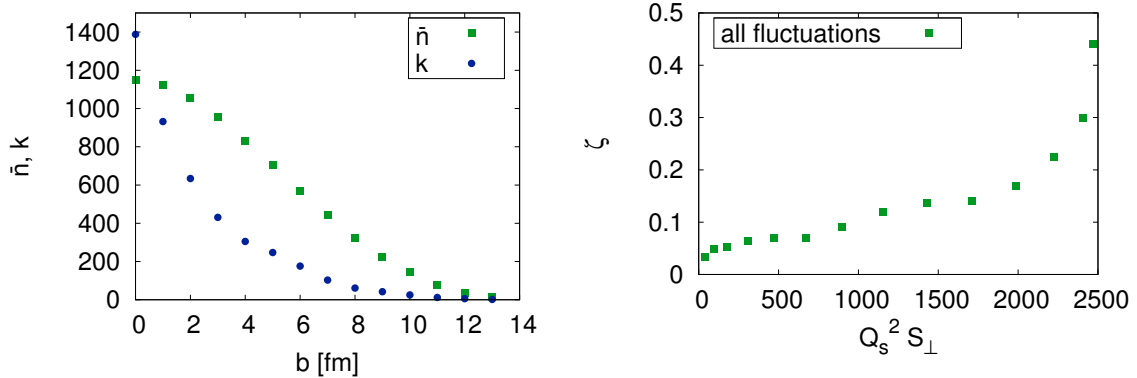
number of flux tubes $Q_s^2 S_\perp$, where S_\perp is the transverse size of the system. (Hence smaller systems at a fixed energy generate more fluctuations.) In the expression above, ζ is an intrinsically non-perturbative function which can be computed *ab initio* from solutions of the CYM equations. To determine ζ it is sufficient to compute the double inclusive distribution by solving CYM equations as done in Ref. [313]. Here we are computing the n-particle inclusive distribution, and can thus also extract ζ if the NBD description of these distributions is robust. ζ in general can depend on $Q_s^2 S_\perp$; however, a powerful test of how robust the Glasma flux tube picture is depends on this dependence being weak for large values of $Q_s^2 S_\perp$. We will therefore discuss the behavior of ζ below and what the results tell us about the nature of different sources of quantum fluctuations.

Within the IP-Glasma model, we determine $\zeta(Q_s^2 S_\perp)$ by extracting k from a fit with an NBD and computing an average $\langle Q_s^2 S_\perp \rangle$ by summing over the minimum of the two $Q_{s,A(B)}^2$ in the whole transverse plane.

We first determine \bar{n} and k of Eq.(4.27) from the fit to the multiplicity distributions at fixed impact parameter b . The results are shown in Fig. 4.30(a). Interestingly, the ratio k/\bar{n} is greater than one for central collisions and at large impact parameters approaches approximately $k/\bar{n} \approx 0.14$, which is close to the value determined from fits to distributions in p+p collisions [314].

The corresponding ζ -values are shown in Fig. 4.30(b) as a function of the average values of $Q_s^2 S_\perp$ for a given b . We observe a strong dependence of ζ on $Q_s^2 S_\perp$, which is in disagreement with the flux tube picture. The reason is that the effect of fluctuations in the number of wounded nucleons (which were not considered in the derivation of Eq.(4.55)) in addition to fluctuations in the color charge distributions, make the distribution wider (ζ smaller), especially at large impact parameters (small $Q_s^2 S_\perp$) where geometrical fluctuations dominate.

This behavior of ζ is compatible with the previously extracted values from fits based on k_\perp factorization to multiplicity distributions [92] described in section 4.5.4, where small dN/dy required small values of ζ and large dN/dy larger values to achieve a good fit. The IP-Glasma



(a) Average gluon number \bar{n} and width parameter k as a function of impact parameter b at $\sqrt{s} = 200$ GeV. (b) Proportionality factor ζ at RHIC energy in $k = (\zeta(N_c^2 - 1)/(2\pi))Q_s^2 S_\perp$ as a function of $Q_s^2 S_\perp$ including all fluctuations. $Q_s^2 S_\perp$ corresponds to the average value for a given b . b was varied in 1 fm steps from 0 to 13 fm.

Figure 4.30: Parameters of NBD in the non-perturbative framework.

model automatically produces this variation of ζ , leading to very good agreement with the experimental data as shown in Fig. 4.28.

To be able to better compare to the flux tube picture and Eq. (4.55), we now consider only the effect of fluctuations in color charges. To do so we average over the nuclear color charge density squared over many nucleon configurations. This results in a smooth distribution that removes fluctuations in the wounded nucleon number and positions.

This is in the spirit of the original Glasma flux tube perturbative [312] and non-perturbative [313] computations. The result for this ζ_{smooth} is shown in Fig. 4.31. After starting out near 1, ζ_{smooth} drops and approaches a constant value of approximately $\zeta_{\text{smooth}} = 0.2$ for large $Q_s^2 S_\perp$. This means that at low parton densities, k is initially more constant than expected in the Glasma flux tube picture but then becomes proportional to $Q_s^2 S_\perp$ at high parton densities as anticipated.

The fact that ζ at small impact parameters (cf. Fig. 4.30(b)) approaches that in the smooth case for the same $Q_s^2 S_\perp$ gives hope that there is a chance to experimentally access a regime where the flux tube picture is valid. Fixing $b = 0$ fm and increasing the energy, and this way increasing $Q_s^2 S_\perp$ while keeping S_\perp as constant as possible, reduces fluctuations in the nucleon

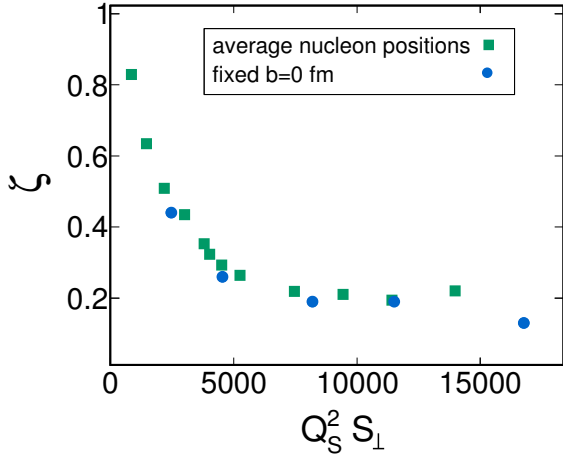


Figure 4.31: Proportionality factor ζ in $k = (\zeta(N_c^2 - 1)/(2\pi))Q_s^2 S_\perp$ as a function of $Q_s^2 S_\perp$ for averaged nucleon positions (squares) and with nucleon fluctuations at fixed impact parameter $b = 0$ fm (circles). At large $Q_s^2 S_\perp$ the result for the smooth distribution approaches a constant as predicted by the Glasma flux tube model for n-gluon correlations. The result for fluctuating nucleon positions at constant $b = 0$ fm is very similar and becomes very weakly dependent on $Q_s^2 S_\perp$.

number. Indeed we find that the result for the extracted ζ , shown as blue circles in Fig. 4.31, is very close to the one obtained with smooth initial distributions, and its dependence on $Q_s^2 S_\perp$ becomes weak at large $Q_s^2 S_\perp$.

4.7 Initial state geometry and fluctuation in heavy ion collisions

In this section we discuss how initial state fluctuation influence bulk observables other than multiplicity. Aforementioned, several sources of fluctuations in the initial stages of heavy ion collisions. The dominant ones are the geometric fluctuations of nucleon positions and fluctuations of the impact parameter. In collisions of deformed (non-spherical) nuclei the orientations of the nuclei, characterized by four spherical angles, also fluctuate from event to event. For each such configuration of the collision geometry, additional sub-nucleonic fluctuations of color charges lead to fluctuations in the produced gluon fields.

The combined effect of these fluctuations is reflected in the distributions of global observ-

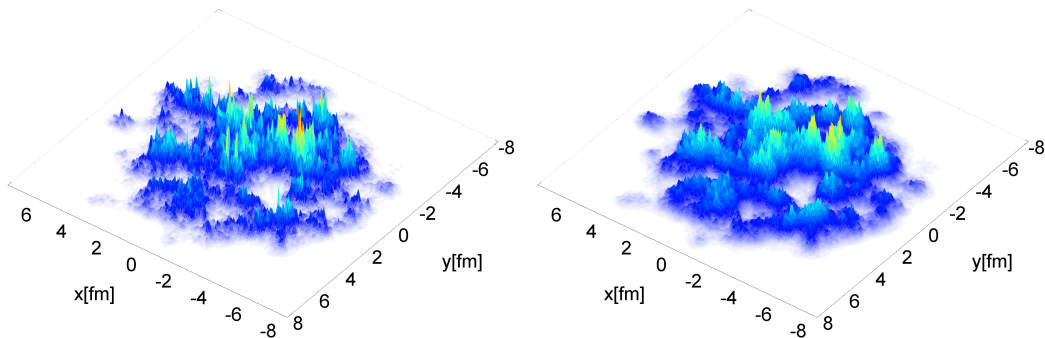


Figure 4.32: Energy density (arbitrary units) in the transverse plane at $\tau = 0$ fm (upper panel) and $\tau = 0.2$ fm (lower panel). The structures are smoothed by the evolution over the first $\Delta\tau \sim 1/Q_s$.

ables such as anisotropic flow and its fluctuations. The IP-Glasma model, that incorporates different sources of initial state fluctuations and includes an *ab initio* description of multi particle production, therefore serves as an ideal framework to simulate the initial stage of heavy ion collisions. Several other frameworks like Monte-Carlo Glauber-type models (MC-Glauber) and Monte-Carlo implementations of the KLN model (MC-KLN) [315–317] are widely known models for initial conditions for heavy ion collisions. A comparison between different models of initial condition is described in Table.4.7.

Fig. 4.33 shows the structure of the energy density in the transverse plane after the collision, at time $\tau = 0$ fm and after classical Yang-Mills evolution in 2+1 dimensions for $\Delta\tau = 0.2$ fm, which is of the order of $1/Q_s$, the time scale over which interactions are still significant. After this time, expansion causes the fields to become weak and the system becomes freely streaming.

We now show the energy density distribution in the transverse plane in Fig. (4.33). We compare to the MC-KLN model and to an MC-Glauber model that was tuned to reproduce experimental data [306, 318]. In the latter, for every participant nucleon, a Gaussian distributed energy density is added. Its parameters are the same for every nucleon in every event, with the width chosen to be 0.4 fm to best describe anisotropic flow data. We will also present results for a model where the same Gaussians are assigned to each binary collision. The resulting initial energy densities differ significantly. In particular, fluctuations in the present computation occur

I.C.	Geometry (MC-Glauber)	k_T -factorization (MC-KLN)	Classical Yang-Mills (IP-Glasma)
framework	2-component model	CGC perturbative	CGC non-perturbative
E-by-E	✓	✓	✓
Sub-nucleonic fluctuation	×	×	✓
Time evolution	×	×	✓
Initial flow	×	×	✓
NBD fluctuation	by hand	by hand	✓

Table 4.3: Comparison between different models of initial conditions.

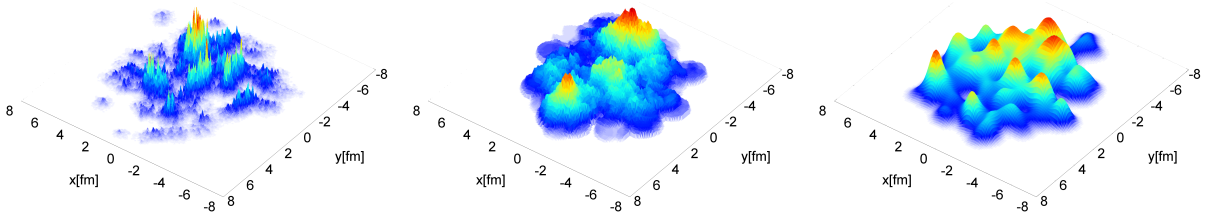


Figure 4.33: Initial energy density (arbitrary units) in the transverse plane in three different heavy-ion collision events: from left to right, IP-Glasma, MC-KLN and MC-Glauber [318] models.

on the length-scale $Q_s^{-1}(\mathbf{x}_\perp)$, leading to finer structures in the initial energy density relative to the other models. As noted in [314], this feature of CGC physics is missing in the MC-KLN model.

The n -th order spatial eccentricity that characterizes the initial state geometry is defined as

$$\varepsilon_n = \frac{\sqrt{\langle r^n \cos(n\phi) \rangle^2 + \langle r^n \sin(n\phi) \rangle^2}}{\langle r^n \rangle} \quad (4.56)$$

Here $\langle \cdot \rangle$ is the energy density $\epsilon(r, \phi, \tau)$ weighted average. To eliminate noise in the computation of eccentricities, we only include cells in which the energy density is greater than $\epsilon_{\min} = \Lambda_{\text{QCD}}^4$, where Λ_{QCD} is chosen to be 200 MeV. The effect of variation of ϵ_{\min} was previously studied in Ref. [319]. The system size calculated was found to be sensitive to the choice of ϵ_{\min} . However,

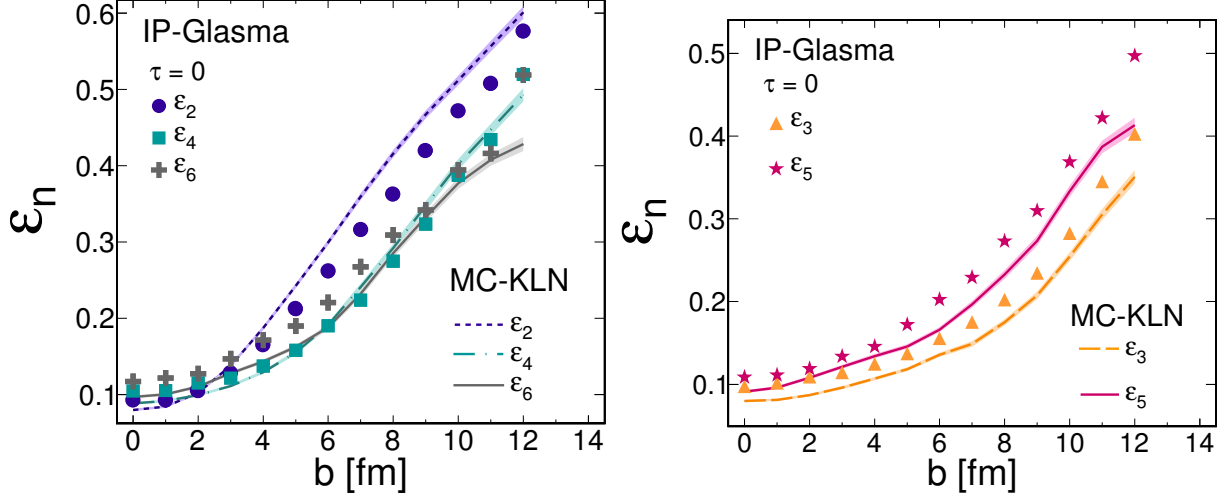


Figure 4.34: Even (upper panel) and odd (lower panel) eccentricities from the IP-Glasma model compared to those from MC-KLN.

we find that variation of ϵ_{\min} has only a negligible effect on the ϵ_n we compute here, because they are ratios of quantities proportional to the system size. Fig. 4.34 shows the results for ϵ_n up to $n = 6$ in Au+Au collisions at $\sqrt{s} = 200\text{GeV}$ from the IP-Glasma model which is compared to the predictions from the MC-KLN model. One can see that the purely fluctuation driven odd harmonics ϵ_3 and ϵ_5 from the IP-Glasma model are larger than those from the MC-KLN model for all b , while ϵ_2 is smaller than that computed in the MC-KLN model, in particular for $b > 3\text{fm}$. As a consequence, the ratio ϵ_2/ϵ_3 is smaller than in the MC-KLN model, which is going to decrease the ratio of v_2/v_3 obtained after hydrodynamic evolution, making it more compatible with experimental observation. ϵ_4 and ϵ_6 are almost equal or larger than those from the MC-KLN model. We make the comparison to MC-KLN at $\tau = 0\text{fm}/c$, because at later times we would also have to take into account the pre-equilibrium flow built up in the CYM simulation.

4.8 Summary

In this chapter we study the multi-particle correlations in the framework of Color Glass Condensate. This framework consistently includes several sources of initial state fluctuations and provides an *ab initio* description of particle production. The study includes the extraction of hadronic and nuclear wave functions using saturation models of HERA DIS data to predict the inclusive multiplicity and its fluctuation in p+p, p+A and A+A collisions at RHIC and LHC. To study different sources of fluctuations at the initial stages of collisions we have developed a new framework of fluctuating initial condition “Impact Parameter dependent Glasma” (IP-Glasma) model which computes the initial gluon fields and their Yang-Mills evolution on a two dimensional real-time lattice. This model goes beyond the widely known MC-KLN implementation by using CYM solutions instead of k_{\perp} -factorization and including quantum fluctuations on the dynamically generated transverse length scale $1/Q_s$. Further, unlike MC-KLN, its parameters are fixed by HERA inclusive and diffractive e+p DIS data. At fixed impact parameter, this model naturally produces Negative Binomial multiplicity fluctuations that are known to describe $p + p$ and $A + A$ multiplicity distributions, and its ratio of initial triangularity to eccentricity is more compatible with experimental data of harmonic flow coefficients. This model naturally describes inclusive multiplicity fluctuations and can be used to study wide range of systems like p+p, p+A/d+A and A+A. This model can be used as an input to viscous hydrodynamic simulations.

Summary

This thesis work includes two major topics : modelling of inclusive multiplicity fluctuations, and measurement of inclusive multiplicity fluctuation in ultra relativistic heavy ion collisions. The goal was to develop an understanding of how observed multiplicity fluctuation arises from different stages of heavy ion collisions. Over several years, experimental results have suggested that the observed distribution of inclusive multiplicity in hadronic collisions are well described by the Negative-Binomial distributions (NBDs). For heavy ion collisions it turns out that the minimum bias multiplicity distribution is a convolution of many such NBDs. Although several models have predicted the origin of such a distribution, a first principle QCD motivated explanation was missing. This work is the first to demonstrate the origin of Negative-Binomial fluctuations in a non-perturbative approach by employing a framework of high energy effective field theory of QCD known as the Color Glass Condensate. Such fluctuations are essential in describing the fluctuation of the multiplicity of gluons produced in the early stages of collisions which further fragment into charged and neutral particles.

According to the conventional model of heavy ion collisions, the initial gluonic matter created after collisions, eventually thermalises to form a strongly correlated system of QCD matter known as the Quark Gluon Plasma (QGP). The QGP phase eventually undergoes a phase transition to hadronic matter. This phase transition is associated with the de-confinement transition and the restoration of QCD chiral symmetry. Several experimental observables that are sensitive to the de-confinement transition, indicate the formation of a thermalised QCD matter in heavy ion collisions. Fluctuation of the multiplicity of conserved charges is one such

observable. So far there are very few observables that directly probe the QCD chiral phase transitions.

This thesis work focuses on the experimental search for the possible signature of chiral phase transitions using the fluctuation of inclusive multiplicity of charged and neutral particles. When the system passes from a chirally symmetric phase to a broken phase, in a scenario of rapid cooling, there could be formation of metastable domains of disoriented chiral condensate (DCC). Formation and decay of DCC domains could lead to a distinct distribution of the neutral pion fraction compared to that from generic production of pions under isospin symmetry. If this phenomenon survives the final-state interactions, it will appear as anti-correlation, between the yields of charged and neutral pions. In heavy-ion collisions, charged and neutral particle productions are dominant in the form of charged and neutral pions. One can use inclusive charged particle multiplicity as a surrogate for charged pions and photons for the neutral pions. Any form of correlation between charged and neutral pions is thus expected to affect the correlation between measured charged particles (ch) and photons (γ). This is the main motivation for the measurement of event-by-event multiplicities of charged particles and photons and to study their ratio fluctuations. This thesis work presents the details of the measurement of event-by-event multiplicity of charged particle and photons at the STAR experiment at RHIC. The final stages of heavy ion collisions involve decay of resonances and detection related artefacts that introduces spurious fluctuation of the observed multiplicity. This thesis work presents a detailed discussion to develop an analysis technique to separate the dynamical fluctuations in the multiplicity from various other spurious effects.

Using an approach based on moment generating function, the robustness of fluctuation observables on various detector related effects have been studied. It was shown that observables constructed out of ratios of factorial moments are immune to detector in-efficiency. However effects of mis-identification can not be removed by the construction of observables. Sensitivity to dynamical signals of fluctuation and correlation was also studied in the same approach. A method to study the event-by-event fluctuation of the multiplicity of inclusive charged particles

and photons (neutral particles) has been developed. Sensitivity of two widely used fluctuation observables ν_{dyn} and $r_{m,1}$ to different sources of dynamical fluctuation and detector effects have been studied using analytical and Monte-Carlo approach. These observables are further used for data analysis and model studies. The two major sources of dynamical fluctuations of charged to photon multiplicity ratio (i.e. charged-neutral correlation) are from DCC-like signals and from resonance decays. Using generating function approach analytical expression for ν_{dyn} and $r_{m,1}$ in terms of the fraction of DCC events (x) and fraction of DCC candidates (y) was derived. A Monte-Carlo model to simulate DCC events using inputs from HIJING event generator was developed. The effect of resonance decay on these fluctuation observables was also studied. The method developed for studying the correlation and fluctuation of charged particle and photon multiplicity was used to analyse the data from the STAR experiment at RHIC.

This thesis work presents the measurement of event-by-event multiplicity and the correlations between photon and charged particles in the pseudo-rapidity range of $-3.7 < \eta < -2.8$ in STAR using the Photon Multiplicity Detector and the Forward Time Projection Chamber in Au+Au collisions at $\sqrt{s_{NN}}=200$ GeV. The observables $\nu_{\text{dyn}}^{\gamma\text{-ch}}$ and $r_{m,1}^{\gamma\text{-ch}}$ have been used as measures of correlation. Measured ν_{dyn} from data shows a non-zero, positive value that exceeds the predictions from HIJING, mixed event and HIJING+GEANT when charged particles and photons are measured in the same acceptance. When charged particles are measured in a different acceptance ($3.7 > \eta > 2.8$) compared to photons ($-3.7 < \eta < -2.8$), the difference between model prediction and data is found to be negligible. This indicates the presence of dynamical fluctuations in the ratio of inclusive charged to photon multiplicities when measured in the same acceptance. ν_{dyn} shows an approximate $1/\sqrt{\langle N_{\text{ch}}N_{\gamma} \rangle}$ dependence as expected from the Central Limit Theorem. The charge dependence of $\nu_{\text{dyn}}^{\gamma\text{-ch}}$ shows that different combinations of $\gamma - \text{ch}$ correlations are alike, but behave differently (both in magnitude and sign) when compared to $\nu_{\text{dyn}}^{\text{ch}^+\text{-ch}^-}$ obtained for the combination of positively and negatively charged particles in the same acceptance. This indicates that the mechanism of correlated production of oppositely charged particles is different from the correlated production of neutral and charged particles and, at the

same time, the $\gamma - \text{ch}$ correlation is not dominated by correlations from decays. The observable $r_{m,1}$ has been used to extract any deviation of $\gamma - \text{ch}$ correlation from the expectation of generic pion production. The centrality dependence of $r_{m,1}(m=1-3)$ shows a different trend compared to that from mixed events and HIJING. $r_{m,1}$ is below the generic (or Poisson) limit at higher multiplicity. For central events, $r_{m,1}$ as a function of the order m shows a trend opposite to that from models, suggesting a small deviation from the expectation of the generic production of pions. The analytical expressions derived in the generating function approach was used to extract an upper limit of DCC like signal formation in the data sample.

Origin of multiplicity fluctuation from the initial stages of heavy ion collision was investigated in this thesis work. The Color Glass Condensate framework of multi-particle production provides an *ab initio* approach to such a problem. In this work, impact parameter dependent unintegrated gluon distributions were extracted from fits to the HERA inclusive and exclusive data in the IP-Sat, b-CGC and rc-BK models. All these models implement the physics of saturation but differ in their dynamical assumptions. The impact parameter gluon distributions combined with the k_{\perp} factorization formalism allows one to compute single inclusive rapidity and p_{\perp} distributions in p+p collisions at the LHC. These give quite reasonable agreement with the LHC data up to $\sqrt{s}=7$ TeV. These impact parameter dependent distributions also allows one to compute the multiplicity distribution, which in the Color Glass Condensate/Glasma formalism is predicted to be a negative binomial distribution with particular values for the parameter controlling the width of the distribution. Using these assumptions, the multiplicity distributions are well reproduced in the framework of k_{\perp} -factorization. These results suggest that particle emission from Glasma flux tubes generated in collisions of “hot spots” of size $1/Q_S$ are a strong candidate for generating the multi-parton correlations underlying the multiplicity distribution. The same study has been performed using full numerical solution of the Classical Yang Mills equations on 2+1 D lattice. In this thesis work, the IP-Glasma model of fluctuating initial conditions for heavy-ion collisions has been developed. This model goes beyond the conventional implementation by using CYM solutions instead of k_{\perp} -factorization and including quantum fluctuations on

the dynamically generated transverse length scale $1/Q_s$. The parameters of this model are fixed by HERA inclusive and diffractive e+p DIS data. At fixed impact parameter, this model naturally produces NBD multiplicity fluctuations that are known to describe $p + p$ and $A + A$ multiplicity distributions, and its ratio of initial triangularity to eccentricity is more compatible with experimental data of harmonic flow coefficients.

In summary, in this work we have developed a new model of initial condition based on the framework of Color Glass Condensate which naturally describes the inclusive multiplicity distribution in $p + p$, $p + A$ collisions at RHIC and LHC energies. This model includes various sources of initial state fluctuations and produces eccentricities that are compatible to experimental data of harmonic flow coefficients and can be used as an input to hydrodynamic simulations. We develop method to study inclusive multiplicity fluctuation and correlations in heavy ion collisions. As an experimental investigation of such fluctuations, we present measurement in Au+Au collisions at top RHIC energy on the event-by-event fluctuation and the correlation of the multiplicity of neutral (photons) and charged particles. We study different models and measurement related artefacts on the observables of multiplicity fluctuations. The centrality dependence of the fluctuation in this analysis shows a small but non-zero signal of anti-correlation in the production of charged and neutral particles for most central events. The origin of such fluctuation was investigated using a DCC based model that was implemented using the moment generating function approach. An upper limit of DCC like domain formation in a medium passing through QCD chiral phase transitions in the data sample has been investigated.

Bibliography

- [1] E. Fermi, Notes on Thermodynamics and Statistics (1953).
- [2] I. Ya. Pomeranchuk, Doklady Akad. Nauk. SSSR 78 (1951) 889.
- [3] R. Hagedorn, Nuovo Cim. Suppl. 3 (1965) 147.
- [4] D.J. Gross, F.Wilczek, Phys. Rev. D **8**, (1973).
- [5] H.D. Politzer, Phys. Rev. Lett. **30**, (1973).
- [6] K.G. Wilson, Phys. Rev. D **10**, 2445 (1974).
- [7] A. M. Polyakov, Nucl. Phys. B120 (1977) 429.
- [8] J.C. Collins, M.J. Perry, Phys. Rev. Lett. 34, 1353 (1975).
- [9] N. Cabibbo and G. Parisi, Phys. Lett. 59B (1975) 67.
- [10] E.V. Shuryak, Phys. Rept. 61, 71 (1980).
- [11] M. Oevers, F. Karsch, E. Laermann, and P. Schmidt, Nucl. Phys. Proc. Suppl. 73, 465 (1999).
- [12] L. McLerran , Rev. Mod. Phys. 58, 1021 (1986).
- [13] I. Arsene et al. [BRAHMS Collaboration], Nucl. Phys. A 757, 1 (2005) [arXiv:nucl-ex/0410020].
- [14] K. Adcox et al. [PHENIX Collaboration], Nucl. Phys. A 757, 184 (2005) [arXiv:nucl-ex/0410003].
- [15] B. B. Back et al. [PHOBOS Collaboration], Nucl. Phys. A 757, 28 (2005) [arXiv:nucl-ex/0410022].
- [16] J. Adams et al. [STAR Collaboration], Nucl. Phys. A 757, 102 (2005) [arXiv:nucl-ex/0501009].
- [17] P. Senger, Nucl. Phys. A **862-863**, 139-145 (2011).
- [18] D. J. Schwarz, Annalen Phys. **12**, 220 (2003) [astro-ph/0303574].

- [19] K. A. Olive, Nucl. Phys. B **190**, 483 (1981).
- [20] F. Wilczek, hep-ph/0003183.
- [21] K. Rajagopal and F. Wilczek, In *Shifman, M. (ed.): At the frontier of particle physics, vol. 3* 2061-2151 [hep-ph/0011333].
- [22] G. Boyd, F. Karsch, E. Laermann and M. Oevers, hep-lat/9607046.
- [23] P. W. Higgs, Phys. Lett. **12**, 132 (1964).
- [24] Y. Aoki, G. Endrodi, Z. Fodor, S. D. Katz and K. K. Szabo, Nature **443**, 675 (2006) [hep-lat/0611014].
- [25] Y. Aoki, Z. Fodor, S. D. Katz and K. K. Szabo, Phys. Lett. B **643**, 46 (2006) [hep-lat/0609068].
- [26] F. Karsch and H. Satz, Phys. Rev. D **21**, 1168 (1980).
- [27] J. Kuti, B. Lukacs, J. Polonyi and K. Szlachanyi, Phys. Lett. B **95**, 75 (1980).
- [28] A. Barducci, R. Casalbuoni, S. De Curtis, R. Gatto and G. Pettini, Phys. Lett. B **231**, 463 (1989).
- [29] A. Barducci, R. Casalbuoni, S. De Curtis, R. Gatto and G. Pettini, Phys. Rev. D **41**, 1610 (1990).
- [30] A. Barducci, R. Casalbuoni, G. Pettini and R. Gatto, Phys. Rev. D **49**, 426 (1994).
- [31] S. P. Klevansky, Rev. Mod. Phys. **64**, 649 (1992).
- [32] M. A. Stephanov, Phys. Rev. Lett. **76**, 4472 (1996) [hep-lat/9604003].
- [33] A. M. Halasz, A. D. Jackson, R. E. Shrock, M. A. Stephanov and J. J. M. Verbaarschot, Phys. Rev. D **58**, 096007 (1998) [hep-ph/9804290].
- [34] Z. Fodor and S. D. Katz, JHEP **0203**, 014 (2002) [hep-lat/0106002].
- [35] M. M. Aggarwal *et al.* (STAR Collaboration), arXiv:1007.2613v1 [nucl-ex]
- [36] B. Muller, Acta Phys. Polon. B **38**, 3705 (2007) [arXiv:0710.3366 [nucl-th]].
- [37] M. Alford, K. Rajagopal and F. Wilczek, Phys. Lett. **B422**, 247 (1998) [hep-ph/9711395].
- [38] R. Rapp, T. Schäfer, E. V. Shuryak and M. Velkovsky, Phys. Rev. Lett. **81**, 53 (1998) [hep-ph/9711396].
- [39] E. Iancu, R. Venugopalan, Quark Gluon Plasma 3, Eds. R.C. Hwa, X.N. Wang, World Scientific, hep-ph/0303204; H. Weigert, Prog. Part. Nucl. Phys. **55**, 461 (2005); F. Gelis, E. Iancu, J. Jalilian-Marian, R. Venugopalan, arXiv:1002.0333.

- [40] F. Gelis, T. Lappi, L. McLerran, Nucl. Phys. A828 (2009) 149.
- [41] J. M. Maldacena, Adv. Theor. Math. Phys. **2**, 231 (1998) [hep-th/9711200].
- [42] P. Kovtun, D. T. Son and A. O. Starinets, JHEP **0310**, 064 (2003) [hep-th/0309213].
- [43] P. P. Bhaduri, P. Hegde, H. Satz and P. Tribedy, Lect. Notes Phys. **785**, 179 (2010) [arXiv:0812.3856 [hep-ph]].
- [44] T. Matsui and H. Satz, Phys. Lett. B **178**, 416 (1986).
- [45] review by H. Satz, Nucl. Phys. A 783 (2007) 249c., J. Phys. G 32 (2006) R25.
- [46] F. Karsch, M.-T. Mehr and H. Satz, Z. Phys. C 37 (1988)
- [47] E. Eichten et al., Phys. Rev. D17 (1978) 3090; Phys. Rev. D 21 (1980) 203.
- [48] S. Digal, P. Petreczky and H. Satz, Phys. Lett. B 514 (2001) 57.
- [49] E. Shuryak and I. Zahed, Phys. Rev. D **70**, 054507 (2004).
- [50] C.-Y. Wong, Phys. Rev. C 72 (2004) 034906;
C.-Y. Wong, hep-ph/0509088;
C.-Y. Wong, Phys. Rev. C 76 (2007) 014902.
- [51] W. Alberico et al., Phys. Rev. D 72 (2005) 114011.
- [52] S. Digal et al., Europ. Phys. J. C 43 (2005) 71.
- [53] T. Umeda et al., Int. J. Mod. Phys. A16 (2001) 2215.
- [54] M. Asakawa and T. Hatsuda, Phys. Rev. Lett. 92 (2004).
- [55] S. Datta et al., Phys. Rev. D 69 (2004) 094507
- [56] H. Iida et al., PoS LAT2005 (2006) 184.
- [57] A. Jacovac et al., Phys. Rev. D 75 (2007) 014506.
- [58] R. Morrin et al., PoS LAT2005 (2006) 176;
G. Aarts et al., Nucl. Phys. A 785 (2007) 198.
- [59] P. Braun-Munzinger and J. Stachel, Nucl. Phys. A690 (2001) 119.
- [60] R. L. Thews et al., Phys. Rev. C 63 (2001) 054905.
- [61] L. Grandchamp and R. Rapp, Nucl. Phys. A 709 (2002) 415.
- [62] M. C. Abreu *et al.* [NA50 Collab.], Phys. Lett. B **410** (1997) 327, 337
- [63] M. Gonin et al. (NA50 Collab.), Nucl. Phys. A 610 (1996) 404c.

- [64] M. C. Abreu *et al.* [NA50 Collaboration], Phys. Lett. B **477**, 28 (2000).
- [65] S. Chatrchyan *et al.* [CMS Collaboration], Phys. Rev. Lett. **107** (2011) 052302 [arXiv:1105.4894 [nucl-ex]].
- [66] B. Abelev *et al.* [ALICE Collaboration], Phys. Rev. Lett. **109**, 072301 (2012) [arXiv:1202.1383 [hep-ex]].
- [67] P. Pillot [ALICE Collaboration], J. Phys. G **38**, 124111 (2011) [arXiv:1108.3795 [hep-ex]].
- [68] R. Vogt, Phys. Rept. **310**, 197 (1999).
- [69] A. Mocsy, P. Petreczky and M. Strickland, Int. J. Mod. Phys. A **28**, 1340012 (2013) [arXiv:1302.2180 [hep-ph]].
- [70] D. Teaney, J. Lauret and E. V. Shuryak, Phys. Rev. Lett. **86**, 4783 (2001) [nucl-th/0011058].
- [71] J. -Y. Ollitrault, Phys. Rev. D **46**, 229 (1992).
- [72] H. Appelshauser *et al.* [NA49 Collaboration], Phys. Rev. Lett. **80**, 4136 (1998) [nucl-ex/9711001].
- [73] J. Bachler *et al.* [NA49 Collaboration], Nucl. Phys. A **661**, 45 (1999).
- [74] C. Pinkenburg *et al.* [E895 Collaboration], Phys. Rev. Lett. **83**, 1295 (1999) [nucl-ex/9903010].
- [75] K. H. Ackermann *et al.* [STAR Collaboration], Phys. Rev. Lett. **86**, 402 (2001) [nucl-ex/0009011].
- [76] P. Huovinen, In *Hwa, R.C. (ed.) et al.: Quark gluon plasma* 600-633 [nucl-th/0305064].
- [77] P. F. Kolb and U. W. Heinz, In *Hwa, R.C. (ed.) et al.: Quark gluon plasma* 634-714 [nucl-th/0305084].
- [78] A. Adare *et al.* [PHENIX Collaboration], Phys. Rev. Lett. **98**, 162301 (2007) [nucl-ex/0608033].
- [79] B. Abelev *et al.* [STAR Collaboration], Phys. Rev. Lett. **99**, 112301 (2007) [nucl-ex/0703033].
- [80] D. Molnar and S. A. Voloshin, Phys. Rev. Lett. **91**, 092301 (2003) [nucl-th/0302014].
- [81] R. J. Fries, B. Muller, C. Nonaka and S. A. Bass, Phys. Rev. C **68**, 044902 (2003) [nucl-th/0306027].
- [82] A. P. Mishra, R. K. Mohapatra, P. S. Saumia and A. M. Srivastava, Phys. Rev. C **77**, 064902 (2008) [arXiv:0711.1323 [hep-ph]].

- [83] B. Alver and G. Roland, Phys. Rev. C **81**, 054905 (2010) [Erratum-ibid. C **82**, 039903 (2010)] [arXiv:1003.0194 [nucl-th]].
- [84] U. Heinz and R. Snellings, Ann. Rev. Nucl. Part. Sci. **63**, 123 (2013) [arXiv:1301.2826 [nucl-th]].
- [85] C. Gale, S. Jeon and B. Schenke, Int. J. Mod. Phys. A **28**, 1340011 (2013) [arXiv:1301.5893 [nucl-th]].
- [86] D. A. Appel, Phys. Rev. D **33**, 717 (1986).
- [87] J. P. Blaizot and L. D. McLerran, Phys. Rev. D **34**, 2739 (1986).
- [88] M. Gyulassy and M. Plumer, Phys. Lett. B **243**, 432 (1990).
- [89] X. -N. Wang and M. Gyulassy, Phys. Rev. Lett. **68**, 1480 (1992).
- [90] X. -N. Wang, M. Gyulassy and M. Plumer, Phys. Rev. D **51**, 3436 (1995) [hep-ph/9408344].
- [91] E. Wang and X. -N. Wang, Phys. Rev. Lett. **89**, 162301 (2002) [hep-ph/0202105].
- [92] P. Tribedy and R. Venugopalan, Phys. Lett. B **710**, 125 (2012) [arXiv:1112.2445 [hep-ph]].
- [93] J. L. Albacete, A. Dumitru, H. Fujii and Y. Nara, Nucl. Phys. A **897**, 1 (2013) [arXiv:1209.2001 [hep-ph]].
- [94] I. Helenius, K. J. Eskola, H. Honkanen and C. A. Salgado, arXiv:1207.6869 [hep-ph].
- [95] B. Abelev *et al.* [ALICE Collaboration], Phys. Rev. Lett. **110**, 082302 (2013) [arXiv:1210.4520 [nucl-ex]].
- [96] K. Adcox *et al.* [PHENIX Collaboration], Phys. Rev. Lett. **88**, 022301 (2002) [nucl-ex/0109003].
- [97] C. Adler *et al.* [STAR Collaboration], Phys. Rev. Lett. **89**, 202301 (2002) [nucl-ex/0206011].
- [98] S. S. Adler *et al.* [PHENIX Collaboration], Phys. Rev. Lett. **91**, 072303 (2003) [nucl-ex/0306021].
- [99] J. Adams *et al.* [STAR Collaboration], Phys. Rev. Lett. **91**, 072304 (2003) [nucl-ex/0306024].
- [100] K. Aamodt *et al.* [ALICE Collaboration], Phys. Lett. B **696**, 30 (2011) [arXiv:1012.1004 [nucl-ex]].
- [101] S. Chatrchyan *et al.* [CMS Collaboration], Eur. Phys. J. C **72**, 1945 (2012) [arXiv:1202.2554 [nucl-ex]].
- [102] R. Baier, Y. L. Dokshitzer, A. H. Mueller, S. Peigne and D. Schiff, Nucl. Phys. B **484**, 265 (1997) [hep-ph/9608322].

- [103] R. Baier, Y. L. Dokshitzer, A. H. Mueller, S. Peigne and D. Schiff, Nucl. Phys. B **483**, 291 (1997) [hep-ph/9607355].
- [104] R. Baier, D. Schiff and B. G. Zakharov, Ann. Rev. Nucl. Part. Sci. **50**, 37 (2000) [hep-ph/0002198].
- [105] S. Wicks, W. Horowitz, M. Djordjevic and M. Gyulassy, Nucl. Phys. A **784**, 426 (2007) [nucl-th/0512076].
- [106] K. M. Burke, A. Buzzatti, N. Chang, C. Gale, M. Gyulassy, U. Heinz, S. Jeon and A. Majumder *et al.*, arXiv:1312.5003 [nucl-th].
- [107] Y. Mehtar-Tani, J. G. Milhano and K. Tywoniuk, Int. J. Mod. Phys. A **28**, 1340013 (2013) [arXiv:1302.2579 [hep-ph]].
- [108] E. V. Shuryak, Phys. Lett. B **78**, 150 (1978) [Sov. J. Nucl. Phys. **28**, 408 (1978)] [Yad. Fiz. **28**, 796 (1978)].
- [109] B. Sinha, Phys. Lett. B **128**, 91 (1983).
- [110] L. D. McLerran and T. Toimela, Phys. Rev. D **31**, 545 (1985).
- [111] C. Gale and J. I. Kapusta, Phys. Rev. D **43**, 3080 (1991).
- [112] D. K. Srivastava, B. Sinha, M. Gyulassy and X. -N. Wang, Phys. Lett. B **276**, 285 (1992).
- [113] H. A. Weldon, Phys. Rev. Lett. **66**, 293 (1991).
- [114] J. Alam, B. Sinha and S. Raha, Phys. Rept. **273**, 243 (1996).
- [115] J. I. Kapusta, P. Lichard and D. Seibert, Phys. Rev. D **44**, 2774 (1991) [Erratum-ibid. D **47**, 4171 (1993)].
- [116] R. Baier, H. Nakkagawa, A. Niegawa and K. Redlich, Z. Phys. C **53**, 433 (1992).
- [117] P. B. Arnold, G. D. Moore and L. G. Yaffe, JHEP **0112**, 009 (2001) [hep-ph/0111107].
- [118] J. Ghiglieri, J. Hong, A. Kurkela, E. Lu, G. D. Moore and D. Teaney, JHEP **1305**, 010 (2013) [arXiv:1302.5970 [hep-ph]].
- [119] L. Xiong, E. V. Shuryak and G. E. Brown, Phys. Rev. D **46**, 3798 (1992) [hep-ph/9208206].
- [120] C. Song, Phys. Rev. C **47**, 2861 (1993).
- [121] J. Alam, S. Sarkar, P. Roy, T. Hatsuda and B. Sinha, Annals Phys. **286**, 159 (2001) [hep-ph/9909267].
- [122] J. -eAlam, P. Roy and S. Sarkar, Phys. Rev. C **68**, 031901 (2003).
- [123] S. Turbide, R. Rapp and C. Gale, Phys. Rev. C **69**, 014903 (2004) [hep-ph/0308085].

- [124] P. Aurenche, M. Fontannaz, J. P. Guillet, B. A. Kniehl, E. Pilon and M. Werlen, Eur. Phys. J. C **9**, 107 (1999) [hep-ph/9811382].
- [125] R. J. Fries, B. Müller and D. K. Srivastava Phys. Rev. Lett. **90**, 132301(2003) [nucl-th/0208001].
- [126] B. G. Zakharov JETP Lett. **80** (2004) 1-6 [hep-ph/0405101].
- [127] M. M. Aggarwal *et al.* [WA98 Collaboration], Phys. Rev. Lett. **85**, 3595 (2000) [nucl-ex/0006008].
- [128] S. S. Adler *et al.* [PHENIX Collaboration], Phys. Rev. Lett. **94**, 232301 (2005) [nucl-ex/0503003].
- [129] S. S. Adler *et al.* [PHENIX Collaboration], Phys. Rev. C **76**, 034904 (2007) [nucl-ex/0611007].
- [130] R. Chatterjee, E. S. Frodermann, U. W. Heinz and D. K. Srivastava, Phys. Rev. Lett. **96**, 202302 (2006) [nucl-th/0511079].
- [131] D. K. Srivastava and J. I. Kapusta, Phys. Rev. C **48**, 1335 (1993).
- [132] D. K. Srivastava and J. I. Kapusta, Phys. Lett. B **307**, 1 (1993).
- [133] A. Adare *et al.* [PHENIX Collaboration], Phys. Rev. Lett. **104**, 132301 (2010) [arXiv:0804.4168 [nucl-ex]].
- [134] M. Wilde [ALICE Collaboration], Nucl. Phys. A **904-905**, 573c (2013) [arXiv:1210.5958 [hep-ex]].
- [135] R. Rapp and J. Wambach, Adv. Nucl. Phys. **25**, 1 (2000) [hep-ph/9909229].
- [136] G. Agakichiev *et al.*, CERES collaboration, Phys. Rev. Lett. **75**, 1272 (1995); Phys. Lett. **B422**, 405 (1998); Nucl. Phys. **A661**, 23 (1999).
- [137] N. Masera *et al.* (HELIOS-3 collaboration), Nucl. Phys. **A590**, 93c (1995); A.L.S. Angelis *et al.* (HELIOS-3 collaboration), preprint CERN-EP/98-82.
- [138] M.C. Abreu *et al.* (NA38/NA50 collaboration), preprint CERN-EP/99-112; E. Scomparin *et al.* (NA50 collaboration), J. Phys. **G25**, 235 (1999); P. Bordalo *et al.* (NA50 collaboration), Nucl. Phys. **A661**, 538 (1999).
- [139] R. Arnaldi *et al.* [NA60 Collaboration], Phys. Rev. Lett. **96**, 162302 (2006) [nucl-ex/0605007].
- [140] F. Geurts *et al.* [STAR Collaboration] 217c (2013). Nucl.Phys., **A904-905**, 217
- [141] S. Jeon and V. Koch, Phys. Rev. Lett. **85**, 2076 (2000) [hep-ph/0003168].
- [142] S. Jeon and V. Koch, Phys. Rev. Lett. **83**, 5435 (1999) [nucl-th/9906074].

- [143] M. Asakawa, U. W. Heinz and B. Muller, Phys. Rev. Lett. **85**, 2072 (2000) [hep-ph/0003169].
- [144] M. A. Stephanov, K. Rajagopal and E. V. Shuryak, Phys. Rev. D **60**, 114028 (1999) [hep-ph/9903292].
- [145] J.D. Bjorken, What lies ahead?, SLAC-PUB-5673, 1991.
- [146] J. P. Blaizot and A. Krzywicki, Phys. Rev. D **46**, 246 (1992).
- [147] K. Rajagopal and F. Wilczek, Nucl. Phys. B **399**, 395 (1993) [arXiv:hep-ph/9210253].
- [148] K. Rajagopal, arXiv:hep-ph/9504310.
- [149] A. M. Srivastava, Pramana - J. Phys. **55**, 1-2 (2000) 53-62
- [150] T. C. Brooks *et al.* [MiniMax Collaboration], Phys. Rev. D **55**, 5667 (1997) [arXiv:hep-ph/9609375].
- [151] C. Pruneau, S. Gavin and S. Voloshin, Phys. Rev. C **66**, 044904 (2002) [arXiv:nucl-ex/0204011].
- [152] B. I. Abelev *et al.* [STAR Collaboration], Phys. Rev. Lett. **103**, 092301 (2009) [arXiv:0901.1795 [nucl-ex]].
- [153] S. M. Dogra [STAR Collaboration], J. Phys. G **35**, 104094 (2008).
- [154] J. Pumphin, Phys. Rev. D **50**, 6811 (1994) [arXiv:hep-ph/9407332].
- [155] C. Pruneau *et al.* Phys. Rev. C **66**, 044904 (2002)
- [156] T. A. Trainor, [hep-ph/0001148].
- [157] X. F. Luo, B. Mohanty, H. G. Ritter and N. Xu, J. Phys. G **37**, 094061 (2010) [arXiv:1001.2847 [nucl-ex]].
- [158] V. V. Begun, M. Gazdzicki, M. I. Gorenstein and O. S. Zozulya, Phys. Rev. C **70**, 034901 (2004) [arXiv:nucl-th/0404056].
- [159] V. V. Begun, M. I. Gorenstein and O. A. Mogilevsky, Phys. Rev. C **82**, 024904 (2010) [arXiv:1004.2918 [nucl-th]].
- [160] X. N. Wang and M. Gyulassy, Phys. Rev. D **44**, 3501(1991).
- [161] Z. W. Lin, C. M. Ko, B. A. Li, B. Zhang and S. Pal, Phys. Rev. C **72**, 064901 (2005) [arXiv:nucl-th/0411110].
- [162] S. A. Bass *et al.*, Prog. Part. Nucl. Phys. **41**, 255 (1998) [Prog. Part. Nucl. Phys. **41**, 225 (1998)] [arXiv:nucl-th/9803035].
- [163] B. Mohanty and J. Serreau, Phys. Rept. **414**, 263 (2005) [arXiv:hep-ph/0504154].

- [164] R. S. Longacre, arXiv:1105.5321 [nucl-th].
- [165] P. Christiansen *et al.* Phys. Rev. C **80**, 034903 (2009). [arXiv:0902.4788 [hep-ex]].
- [166] P. Tribedy *et al.* Phys. Rev. C **85**, 024902 (2012). [arXiv:1108.2495 [nucl-ex]]
- [167] T. C. Brooks *et al.* [MiniMax Collaboration], Phys. Rev. D **61**, 032003 (2000) [arXiv:hep-ex/9906026].
- [168] M. Anderson *et al.*, Nucl. Instrum. Meth. A **499** (2003) 659
- [169] L. Kotchenda *et al.*, Nucl. Instrum. Meth. A **499** (2003) 703
- [170] C. Adler *et al.* [STAR Collaboration], Nucl. Instrum. Meth. A **499** (2003) 633
- [171] M. Beddo *et al.*, Nucl. Instrum. Meth. A **499** (2003) 725
- [172] C. E. Allgower *et al.*, Nucl. Instrum. Meth. A **499** (2003) 740
- [173] W.J. Llope *et al.*, Nucl. Instrum. Meth. A **522** (2004) 252
- [174] J. Adams *et al.* [STAR Collaboration], [arXiv:nucl-ex/0511026].
- [175] K. H. Ackermann *et al.*, Nucl. Instr. Meth. A **499**, 713 (2003).
- [176] M. M. Aggarwal *et al.*, Nucl. Instr. Meth. A **499**, 751 (2003); M. M. Aggarwal *et al.*, Nucl. Instr. Meth. A **488**, 131 (2002).
- [177] X. Luo, J. Xu, B. Mohanty and N. Xu, J. Phys. G **40**, 105104 (2013) [arXiv:1302.2332 [nucl-ex]].
- [178] L. Adamczyk *et al.* [STAR Collaboration], Phys. Rev. Lett. **112**, 032302 (2014) [arXiv:1309.5681 [nucl-ex]].
- [179] L. Adamczyk *et al.* [STAR Collaboration], arXiv:1402.1558 [nucl-ex].
- [180] B. I. Abelev *et al.* [STAR Collaboration], Phys. Rev. C **79**, 024906 (2009) [arXiv:0807.3269 [nucl-ex]].
- [181] A. M. Poskanzer and S. A. Voloshin, Phys. Rev. C **58**, 1671 (1998) [nucl-ex/9805001].
- [182] HERA Structure Function Working Group, Nucl. Phys. B **181-182** (2008) 57-61
- [183] K. Nakamura *et al.* (Particle Data Group), J. Phys. G **37**, 075021 (2010).
- [184] J. Breitweg *et al.*, Eur. Phys. J. **67**, 609 (1999) and references therein.
- [185] L.V. Gribov, E.M. Levin, M.G. Ryskin, Phys. Rept. **100**, 1 (1983); A.H. Mueller, J-W. Qiu, Nucl. Phys. **B 268**, 427 (1986).

- [186] R. P. Feynman, Photon-Hadron Interactions. Reading, Massachusetts: W.A. Benjamin. (1972); Feynman R.P. Phys. Rev. Lett. 23: 1415, 1969; Bjorken J.D. and Paschos E.A. Phys. Rev. 185: 1975, 1969
- [187] P.A.M. Dirac, Rev. Mod. Phys. **21**, 392 (1949).
- [188] S. Weinberg, Phys. Rev. **150**, 1313 (1966).
- [189] L. Susskind, Phys. Rev. **165**, 1535, (1968).
- [190] L.D. McLerran, R. Venugopalan, Phys. Rev. **D 49**, 2233 (1994); *ibid.*, **D 49**, 3352 (1994); *ibid.* **D 50**, 2225 (1994); Yu.V. Kovchegov, Phys. Rev. **D 54**, 5463 (1996); J. Jalilian-Marian, A. Kovner, L.D. McLerran, H. Weigert, Phys. Rev. **D 55**, 5414 (1997); E. Iancu, A. Leonidov and L. D. McLerran, Nucl. Phys. A **692**, 583 (2001).
- [191] J. Jalilian-Marian, A. Kovner, L. D. McLerran, H. Weigert, *Phys. Rev.* **D55**, 5414 (1997).
- [192] L. D. McLerran, R. Venugopalan, Phys. Rev. D **59**, 094002 (1999); R. Venugopalan, Acta Phys. Polon. B **30**, 3731 (1999).
- [193] N. N. Nikolaev, B. G. Zakharov, Z. Phys. C **49**, 607 (1991); A. H. Mueller, Nucl. Phys. B **335**, 115 (1990).
- [194] K. J. Golec-Biernat, M. Wusthoff, Phys. Rev. D **59**, 014017 (1998); K. J. Golec-Biernat, M. Wusthoff, Phys. Rev. D **60**, 114023 (1999)
- [195] Jalilian-Marian, A. Kovner, A. Leonidov, H. Weigert, Nucl. Phys. **B 504**, 415 (1997); *ibid.*, Phys. Rev. **D 59**, 014014 (1999); E. Iancu, A. Leonidov, L.D. McLerran, Nucl. Phys. **A 692**, 583 (2001); E. Ferreiro, E. Iancu, A. Leonidov, L.D. McLerran, Nucl. Phys. **A 703**, 489 (2002).
- [196] I. Balitsky, Nucl. Phys. **B 463**, 99 (1996); Yu.V. Kovchegov, Phys. Rev. **D 61**, 074018 (2000).
- [197] H. Kowalski, D. Teaney, Phys. Rev. D **68**, 114005 (2003).
- [198] J. Bartels, K. J. Golec-Biernat, H. Kowalski, Phys. Rev. D **66**, 014001 (2002).
- [199] H. Kowalski, L. Motyka, G. Watt, Phys. Rev. D **74**, 074016 (2006)
- [200] S. Chekanov *et al.* [ZEUS Collaboration], Eur. Phys. J. C **21**, 443 (2001).
- [201] C. Adloff *et al.* [H1 Collaboration], Eur. Phys. J. C **21**, 33 (2001).
- [202] S. Chekanov *et al.* (ZEUS Collaboration), Eur. Phys. J. C **24**, 345 (2002), Nucl. Phys. **B695**, 3 (2004).
- [203] A. Aktas *et al.* (H1 Collaboration), Eur. Phys. J. C **46**, 585 (2006).
- [204] G. Watt, H. Kowalski, Phys. Rev. D **78**, 014016 (2008)

- [205] E. Iancu, K. Itakura, S. Munier, Phys. Lett. B **590**, 199 (2004).
- [206] J. L. Albacete, Y. V. Kovchegov, Phys. Rev. D **75**, 125021 (2007).
- [207] I. Balitsky, Phys. Rev. D **75**, 014001 (2007).
- [208] Y. V. Kovchegov, H. Weigert, Nucl. Phys. A **784**, 188 (2007).
- [209] I. Balitsky, G. A. Chirilli, Phys. Rev. D **77**, 014019 (2008); G. Beuf, arXiv:1008.0498 [hep-ph].
- [210] J. Berger, A. Stasto, arXiv:1010.0671 [hep-ph].
- [211] J. L. Albacete, N. Armesto, J. G. Milhano, C. A. Salgado, Phys. Rev. D **80**, 034031 (2009).
- [212] K. Dusling, F. Gelis, T. Lappi, R. Venugopalan, Nucl. Phys. A **836**, 159 (2010).
- [213] J. L. Albacete, C. Marquet, Phys. Lett. B **687**, 174 (2010).
- [214] J. L. Albacete, C. Marquet, Phys. Rev. Lett. **105**, 162301 (2010).
- [215] J.P. Blaizot, F. Gelis, R. Venugopalan, Nucl. Phys. A **743**, 57 (2004).
- [216] M.A. Braun, Phys. Lett. B **483**, 105 (2000).
- [217] F. Gelis, A. M. Stasto, R. Venugopalan, Eur. Phys. J. C **48**, 489 (2006).
- [218] V. N. Gribov, arXiv:hep-ph/0006158.
- [219] B. A. Kniehl, G. Kramer, B. Potter, Nucl. Phys. B **582**, 514 (2000).
- [220] S. Eidelman et al. [Particle Data Group Collaboration], “Review of particle physics”, Phys. Lett. B **592** 1 (2004).
- [221] ALICE Collaboration, Eur. Phys. J. C **65** (2010) 111 [arXiv:0911.5430]; arXiv:1004.3034.
- [222] CMS Collaboration, Phys Rev Lett **105**, 022002 (2010).
- [223] STAR Collaboration, Phys. Rev. Lett. **91**, 172302 (2003), Phys. Rev. C **79**, 034909 (2009).
- [224] ATLAS Collaboration, Phys. Lett. B **688** (2010) 21 [arXiv:1003.3124].
- [225] L. McLerran, M. Praszalowicz, Acta Phys. Polon. B **41**, 1917 (2010).
- [226] ALICE Collaboration, Eur.Phys.J.C **68**:345-354,2010 [arXiv:1004.3514].
- [227] CDF collaboration, Phys. Rev. D **41** (1990) 2330; Phys. Rev. Lett. **61** (1988) 1819.
- [228] UA5 collaboration, Z. Phys. C **33** (1986) 1.
- [229] E735 Collaboration, T. Alexopoulos et al., Phys. Rev. Lett. **60**, 1622 (1988).

- [230] UA1 collaboration, A. M. Rossi et al., Nucl. Phys. B84 (1975) 269.
- [231] J. Adams *et al.* [STAR Collaboration], Phys. Rev. Lett. **97**, 152302 (2006).
- [232] I. Arsene *et al.* [BRAHMS Collaboration], Phys. Rev. Lett. **93**, 242303 (2004).
- [233] B. B. Back, *et al.*, Phys. Rev. Lett. **93**, 082301 (2004).
- [234] I. Arsene *et al.* [BRAHMS Collaboration], Phys. Rev. Lett. **94**, 032301 (2005).
- [235] D. d'Enterria, G. K. Eyyubova, V. L. Korotkikh, I. P. Lokhtin, S. V. Petrushanko, L. I. Sarycheva and A. M. Snigirev, Eur. Phys. J. C **66**, 173 (2010).
- [236] H. Kowalski, T. Lappi, R. Venugopalan, Phys. Rev. Lett. **100**, 022303 (2008).
- [237] K. Dusling, F. Gelis, T. Lappi and R. Venugopalan, Nucl. Phys. A **836**, 159 (2010).
- [238] D. Kharzeev and M. Nardi, Phys. Lett. B **507**, 121 (2001).
- [239] K. Aamodt *et al.* [ALICE Collaboration], Eur. Phys. J. C **68**, 89 (2010).
- [240] V. Khachatryan *et al.* [CMS Collaboration], JHEP **1002**, 041 (2010).
- [241] K. Aamodt *et al.* [ALICE Collaboration], Eur. Phys. J. C **68**, 345 (2010).
- [242] **UA5** collaboration, G. J. Alner *et al.*, *Z. Phys.* **C33** (1986) 1; **UA1** collaboration, C. Albajar *et al.*, *Nucl. Phys.* **B335** (1990) 261; **CDF** collaboration, F. Abe *et al.*, *Phys. Rev.* **D41** (1990) 2330
- [243] B. I. Abelev *et al.* [STAR Collaboration], Phys. Rev. C **79**, 034909 (2009).
- [244] **STAR** collaboration, C. Adler *et al.*, *Phys. Rev. Lett.* **87** (2001) 112303; **PHOBOS** collaboration, B. B. Back *et al.*, *Phys. Rev. Lett.* **85** (2000) 3100; **BRAHMS** collaboration, I. G. Bearden *et al.*, *Phys. Lett.* **B523** (2001) 227; **BRAHMS** collaboration, I. G. Bearden *et al.*, *Phys. Rev. Lett.* **88** (2002) 202301; **PHOBOS** collaboration, B. B. Back *et al.*, *Phys. Rev.* **C65** (2002) 061901; **PHENIX** collaboration, S. S. Adler *et al.*, *Phys. Rev.* **C71** (2005) 034908.
- [245] R. Baier, A. H. Mueller, D. Schiff and D. T. Son, arXiv:1103.1259 [nucl-th].
- [246] J. -P. Blaizot, F. Gelis, J. Liao, L. McLerran and R. Venugopalan, arXiv:1107.5296 [hep-ph].
- [247] B. B. Back *et al.* [PHOBOS Collaboration], Phys. Rev. C **65**, 061901 (2002).
- [248] K. Aamodt *et al.* [ALICE Collaboration], Phys. Rev. Lett. **106**, 032301 (2011).
- [249] B. B. Back, M. D. Baker, D. S. Barton, R. R. Betts, M. Ballintijn, A. A. Bickley, R. Bindel and A. Budzanowski *et al.*, Phys. Rev. Lett. **91**, 052303 (2003).
- [250] S. Chatrchyan *et al.* [CMS Collaboration], JHEP **1108**, 141 (2011).

- [251] H. I. Miettinen, J. Pumplin, *Phys. Rev. D* **18**, 1696 (1978).
- [252] T. Lappi, L.D. McLerran, *Nucl. Phys. A* **772**, 200 (2006).
- [253] F. Gelis, T. Lappi, R. Venugopalan, *Phys. Rev. D* **78**, 054019 (2008); *ibid.*, **78**, 054020 (2008); *ibid.*, **79**, 094017 (2009).
- [254] A. Dumitru, F. Gelis, L. McLerran, R. Venugopalan, *Nucl. Phys. A* **810**, 91 (2008).
- [255] N. Armesto, L. McLerran, C. Pajares, *Nucl. Phys. A* **781**, 201 (2007).
- [256] T. Lappi, L. McLerran, *Nucl. Phys. A* **832**, 330 (2010).
- [257] K. Dusling, D. Fernandez-Fraile and R. Venugopalan, *Nucl. Phys. A* **828**, 161 (2009) [arXiv:0902.4435 [nucl-th]]
- [258] E. A. De Wolf, I. M. Dremin, W. Kittel, *Phys. Rept.* **270**, 1 (1996).
- [259] PHENIX collaboration, A. Adare et. al., *Phys. Rev. C* **78** (2008) 044902.
- [260] A. Dumitru, L. D. McLerran, *Nucl. Phys. A* **700**, 492 (2002).
- [261] D. d'Enterria, G. K. Eyyubova, V. L. Korotkikh, I. P. Lokhtin, S. V. Petrushanko, L. I. Sarycheva, A. M. Snigirev, *Eur. Phys. J. C* **66**, 173 (2010).
- [262] L. Frankfurt, M. Strikman, C. Weiss, *Ann. Rev. Nucl. Part. Sci.* **55**, 403 (2005).
- [263] M. L. Miller, K. Reygers, S. J. Sanders, P. Steinberg, *Ann. Rev. Nucl. Part. Sci.* **57**, 205 (2007).
- [264] F. Gelis, R. Venugopalan, *Nucl. Phys. A* **776**, 135 (2006); *ibid. A* **779**, 177 (2006).
- [265] UA5 Collaboration, *Z. Phys. C* **43** (1989) 357.
- [266] J. Bartels, K. J. Golec-Biernat, H. Kowalski, *Phys. Rev. D* **66**, 014001 (2002).
- [267] H. Kowalski, D. Teaney, *Phys. Rev. D* **68**, 114005 (2003).
- [268] A. Kovner, L. D. McLerran, H. Weigert, *Phys. Rev. D* **52**, 6231 (1995).
- [269] Y. V. Kovchegov, D. H. Rischke, *Phys. Rev. C* **56**, 1084 (1997).
- [270] A. Krasnitz, R. Venugopalan, *Nucl. Phys. B* **557**, 237 (1999).
- [271] A. Krasnitz, R. Venugopalan, *Phys. Rev. Lett.* **84**, 4309 (2000).
- [272] A. Krasnitz and R. Venugopalan, *Phys. Rev. Lett.* **86**, 1717 (2001) [hep-ph/0007108].
- [273] T. Lappi, *Phys. Rev. C* **67**, 054903 (2003).
- [274] A. Krasnitz, R. Venugopalan, *Phys. Rev. Lett.* **84**, 4309 (2000).

- [275] T. Lappi, *Phys. Rev.* **C67**, 054903 (2003).
- [276] B. Schenke, P. Tribedy, R. Venugopalan, *Phys. Rev. Lett.* **108**, 252301 (2012).
- [277] B. Schenke, P. Tribedy, R. Venugopalan, *Phys. Rev.* **C86**, 034908 (2012).
- [278] B. Schenke, P. Tribedy and R. Venugopalan, *Phys. Rev. C* **89**, 024901 (2014) [arXiv:1311.3636 [hep-ph]].
- [279] R. S. Mackintosh. 1977. Rept. Prog. Phys., **40**, 731
- [280] T. Lappi, *Eur. Phys. J.* **C55**, 285 (2008).
- [281] Y. V. Kovchegov, *Phys. Rev.* **D54**, 5463 (1996).
- [282] A. Krasnitz, Y. Nara, R. Venugopalan, *Phys. Rev. Lett.* **87**, 192302 (2001).
- [283] R. Anson, *et al.*, *Z.Phys.* **C43**, 357 (1989).
- [284] V. Khachatryan, *et al.*, *Phys.Rev.Lett.* **105**, 022002 (2010).
- [285] S. Chatrchyan, *et al.*, *Phys.Lett.* **B722**, 5 (2013).
- [286] B. A. Kniehl, G. Kramer, B. Potter, *Nucl.Phys.* **B582**, 514 (2000).
- [287] G. Aad, *et al.*, *New J.Phys.* **13**, 053033 (2011).
- [288] J. L. Albacete and A. Dumitru, arXiv:1011.5161 [hep-ph].
- [289] J. L. Albacete, N. Armesto, J. G. Milhano, C. A. Salgado, *Phys. Rev.* **D80**, 034031 (2009).
- [290] T. Lappi and H. Mantysaari, *Phys. Rev. D* **88**, 114020 (2013) [arXiv:1309.6963 [hep-ph]].
- [291] A. Dumitru and E. Petreska, *Nucl. Phys. A* **879**, 59 (2012) [arXiv:1112.4760 [hep-ph]].
- [292] R. Sassot, P. Zurita and M. Stratmann, *Phys. Rev. D* **82**, 074011 (2010) [arXiv:1008.0540 [hep-ph]].
- [293] A. Kovner, L. D. McLerran, H. Weigert, *Phys. Rev.* **D52**, 3809 (1995).
- [294] M. Gyulassy, L. D. McLerran, *Phys. Rev.* **C56**, 2219 (1997).
- [295] A. Dumitru, L. D. McLerran, *Nucl. Phys.* **A700**, 492 (2002).
- [296] J. P. Blaizot, F. Gelis, R. Venugopalan, *Nucl. Phys.* **A743**, 57 (2004).
- [297] D. Kharzeev, E. Levin, M. Nardi, *Nucl. Phys.* **A730**, 448 (2004).
- [298] J. Albacete, *et al.*, *Int.J.Mod.Phys.* **E22**, 1330007 (2013).
- [299] I. Arsene, *et al.*, *Phys.Rev.Lett.* **94**, 032301 (2005).
- [300] B. Abelev, *et al.*, *Phys.Rev.Lett.* **110**, 032301 (2013).

- [301] A. Iordanova, *J.Phys.Conf.Ser.* **458**, 012004 (2013).
- [302] S. S. Adler, *et al.*, *Phys. Rev.* **C71**, 034908 (2005).
- [303] K. Aamodt, *et al.*, *Phys. Rev. Lett.* **106**, 032301 (2011).
- [304] C. Gale, S. Jeon, B. Schenke, P. Tribedy, R. Venugopalan, *Phys.Rev.Lett.* **110**, 012302 (2013).
- [305] B. Schenke, S. Jeon, C. Gale, *Phys. Rev.* **C82**, 014903 (2010).
- [306] B. Schenke, S. Jeon, C. Gale, *Phys. Rev. Lett.* **106**, 042301 (2011).
- [307] V. Khachatryan *et al.* [CMS Collaboration], *JHEP* **1101**, 079 (2011) [arXiv:1011.5531 [hep-ex]].
- [308] A. Dumitru and E. Petreska, arXiv:1209.4105 [hep-ph].
- [309] B. I. Abelev, *et al.*, *Phys. Rev.* **C79**, 034909 (2009).
- [310] A. Dumitru, F. Gelis, L. McLerran, R. Venugopalan (2008).
- [311] S. Gavin, L. McLerran, G. Moschelli, *Phys. Rev.* **C79**, 051902 (2009).
- [312] F. Gelis, T. Lappi, L. McLerran, *Nucl. Phys.* **A828**, 149 (2009).
- [313] T. Lappi, S. Srednyak, R. Venugopalan, *JHEP* **01**, 066 (2010).
- [314] A. Dumitru, Y. Nara, *Phys.Rev.* **C85**, 034907 (2012).
- [315] T. Hirano, U. W. Heinz, D. Kharzeev, R. Lacey and Y. Nara, *Phys. Lett. B* **636**, 299 (2006) [nucl-th/0511046].
- [316] H. -J. Drescher, A. Dumitru, A. Hayashigaki and Y. Nara, *Phys. Rev. C* **74**, 044905 (2006) [nucl-th/0605012].
- [317] H. -J. Drescher and Y. Nara, *Phys. Rev. C* **76**, 041903 (2007) [arXiv:0707.0249 [nucl-th]].
- [318] B. Schenke, S. Jeon and C. Gale, *Phys. Rev. C* **85**, 024901 (2012) [arXiv:1109.6289 [hep-ph]].
- [319] A. Bzdak, B. Schenke, P. Tribedy and R. Venugopalan, *Phys. Rev. C* **87**, no. 6, 064906 (2013) [arXiv:1304.3403 [nucl-th]].

Index

- J/ψ , 34, 127
- k_{\perp} factorization, 129

- AGS, 27

- b-CGC model, 126, 127
- Baryon chemical potential, 30
- Big-Bang, 27
- BK equation, 123
- Boltzmann gas, 62
- Born-Oppenheimer separation, 120

- Central limit theorem, 59
- CGC, 31, 118, 122
- Chiral condensate, 43
- Chiral phase transition, 43
- Chiral symmetry, 29
- Classical Yang-Mills, 150
- Color charge density, 152
- Color Glass Condensate, 31, 118, 122
- Correlation, 39
- Correlation- γ – ch, 55
- Correlation-away side, 111
- Correlation-charged-to-neutral, 105
- Correlation-color charge density, 152
- Correlation-n-particle, 143
- Correlation-net charge, 108
- Correlation-same side, 110
- Correlation-spurious, 55

- DCC, 44, 46, 49, 61
- DCC-model, 70
- DCC-Monte Carlo, 70
- DCC-pion distributions, 65
- DCC-pion fraction, 68, 73

- DCC-upper limit, 116
- De-confinement transition, 33
- Di-leptons, 38
- Dipole cross section, 124, 126
- Dipole model, 122
- Dipole-cross section, 123
- Dipole-nucleus cross section, 151
- Disoriented Chiral Condensate, 44

- Eccentricity, 170, 171
- Efficiency, 50, 54
- Electromagnetic probes, 37
- Energy loss, 36
- Error-analysis, 98
- Error-Bootstrap method, 98
- Error-statistical, 98, 99
- Error-systematic, 100, 102

- Field-tensor, 154
- Flow-anisotropic, 34, 41
- Flow-effect on γ – ch correlation, 113
- Fluctuation- γ – ch, 77
- Fluctuation-charge-to-neutral, 77
- Fluctuation-initial state, 118
- Fluctuation-net charge, 108
- Fluctuations, 39
- Fluctuations-conserved charges, 39
- Fluctuations-dynamical, 44
- Fluctuations-energy density, 165
- Fluctuations-geometric, 40
- Fluctuations-initial state, 40, 41
- Fluctuations-intial geometry, 35
- Fluctuations-multiplicity, 39, 42, 165
- Fluctuations-observables, 49

Fluctuations-quantum, 40
 Fluctuations-spurious, 41
 Fragmentation functions, 131, 157

 Gauge-Coulomb, 155
 Gauge-Fock-Schwinger, 153
 Gauge-light cone, 153
 Gauge-Lorentz, 153
 GBW model, 122, 123
 GEANT simulation, 101, 104
 Generic-pion production, 65, 68
 Glasma, 31, 143
 Glasma fields, 154
 Glasma fields, 150
 Glasma flux tubes, 145
 Gluon saturation, 119
 Grand canonical ensemble, 39, 42, 62
 Gribov diffusion, 131

 HERA-data, 118
 HERA-DIS, 119, 122
 Higgs, 29
 Higgs field, 28

 Infinite momentum frame, 120
 Initial state-fluctuations, 168
 Initial state-geometry, 168
 IP-Glasma model, 150
 IP-Sat model, 123–125, 136, 150

 Jacobian, 130, 155
 Jet quenching, 35
 JIMWLK equation, 121

 Lattice implementation, 154
 LHC, 27
 Light front co-ordinates, 120

 MC-Glauber model, 169
 MC-KLN model, 169
 McLerran-Venugopalan model, 121, 129
 Mis-identification, 54
 Mixed event analysis, 89, 92–94
 Moment-factorial, 46, 48, 51
 Moment-generating functions, 41, 47–51, 55, 57

 Multiplicity distributions-charge particles, 94
 Multiplicity distributions-in A+A, 150, 164, 165
 Multiplicity distributions-in p+p, 147, 163
 Multiplicity distributions-photons, 93

 Negative Binomial distribution, 144, 165, 167

 Observable- ν_{dyn} , 49, 51, 52, 66, 67, 77, 106
 Observable-fluctuations, 49
 Observable-robust, 66, 67, 78
 Observables-robust, 49
 Opacity, 35

 Perfect fluid, 34
 Phase diagram of QCD, 30
 Phase transitions, 28
 Phase transitions in QCD, 28
 Phase transitions, first order, 28
 Photons-direct, 37
 Photons-spectra, 37
 Photons-thermal, 37

 QCD critical point, 29, 30
 QCD mass, 29
 QCD scale, 29
 QCD-running coupling, 124, 155
 QGP, 26
 Quality assurance studies, 86–89, 91
 Quark condensate, 29
 Quark Gluon Plasma, 26
 Quark mass, 30
 Quarkonia, 33, 34
 Quarkonia suppression, 33

 Rapidity gap, 58
 rc-BK model, 128, 136
 Regge-Gribov limit, 120
 Resonance decay, 56
 Results- γ – ch correlation, 106
 Results- ν_{dyn} , 106
 Results- N_{part} dependence, 112
 Results-A+A collisions, 140, 142, 161

Results-asymmetric nuclear collision, 160
 Results-charge fluctuations, 105
 Results-d+A collisions, 137, 138, 140, 158
 Results-deformed nuclear collision, 160
 Results-net charge, 108
 Results-p+A collisions, 137, 138, 140, 158
 Results-p+p collisions, 132, 133, 137, 138, 156
 Results-photon fluctuations, 105
 Results-rapidity distributions, 132, 137, 160
 Results-rapidity gap, 110
 Results-robust observable, 108, 112
 Results-transverse momentum distributions, 133, 137, 138, 158, 159
 RHIC, 27, 34
 Saturation models, 122
 Saturation scale, 31, 146, 147
 Screening mass, 33
 Small-x limit, 120
 SPS, 27, 34
 sQGP, 31
 STAR-BEMC, 81
 STAR-detector, 79
 STAR-EEMC, 81
 STAR-Electromagnetic Calorimeter, 81
 STAR-experiment, 79
 STAR-Forward Time Projection Chambers, 82
 STAR-Photon Multiplicity Detector, 82, 85
 STAR-Time of Flight, 81
 STAR-Time Projection Chamber, 80
 STAR-ZDC, 84
 Stress-Energy tensor, 154
 Wilson lines, 153
 Woods-Saxon distribution, 151
 Yang-Mills equation, 153